Physica B 676 (2024) 415654

Contents lists available at ScienceDirect

Physica B: Condensed Matter

journal homepage: www.elsevier.com/locate/physb

Investigation of linear and nonlinear optical properties in quantum dots: Influence of magnetic and AB flux fields

Munesh Bansal [a], Vinod Kumar [b], Sahil [a], S.B. Bhardwaj [c], Ram Mehar Singh [a,*], Fakir Chand [b]

[a] Department of Physics, Chaudhary Devi Lal University, Sirsa, 125055, Haryana, India
[b] Department of Physics, Kurukshetra University, Kurukshetra, 136119, Haryana, India
[c] Department of Physics, S. U. S. Govt. College, Indri, Karnal, 132041, Haryana, India

ARTICLE INFO

Keywords:
Schrödinger equation
IQHY potential
NUFA method
Eigenvalues spectra
Optical properties

ABSTRACT

In the present work, analytical expressions for the energy eigenvalues and eigen functions are obtained by solving the radial Schrödinger equation for inverse quadratic Hellmann plus Yukawa (IQHY) potential using Nikiforov-Uvarov functional analysis method. As an application part of this work, expressions for the linear and third-order nonlinear absorption coefficients and refractive index changes are computed to study the optical properties of the spherical GaAs quantum dots. We extend the investigation of the IQHY potential by incorporating the effects of magnetic and Aharonov–Bohm (AB) flux fields. Our results reveal that the optical properties of the GaAs quantum dots are strongly influenced by variations in the dot radius, potential height and intensity of incident photons. Specifically, we observe that the introduction of magnetic and AB flux fields significantly alters the energy eigenvalues and eigenfunctions, leading to distinct optical characteristics. The results of present study are found in consistent with other theoretical studies available in the literature.

1. Introduction

The interest of scientific community is growing rapidly in the area of semiconductor technology due to their ability of fabricating structures with diverse geometrical forms and having applications in high speed electro-optical modulators, infrared photo-detectors, and other semiconductor devices [1,2]. In case of low dimensional semiconductor materials, the development of electrical and opto-electronic devices depend on the induction of nonlinear optical effects by quantum confinement phenomena. Lots of theoretical as well as experimental results are available in literature for linear as well as nonlinear optical properties of structures like quantum wells, quantum wires, and quantum dots (QDs) [3–16]. In order to calculate optical properties of QDs, numerous potential models have been explored in past and few of them are summarized as follows.

Khordad and Mirhosseini [17,18] derived expressions for linear and third-order nonlinear absorption coefficients (AC) and refractive index changes (RIC) using the Teitz and Rosen–Morse potentials for spherical GaAs QDs. Xie [19] theoretically investigated the optical AC and RIC of spherical GaAs−$Ga_{1-x}Al_xAs$ QDs by using the Gaussian confinement potential. Employing modified Kratzer potential, Khordad [20] computed the electronic and optical properties for spherical GaAs – $Ga_{1-x}Al_xAs$ QDs using numerical diagonalization of the Hamiltonian matrix. Zhang et al. [21] studied the optical AC by considering the electron–phonon interaction in asymmetrical quantum wells and showed that the optical AC depend strongly on the parameters of quantum well.

Using the compact density matrix and iterative approaches, Liu and Guo [22] computed the optical properties of spherical QDs with ring-shaped non-spherical oscillator potential. Further, using the Hulthén and Manning-Rosen potentials, Onyeaju et al. [23,24] studied optical properties of spherical GaAs/AlGaAs QDs and found that the dot radius, the dipole matrix and the energy terms, greatly influence the optical properties of QDs. Within the framework of effective mass approximation scheme, Lu et al. [25] studied the effects of intense laser fields on the nonlinear optical properties of donor impurities in GaAs/AlGaAs QDs using the Woods–Saxon potential. For the same potential model, Xie [26] studied the optical properties of spherical QDs (GaAs/AlGaAs) by using numerical diagonalization of the Hamiltonian matrix. Liu and Xu et al. [27] studied the optical properties of cylindrical GaAs/$Al_\beta Ga_{1-\beta}As$ QDs by using the density matrix formalism and found that these properties depend not only on the incident optical intensity but also on the dot size and the presence of Al mole fraction in the material.

Recently, Rani and Chand [28] investigated the electronic energy spectra of a two dimensional two electrons parabolic quantum dot using the series and the Taylor expansion methods with an ansatz to the wave function. Using iterative and matrix diagonalization methods, E. B. Al

* Corresponding author.
E-mail address: dixit_rammehar@yahoo.co.in (R.M. Singh).

https://doi.org/10.1016/j.physb.2023.415654
Received 9 November 2023; Received in revised form 17 December 2023; Accepted 28 December 2023
Available online 8 January 2024

et al. [29] calculated the linear, third-order nonlinear and total optical AC and observed that the donor position, magnetic field and dot size cause significant changes in the optical AC. Rahimi et al. [30] investigated the effect of magnetic field on electronic and optical spectra of spherical QD and quantum anti-dot (QAD) by using the finite difference method and dipole approximation approach. Solaimani [31] studied the effects of magnetic field on linear optical properties of GaN/AlN multi-well quantum rings and dots with constant total effective radii.

Using the diagonalization method, Servatkhah and Pourmand [32] studied the effects of strain and magnetic field on optical properties of a two dimensional GaAs QD. Gammon et al. [33] studied fine and hyperfine splittings arising from electron, hole, and nuclear spin interactions in the magneto optical spectra of individual localized excitons in single GaAs QDs and also explained the magnetic field dependence of the energy splitting through competition between Zeeman, exchange, and hyperfine interactions. Xie [34] investigated the nonlinear optical properties of an exciton bound to an ionized donor impurity in a disc-like parabolic QD by using the matrix diagonalization method and the compact density-matrix approach.

Recently, Kumar et al. [35] investigated the optical properties and effect of magnetic field on energy spectra of a GaAs spherical QD within the framework of Coulomb plus linear harmonic potential. Vaseghi et al. [36] studied the simultaneous effects of spin–orbit interaction and external electric field on the linear and nonlinear optical properties of a cubic QD. Recently, solving the SE using Nikiforov–Uvarov (NU) method, Ghanbari [37] studied the third harmonic generation in a spherical QD under inversely quadratic Hellmann potential. Using the NU method and compact density matrix theory, Li et al. [38,39] studied effects of QD radius, confinement potential depth and controllable effective mass on the optical rectification coefficient (ORC) in spherical QDs, confined with Modified Kratzer–Coulomb and Woods–Saxon plus attractive inversely quadratic potentials.

Recent studies are mainly focused on the concept that how magnetic and AB flux fields [40] affect the low dimensional systems. Khordad [41] studied the effect of an external magnetic field on the direct inter-band optical transitions in QDs. Within the framework of a general interaction potential, Rani et al. [42] obtained the analytical solutions to the radial SE for a two dimensional two-electron QD system using the Taylor expansion method. They have also presented the effects of anharmonic potential, the Coulomb interaction terms and the magnetic field on the energy spectra of QDs. Employing the asymptotic iteration method, Aygun et al. [43] obtained the solutions to radial SE for the Kratzer potential with and without a constant magnetic field.

In the presence of an AB flux field, Ferkous and Bounames [44] solved the two dimensional Pauli equation with the Hulthen potential for spin half particles and observed that the AB flux field remove the degeneracy of energy levels. Ikhdair et al. [45] studied the effects of magnetic and AB flux fields on the energy eigenvalues and eigen functions of Klein–Gordon (KG) equation using harmonic oscillator potential model. Hedin et al. [46] investigated the combined AB flux field and Zeeman spin-polarization effects in a double QD ring. Using compact density matrix and iterative methods, Li et al. [47] theoretically investigated the second-harmonic generation coefficient for GaAs/AlGaAs parabolic QDs subject to applied electric and magnetic fields.

Oyewumi et al. [48] investigated the Hellmann potential in the presence of external magnetic and AB flux fields and obtained expressions for the energy eigenvalues and eigen functions by using the NU method. Ikot et al. [49] investigated the impact of magnetic and AB flux fields on the bound state solutions of the SE with screened Kratzer potential by using the factorization method. Similarly, Karayer [50] used the extended NU method to solve the radial SE in the presence of external magnetic and AB flux fields. Within the framework of non-relativistic quantum mechanics, Horchani et al. [51] investigated the inversely quadratic Yukawa potential in the presence of external magnetic and AB flux fields by solving the SE via NUFA method, and then obtained

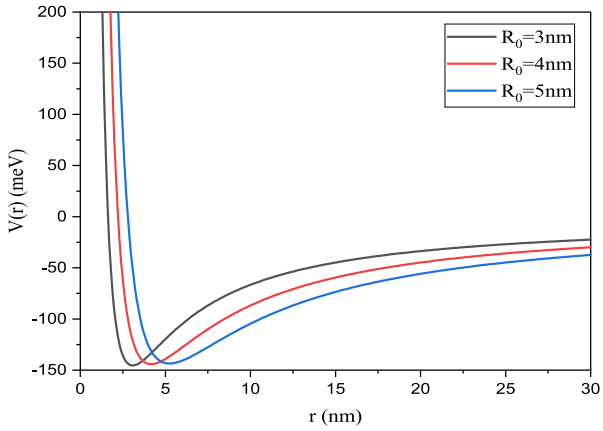

Fig. 1. The variation of IQHY potential w.r.t. r for $V_o = 224.46$ meV.

energy eigenvalues and eigen functions. In the study conducted by Edet et al. [52], the effect of magnetic field on different properties of a spherical GaAs QD doped with a donor impurity is discussed. Zhang et al. [53] investigated the impact of an applied electric field on the energy levels and optical properties of a Gaussian confinement QD.

So, in present work, we consider the IQHY potential which is a combination of inversely quadratic Hellman and Yukawa potentials i.e.,

$$V(r) = -\frac{a}{r} + \frac{b}{r^2}e^{-\alpha r} - \frac{V_o}{r^2}e^{-2\alpha r}, \tag{1}$$

where α is an adjustable screening parameter which defines the dot radius $R_0 = \frac{1}{\alpha}$. Here, a and b are connected to the potential height V_0 through $a = V_0 R_0$ and $b = V_0 R_0^2$. Eq. (1) is a three-term potential that consists of a Coulomb term, a screened Coulomb term, and a repulsive term. The first term $-\frac{a}{r}$ represents the Coulomb interaction between charged particles. The second term $\frac{b}{r^2}e^{-\alpha r}$ describes the screened Coulomb interaction between the particles, where b is a constant related to the strength of the interaction. The third term $-\frac{V_o}{r^2}e^{-2\alpha r}$ represents a repulsive potential, where V_o is a constant related to the strength of the repulsion. One advantage of this potential is that it can describe the behavior of charged particles in systems with screening effects and repulsive interactions, which are common in molecular and solid-state systems. Moreover, the goal of combining at least two potential models is to improve results because potential with more parameters tends to do so. In Fig. 1, the IQHY potential, Eq. (1) is plotted with the distance r for various value of the QD radius R_o.

Present analytical approach provides a novel and efficient method for understanding the quantum mechanical behavior of particles in the IQHY potential landscapes. Furthermore, the incorporation of magnetic and AB flux fields into the investigation of the optical properties represents a unique aspect of this research. The consideration of these additional factors expands the scope of the study and enhances the understanding of how magnetic and AB flux fields influence the optical properties of spherical GaAs QDs. The study is not merely obtaining analytical expressions but goes beyond to apply its findings to calculate linear and third-order nonlinear AC as well as RIC. This application-oriented approach provides practical insights into the optical properties of QDs, emphasizing the real-world implications of the theoretical framework developed in the present work.

The paper is organized as follows. In Section 2, we briefly describe mathematical formalism of the NUFA method. The energy eigenvalues and eigen functions to the SE with IQHY potential are calculated in Section 3. In Section 4, we explore how magnetic and AB flux fields affect the energy eigenvalues spectra. Various optical properties of spherical GaAs QDs are summarized and plotted in Section 5. Results and discussion part are covered in Section 6. Finally, the concluding remarks are addressed in Section 7.

2. Mathematical formalism

The NUFA method is considered a combination of the NU [54,55], parametric NU [56], and functional analysis techniques. In order to explain the mathematical formalism of this method [57–59], consider the differential equation of the form

$$\frac{d^2\psi(s)}{ds^2}+\frac{\alpha_1-\alpha_2 s}{s(1-\alpha_3 s)}\frac{d\psi(s)}{ds} + \frac{1}{s^2(1-\alpha_3 s)^2}\left[-\xi_1 s^2+\xi_2 s-\xi_3\right]\psi(s)=0. \tag{2}$$

With the following choice of the wave function

$$\psi(s)=s^{\lambda}(1-\alpha_3 s)^{\nu} f(s), \tag{3}$$

the Eq. (2) reduces to

$$\begin{aligned} &s(1-\alpha_3 s)\frac{d^2 f(s)}{ds^2}+\left[\alpha_1+2\lambda-(2\lambda\alpha_3+2\nu\alpha_3+\alpha_2)s\right]\frac{df(s)}{ds} \\ &-\alpha_3\left(\lambda+\nu+\frac{1}{2}\left(\frac{\alpha_2}{\alpha_3}-1\right)+\sqrt{\frac{1}{4}\left(\frac{\alpha_2}{\alpha_3}-1\right)^2+\frac{\xi_1}{\alpha_3^2}}\right) \\ &\times\left(\lambda+\nu+\frac{1}{2}\left(\frac{\alpha_2}{\alpha_3}-1\right)+\sqrt{\frac{1}{4}\left(\frac{\alpha_2}{\alpha_3}-1\right)^2+\frac{\xi_1}{\alpha_3^2}}\right) \\ &+\left[\frac{\lambda(\lambda-1)+\alpha_1\lambda-\xi_3}{s} \right. \\ &\left.+\frac{\alpha_2\nu-\alpha_1\alpha_3\nu+\nu(\nu-1)\alpha_3+\xi_2-\xi_3\alpha_3-\frac{\xi_1}{\alpha_3}}{(1-\alpha_3 s)}\right] f(s)=0. \end{aligned} \tag{4}$$

Further, Eq. (4) turns out to be a Gauss hypergeometric type equation if and only if

$$\lambda(\lambda-1)+\alpha_1\lambda-\xi_3=0, \tag{5}$$

$$\alpha_2\nu-\alpha_1\alpha_3\nu+\nu(\nu-1)\alpha_3+\xi_2-\xi_3\alpha_3-\frac{\xi_1}{\alpha_3}=0, \tag{6}$$

condition hold.

Eq. (4) therefore turns out to be

$$\begin{aligned} &s(1-\alpha_3 s)\frac{d^2 f(s)}{ds^2}+\left[\alpha_1+2\lambda-(2\lambda\alpha_3+2\nu\alpha_3+\alpha_2)s\right]\frac{df(s)}{ds} \\ &-\alpha_3\left(\lambda+\nu+\frac{1}{2}\left(\frac{\alpha_2}{\alpha_3}-1\right)+\sqrt{\frac{1}{4}\left(\frac{\alpha_2}{\alpha_3}-1\right)^2+\frac{\xi_1}{\alpha_3^2}}\right)\times \\ &\left(\lambda+\nu+\frac{1}{2}\left(\frac{\alpha_2}{\alpha_3}-1\right)+\sqrt{\frac{1}{4}\left(\frac{\alpha_2}{\alpha_3}-1\right)^2+\frac{\xi_1}{\alpha_3^2}}\right)=0. \end{aligned} \tag{7}$$

The solutions to the quadratic Eqs. (5) and (6) are conveniently written as

$$\lambda=\frac{(1-\alpha_1)}{2}\pm\frac{1}{2}\sqrt{(1-\alpha_1)^2+4\xi_3}, \tag{8}$$

.

$$\nu=\frac{(\alpha_3+\alpha_1\alpha_3-\alpha_2)\pm\sqrt{(\alpha_3+\alpha_1\alpha_3-\alpha_2)^2+4\left(\frac{\xi_1}{\alpha_3}+\alpha_3\xi_3-\xi_2\right)}}{2\alpha_3}. \tag{9}$$

Eq. (7) is a hypergeometric type equation of the form

$$x(1-x)f''(x)+[c_1+(a_1+b_1+1)x]f'(x)-[a_1b_1]f(x)=0, \tag{10}$$

where, the parameters a_1, b_1 and c_1 are defined as

$$a_1=\sqrt{\alpha_3}\left(\lambda+\nu+\tfrac{1}{2}\left(\tfrac{\alpha_2}{\alpha_3}-1\right)+\sqrt{\tfrac{1}{4}\left(\tfrac{\alpha_2}{\alpha_3}-1\right)^2+\tfrac{\xi_1}{\alpha_3^2}}\right), \tag{11}$$

$$b_1=\sqrt{\alpha_3}\left(\lambda+\nu+\tfrac{1}{2}\left(\tfrac{\alpha_2}{\alpha_3}-1\right)-\sqrt{\tfrac{1}{4}\left(\tfrac{\alpha_2}{\alpha_3}-1\right)^2+\tfrac{\xi_1}{\alpha_3^2}}\right), \tag{12}$$

$$c_1=\alpha_1+2\lambda. \tag{13}$$

The hypergeometric function *f(s)* would be a polynomial of degree *n* if a_1 or b_1 equals to a negative integer (say, *-n*). Under quantum condition $a_1=-n$, Eq. (11) reduces to

$$\lambda+\nu+\frac{1}{2}\left(\frac{\alpha_2}{\alpha_3}-1\right)+\frac{n}{\sqrt{\alpha_3}}=-\sqrt{\frac{1}{4}\left(\frac{\alpha_2}{\alpha_3}-1\right)^2+\frac{\xi_1}{\alpha_3^2}}. \tag{14}$$

Eq. (14) may be simplified as

$$\begin{aligned} &\lambda^2+2\lambda\left(\nu+\frac{1}{2}\left(\frac{\alpha_2}{\alpha_3}-1\right)+\frac{n}{\sqrt{\alpha_3}}\right) \\ &+\left(\nu+\frac{1}{2}\left(\frac{\alpha_2}{\alpha_3}-1\right)+\frac{n}{\sqrt{\alpha_3}}\right)^2 \\ &-\frac{1}{4}\left(\frac{\alpha_2}{\alpha_3}-1\right)^2-\frac{\xi_1}{\alpha_3^2}=0. \end{aligned} \tag{15}$$

Using Eqs. (8) and (9) in Eq. (3), we have

$$\begin{aligned} \psi(s)=&Ns^{\frac{(1-\alpha_1)+\sqrt{(1-\alpha_1)^2+4\xi_3}}{2}} \\ &\times(1-\alpha_3 s)^{\frac{(\alpha_3+\alpha_1\alpha_3-\alpha_2)+\sqrt{(\alpha_3+\alpha_1\alpha_3-\alpha_2)^2+4\left(\frac{\xi_1}{\alpha_3^2}+\alpha_3\xi_3-\xi_2\right)}}{2}} \\ &\times{}_2F_1(a_1,b_1,c_1;s). \end{aligned} \tag{16}$$

Here, N is the normalization constant and ${}_2F_1(a_1,b_1,c_1;s)$ is a hypergeometric type function.

3. Bound state solutions to the radial SE

The radial SE with IQHY potential (1) is written as

$$\frac{d^2R(r)}{dr^2}+\frac{2\mu}{\hbar^2}\left[E+\frac{a}{r}-\frac{b}{r^2}e^{-\alpha r}+\frac{V_o}{r^2}e^{-2\alpha r}-\frac{l(l+1)\hbar^2}{2\mu r^2}\right]R(r)=0. \tag{17}$$

Now, through the Greene-Aldrich approximation [60–62], the centrifugal term is written as,

$$\frac{1}{r^2}\approx\frac{\alpha^2}{(1-e^{-\alpha r})^2}, \tag{18}$$

Thereby, the radial SE (17) reduces to

$$\begin{aligned} \frac{d^2R(r)}{dr^2}+\frac{\alpha^2}{(1-e^{-\alpha r})^2}&\left[\frac{2\mu E(1-e^{-\alpha r})^2}{\hbar^2\alpha^2}+\frac{2\mu a(1-e^{-\alpha r})}{\hbar^2\alpha}\right. \\ &\left.-\frac{2\mu b e^{-\alpha r}}{\hbar^2}+\frac{2\mu V_o e^{-2\alpha r}}{\hbar^2}-l(l+1)\right]R(r)=0. \end{aligned} \tag{19}$$

Next through a co-ordinate transformation, $e^{-\alpha r}=s$ and after neglecting the terms of higher powers of s, *i.e.* s^3 and s^4, we obtain

$$\begin{aligned} \frac{d^2R(s)}{ds^2}+\frac{1}{s}\frac{dR(s)}{ds}+\frac{1}{s^2(1-s)^2}&\left[\left(\frac{2\mu E}{\hbar^2\alpha^2}+\frac{2\mu V_o}{\hbar^2}\right)s^2\right. \\ &+\left(-\frac{4\mu E}{\hbar^2\alpha^2}-\frac{2\mu a}{\hbar^2\alpha}-\frac{2\mu b}{\hbar^2}\right)s+\frac{2\mu E}{\hbar^2\alpha^2}+\frac{2\mu a}{\hbar^2\alpha} \\ &\left.-l(l+1)\right]R(s)=0. \end{aligned} \tag{20}$$

A comparison of Eqs. (2) and (20) leads to the following parameters

$$\begin{aligned} &\alpha_1=\alpha_2=\alpha_3=1, \quad \xi_1=\epsilon+\tau_1, \\ &\xi_2=2\epsilon+\tau_2, \quad \xi_3=\epsilon+\tau_3, \end{aligned} \tag{21}$$

where

$$\begin{aligned} &\epsilon=-\frac{2\mu E}{\hbar^2\alpha^2}, \quad \tau_1=-\frac{2\mu V_o}{\hbar^2}, \\ &\tau_2=-\frac{2\mu a}{\hbar^2\alpha}-\frac{2\mu b}{\hbar^2}, \quad \tau_3=-\frac{2\mu a}{\hbar^2\alpha}+l(l+1). \end{aligned} \tag{22}$$

After invoking Eqs. (21) and (22) in Eqs. (15) and (16), the energy eigenvalues and corresponding eigen functions expressions become

$$E = -\frac{\hbar^2\alpha^2}{2\mu}\left[\frac{\tau_1 - \tau_3 - (\nu+n)^2}{2(\nu+n)}\right]^2 + \frac{\hbar^2\alpha^2\tau_3}{2\mu}, \tag{23}$$

$$R_{nl}(r) = Ns^{\sqrt{\epsilon+\tau_3}}\cdot(1-s)^{\frac{1}{2}+\frac{1}{2}\sqrt{1+4(\tau_1-\tau_2+\tau_3)}} \times {}_2F_1(a_1,b_1,c_1;s). \tag{24}$$

Here

$$a_1 = \lambda+\nu+\sqrt{\xi_1}, \quad b_1 = \lambda+\nu-\sqrt{\xi_1}, \quad c_1 = 1+2\lambda. \tag{25}$$

To check the effects of potential height V_o and QD radius R_o, replace the potential parameters as $a = V_oR_o$ and $b = V_oR_o^2$, in Eq. (1) as

$$V(r) = -\frac{V_oR_o}{r} + \frac{V_oR_o^2}{r^2}e^{-\alpha r} - \frac{V_o}{r^2}e^{-2\alpha r}, \tag{26}$$

and the energy eigenvalues Eq. (23) becomes

$$E = -\frac{\hbar^2\alpha^2}{2\mu}\left[\frac{-\frac{2\mu V_o}{\hbar^2} + \frac{2\mu V_oR_o}{\hbar^2\alpha} - l(l+1) - (\beta+n)^2}{2(\beta+n)}\right]^2 + \frac{\hbar^2\alpha^2\left(-\frac{2\mu V_oR_o}{\hbar^2\alpha} + l(l+1)\right)}{2\mu}, \tag{27}$$

where

$$\beta = \frac{1}{2} + \frac{1}{2}\sqrt{1+4\left(-\frac{2\mu V_o}{\hbar^2} + \frac{2\mu V_oR_o^2}{\hbar^2} + l(l+1)\right)}. \tag{28}$$

3.1. Special cases

By appropriately adjusting the parameters of the general potential (1), it is possible to readily obtain various potential forms of practical implications.

3.1.1. Inverse quadratic Hellmann potential

When the value of V_o is set to zero, the potential (1) simplifies to the inverse quadratic Hellmann potential

$$V(r) = -\frac{a}{r} + \frac{b}{r^2}e^{-\alpha r}, \tag{29}$$

and the corresponding energy eigenvalues equation for this potential becomes

$$E = -\frac{\hbar^2\alpha^2}{2\mu}\left[\frac{\frac{2\mu a}{\hbar^2\alpha} - l(l+1) - \left(\frac{1}{2}+\frac{1}{2}\sqrt{1+4\left(\frac{2\mu b}{\hbar^2}+l(l+1)\right)}+n\right)^2}{2\left(\frac{1}{2}+\frac{1}{2}\sqrt{1+4\left(\frac{2\mu b}{\hbar^2}+l(l+1)\right)}+n\right)}\right]^2 + \frac{\hbar^2\alpha^2\left(-\frac{2\mu a}{\hbar^2\alpha}+l(l+1)\right)}{2\mu}. \tag{30}$$

3.1.2. Inverse quadratic Yukawa potential

By substituting $a = b = 0$, the potential (1) reduces to inverse quadratic Yukawa potential

$$V(r) = -\frac{V_o}{r^2}e^{-2\alpha r}, \tag{31}$$

and the corresponding energy eigenvalues equation is written as

$$E = -\frac{\hbar^2\alpha^2}{2\mu}\left[\frac{-\frac{2\mu V_o}{\hbar^2} - l(l+1) - \left(\frac{1}{2}+\frac{1}{2}\sqrt{1+4\left(-\frac{2\mu V_o}{\hbar^2}l(l+1)\right)}+n\right)^2}{2\left(\frac{1}{2}+\frac{1}{2}\sqrt{1+4\left(-\frac{2\mu V_o}{\hbar^2}l(l+1)\right)}+n\right)}\right]^2 + \frac{\hbar^2\alpha^2\left(l(l+1)\right)}{2\mu}. \tag{32}$$

4. Effects of magnetic and AB flux fields

In the presence of external magnetic and AB flux fields, the dynamics of a charged particle can be explained using the IQHY potential. The corresponding Hamiltonian operator is then represented in cylindrical coordinates and the SE for Eq. (1) becomes [63]

$$\left(i\hbar\vec{\nabla} - \frac{e}{c}\vec{A}\right)^2\psi(r,\phi,z) = 2\mu\left[E_{nm} + \frac{a}{r} - \frac{b}{2r^2}e^{-\alpha r} + \frac{V_o}{r^2}e^{-2\alpha r}\right]\psi(r,\phi,z). \tag{33}$$

Here, E_{nm} represents the energy and μ is the effective mass of the system. Vector potential, $\vec{A}$ can be expressed as a superposition of two terms $\vec{A} = \vec{A}_1 + \vec{A}_2$, with the azimuthal components [64] and external magnetic field $\vec{\nabla}\times\vec{A}_1 = \vec{B}, \vec{\nabla}\times\vec{A}_2 = 0$, where $\vec{B}$ is the magnetic field. To represent the additional magnetic flux, (Φ_{AB}) produced by a solenoid, we select $\vec{A}_1 = \frac{\vec{B}e^{-\alpha r}}{1-e^{-\alpha r}}$ and $\vec{A}_2 = \frac{\Phi_{AB}}{2\pi r}$. In its simplest form, the vector potential $\vec{A}$ is written as

$$\vec{A} = \left(0, \frac{\vec{B}e^{-\alpha r}}{1-e^{-\alpha r}} + \frac{\Phi_{AB}}{2\pi r}\hat{\Phi}_{AB}, 0\right). \tag{34}$$

Now consider a wave function in the cylindrical coordinates as

$$\psi(r,\phi,z) = \frac{1}{\sqrt{2\pi r}}e^{im\phi}R_{nm}(r), \tag{35}$$

where m denotes the magnetic quantum number.

In view of Eqs. (18) and (34), Eq. (33) reduces to

$$\frac{d^2R(r)}{dr^2} + \frac{\alpha^2}{(1-e^{-\alpha r})^2}\left[\frac{2\mu E(1-e^{-\alpha r})^2}{\hbar^2\alpha^2} + \frac{2\mu a(1-e^{-\alpha r})}{\hbar^2\alpha} - \frac{2\mu be^{-\alpha r}}{\hbar^2} + \frac{2\mu V_oe^{-2\alpha r}}{\hbar^2} + \frac{2m\kappa\vec{B}e^{-\alpha r}}{\hbar\alpha} - \frac{\kappa^2\vec{B}^2e^{-2\alpha r}}{\hbar^2\alpha^2} - \frac{\kappa^2\vec{B}\Phi_{AB}e^{-\alpha r}}{\hbar^2\alpha\pi} - \left((m+\eta)^2 - \frac{1}{4}\right)\right]R(r) = 0, \tag{36}$$

where $\kappa = -\frac{e}{c}, \Phi_0 = \frac{hc}{e}$, $\eta = \frac{\Phi_{AB}}{\Phi_0}$ and c is the speed of light.

After using a co-ordinate transformation, $e^{-\alpha r} = s$ and neglecting terms of higher powers of s *i.e.* s^3 and s^4, we obtain

$$\frac{d^2R(s)}{ds^2} + \frac{1}{s}\frac{dR(s)}{ds} + \frac{1}{s^2(1-s)^2}\left[\left(\frac{2\mu E}{\hbar^2\alpha^2} + \frac{2\mu V_o}{\hbar^2} - \frac{\kappa^2\vec{B}^2}{\hbar^2\alpha^2}\right)s^2 + \left(-\frac{4\mu E}{\hbar^2\alpha^2} - \frac{2\mu a}{\hbar^2\alpha} - \frac{2\mu b}{\hbar^2} + \frac{2m\kappa\vec{B}}{\hbar\alpha} - \frac{\kappa^2\vec{B}\Phi_{AB}}{\hbar^2\alpha\pi}\right)s + \frac{2\mu E}{\hbar^2\alpha^2} + \frac{2\mu a}{\hbar^2\alpha} - \left((m+\eta)^2 - \frac{1}{4}\right)\right]R(s) = 0. \tag{37}$$

A comparison of above equation with Eq. (2), provides us

$$\alpha_1 = \alpha_2 = \alpha_3 = 1, \quad \xi_1 = \epsilon+\zeta_1, \quad \xi_2 = 2\epsilon+\zeta_2, \quad \xi_3 = \epsilon+\zeta_3, \tag{38}$$

where

$$\epsilon = -\frac{2\mu E}{\hbar^2\alpha^2}, \quad \zeta_1 = -\frac{2\mu V_o}{\hbar^2} + \frac{\kappa^2\vec{B}^2}{\hbar^2\alpha^2}, \quad \zeta_2 = -\frac{2\mu a}{\hbar^2\alpha} - \frac{2\mu b}{\hbar^2} + \frac{2m\kappa\vec{B}}{\hbar\alpha} - \frac{\kappa^2\vec{B}\Phi_{AB}}{\hbar^2\alpha\pi}, \quad \zeta_3 = -\frac{2\mu a}{\hbar^2\alpha} + (m+\eta)^2 - \frac{1}{4}. \tag{39}$$

After using the result of Eqs. (38) and (39) in Eq. (15), the energy eigenvalues equation for potential (1) in the presence of magnetic and AB flux fields is written as

$$E = -\frac{\hbar^2\alpha^2}{2\mu}\left[\frac{\zeta_1 - \zeta_3 - (\nu_1+n)^2}{2(\nu_1+n)}\right]^2 + \frac{\hbar^2\alpha^2\zeta_3}{2\mu}, \tag{40}$$

where

$$\nu_1 = \frac{1}{2} + \frac{1}{2}\sqrt{1 + 4(\zeta_1 - \zeta_2 + \zeta_3)}. \tag{41}$$

5. Optical properties

In this study, density matrix formalism [65] is applied to calculate the AC and RIC of spherical GaAs QDs. For QDs, the inter-subband transition between two levels occurs only when an incident photon having energy equivalent to the energy difference between these two sub-bands i.e. $\hbar\omega = E_2 - E_1$. Here, $\hbar\omega$ represents the incident photons energy, E_1 and E_2 are the ground and first excited states energies of QDs, respectively.

Here, excitation electromagnetic field is considered as [5]

$$E(t) = \tilde{E}e^{i\omega t} + \tilde{E}^* e^{-i\omega t}, \tag{42}$$

where ω and $\tilde{E}$ are the frequency and amplitude of the electric field. In case of the one-electron density operator ρ, the temporal evolution of the matrix elements can carried out employing [6,7]

$$\frac{\partial\hat{\rho}}{\partial t} = \frac{1}{i\hbar}[H_o - e\hat{z}E(t), \hat{\rho}] - \Gamma(\hat{\rho} - \hat{\rho}^{(0)}), \tag{43}$$

where H_o is the Hamiltonian in the absence of electromagnetic field $E(t)$ with e being the electronic charge, $\hat{\rho}^{(0)}$ is the unperturbed density matrix operator. Γ is assumed to be a diagonal matrix with elements equal to the inverse of relaxation time *i.e.* , $\Gamma = \frac{1}{\tau}$ [18]. Eq. (43) can be solved using standard iterative method [24] by considering

$$\hat{\rho}(t) = \sum_{n=0} \rho^n(t), \tag{44}$$

with

$$\begin{aligned}\frac{\partial\rho_{ij}^{(n-1)}}{\partial t} =& \frac{1}{i\hbar}\left\{[H_o, \rho^{(n+1)}]_{ij} - i\hbar\Gamma_{ij}\rho_{ij}^{n+1}\right\} \\ &- \frac{1}{i\hbar}[ez, \rho^n]_{ij}E(t).\end{aligned} \tag{45}$$

The electronic polarization $P(t)$ can be expressed as

$$P(t) = \epsilon_o\chi(w)\tilde{E}e^{-i\omega t} + \epsilon_o\chi(-w)\tilde{E}^* e^{i\omega t} = \left(\frac{1}{V}\right)Tr(\rho M), \tag{46}$$

where $\chi(w)$ is the susceptibility, M is the dipole operator, V is the system volume and ϵ_o is the permittivity of vacuum. Due to the inversion symmetry of the system, the susceptibility $\chi(w)$ is expanded in series for accounting the coefficients up to the third-order, the even orders of susceptibility vanishes. The analytical expressions for the linear $\chi^{(1)}$ and third-order nonlinear $\chi^{(3)}$ susceptibility coefficients are written as [66]

$$\epsilon_o\chi^{(1)}(w) = \frac{\sigma_v|M_{21}|^2}{E_{21} - \hbar w - i\hbar\Gamma_{12}}, \tag{47}$$

and

$$\begin{aligned}\epsilon_o\chi^{(3)}(w) = -\frac{\sigma_v|M_{21}|^2|\tilde{E}|^2}{E_{21} - \hbar w - i\hbar\Gamma_{12}}&\left[\frac{4|M_{21}|^2}{(E_{21} - \hbar w)^2 + (\hbar\Gamma_{21})^2}\right. \\ &\left. - \frac{|M_{22} - M_{11}|^2}{(E_{21} - i\hbar\Gamma_{12})(E_{21} - \hbar w - i\hbar\Gamma_{12})}\right],\end{aligned} \tag{48}$$

where σ_v is the carrier density. Here, the matrix element M_{ij} of electric dipole moment is calculated from

$$M_{ij} = e\int \psi^*_{n_i l_i m_i}(r,\theta,\phi)z\psi_{n_j l_j m_j}(r,\theta,\phi)r^2 dr\sin\theta d\theta d\phi, \tag{49}$$

with $z = r\cos\theta$. The matrix element of electric dipole moment (49) is proportional to the inter-subband optical transition probability amplitude between two electronic states described by the wave function $\psi_{n_1 l_1 m_1}$ and $\psi_{n_2 l_2 m_2}$.

The AC, $\alpha(w)$ can be calculated from $\chi(w)$ by using the following relation [18,24]

$$\alpha(w) = w\sqrt{\frac{\mu_o}{\epsilon}}Im[\epsilon_o\chi(w)], \tag{50}$$

where $\epsilon = n_r^2\epsilon_o$ is permittivity of the material, n_r and μ_o are the refractive index and permeability of vacuum respectively.

Now using Eqs. (47) and (48) in Eq. (50), the expressions for linear and third-order nonlinear AC turn out to be

$$\alpha^{(1)}(w) = w\sqrt{\frac{\mu_o}{\epsilon}}\frac{\sigma_v 4|M_{21}|^2\Gamma_{12}}{(E_{21} - \hbar w)^2 + (\hbar\Gamma_{21})^2}, \tag{51}$$

and

$$\begin{aligned}\alpha^{(3)}(w, I) = -w\sqrt{\frac{\mu_o}{\epsilon}}&\frac{\sigma_v\hbar|M_{21}|^2\Gamma_{12}}{[(E_{21} - \hbar w)^2 + (\hbar\Gamma_{12})^2]^2}\frac{I}{2\epsilon_o n_r C} \\ &\times\left[4|M_{21}|^2 - \frac{|M_{22} - M_{11}|^2[3E_{21}^2 - 4E_{21}\hbar w + \hbar^2(w^2 - \Gamma_{12}^2)]}{E_{21}^2 + (\hbar\Gamma_{12})^2}\right],\end{aligned} \tag{52}$$

where $I = 2\epsilon_o n_r c|\tilde{E}|^2$ represents the incident optical intensity with c being the velocity of light in vacuum. The third-order non-linear AC, $\alpha^{(3)}(w, I)$ is negative and also proportional to the incident optical intensity. Due to spherical symmetry of the system, diagonal matrix elements will be zero i.e., $M_{ii} = 0$.

The total AC is therefore written as a sum of linear and third-order nonlinear AC [23,24]

$$\alpha(w, I) = \alpha^1(w) + \alpha^3(w, I). \tag{53}$$

Further, the RIC is connected to susceptibility through the relation [66,67]

$$\frac{\Delta n(w)}{n_r} = R_e\left(\frac{\chi(w)}{2n_r^2}\right). \tag{54}$$

Using Eqs. (47), (48) and (54), expressions for linear and third-order nonlinear RIC become

$$\frac{\Delta n^1(w)}{n_r} = \frac{1}{2n_r^2\epsilon_o}|M_{21}|^2\sigma_v\left[\frac{E_{21} - \hbar w}{(E_{21} - \hbar w)^2 + (\hbar\Gamma_{12})^2}\right], \tag{55}$$

and

$$\begin{aligned}\frac{\Delta n^3(w)}{n_r} = -\frac{\sigma_v|M_{21}|^2}{4n_r^2\epsilon_o}&\frac{\mu_o c I}{[(E_{21} - \hbar w)^2 + (\hbar\Gamma_{12})^2]^2} \\ &\left\{4(E_{21} - \hbar w)|M_{21}|^2 - \frac{|M_{22} - M_{11}|^2}{(E_{21} - \hbar w)^2 + (\hbar\Gamma_{12})^2}\right. \\ &\times[(E_{21} - \hbar w)[E_{21}(E_{21} - \hbar w) - (\hbar\Gamma_{12})^2] \\ &\left. - (\hbar\Gamma_{12})^2(2E_{21} - \hbar w)]\right\}.\end{aligned} \tag{56}$$

From Eqs. (55) and (56), the expression for total RIC is written as

$$\frac{\Delta n^{total}(w)}{n_r} = \frac{\Delta n^1(w)}{n_r} + \frac{\Delta n^3(w)}{n_r}. \tag{57}$$

Eqs. (27), (51)–(53) and (55)–(57) provide a framework for evaluating the optical properties of the system without the influence of any external fields. However, when considering the presence of magnetic and AB flux fields, Eq. (40) becomes instrumental in determining the energy eigenvalues. By utilizing Eq. (40) in conjunction with Eqs. (51), (52), and (53), we can calculate the values of the linear, nonlinear, and total AC in the presence of these external fields. Similarly, employing Eq. (40) in conjunction with Eqs. (55), (56), and (57) enables us to obtain the values of the linear, nonlinear, and total RIC under the influence of the magnetic and AB flux fields. By employing these equations, we can systematically explore the optical properties of the system under different conditions. The inclusion of magnetic and AB flux fields provides valuable insight that how these external influences affect the linear and nonlinear optical behavior, enabling a more comprehensive understanding of the system's response. This analytical approach allows

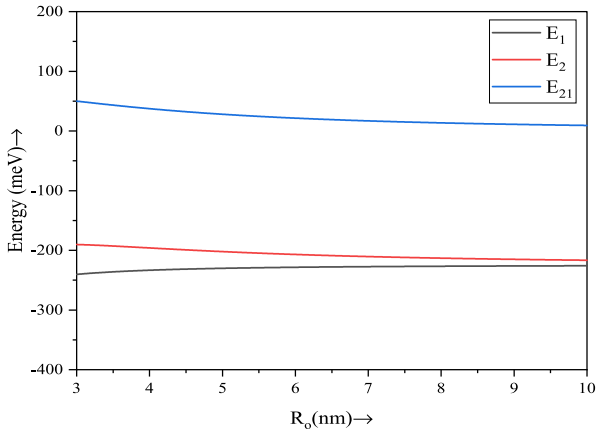

Fig. 2. Variation of the transition energy (E_{21}) as a function of R_o.

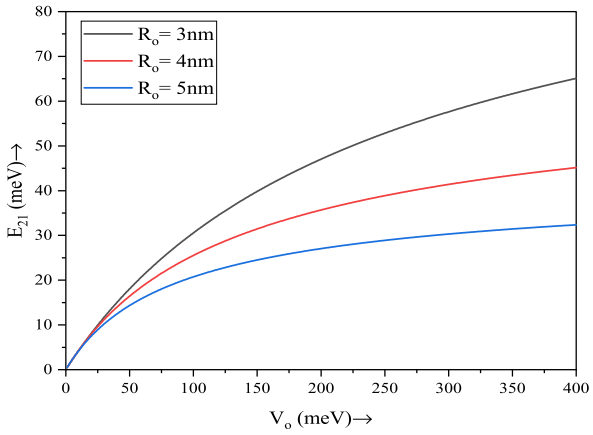

Fig. 4. The transition energy E_{21} as a function of V_o for three different values of R_o.

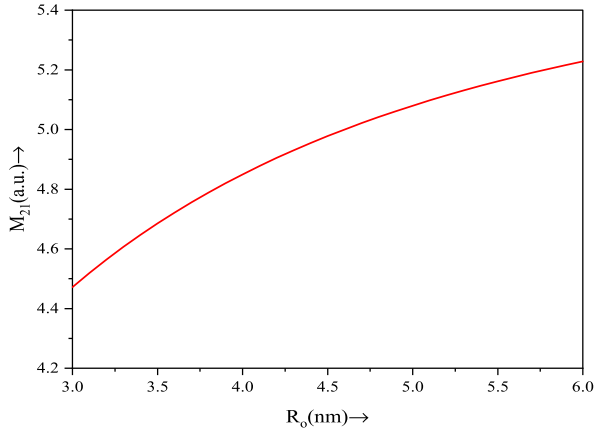

Fig. 3. The dipole matrix element M_{21} as a function of R_o with $V_o = 224.46$ meV.

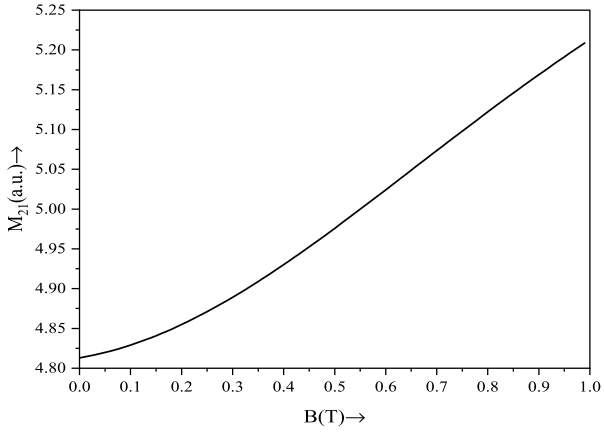

Fig. 5. Variation of dipole transition element with magnetic field.

one, a precise calculation of the optical properties in the presence of external fields, enhancing our ability to predict and adjust the system's behavior for various applications.

6. Results and discussions

In order to the describe optical properties of spherical GaAs QDs by using the density matrix formalism following parameters are chosen: refractive index, n_r=3.2, carrier density, $\sigma_v = 5 \times 10^{22}$ m^{-3}, reduced mass, $\mu = 0.067\ m_e$ (where m_e is the free electron mass), vacuum permeability, $\mu_o = 12.56 \times 10^{-7}$ H/m, vacuum permittivity, $\epsilon_o = 8.85 \times 10^{-12}$ F/m and inverse of the relaxation time, $\Gamma_{12} = \frac{1}{T_{12}}$ with $T_{12} = 0.14$ ps [68]. The quantum numbers are chosen as $n = 0, l = 0$ and $n = 0, l = 1$ for the ground and first excited states, respectively.

6.1. In the absence of magnetic and AB flux fields

The graph between E_{21} and R_o, Fig. 2, demonstrates an anticipated trend where an increase in R_o is associated with a simultaneous reduction in E_{21}. The matrix element M_{21} rises with an increase in R_o as illustrated in Fig. 3. We have additionally drawn the relationship between E_{21} and V_0 in Fig. 4, considering three distinct values of R_0. Our observations indicate a positive correlation, with E_{21} demonstrating an increase as V_0 rises. Fig. 5 portrayed the variation of dipole transition element with magnetic field.

To investigate the effect of R_o, we plot the linear, third-order nonlinear and total AC as function of the incident photon energy ($\hbar w$) with optical intensity $I = 8{\times}10^9$ W/m^2 and potential height $V_o = 224.46$ meV for three different values of R_o as shown in Fig. 6. When $\hbar w = E_{21}$, the third-order nonlinear AC is at its lowest value and the linear along with the total AC are at their maximum value. As R_o increases, it is observed that the maxima of the linear, third-order nonlinear, and total optical AC move towards the lower energies (red shift). This is because when R_o increases, E_{21} decreases (cf Fig. 2).

With $R_o = 4$ nm and $I = 8 \times 10^9$ W/m^2, the linear, third-order nonlinear, and total AC are plotted in Fig. 7 for three different values of V_o. With increase in V_o, it is observed that the position of resonant peaks for all the three AC shift to the higher energies (blue shift), an attribute of increase in E_{21} with increase in V_o (cf Fig. 4). Fig. 8 depicts the overall variation in total AC with $\hbar\omega$ for different I with $R_o = 4$ nm and $V_o = 224.46$ meV. Here, it should be noted that with increase in I, the amplitude of total AC decreases because the third-order nonlinear AC is a negative parameter (cf Eq. (52)) and depends linearly on I, but the linear AC is independent of I (cf Eq. (51)).

Thus the third-order nonlinear term dominates as I increases, which causes a drop in the total AC and a slight right shift in peak position of total AC is observed. This observed shift in the resonance peak position is attributed to the higher intensity of the incident light, which induces a strong electric field in the QD region. This electric field, in turn, causes a modulation in the energy levels of the QD, impacting the absorption spectra and resulting in a displacement of the total AC peak position. This shift is directed towards the higher energy side due to interaction with the external electric field produces by higher intensity.

For various values of R_o, the variations of linear, third-order nonlinear and total RIC are illustrated in Fig. 9 with $V_o = 224.46$ meV and $I = 8 \times 10^9$ W/m^2. For $\hbar w = E_{21}$, the linear, third-order nonlinear, and

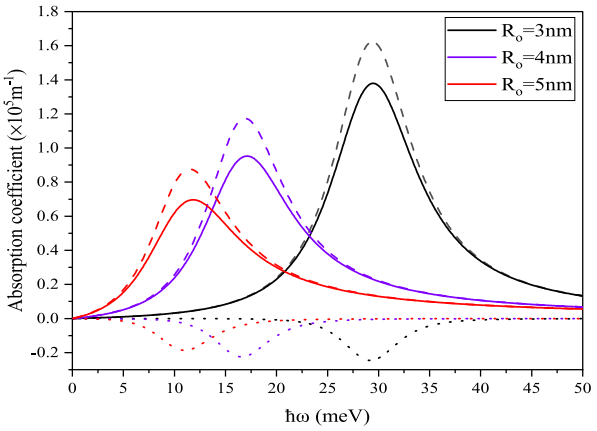

Fig. 6. The linear (dashed line) $\alpha^{(1)}(\omega)$, third-order nonlinear (dotted line) $\alpha^{(3)}(\omega)$ and total (solid line) $\alpha(\omega)$ optical AC as a function of the incident photon energy ($\hbar\omega$) for three different values of R_o with $V_o = 224.46$ meV and $I = 8 \times 10^9$ Wm^{-2}.

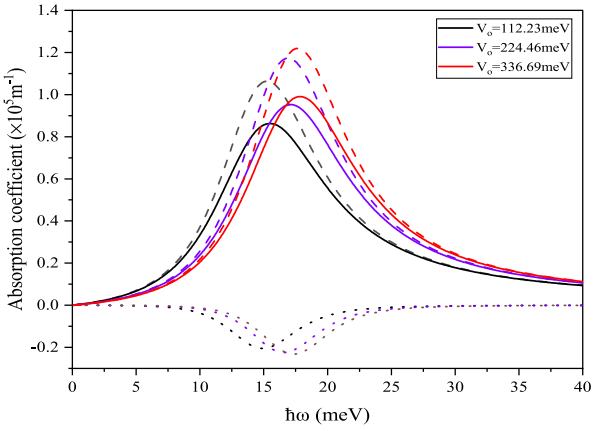

Fig. 7. The linear (dashed line) $\alpha^{(1)}(\omega)$, third-order nonlinear (dotted line) $\alpha^{(3)}(\omega)$ and total (solid line) $\alpha(\omega)$ optical AC as a function of the incident photon energy ($\hbar\omega$) for three different values of V_o with fixed $R_o = 4$ nm and $I = 8 \times 10^9$ Wm^{-2}.

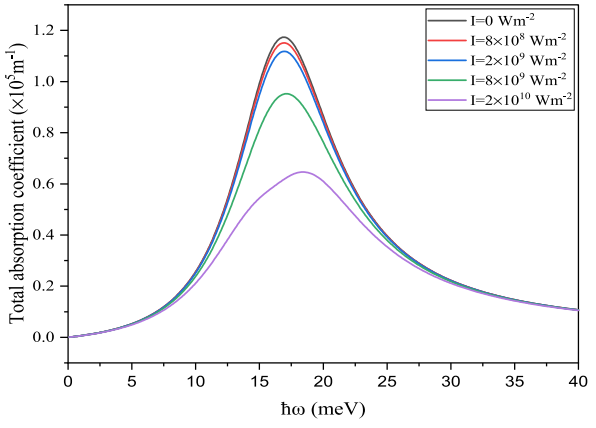

Fig. 8. The total AC $\alpha(\omega)$ as a function of the incident photon energy ($\hbar\omega$) for different values of the I with $R_o = 4$ nm and $V_o = 224.46$ meV.

total RIC reduces to zero. When R_o increases, the peaks shift to lower energies (red shift), the same is also observed in Fig. 2. Fo $I = 8 \times 10^8$ W/m^2 and $R_o = 4$ nm, the linear, third-order nonlinear, and total RIC for various values of V_o are shown in Fig. 10. It shows that as V_o increases, peaks of the linear, third-order nonlinear, and total RIC move to higher energies (blue shift). Shifting of the peaks is caused by increasing V_o, which in turn enhances the E_{21} and this exploration is also confirmed

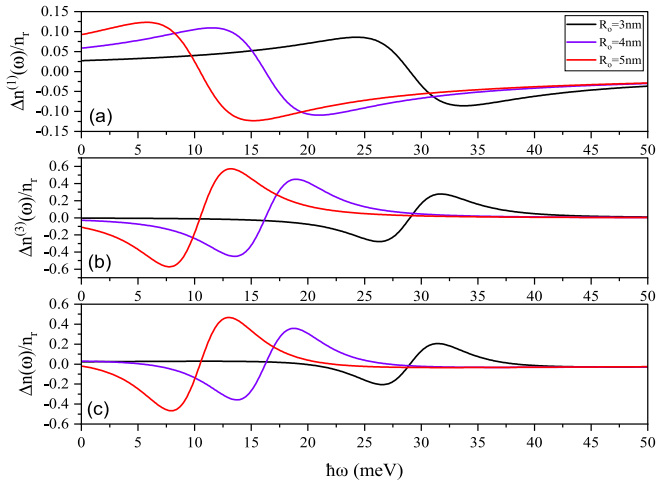

Fig. 9. Variation of (a) linear $\Delta n^{(1)}(\omega)/n_r$, (b) third-order nonlinear $\Delta n^{(3)}(\omega)/n_r$ and (c) total $\Delta n(\omega)/n_r$ RIC as a function of the incident photon energy ($\hbar\omega$) for different values of R_o with $V_o = 224.46$ meV and $I = 8 \times 10^9$ Wm^{-2}.

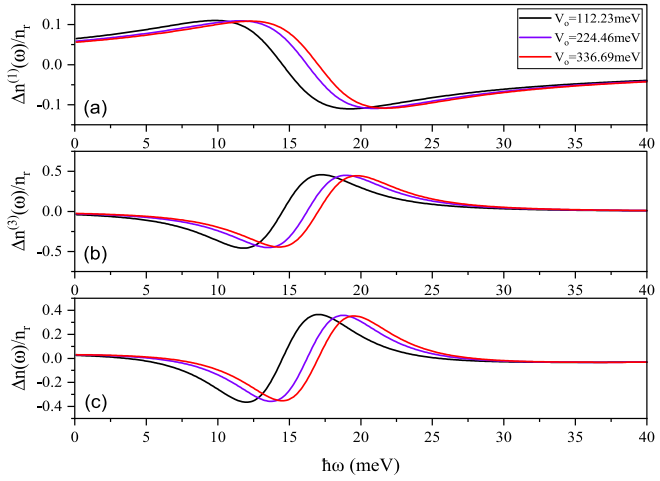

Fig. 10. Variation of (a) linear $\Delta n^{(1)}(\omega)/n_r$, (b) third-order nonlinear $\Delta n^{(3)}(\omega)/n_r$ and (c) total $\Delta n(\omega)/n_r$ RIC as a function of the incident photon energy ($\hbar\omega$) for different V_o with $R_o = 4$ nm and $I = 8 \times 10^9$ Wm^{-2}.

by Fig. 4. Fig. 11 shows the variation of total RIC for different I with $R_o = 4$ nm and $V_o = 224.46$ meV. As the linear RIC is independent to I, Eq. (55) but third-order nonlinear RIC depends linearly, Eq. (56). Thus, the total RIC, along with its magnitude and sign, changes as the intensity rises. It is worth to note that at lower intensities, the linear RIC dominates, while third-order nonlinear RIC dominates at higher intensities.

6.2. *In the presence of magnetic field only*

Fig. 12 illustrates a plot depicting the variation of energy levels for different quantum states ($m = 0, \pm 1$) as a function of the magnetic field. It reveals that separation between energy levels augmented with an increase in the magnetic field strength. Fig. 13 presents a relationship between the linear, non-linear, and total optical AC as a function of $\hbar\omega$ for three different values of R_o. For this analysis, we utilize the parameters $V_o = 224.46$ meV and $B = 1$ T. The results indicate that increasing R_o leads to a red shift in the AC peak values while causing a decrease in their magnitude. In Fig. 14, we plot the curves of the linear, non-linear, and total RIC as functions of $\hbar\omega$, with $B = 1$ T and $V_o = 224.46$ meV, for three different values of R_o. The resonance peak

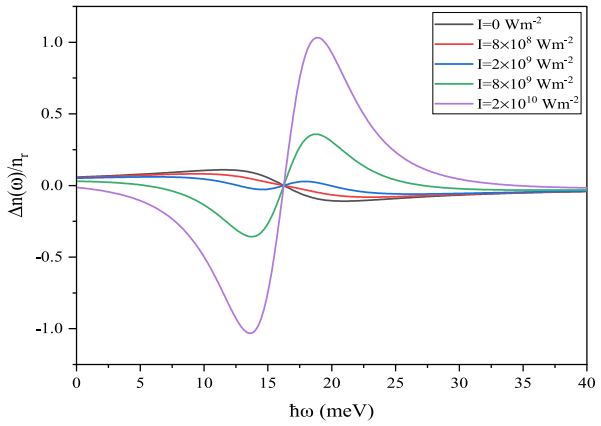

Fig. 11. Variation of total RIC $\Delta n(\omega)/n_r$ as a function of the incident photon energy ($\hbar\omega$) for different I with $R_o = 4$ nm and $V_o = 224.46$ meV.

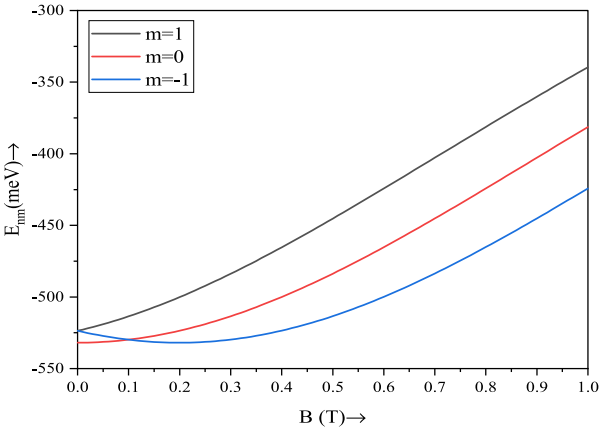

Fig. 12. The energy (E_{nm}) of the quantum dot versus the magnetic field strength (B) with $V_o = 224.46$ meV, $\eta = 0$ and $R_o = 4$ nm.

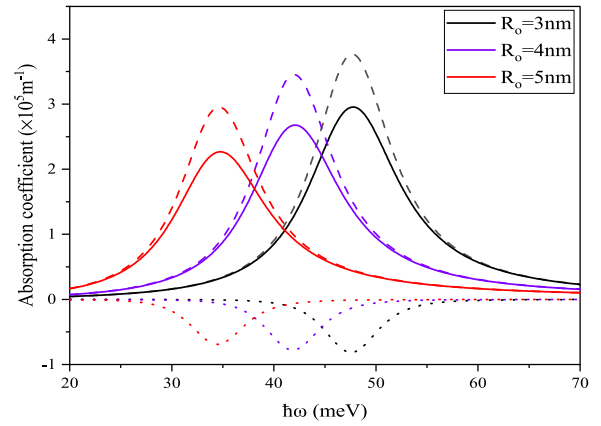

Fig. 13. The linear (dashed line), third order non-linear (dotted line) and total (solid line) optical AC as a function of the photon energy ($\hbar\omega$) with $V_o = 224.46$ meV, $B = 1T$, $\eta = 0$ and $I = 8 \times 10^9$ Wm^{-2}.

values of the linear, non-linear, and total RIC decrease as R_o increases. Furthermore, the peak positions shift towards lower energies with an increase in R_o.

Fig. 15 displays the curves of the linear, non-linear, and total optical AC as functions of $\hbar\omega$, for three different values of V_o. For this analysis, we use $R_o = 4$ nm and $B = 1T$. The findings reveal that increasing V_o of the QD results in a blue shift in the observed spectra while

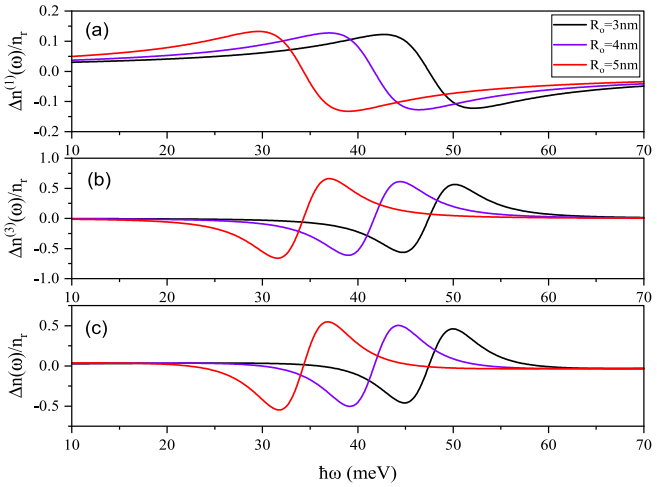

Fig. 14. The (a) linear, (b) third-order nonlinear and (c) total RIC as a function of the photon energy ($\hbar\omega$) with $V_o = 224.46$ meV, $B = 1T$, $\eta = 0$ and $I = 8 \times 10^9$ Wm^{-2}.

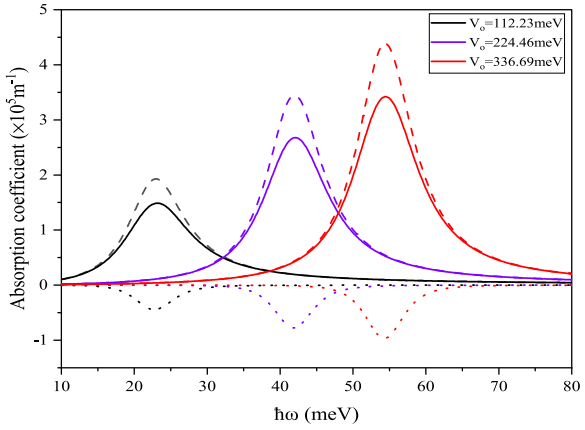

Fig. 15. The linear (dashed line), third order non-linear (dotted line) and total (solid line) optical AC as a function of the photon energy ($\hbar\omega$) with $R_o = 4$ nm, $B = 1T$, $\eta = 0$ and $I = 8 \times 10^9$ Wm^{-2}.

simultaneously increasing the peak value of the AC. In Fig. 16, we plot the curves of the linear, non-linear, and total RIC versus $\hbar\omega$, with $B = 1$ T and $R_o = 4$ nm, for three different values of V_o. In both Figs. 15 and 16, it is observed that the peak positions of the AC and RIC are shifted towards the blue end of the spectrum (higher energy) with an increase in the magnetic field. This shift is attributed to the increase in transition energy caused by the Zeeman effect, where the external magnetic field influences the energy levels of the QD. The amplitudes of both the AC and RIC increase with the rise in magnetic field. This is explained by the enhanced overlap of wave functions between the ground and first excited states of the QD [69]. The enhanced overlap results in a larger dipole matrix element (cf Fig. 5), influencing the transition probabilities and leading to higher peak amplitudes in the absorption spectrum.

Fig. 17 illustrates curves of the linear, non-linear, and total optical AC as functions of $\hbar\omega$ for three different values of magnetic field. The parameters used for this analysis are $R_o = 4$ nm and $V_o = 224.46$ meV. The results demonstrate that an increase in the magnetic field B leads to a blue shift in the observed $\hbar\omega$ and an increase in the peak value of the AC. In Fig. 18, we present plots of the linear, non-linear, and total RIC versus $\hbar\omega$, with $R_o = 4$ nm and $V_o = 224.46$ meV, for three different values of B. Similarly to the previous case, we observe a blue shift in the spectra as B increases. Here, we have investigated the influence

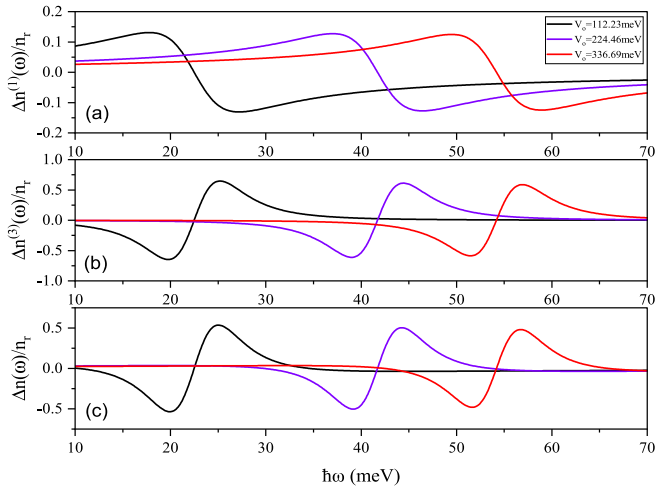

Fig. 16. The (a) linear, (b) third order non-linear and (c) total RIC as a function of the photon energy ($\hbar\omega$) with $B = 1T$, $\eta = 0$ and $I = 8 \times 10^9$ Wm^{-2}.

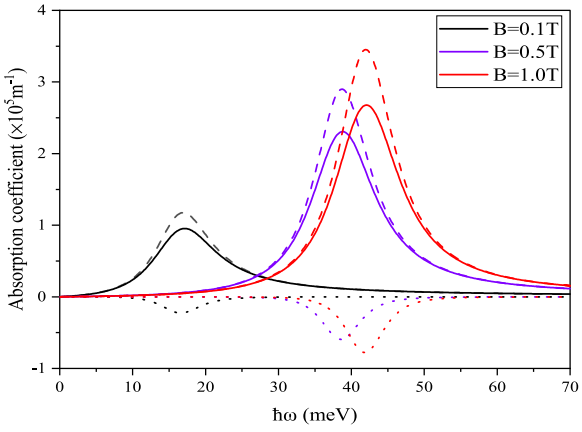

Fig. 17. The linear (dashed line), third order non-linear (dotted line) and total (solid line) optical AC as a function of the photon energy ($\hbar\omega$) with $R_o = 4$ nm, $\eta = 0$ and $V_o = 224.46$ meV.

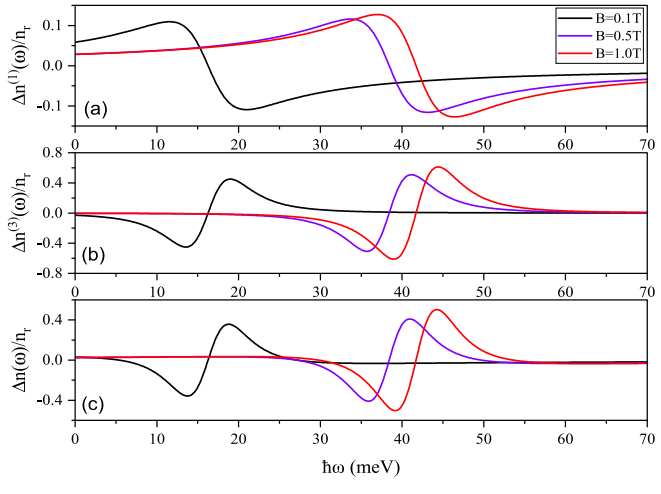

Fig. 18. The (a) linear, (b) third order non-linear and (c) total RIC as a function of the photon energy ($\hbar\omega$) with $V_o = 224.46$ meV, $\eta = 0$ and $I = 8 \times 10^9$ Wm^{-2}.

of varying R_o and V_o on the AC and RIC, considering the presence of a magnetic field. Our analysis reveals that the shifting behavior

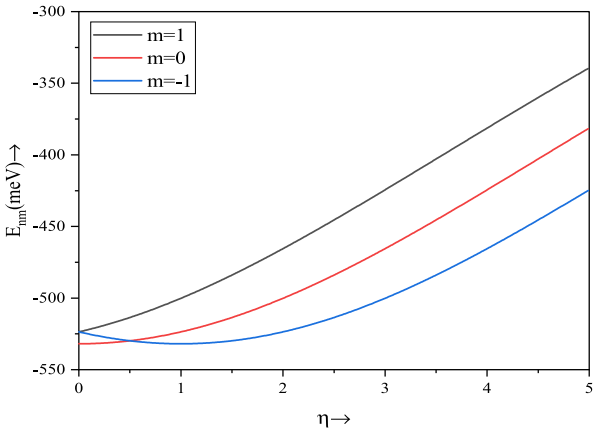

Fig. 19. The energy (E_{nm}) of the quantum dot versus the AB flux field strength (η) with $V_o = 224.46$ meV, $B = 0$ T and $R_o = 4$ nm.

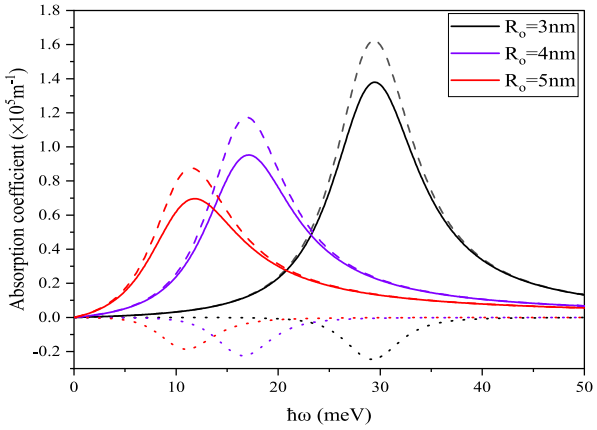

Fig. 20. The linear (dashed line), third order non-linear (dotted line) and total (solid line) optical AC as a function of the photon energy ($\hbar\omega$) with $V_o = 224.46$ meV, $\eta = 0.5$, $B = 0T$ and $I = 8 \times 10^9$ Wm^{-2}.

of the AC and RIC follows a similar trend to that observed in the absence of a magnetic field. However, a notable distinction arises in the positions of resonant peaks, which manifest higher energy values. This disparity can be attributed to the substantial increase in the separation between energy levels, as depicted in Fig. 12, in response to the applied magnetic field.

6.3. *In the presence of AB flux field only*

In Fig. 19, we present a graph illustrating the energy levels for various quantum states ($m = 0, \pm 1$) as a function of the AB flux field. Our analysis reveals a distinct trend, where an increase in the AB flux field leads to more separation between energy levels. Fig. 20 presents a relationship between linear, non-linear, and total optical AC as a function of $\hbar\omega$ for three different values of R_o. For this case, we utilize the parameters $V_o = 224.46$ meV and $\eta = 0.5$. The results indicate that increasing R_o leads to a red shift in AC peak values while causing a decrease in their magnitude. Fig. 21 depicts the curves of linear, non-linear, and total RIC as functions of $\hbar\omega$, with $\eta = 0.5$ and $V_o = 224.46$ meV, for three different values of R_o. The resonance peak values of linear, non-linear, and total RIC decrease as R_o increases. Furthermore, the peak positions shift towards lower energies with an increase in R_o.

Fig. 22 displays the curves of linear, non-linear, and the total optical AC as functions of $\hbar\omega$. For this analysis, we use $R_o = 4$ nm and $\eta = 0.5$. The findings reveal that increasing the potential height V_o of the QD results in a blue shift in the observed spectra while simultaneously

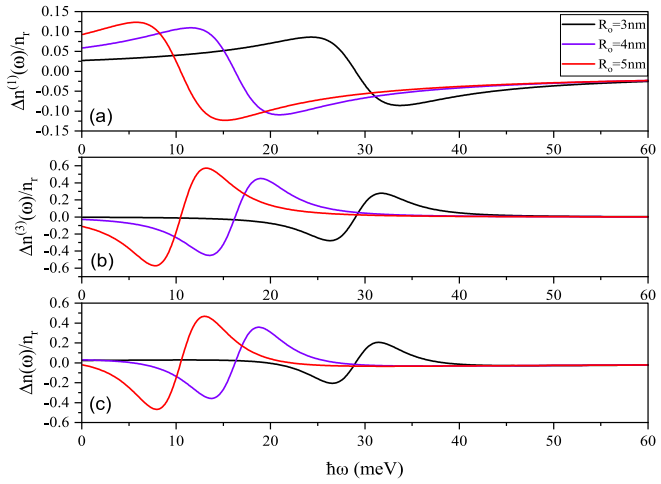

Fig. 21. The (a) linear, (b) third order non-linear and (c) total RIC as a function of the photon energy ($\hbar\omega$) with $V_o = 224.46$ meV, $\eta = 0.5$, $B = 0$ T and $I = 8 \times 10^9$ Wm^{-2}.

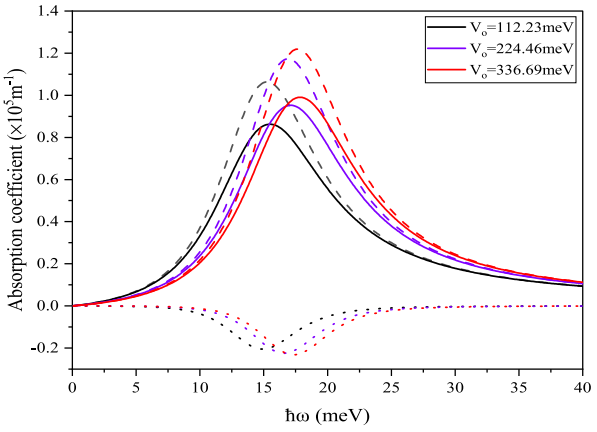

Fig. 22. The linear (dashed line), third order non-linear (dotted line) and total (solid line) optical AC as a function of the photon energy ($\hbar\omega$) with $R_o = 4$ nm, $\eta = 0.5$, $B = 0$ T and $I = 8 \times 10^9$ Wm^{-2}.

increasing the peak value of the AC. In Fig. 23, we plot the curves of linear, non-linear, and total RIC versus $\hbar\omega$, with $\eta = 0.5$ and $R_o = 4$ nm, for three different values of V_o. Here, it is observed that the peak positions shift towards higher energies as V_o increases. Fig. 24 illustrates the curves of linear, non-linear, and total AC as functions of $\hbar\omega$. The parameters used for this analysis are $R_o = 4$ nm and $V_o = 224.46$ meV. The findings demonstrate that an increase in the AB flux field leads to a blue shift in the observed $\hbar\omega$ and an increase in the peak values of the AC. Fig. 25 represents the curves of linear, non-linear, and total RIC versus $\hbar\omega$, with $R_o = 4$ nm and $V_o = 224.46$ meV, for three different values of η. Similar to the previous case, we observe a blue shift as η increases.

Here, we have conducted an in-depth investigation into the impact of varying R_o and V_o on AC and RIC, while considering the presence of an AB flux field. Our analysis demonstrates that the shifting behavior of the AC and RIC in the presence of an AB flux field follows a similar trend to that observed without the AB flux field. However, a distinct feature emerges in the position of the resonant peaks, which occur at higher energy values. This distinction can be attributed to the significant increase in the separation between energy levels induced by the AB flux field, as evidenced in Fig. 19.

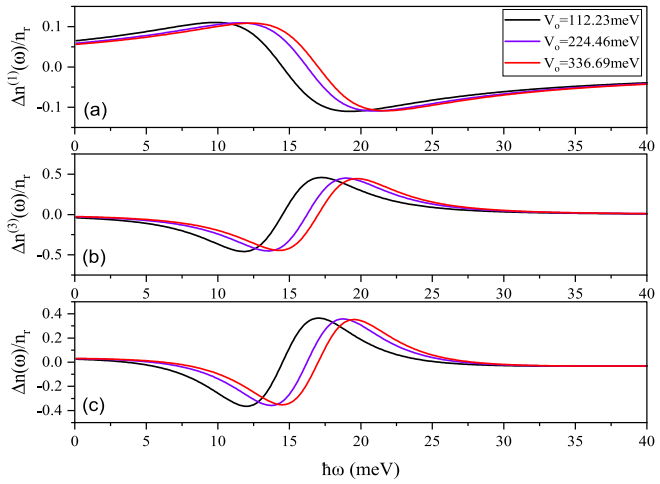

Fig. 23. The (a) linear, (b) third order non-linear and (c) total RIC as a function of the photon energy ($\hbar\omega$) with $R_o = 4$ nm, $\eta = 0.5$, $B = 0$ T and $I = 8 \times 10^9$ Wm^{-2}.

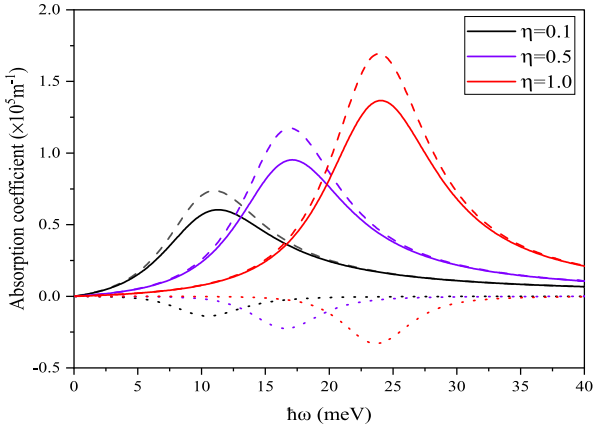

Fig. 24. The linear (dashed line), non-linear (dotted line)and total (solid line) optical AC as a function of the photon energy ($\hbar\omega$) with $R_o = 4$ nm, $V_o = 224.46$ meV, $B = 0T$ and $I = 8 \times 10^9$ Wm^{-2}.

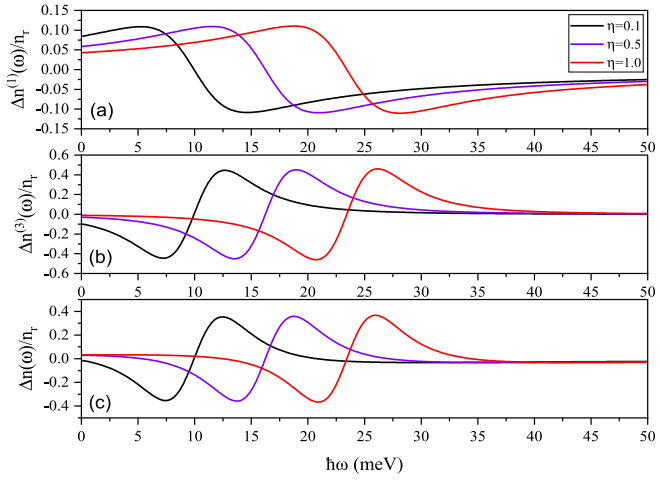

Fig. 25. The (a) linear, (b) third order non-linear and (c) total RIC as a function of the photon energy with $R_o = 4$ nm, $V_o = 224.46$ meV, $B = 0T$ and $I = 8 \times 10^9$ Wm^{-2}.

6.4. *In the presence of magnetic and AB flux fields*

As a final analysis, we examine the scenario where magnetic and AB flux fields coexist. Fig. 26 illustrates the overall values of AC, while

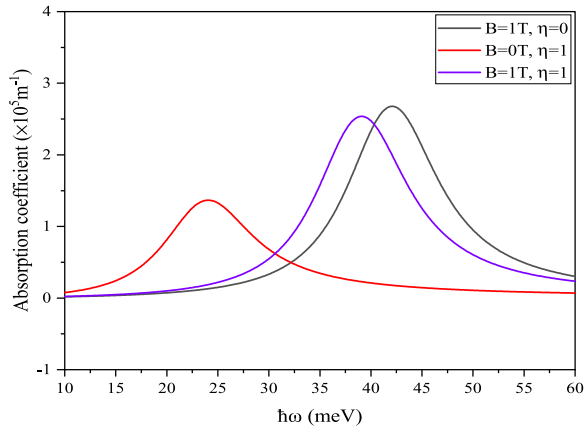

Fig. 26. The total AC as a function of the photon energy with $R_o = 4$ nm, $V_o = 224.46$ meV and $I = 8 \times 10^9$ Wm^{-2}.

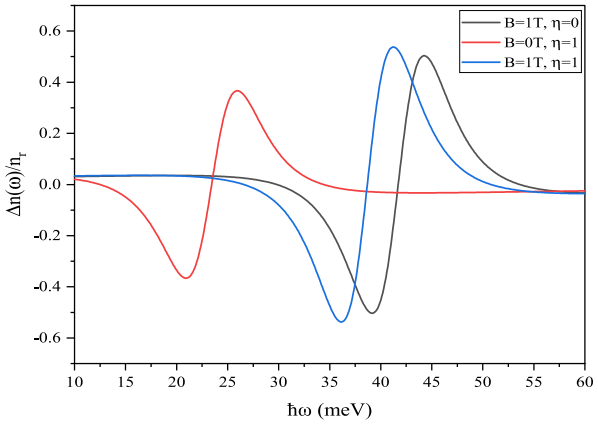

Fig. 27. The Total RIC as a function of the photon energy with $R_o = 4$ nm, $V_o = 224.46$ meV and $I = 8 \times 10^9$ Wm^{-2}.

Fig. 27 depicts the total RIC. As shown in Fig. 26, the peak position of AC with $B = 1T$ and $\eta = 1$ lies between the peaks of AC for $B = 1T$, $\eta = 0$ and $B = 0$, $\eta = 1$. Similarly, as depicted in Fig. 27, the peak position of RIC with $B = 1T$ and $\eta = 1$ is located between the peaks of AC for $B = 1T, \eta = 0$ and $B = 0T, \eta = 1$. In Figs. 26 and 27, it was noted that the peak energy is maximized when $B = 1T$ and $\eta = 0$, while the minimum energy position is associated with $B = 0$ and $\eta = 1$.

7. Conclusions

In this study, we have conducted comprehensive investigations into the linear and nonlinear optical properties of spherical GaAs quantum dots subjected to the inverse quadratic Hellmann plus Yukawa potential, employing the density matrix formalism. By solving the radial SE using the Nikiforov-Uvarov functional analysis method, we have obtained the energy eigenvalues and eigenfunctions, enabling a detailed analysis of the optical behavior of the system. Our findings demonstrate that by varying the QD's radius and potential height, it is possible to achieve pronounced shifts in the optical energy spectra. Specifically, adjustments in these parameters lead to either a blue or red shift in the observed spectra. Additionally, we have observed that the optical absorption coefficients and refractive index changes are notably influenced by the incident light intensity.

Furthermore, we have found that, compared to alternative potential models, the nonlinear components in our results exhibit relatively reduced magnitudes for various coefficients, suggesting distinctive characteristics associated with the IQHY potential. Expanding upon our investigations, we have extended our analysis to include the effects of a magnetic field and Aharonov–Bohm flux field on the linear and nonlinear optical properties of the GaAs QDs. Our results reveal a strong correlation between the magnetic field strength and the separation between energy levels, ultimately leading to a prominent blue shift in the optical energy spectra. Similarly, the AB flux field induces a comparable blue shift effect. These noteworthy observations underscore the substantial influence exerted by magnetic and AB flux fields on the linear and nonlinear optical properties of GaAs QDs. We hope that present theoretical results would play important role in future theoretical and experimental studies related to QDs.

CRediT authorship contribution statement

Munesh Bansal: Writing – original draft, Software, Investigation. **Vinod Kumar:** Conceptualization, Validation. **Sahil:** Methodology. **S.B. Bhardwaj:** Writing – review & editing, Conceptualization. **Ram Mehar Singh:** Writing – review & editing, Supervision. **Fakir Chand:** Writing – review & editing, Conceptualization.

Declaration of competing interest

The authors declare that they have no known competing financial interests or personal relationships that could have appeared to influence the work reported in this paper.

Data availability

No data was used for the research described in the article.

Acknowledgment

One of the authors, Munesh Bansal acknowledges the University Grants Commission (UGC), New Delhi (India) for granting financial support through Junior Research Fellowship.

References

[1] A.Y. Cho, J.R. Arthur, Prog. Solid State Chem. 10 (1975) 157.
[2] J. Marks, J. Schindler, C.R. Kannewurf, Mat. Res. Soc. Symp. Proc., vol. 335, 1994, p. 285.
[3] S. Nasa, S.P. Purohit, Phys. E: Low-dim. Syst. Nanostr. 118 (2020) 113913.
[4] Y. Yakar, B. Cakir, A. Özmen, Commun. Theor. Phys. 53 (2010) 1185.
[5] L. Máthé, C.P. Onyenegecha, A.A. Farcaş, L.M. Pioraş Ţimbolmaş, M. Solaimani, H. Hassanabadi, Phys. Lett. A 397 (2021) 127262.
[6] M.R.K. Vahdani, Superlatt. Microstr. 76 (2014) 326.
[7] S. Ünlü, I. Karabulut, H. Şafak, Phys. E: Low-dim. Syst. Nanostr. 33 (2006) 319.
[8] Z.H. Zhang, Y.S. Shi, J.-H. Yuan, Commun. Theor. Phys. 74 (2022) 065502.
[9] K.X. Guo, S.W. Gu, Phys. Rev. B 47 (1993) 24.
[10] E. Kasapoglu, H. Sari, I. Sökmen, Superlatt. Microstr. 29 (2001) 1.
[11] Y.B. Yu, S.N. Zhu, K.X. Guo, Solid State Commun. 139 (2006) 2.
[12] D.H. Feng, Z.Z. Xu, T.Q. Jia, X.X. Li, S.Q. Gong, Phys. Rev. B 68 (2003) 3.
[13] M. Tanaka, H. Yamada, T. Maruyama, K. Akimoto, Phys. Rev. B 67 (2003) 4.
[14] M. Tshipa, Opt. Quan. Elect. 51 (2019) 225.
[15] Z. Zhao, X. Li, Y. Duan, C. Chang, L. Zhang, Opt. Quan. Elect. 54 (2022) 564.
[16] F. Ungan, M.K. Bahar, S. Pal, M.E. Mora Ramos, Commun. Theor. Phys. 72 (2020) 075505.
[17] R. Khordad, B. Mirhosseini, Pramana-J. Phys. 85 (2015) 4.
[18] R. Khordad, B. Mirhosseini, Opt. Spectro. 117 (2014) 3.
[19] W. Xie, Superlatt. Microstr. 48 (2010) 239.
[20] R. Khordad, Ind. J. Phys. 87 (2013) 7.
[21] C. Zhang, C. Min, B. Zhao, Phys. Lett. A 383 (2019) 34.
[22] G. Liu, K. Guo, Superlatt. Microstr. 52 (2012) 997.
[23] M.C. Onyeaju, J.O.A. Idiodi, A.N. Ikot, M. Solaimani, H. Hassanabadi, Few-Body Syst. 57 (2016) 793.
[24] M.C. Onyeaju, J.O.A. Idiodi, A.N. Ikot, M. Solaimani, H. Hassanabadi, J. Opt. 46 (2017) 3.
[25] L. Lu, W. Xie, H. Hassanabadi, J. Lumin. 131 (2011) 2538.
[26] W. Xie, Superlatt. Microstr. 46 (2009) 693.
[27] C.H. Liu, B.R. Xu, Phys. Lett. A 372 (2008) 6.
[28] R. Rani, F. Chand, Ind. J. Phys. 92 (2018) 2.
[29] E.B. Al, E. Kasapoglu, H.N. Sari, I. Sökmen, Physica B 613 (2021) 412874.

[30] F. Rahimi, T. Ghaffary, Y. Naimi, H. Khajehazad, Opt. Quan. Elect. 53 (2021) 47.
[31] M. Solaimani, Opt. Quan. Elect. 48 (2016) 161.
[32] M. Servatkhah, R. Pourmand, Eur. Phys. J. Plus 135 (2020) 754.
[33] D. Gammon, A.L. Efros, T.A. Kennedy, M. Rosen, D.S. Katzer, D. Park, S.W. Brown, V.L. Korenev, I.A. Merkulov, Phys. Rev. Lett. 86 (2001) 22.
[34] W. Xie, Phys. Lett. A 375 (2011) 8.
[35] V. Kumar, S.B. Bhardwaj, R.M. Singh, F. Chand, Eur. Phys. J. Plus 138 (2023) 191.
[36] B. Vaseghi, G. Rezaei, V. Azizi, Opt. Quan. Elect. 42 (2011) 841.
[37] A. Ghanbari, Opt. Quan. Elect. 55 (2023) 222.
[38] X. Li, C. Chang, Y. Ma, Commun. Theor. Phys. 74 (2022) 065703.
[39] X. Li, Y. Duan, Y. Ma, Commun. Theor. Phys. 74 (2022) 085702.
[40] Y. Aharonov, D. Bohm, Phys. Rev. 115 (1959) 485.
[41] R. Khordad, Solid State Sci. 12 (2010) 1253.
[42] R. Rani, V. Kumar, S.B. Bhardwaj, R.M. Singh, F. Chand, Ind. J. Phys. 94 (2020) 11.
[43] M. Aygun, O. Bayrak, I. Boztosun, Y. Sahin, Eur. Phys. J. D 66 (2012) 35.
[44] N. Ferkous, A. Bounames, Commun. Theor. Phys. 59 (2013) 6.
[45] S.M. Ikhdair, B.J. Falaye, M. Hamzavi, Ann. Physics 353 (2015) 282.
[46] E.R. Hedin, A.C. Perkins, Y.S. Joe, Phys. Lett. A 375 (2011) 3.
[47] B. Li, K.X. Guo, C.J. Zhang, Y.B. Zheng, Phys. Lett. A 367 (2007) 6.
[48] K.J. Oyewumi, E.O. Titiloye, A.B. Alabi, B.J. Falaye, J. Nigerian Math. Soc. 35 (2016) 460.
[49] A.N. Ikot, C.O. Edet, P.O. Amadi, U.S. Okorie, G.J. Rampho, H.Y. Abdullah, Eur. Phys. J. D 74 (2020) 159.
[50] H. Karayer, Eur. Phys. J. Plus 135 (2020) 70.
[51] R. Horchani, H.A. Aamri, N.A. Kindi, A.N. Ikot, U.S. Okorie, G.J. Rampho, H. Jelassi, Eur. Phys. J. D 75 (2021) 36.
[52] C.O. Edet, E.B. Al, F. Ungan, N. Ali, N. Rusli, S.A. Aljunid, R. Endut, M. Asjad, Nanomaterials 12 (2022) 2741.
[53] Z.H. Zhang, J.H. Yuan, Phys. E: Low-dim. Syst. Nanostr. 147 (2023) 115594.
[54] F. Ahmed, Phys. Scr. 98 (2022) 015403.
[55] Y.B. Ateş, U.S. Okorie, A.N. Ikot, E. Olğar, Phys. Scr. 94 (2019) 115705.
[56] S.M. Ikhdair, Phys. Scr. 88 (2013) 065007.
[57] A.N. Ikot, U.S. Okorie, P.O. Amadi, C.O. Edet, G.J. Rampho, R. Sever, Few-Body Syst. 62 (2021) 1.
[58] V. Kumar, R.M. Singh, S.B. Bhardwaj, R. Rani, F. Chand, Modern Phys. Lett. A 37 (2022) 2.
[59] V. Kumar, S.B. Bhardwaj, R.M. Singh, F. Chand, Mol. Phys. 120 (2022) e2132185.
[60] R.L. Greene, C. Aldrich, Phys. Rev. A 14 (1976) 6.
[61] V. Kumar, S.B. Bhardwaj, R.M. Singh, F. Chand, Phys. Scr. 97 (2022) 055301.
[62] V. Kumar, R.M. Singh, S.B. Bhardwaj, F. Chand, Fun. Mat. App. Phys. Proc. 22 (2022) 7.
[63] K.J. Oyewumi, E.O. Titiloye, A.B. Alabi, B.J. Falaye, J. Nigerian Math. Soc. 35 (2016) 460.
[64] B.J. Falaye, G.H. Sun, R. Silva O., S.H. Dong, Phys. Rev. E 93 (2016) 053201.
[65] S. Ünlü, I. Karabulut, H. Şafak, Phys. E: Low-dim. Syst. Nano. 33 (2006) 319.
[66] D. Ahn, S.L. Chuang, IEEE J. Quan. Electro. 23 (1987) 12.
[67] R. Khordad, J. Lumin. 134 (2013) 201.
[68] L. Lu, W. Xie, Phys. Scr. 84 (2011) 025703.
[69] C.O. Edet, E.B. Al, F. Ungan, N. Ali, N. Rusli, S.A. Aljunid, R. Endut, M. Asjad, Nanomaterials 12 (2020) 2741.

HIGHER ORDER POLYNOMIAL COMPLEX INVARIANTS FOR ONE-DIMENSIONAL ANHARMONIC POTENTIALS

S. B. Bhardwaj*

Department of Physics, SUS Govt. College, Matak Majri, Karnal-132041, India
(e-mail: sbbhardwaj09@gmail.com)

Ram Mehar Singh, Vipin Kumar

Department of Physics, Chaudhary Devi Lal University, Sirsa-125055, India
(e-mails: dixit_rammehar@yahoo.co.in, vipinmtep@gmail.com)

Narender Kumar

Department of Physics, Government College, Jind-126102, India
(e-mail: nkc_phy_kuk@yahoo.com)

Fakir Chand

Department of Physics, Kurukshetra University, Kurukshetra-136119, India
(e-mail: fchand@kuk.ac.in)

and

Shalini Gupta

Department of Physics, HMR Institute of Technology & Management, Delhi
(e-mail: shalini.hmritm@gmail.com)

(*Received March 15, 2023*)

Exact quadratic in momenta complex invariants are investigated for both time independent and time dependent one-dimensional Hamiltonian systems possessing higher order nonlinearities within the framework of the rationalization method. The extended complex phase space approach is utilized to map a real system into complex space. Such invariants are expected to play a role in the analysis of complex trajectories and help to understand some new phenomena associated with complex potentials.

Keywords: exact invariants, complex Hamiltonian, rationalization method, extended complex phase space approach.

1. Introduction

The dynamics of an integrable system can be understood in terms of real invariants of the system. In the past, several efforts have been made to explore the role of invariants in the qualitative study of classical as well as quantum dynamical systems. The

*Corresponding Author.

availability and subsequently investigation (if possible) of invariants for a given system is of immense importance to understand the underlying dynamics of the system [1–7].

Several authors have studied the construction of invariant for one- and two-dimensional Hamiltonian systems. Invariants play an important role in different fields, viz. laser physics, plasma physics, fiber optics, astrophysics, accelerator physics, condensed matter physics and biophysics [7–9]. Invariants, in particular, are used to lower the order of differential equations, to check the accuracy of numerical simulations of time dependent Hamiltonian systems [10, 11], stability of differential equations [12, 13] etc. The higher order invariants give the idea of the internal symmetry of physical systems specially in molecular dynamics [14, 15].

Information related to various physical properties of a dynamical system can be obtained by its real Hamiltonian representation, however some other aspects of a dynamical system can be ascertained effectively by considering its complex Hamiltonian form only [16, 17]. As far as a complex Hamiltonian is concerned, it is studied in the context of quantum mechanics and semiclassical field theories. So it is necessary to understand such systems at classical level too, and thus investigation of the associated dynamical invariants open new vistas in the field of both classical and quantum mechanics [2, 7]. It is also seen that a complex invariant exists for a real system too (simple harmonic oscillator, $I = \ln(p + im\omega x) - i\omega t$) and integrability of such systems requires further investigation. Real invariants exist under some prescription but there is no such prescription for complex invariants. Complex Hamiltonians are used in various branches of physics, namely in atomic and molecular physics, nuclear physics, population biology, chemical reactions and flux transitions in type-II superconductors [18–21].

For complex Hamiltonian systems, various complexification schemes are available in literature [7, 22–24]. One such approach, known as extended complex phase space (ECPS) approach and characterized by

$$x = x_1 + ip_2, \quad p = p_1 + ix_2, \tag{1}$$

has been profitably explored by many workers in different studies [7, 9, 25]. Many authors utilized this scheme to study quantum aspects of various complex Hamiltonians by calculating eigenvalues and corresponding eigenfunctions [26–30], whereas, the classical aspects are discussed by Kaushal et al. [31, 32] for low order potentials only and not much attempts are made on higher order anharmonic potentials. In fact, quadratic invariants are widely studied because of their resemblance with system's Hamiltonian whose kinetic energy part is also quadratic in momenta. Naturally one can be curious to look for higher-order invariants and their possible implications in different branches of natural sciences. Such studies can also be applied to check the veracity of the existing methods for construction of invariants. In this direction, many authors worked out cubic and quartic invariants and their applications [2, 7, 33]. The higher-order invariants are particularly interesting for establishing super integrability of dynamical systems [34, 35].

In the past, some authors have also investigated invariants for some classical systems [36–45], within the framework of ECPS approach. But majority of the

work is limited to lower order time-independent (TID) potentials. So extension of such work to higher order TID and time dependent (TD) anharmonic potentials is desirable. With this motivation, we investigate the corresponding dynamical invariant for various TID complex potentials like quartic, odd power quintic and even power sextic potentials by exploiting the rationalization method.

Recently, Struckmeir and Riedel (SR) proposed an elegant technique to determine TD quadratic invariants and utilised such invariants to check the numerical accuracy of simulation of some Hamiltonian systems [10, 11]. Here we extend this approach, first time to the best of our knowledge, for complex Hamiltonian systems and find TD invariants for a general one-dimensional TD quartic potential which has been extensively used earlier by many authors [10, 11, 39] for variety of real and complex invariants for classical dynamical systems.

The present work is structured like this. In Section 2, we describe the rationalization method in ECPS and construct quadratic TID invariants for quartic, odd power quintic and even power sextic potentials. Then, in Section 3, we illustrate S-R approach to construct complex invariants for TD quartic anharmonic potential. Finally concluding remarks are presented in Section 4.

2. The rationalization method

In this section, we develop the rationalization method within the framework of ECPS approach for the investigation of exact quadratic invariants for some higher-order anharmonic potentials.

A complex Hamiltonian $H(x,p)$ for a dynamical system is written as [25]

$$H(x,p) = H_1\left(x_1,p_1,x_2,p_2\right) + iH_2\left(x_1,p_1,x_2,p_2\right). \tag{2}$$

Employing the transformations (1), we obtain

$$\frac{d}{dx} = \frac{1}{2}\left(\frac{\partial}{\partial x_1} - i\frac{\partial}{\partial p_2}\right), \qquad \frac{d}{dp} = \frac{1}{2}\left(\frac{\partial}{\partial p_1} - i\frac{\partial}{\partial x_2}\right). \tag{3}$$

The invariant $I(x,p)$ in ECPS is written as

$$I(x,p) = I_1\left(x_1,p_1,x_2,p_2\right) + iI_2\left(x_1,p_1,x_2,p_2\right). \tag{4}$$

For the existence of invariant, the system must satisfy following invariance relation

$$\frac{dI}{dt} = \frac{\partial I}{\partial t} + [I,H] = 0, \tag{5}$$

where $[I,H]$ is the Poisson bracket.

After using Eqs. (2)–(4) in Eq. (5) and on rationalizing the resultant expression and after separating real and imaginary parts, the following pair of equations is obtained

$$\begin{aligned}\partial_t I_1 &+ \left(\partial_{x_1} I_1 + \partial_{p_2} I_2\right)\left(\partial_{p_1} H_1 + \partial_{x_2} H_2\right) - \left(\partial_{x_1} I_2 - \partial_{p_2} I_1\right)\left(\partial_{p_1} H_2 - \partial_{x_2} H_1\right)\\ &- \left(\partial_{p_1} I_1 + \partial_{x_2} I_2\right)\left(\partial_{x_1} H_1 + \partial_{p_2} H_2\right) + \left(\partial_{p_1} I_2 - \partial_{x_2} I_1\right)\left(\partial_{x_1} H_2 - \partial_{p_2} H_1\right) = 0,\end{aligned} \tag{6}$$

$$\partial_t I_2 + \left(\partial_{x_1} I_2 - \partial_{p_2} I_1\right)\left(\partial_{p_1} H_1 + \partial_{x_2} H_2\right) + \left(\partial_{x_1} I_2 + \partial_{p_2} I_2\right)\left(\partial_{p_1} H_2 - \partial_{x_2} H_1\right) - \left(\partial_{p_1} I_2 - \partial_{x_2} I_1\right)\left(\partial_{x_1} H_1 + \partial_{p_2} H_2\right) - \left(\partial_{p_1} I_1 + \partial_{x_2} I_2\right)\left(\partial_{x_1} H_2 - \partial_{p_2} H_1\right) = 0. \quad (7)$$

If the system is explicitly time independent, then $\partial_t I_1$ and $\partial_t I_2$ become zero in Eqs. (6) and (7) and the complex invariant for a system is obtained by transforming the given Hamiltonian H with (1).

The recipe to construct an invariant for a Hamiltonian system using rationalization method, in brief, is as follows. Choose a proper form of invariant I, in general, a polynomial in momenta, with some space and time dependent unknown co-efficients. By separating the real and imaginary parts of H and I, i.e. H_1, H_2, I_1 and I_2 respectively, insert these real and imaginary parts in Eqs. (6) and (7) and subsequently the rationalization of the resultant expressions in powers of p_1, x_2 and of their products yields a set of coupled partial differential equations (PDEs) for arbitrary co-efficient functions appearing in I_1 and I_2. Next, solve these PDEs successively for various coefficients. In the end, substitute these solutions in Eq. (4) to find the final form of an invariant I.

2.1. Invariants for TID Hamiltonian systems

We now construct complex dynamical invariants for a variety of TID potentials like quartic, odd power quintic and even power sextic potentials by employing the above described procedure.

2.1.1. Invariants for a quartic potential

Consider the Hamiltonian for a general one-dimensional complex quartic potential as

$$H(x) = p^2 + \eta_1 x + \eta_2 x^2 + \eta_3 x^3 + \eta_4 x^4, \quad (8)$$

where η_i $(i = 1, 2, 3, 4)$ are arbitrary constant potential parameters.

After employing Eq. (1) in Eq. (8), the real and imaginary parts of H are separately written as

$$H_1 = (p_1^2 - x_2^2) - \eta_1 x_1 + \eta_2\left(x_1^2 - p_2^2\right) + \eta_3 x_1\left(x_1^2 - 3p_2^2\right) + \eta_4\left(x_1^4 - 6x_1^2 p_2^2 + p_2^4\right), \quad (9)$$

$$H_2 = 2p_1 x_2 + \eta_1 p_2 + 2\eta_2 x_1 p_2 + \eta_3 p_2\left(-p_2^2 + 3x_1^2\right) + 4\eta_4 x_1 p_2\left(x_1^2 - p_2^2\right). \quad (10)$$

Next, suppose the system (8) possesses an invariant, a second-order polynomial in momenta, of the form

$$I = a(x) + b(x)\ p^2, \quad (11)$$

where $a(x)$ and $b(x)$ are complex functions of position of the form $a(x) = a_r(x) + i\ a_i(x)$ and $b(x) = b_r(x) + i\ b_i(x)$.

Under the transformation (1), the real and imaginary parts of Eq. (11) are respectively written as

$$I_1 = a_r + b_r\left(p_1^2 - x_2^2\right) - 2b_i p_1 x_2, \quad (12)$$

$$I_2 = a_i + b_i\left(p_1^2 - x_2^2\right) + 2b_r p_1 x_2. \quad (13)$$

Substituting Eqs. (9), (10), (12) and (13) in Eq. (6) and then after rationalization of the resultant expression, the following set of equations is obtained:

$$\partial_{x_1} b_r + \partial_{p_2} b_i = 0, \tag{14}$$

$$\partial_{x_1} b_i - \partial_{p_2} b_r = 0, \tag{15}$$

$$\begin{aligned}(\partial_{x_1} a_r + \partial_{p_2} a_i) - 2b_r\left[\eta_1 + 2\eta_2 x_1 + 3\eta_3\left(x_1^2 - p_2^2\right) + 4\eta_4 x_1\left(x_1^2 - 3p_2^2\right)\right] \\ + 4b_i p_2\left[-\eta_2 + 3\eta_3 x_1 + 2\eta_4 p_2\left(3x_1^2 - p_2^2\right)\right] = 0,\end{aligned} \tag{16}$$

$$\begin{aligned}(\partial_{p_2} a_r - \partial_{x_1} a_i) + 2b_i\left[\eta_1 + 2\eta_2 x_1 + 3\eta_3\left(x_1^2 - p_2^2\right) + 4\eta_4 x_1\left(x_1^2 - 3p_2^2\right)\right] \\ + 4b_r p_2\left[\eta_2 + 3\eta_3 x_1 + 2\eta_4 p_2\left(3x_1^2 - p_2^2\right)\right] = 0.\end{aligned} \tag{17}$$

To obtain the invariant I, the arbitrary coefficients present in Eqs. (12) and (13) are to be determined on solving Eqs. (14)–(17).

(i) Solutions of b_r and b_i: The partial differential equations (14) and (15) can be reduced to similar second order partial differential equations as

$$\partial_{x_1}^2 b_r + \partial_{p_2}^2 b_r = 0, \tag{18}$$

$$\partial_{x_1}^2 b_i + \partial_{p_2}^2 b_i = 0. \tag{19}$$

The coordinate separability for b_r and b_i under addition is given by

$$b_r = X_r(x_1) + P_r(p_2), \qquad b_i = X_i(x_1) + P_i(p_2). \tag{20}$$

Under the assumption of separability condition (20), solutions of Eqs. (18) and (19) can be written as

$$b_r = \beta\left(x_1^2 - p_2^2\right) + \beta_1 p_2 - \beta_2 x_1 + \zeta_1, \tag{21}$$

$$b_i = \gamma\left(x_1^2 - p_2^2\right) + \beta_1 x_1 - \beta_2 p_2 + \zeta_2, \tag{22}$$

where, γ, β, β_1, β_2, ζ_1, and ζ_2 are arbitrary constants of integration.

(ii) Solutions of a_r and a_i: After differentiating Eqs. (16) and (17) w.r.t. x_1 and p_2 respectively and then adding, one gets

$$\begin{aligned}\partial_{x_1}^2 a_r + \partial_{p_2}^2 a_r + 2\left[-\partial_{x_1} b_r + \partial_{p_2} b_i\right]\left[\eta_1 + 2\eta_2 x_1 + 3\eta_3(x_1^2 - p_2^2) + 4\eta_4 x_1(x_1^2 - 3p_2^2)\right] \\ + 4\left(\partial_{x_1} b_i + \partial_{p_2} b_r\right) p_2\left[2\eta_2 + 3\eta_3 x_1 + 2\eta_4(3x_1^2 - p_2^2)\right] = 0.\end{aligned} \tag{23}$$

Further, using Eqs. (21) and (22) in Eq. (23) and employing the condition (20), we obtain

$$\begin{aligned}a_r = \frac{4}{5}\eta_4\left[\left(-\beta_2 x_1^5 + \beta_1 p_2^5\right) + 5x_1 p_2\left(-\beta_1 x_1^3 + \beta_2 p_2^3\right)\right] - \eta_3\left[\beta_2\left(x_1^4 - p_2^4\right) - 2\beta_1 x_1 p_2\left(x_1^2 + p_2^2\right)\right] \\ - \frac{2}{3}\eta_2\left[\left(\beta_2 x_1^3 + \beta_1 p_2^3\right) - 6x_1 p_2\left(\beta_2 p_2 + \beta_1 x_1\right)\right] - \beta_2\eta_1\left(x_1^2 + p_2^2\right).\end{aligned} \tag{24}$$

Similarly, a_i is computed as

$$a_i = \frac{4}{5}\eta_4\left[\left(\beta_1 x_1^5 + \beta_2 p_2^5\right) - 5x_1 p_2\left(\beta_2 x_1^3 + \beta_1 p_2^3\right)\right] + \eta_3\left[\beta_1\left(x_1^4 - p_2^4\right) - 2\beta_2 x_1 p_2\left(x_1^2 + p_2^2\right)\right] + \frac{2}{3}\eta_2\left[\left(\beta_1 x_1^3 - \beta_2 p_2^3\right) + 6x_1 p_2\left(\beta_1 p_2 - \beta_2 x_1\right)\right] + \beta_1\eta_1\left(x_1^2 + p_2^2\right). \tag{25}$$

On employing the arbitrary coefficients, i.e. a_r, a_i, b_r and b_i, in Eqs. (12) and (13), I_1 and I_2 are written as

$$I_1 = \frac{4}{5}\eta_4\left[\left(-\beta_2 x_1^5 + \beta_1 p_2^5\right) + 5x_1 p_2\left(-\beta_1 x_1^3 + \beta_2 p_2^3\right)\right] - \eta_3\left[\beta_2(x_1^4 - p_2^4) - 2\beta_1 x_1 p_2(x_1^2 + p_2^2)\right] - \frac{2}{3}\eta_2\left[(\beta_2 x_1^3 + \beta_1 p_2^3) - 6x_1 p_2(\beta_2 p_2 + \beta_1 x_1)\right] - \beta_2\eta_1\left(x_1^2 + p_2^2\right) + \left(\beta_1 p_2 - \beta_2 x_1\right)\left(p_1^2 - x_2^2\right) - 2\left(\beta_1 x_1 - \beta_2 p_2\right)p_1 x_2, \tag{26}$$

and

$$I_2 = \frac{4}{5}\eta_4\left[\left(\beta_1 x_1^5 + \beta_2 p_2^5\right) - 5x_1 p_2\left(\beta_2 x_1^3 + \beta_1 p_2^3\right)\right] + \eta_3\left[\beta_1(x_1^4 - p_2^4) - 2\beta_2 x_1 p_2\left(x_1^2 + p_2^2\right)\right] + \frac{2}{3}\eta_2\left[\left(\beta_1 x_1^3 - \beta_2 p_2^3\right) + 6x_1 p_2\left(\beta_1 p_2 - \beta_2 x_1\right)\right] + \beta_1\eta_1\left(x_1^2 + p_2^2\right) + \left(\beta_1 x_1 - \beta_2 p_2\right)\left(p_1^2 - x_2^2\right) + 2\left(\beta_1 p_2 - \beta_2 x_1\right)p_1 x_2. \tag{27}$$

After inserting Eqs. (26) and (27) in Eq. (4), the invariant I is given by

$$I = \Omega\left[-\frac{1}{5}\eta_4 x^*(x^{*4} - 5x^4) + \eta_3 x^* x^3 - \frac{1}{3}\eta_2 x^*\left(x^{*2} - 3x^2\right) + \eta_1 x x^* + x^* p^2\right], \tag{28}$$

where $x^* = x_1 - ip_2$, $\Omega = -\beta_2 + i\beta_1$ is an arbitrary constant, which conforms the integrability condition (6) and (7).

2.1.2. Invariants for an odd power quintic potential

For one-dimensional odd power quintic potential, the Hamiltonian is written as

$$H(x) = p^2 + \eta_1 x + \eta_3 x^3 + \eta_5 x^5. \tag{29}$$

Using transformation (1), the real and imaginary parts of Eq. (29) are written as

$$H_1 = (p_1^2 - x_2^2) + \eta_1 x_1 + \eta_3 x_1\left(x_1^2 - 3p_2^2\right) + \eta_5 x_1\left(x_1^5 4 - 10x_1^3 2p_2^2 + 5p_2^4\right), \tag{30}$$

$$H_2 = 2p_1 x_2 + \eta_1 p_2 + \eta_3 p_2\left(-p_2^2 + 3x_1^2\right) + \eta_5 p_2\left(p_2^4 + 5x_1^4 p - 10x_1^2 p_2^2\right). \tag{31}$$

Again, suppose that this system (29) owns an invariant of the form (11). Now, employing Eqs. (12), (13), (30) and (31) in Eq. (6) and then on rationalization the resulting expression, one finds the following two equations, in addition to Eqs. (14)

and (15), as

$$(\partial_{x_1}a_r + \partial_{p_2}a_i) - 2b_r\left[\eta_1 + 3\eta_3(x_1^2 - p_2^2) + 5\eta_5(x_1^4 - 6x_1^2p_2^2 + p_2^4)\right] + 4b_i x_1 p_2\left[3\eta_3 + 10\eta_5(x_1^2 - p_2^2)\right] = 0, \quad (32)$$

$$(\partial_{p_2}a_r - \partial_{x_1}a_i) + 2b_i\left[\eta_1 + 3\eta_3(x_1^2 - p_2^2) + 5\eta_5(x_1^4 - 6x_1^2p_2^2 + p_2^4)\right] + 4b_r x_1 p_2\left[3\eta_3 + 10\eta_5(x_1^2 - p_2^2)\right] = 0. \quad (33)$$

From Eqs. (32) and (33), we easily obtain the following

$$\partial_{x_1}^2 a_r + \partial_{p_2}^2 a_r - 2(\partial_{x_1}b_r - \partial_{p_2}b_i)\left[\eta_1 + 3\eta_3(x_1^2 - p_2^2) + 5\eta_5(x_1^4 - 6x_1^2p_2^2 + p_2^4)\right] + 4x_1p_2(\partial_{x_1}b_i - \partial_{p_2}b_r\left[3\eta_3 + 10\eta_5(x_1^2 - p_2^2)\right] = 0. \quad (34)$$

After, using Eqs. (21) and (22) in Eq. (34), one obtains

$$a_r = -\beta_2\eta_5\left[x_1^6 + p_2^6 - 5x_1^2p_2^2(x_1^2p_2^2 + x_1^2p_2^2)\right] - 4\beta_1\eta_5 x_1 p_2\left(x_1^4 - p_2^4\right) - 2\beta_1\eta_3 x_1 p_2\left(x_1^2 + p_2^2\right) - \beta_2\eta_3\left(x_1^4 - p_2^4\right) - \beta_2\eta_1\left(x_1^2 + p_2^2\right). \quad (35)$$

Similarly, one can find

$$a_i = -4\beta_2 x_1 p_2\left[\frac{1}{2}\eta_3(x_1^2 + p_2^2) + \eta_5(x_1^4 - p_2^4)\right] - 4\beta_1\left[\eta_1(x_1^2 + p_2^2) + \eta_3(x_1^4 - p_2^4) + \eta_5(x_1^6 + p_2^6) - 5x_1^2p_2^2(x_1^2 + p_2^2)\right], \quad (36)$$

Using Eqs. (21) and (22) along with Eqs. (35) and (36) in Eqs. (12) and (13), we find

$$I_1 = -\beta_2\eta_5\left(x_1^6 + p_2^6 - 5x_1^2p_2^2(x_1^2 + p_2^2)\right) - 2\beta_1 x_1 p_2\left(2\eta_5(x_1^4 - p_2^4) - \eta_3(x_1^2 + p_2^32)\right) - \beta_2\left(\eta_3(x_1^4 - p_2^4) - \eta_1(x_1^2 + p_2^2)\right) + \left(\beta_1 p_2 - \beta_2 x_1\right)\left(p_1^2 - x_2^2\right) - 2\left(\beta_1 x_1 + \beta_2 p_2\right)p_1 x_2, \quad (37)$$

$$I_2 = -2\beta_2 x_1 p_2\left[\eta_3(x_1^2 + p_2^2) + 2\eta_5(-x_1^4 - p_2^4)\right] + \beta_1\left[\eta_1(x_1^2 + p_2^2) + \eta_3(x_1^4 - p_2^4) + \eta_5(x_1^6 + p_2^6 - 5x_1^2p_2^2(x_1^2 + p_2^2))\right] + (\beta_1 x_1 - \beta_2 p_2)(p_1^2 - x_2^2) + 2(\beta_1 p_2 - \beta_2 x_1)p_1 x_2. \quad (38)$$

Finally, the invariant $(I = I_1 + \iota I_2)$ is written as

$$I = \Omega x^*\left[\eta_5 x^5 + \eta_3 x^3 + \eta_1 x + p^2\right], \quad (39)$$

where $x^* = x_1 - ip_2$ and $\Omega = -\beta_2 + i\beta_1$ is arbitrary coefficient which conforms the integrability condition.

2.1.3. Invariants for an even power sextic potential

The Hamiltonian for one-dimensional even power sextic potential is written as

$$H(x) = p^2 + \eta_2 x^2 + \eta_4 x^4 + \eta_6 x^6. \quad (40)$$

From Eqs. (1) and (40) we have

$$H_1 = (p_1^2 - x_2^2) - \eta_2(x_1^2 - p_2^2) + \eta_4(x_1^4 - 6x_1^2p_2^2 + p_2^4) + \eta_6(x_1^6 - 15x_1^4p_2^2 + 15x_1^2p_2^4 - p_2^6) \quad (41)$$

$$H_2 = 2p_1x_2 + 2\eta_2x_1p_2 + 4x_1p_2\eta_4(x_1^2 - p_2^2) + 2\eta_6x_1p_2(3x_1^4 - 10x_1^2p_2^2 + 3p_2^4). \quad (42)$$

Again using Eqs. (12), (13), (41) and (42) in Eq. (6) and then after rationalization, the following equations are obtained in addition to Eqs. (14) and (15) as

$$(\partial_{x_1}a_r + \partial_{p_2}a_i) - 2b_rx_1\left[-2\eta_2 + 4\eta_4(x_1^2 - 3p_2^2) - 6\eta_6(x_1^4 - 10x_1^2p_2^2 + 5p_2^4)\right] + 4b_ip_2\left[-\eta_2 + 2\eta_4(3x_1^2 - p_2^2) - 3\eta_6(5x_1^4 - 10x_1^2p_2^2 + p_2^4)\right] = 0, \quad (43)$$

$$(\partial_{p_2}a_r - \partial_{x_1}a_i) + 2b_ix_1\left[-2\eta_2 + 4\eta_4(x_1^2 - 3p_2^2) - 6\eta_6(x_1^4 - 10x_1^32p_2^2 + 5p_2^4)\right] + 4b_rp_2\left[-\eta_2 + 2\eta_4(3x_1^2 - p_2^2) - 3\eta_6(5x_1^4 - 10x_1^2p_2^2 + p_2^4)\right] = 0. \quad (44)$$

From Eqs. (43) and (44) we obtain

$$\partial_{x_1}^2a_r + \partial_{p_2}^2a_r - 4(\partial_{x_1}b_r - \partial_{p_2}b_i)x_1\left[-\eta_2 + 2\eta_4(x_1^2 - 3p_2^2) - 3\eta_6(x_1^4 - 10x_1^2p_2^2 + 5p_2^4)\right] + 4(\partial_{x_1}b_i - \partial_{p_2}b_r) \times p_2\left[-\eta_2 + 2\eta_4(3x_1^2 - p_2^2) - 3\eta_6(5x_1^4 - 10x_1^2p_2^2 + p_2^4)\right] = 0. \quad (45)$$

Using Eqs. (21) and (22) in Eq. (45) we have

$$a_r = -4\beta_2x_1\left[-\eta_2\left(\frac{x_1^2}{6} + \frac{p_2^2}{2}\right) + \eta_4\left(\frac{x_1^4}{5} - p_2^4\right) - \frac{3}{2}\eta_6\left(\frac{x_1^6}{7} - x_1^4p_2^2 - \frac{5}{3}x_1^2p_2^4 + p_2^6\right)\right] - 4\beta_1p_2\left[-\eta_2\left(\frac{p_2^2}{6} + x_1^2\right) + \eta_4\left(x_1^4 - \frac{p_2^4}{5}\right) - \frac{3}{2}\eta_6\left(x_1^6 - \frac{5}{3}x_1^4p_2^2 + \frac{p_2^6}{7} - x_1^2p_2^4\right)\right], \quad (46)$$

Similarly, a_i can be written as

$$a_i = 4\beta_1x_1\left[-\eta_2\left(\frac{x_1^2}{6} + \frac{p_2^2}{2}\right) + \eta_4\left(\frac{x_1^4}{5} - p_2^4\right) - \frac{3}{2}\eta_6\left(\frac{x_1^6}{7} - x_1^4p_2^2 - \frac{5}{3}x_1^2p_2^4 + p_2^6\right)\right] - 4\beta_2p_2\left[-\eta_2\left(\frac{p_2^2}{6} + \frac{x_1^2}{2}\right) + \eta_4\left(x_1^4 - \frac{p_2^4}{5}\right) - \frac{3}{2}\eta_6\left(x_1^6 - \frac{5}{3}x_1^4p_2^2 + \frac{p_2^6}{7} - x_1^2p_2^4\right)\right], \quad (47)$$

Using Eqs. (21) and (22) along with Eqs. (35) and (36) in Eqs. (46) and (47), I_1 and I_2 are written as

$$I_1 = -4\beta_2x_1\left[-\eta_2\left(\frac{x_1^2}{6} + \frac{p_2^2}{2}\right) + \eta_4\left(\frac{x_1^4}{5} - p_2^4\right) - \eta_6\left(\frac{x_1^6}{7} - x_1^4p_2^2 - \frac{5}{3}x_1^2p_2^4 + p_2^6\right)\right] - 4\beta_1p_2\left[-\eta_2\left(\frac{p_2^32}{6} + x_1^2\right) + \eta_4\left(x_1^4 - \frac{p_2^4}{5}\right) - \eta_6\left(2x_1^6 - \frac{5}{3}x_1^4p_2^2 + \frac{p_2^6}{7} - x_1^2p_2^4\right)\right] + (\beta_1 - \beta_2x_1)(p_1^2 - x_2^2) - 2(\beta_1x_1 - \beta_2p_2)p_1x_2 \quad (48)$$

$$I_2 = 4\beta_1 x_1\left[-\eta_2\left(\frac{x_1^2}{6}+\frac{p_2^2}{2}\right)+\eta_4\left(\frac{x_1^4}{5}-p_2^4\right)-\frac{3}{2}\eta_6\left(\frac{x_1^6}{7}-x_1^4p_2^2-\frac{5}{3}x_1^2p_2^4+p_2^6\right)\right]$$
$$-4\beta_2 p_2\left[-\eta_2\left(\frac{p_2^2}{6}+\frac{x_1^2}{2}\right)+\eta_4\left(x_1^4-\frac{p_2^4}{5}\right)-\frac{3}{2}\eta_6\left(x_1^6-\frac{5}{3}x_1^4p_2^2+\frac{p_2^6}{7}-x_1^2p_2^4\right)\right]$$
$$+\left(\beta_1x_1-\beta_2p_2\right)\left(p_1^2-x_2^2\right)+2\left(\beta_1p_2-\beta_2x_1\right)p_1x_2. \tag{49}$$

Using Eqs. (48) and (49) in Eq. (4) we have

$$I = \Omega\left[-\frac{\eta_6}{7}x^*\left(x^{*6}-7x^6\right)-\frac{1}{5}\eta_4x^*\left(x^{*4}-5x^4\right)-\frac{1}{3}\eta_2x^*\left(x^{*2}-3x^2\right)\right], \tag{50}$$

where $x^* = x_1 - ip_2$ and $\Omega = -\beta_2 + i\beta_1$ is the arbitrary coefficient which is in agreement with integrability condition.

3. Invariant for a TD system

Struckmier and Reidel in their seminal work derived exact quadratic invariants (hereafter called SR invariants) for n-degrees of freedom TD Hamiltonian systems. These invariants were found to contain a TD function $f_2(t)$, a solution of a third order differential equation whose coefficients depend on the explicitly known trajectories of N-particle system. The so constructed TD invariants were found vital to assess the accuracy of numerical simulations of some TD Hamiltonian systems [10, 11]. Therefore, keeping in view the importance of SR invariants for real TD Hamiltonian systems, here in what follows, we deduce such an invariant for complex Hamiltonian system within the framework of ECPS approach.

Consider a system of a single particle which is moving in an explicitly TD and velocity-independent potential and described by a Hamiltonian as

$$H = \frac{1}{2}p^2 + V(x,t). \tag{51}$$

The Hamiltonian $H(x,p,t)$ of a one-dimensional system in complex space can be expressed, using Eq. (1), as

$$H = H_1\left(x_1,p_2,p_1,x_2,t\right) + iH_2\left(x_1,p_2,p_1,x_2,t\right). \tag{52}$$

Note that (x_1,p_1), (x_2,p_2) constitute canonical pairs. The Hamiltonian, Eq. (51), in ECPS can be written as

$$H = \frac{1}{2}\left(p_1^2-x_2^2+2ip_1x_2\right)+\left(V_r\left(x_1,p_2,t\right)+iV_i\left(x_1,p_2,t\right)\right), \tag{53}$$

which, after separating real and imaginary parts, can further be written as

$$H_1 = \frac{1}{2}\left(p_1^2-x_2^2\right)+V_r, \tag{54}$$
$$H_2 = p_1x_2+V_i, \tag{55}$$

where V_r and V_i are real and imaginary parts of the potential. The Hamilton's equations of motion for complex H can now be given as

$$\dot{x}_1 = \frac{1}{2}\left(\frac{\partial H_1}{\partial p_1} + \frac{\partial H_2}{\partial x_2}\right), \qquad \dot{p}_2 = \frac{1}{2}\left(\frac{\partial H_2}{\partial p_1} - \frac{\partial H_1}{\partial x_2}\right),$$
$$\dot{p}_1 = -\frac{1}{2}\left(\frac{\partial H_1}{\partial x_1} + \frac{\partial H_2}{\partial p_2}\right), \qquad \dot{x}_2 = -\frac{1}{2}\left(\frac{\partial H_2}{\partial x_1} - \frac{\partial H_1}{\partial p_2}\right). \tag{56}$$

Now consider a complex phase space function $I(x, p, t)$ as

$$I = I_1\big(x_1, p_2, p_1, x_2, t\big) + iI_2\big(x_1, p_2, p_1, x_2, t\big). \tag{57}$$

The function I is said to be a TD invariant of the system in complex phase space if it conforms to the invariance condition Eq. (5). Now we examine the existence of a conserved quantity Eq. (57) for a system described by Eq. (51) with a special ansatz for I being at most quadratic in momenta, i.e.

$$I = f_2(t)\big(p_1^2 - x_2^2 + 2ip_1x_2\big) + f_1\big(x_1, p_2, t\big)\big(p_1 + ix_2\big) + f_0\big(x_1, p_2, t\big), \tag{58}$$

where $f_1 = f_{1r} + if_{1i}$ and $f_0 = f_{0r} + if_{0i}$ that render I invariant which is to be determined as a function of f_2. The above equation is written as

$$I_1 = f_2(p_1^2 - x_2^2) + f_{1r}p_1 - f_{1i}x_2 + f_{0r}, \tag{59}$$

$$I_2 = 2f_2p_1x_2 + f_{1r}x_2 + f_{1i}p_1 + f_{0i}, \tag{60}$$

after separating the real and imaginary parts.

Now using Eqs. (54)–(56), (59) and (60) in Eqs. (6) and (7), we obtain the following expressions

$$\begin{aligned}
&\dot{f}_2(p_1^2 - x_2^2) - f_2\left(\frac{\partial H_1}{\partial x_1} + \frac{\partial H_2}{\partial p_2}\right)p_1 + f_2\left(\frac{\partial H_2}{\partial x_1} - \frac{\partial H_1}{\partial p_2}\right)x_2 + \frac{\partial f_{1r}}{\partial t}p_1 + \frac{\partial f_{1r}}{\partial x_1}\left(\frac{\partial H_1}{\partial p_1} + \frac{\partial H_2}{\partial x_2}\right)\frac{p_1}{2} \\
&\quad - \frac{f_{1r}}{2}\left(\frac{\partial H_1}{\partial x_1} + \frac{\partial H_2}{\partial p_2}\right) + \frac{\partial f_{1i}}{\partial t}x_2 - \frac{\partial f_{1i}}{\partial p_2}\left(\frac{\partial H_2}{\partial p_1} - \frac{\partial H_1}{\partial x_2}\right)\frac{x_2}{2} - \frac{f_{1i}}{2}\left(\frac{\partial H_2}{\partial x_1} - \frac{\partial H_1}{\partial p_2}\right) \\
&\quad + \frac{1}{2}\frac{\partial f_{0r}}{\partial x_1}\left(\frac{\partial H_1}{\partial p_1} + \frac{\partial H_2}{\partial x_2}\right) + \frac{1}{2}\frac{\partial f_{0r}}{\partial p_2}\left(\frac{\partial H_2}{\partial p_1} - \frac{\partial H_1}{\partial x_2}\right) + \frac{\partial f_{0r}}{\partial t} = 0,
\end{aligned} \tag{61}$$

$$\begin{aligned}
&2\dot{f}_2p_1x_2 - f_2\left(\frac{\partial H_1}{\partial x_1} + \frac{\partial H_2}{\partial p_2}\right)x_2 - f_2\left(\frac{\partial H_2}{\partial x_1} - \frac{\partial H_1}{\partial p_2}\right)p_1 + \frac{\partial f_{1r}}{\partial t}x_2 + \frac{\partial f_{1r}}{\partial x_1}\left(\frac{\partial H_1}{\partial p_1} + \frac{\partial H_2}{\partial x_2}\right)\frac{x_2}{2} \\
&\quad - \frac{f_{1r}}{2}\left(\frac{\partial H_2}{\partial x_1} - \frac{\partial H_1}{\partial p_2}\right) + \frac{\partial f_{1i}}{\partial t}p_1 + \frac{\partial f_{1i}}{\partial p_2}\left(\frac{\partial H_2}{\partial p_1} - \frac{\partial H_1}{\partial x_2}\right)\frac{p_1}{2} - \frac{f_{1i}}{2}\left(\frac{\partial H_1}{\partial x_1} + \frac{\partial H_2}{\partial p_2}\right) \\
&\quad + \frac{1}{2}\frac{\partial f_{0i}}{\partial x_1}\left(\frac{\partial H_1}{\partial p_1} + \frac{\partial H_2}{\partial x_2}\right) + \frac{1}{2}\frac{\partial f_{0i}}{\partial p_2}\left(\frac{\partial H_2}{\partial p_1} - \frac{\partial H_1}{\partial x_2}\right) + \frac{\partial f_{0i}}{\partial t} = 0.
\end{aligned} \tag{62}$$

The rationalization of the above pair of equations for a given Hamiltonian with respect to powers of p_1, x_2 and their various products will yield a set of coupled

PDEs for arbitrary unknown complex coefficients appearing in the ansatz for invariant and solutions of which, in turn, will yield the final form of invariant I. Next, we employ the above line of action to determine a complex SR invariant for a general one-dimensional nonlinear complex quartic TD potential.

3.1. Complex SR invariant for a general TD quartic potential

As an example, we now consider a general one-dimensional nonlinear complex Hamiltonian system defined by

$$H = \frac{1}{2}p^2 + a_1(t)x + a_2(t)x^2 + a_3(t)x^3 + a_4(t)x^4. \tag{63}$$

Employing Eq. (1), the real and imaginary parts of the above Hamiltonian are respectively written as

$$\begin{aligned} H_1 = {} & \frac{1}{2}\left(p_1^2 - x_2^2\right) + a_{1r}x_1 - a_{1i}p_2 + a_{2r}\left(x_1^2 - p_2^2\right) - 2a_{2i}x_1p_2 + a_{3r}\left(x_1^3 - 3x_1p_2^2\right) \\ & - a_{3i}\left(3x_1^2p_2 - p_2^3\right) + a_{4r}\left(x_1^4 + p_2^4 - 6x_1^2p_2^2\right) - 4a_{4i}\left(x_1^3p_2 - x_1p_2^3\right), \end{aligned} \tag{64}$$

$$\begin{aligned} H_2 = {} & p_1x_2 + a_{1r}p_2 + a_{1i}x_1 + a_{2i}\left(x_1^2 - p_2^2\right) + 2a_{2r}x_1p_2 + a_{3i}\left(x_1^3 - 3x_1p_2^2\right) \\ & + a_{3r}\left(3x_1^2p_2 - p_2^3\right) + a_{4i}\left(x_1^4 + p_2^4 - 6x_1^2p_2^2\right) + 4a_{4r}\left(x_1^3p_2 - x_1p_2^3\right). \end{aligned} \tag{65}$$

with $a_1 = a_{1r} + ia_{1i}$, $a_2 = a_{2r} + ia_{2i}\ldots$ etc. In view of Eq. (56), Hamiltonian equations of motion for the above case are obtained as

$$\begin{aligned} & \dot{x}_1 = p_1, \qquad \dot{p}_2 = x_2, \\ & \dot{p}_1 = -a_{1r} - 2a_{2r}x_1 + 2a_{2i}p_2 - 3a_{3r}x_1^2 + 3a_{3r}p_2^2 + 6a_{3i}x_1p_2 \\ & \qquad - 4a_{4r}x_1^3 + 12a_{4r}x_1p_2^2 - 4a_{4i}p_2^3 + 12a_{4i}x_1^2p_2, \\ & \dot{x}_2 = -a_{1i} - 2a_{2r}p_2 - 2a_{2i}x_1 - 3a_{3i}x_1^2 + 3a_{3i}p_2^2 - 6a_{3r}x_1p_2 \\ & \qquad + 4a_{4r}p_2^3 - 12a_{4r}x_1^2p_2 - 4a_{4i}x_1^3 + 12a_{4i}x_1p_2^2. \end{aligned} \tag{66}$$

Now, using Eqs. (64) and (65) in Eqs. (61) and (62) and rationalizing the resultant expressions with respect to the powers of momentum p_1, x_2 and their combinations, we get the following set of PDEs as

$$\dot{f}_2 + \frac{\partial f_{1r}}{\partial x_1} = 0, \tag{67}$$

$$\dot{f}_2 + \frac{\partial f_{1i}}{\partial p_2} = 0, \tag{68}$$

$$2\dot{f}_2 + \frac{\partial f_{1r}}{\partial x_1} + \frac{\partial f_{1i}}{\partial p_2} = 0, \tag{69}$$

$$\begin{aligned} \frac{\partial f_{0r}}{\partial x_1} + \frac{\partial f_{1r}}{\partial t} - 2f_2(a_{1r} + 2a_{2r}x_1 - 2a_{2i}p_2 + 3a_{3r}x_1^2 - 3a_{3r}p_2^2 \\ - 6a_{3i}x_1p_2 + 4a_{4r}x_1^3 - 12a_{4r}x_1p_2^2 + 4a_{4i}p_2^3 - 12a_{4i}x_1^2p_2) = 0, \end{aligned} \tag{70}$$

$$\frac{\partial f_{0r}}{\partial p_2} - \frac{\partial f_{1i}}{\partial t} + 2f_2(a_{1i} + 2a_{2r}p_2 + 2a_{2i}x_1 + 3a_{3i}x_1^2 - 3a_{3i}p_2^2 + 6a_{3r}x_1p_2 - 4a_{4r}p_2^3 + 12a_{4r}x_1^2p_2 + 4a_{4i}x_1^3 - 12a_{4i}x_1p_2^2) = 0, \quad (71)$$

$$\frac{\partial f_{0i}}{\partial x_1} + \frac{\partial f_{1i}}{\partial t} - 2f_2(a_{1i} + 2a_{2r}p_2 + 2a_{2i}x_1 + 3a_{3i}x_1^2 - 3a_{3i}p_2^2 + 6a_{3r}x_1p_2 - 4a_{4r}p_2^3 + 12a_{4r}x_1^2p_2 + 4a_{4i}x_1^3 - 12a_{4i}x_1p_2^2) = 0, \quad (72)$$

$$\frac{\partial f_{0i}}{\partial p_2} + \frac{\partial f_{1r}}{\partial t} - 2f_2(a_{1r} + 2a_{2r}x_1 - 2a_{2i}p_2 + 3a_{3r}x_1^2 - 3a_{3r}p_2^2 - 6a_{3i}x_1p_2 + 4a_{4r}x_1^3 - 12a_{4r}x_1p_2^2 + 4a_{4i}p_2^3 - 12a_{4i}x_1^2p_2) = 0, \quad (73)$$

$$\frac{\partial f_{0r}}{\partial t} - f_{1r}(a_{1r} + 2a_{2r}x_1 - 2a_{2i}p_2 + 3a_{3r}x_1^2 - 3a_{3r}p_2^2 - 6a_{3i}x_1p_2 + 4a_{4r}x_1^3 - 12a_{4r}x_1p_2^2 + 4a_{4i}p_2^3 - 12a_{4i}x_1^2p_2) + f_{1i}(a_{1i} + 2a_{2r}p_2 + 2a_{2i}x_1 + 3a_{3i}x_1^2 - 3a_{3i}p_2^2 + 6a_{3r}x_1p_2 - 4a_{4r}p_2^3 + 12a_{4r}x_1^2p_2 + 4a_{4i}x_1^3 - 12a_{4i}x_1p_2^2) = 0, \quad (74)$$

$$\frac{\partial f_{0i}}{\partial t} - f_{1r}(a_{1i} + 2a_{2r}p_2 + 2a_{2i}x_1 + 3a_{3i}x_1^2 - 3a_{3i}p_2^2 + 6a_{3r}x_1p_2 - 4a_{4r}p_2^3 + 12a_{4r}x_1^2p_2 + 4a_{4i}x_1^3 - 12a_{4i}x_1p_2^2) - f_{1i}(a_{1r} + 2a_{2r}x_1 - 2a_{2i}p_2 + 3a_{3r}x_1^2 - 3a_{3r}p_2^2 - 6a_{3i}x_1p_2 + 4a_{4r}x_1^3 - 12a_{4r}x_1p_2^2 + 4a_{4i}p_2^3 - 12a_{4i}x_1^2p_2) = 0. \quad (75)$$

Next, we solve the above set of PDEs for different coupling functions appearing in the invariant. The solutions of Eqs. (67) and (68) are easily obtained as

$$f_{1r} = -\dot{f}_2x_1 + \alpha_1(t), \qquad f_{1i} = -\dot{f}_2p_2 + \alpha_2(t). \quad (76)$$

Here α's are integration constants to be obtained separately. Now, using the results of f_{1r} and f_{1i} from Eq. (76) in Eqs. (70)–(71) and Eqs. (72)–(73) separately, we get

$$f_{0r} = \frac{\ddot{f}_2}{2}(x_1^2 - p_2^2) + 2f_2[a_{1r}x_1 - a_{1i}p_2 + a_{2r}(x_1^2 - p_2^2) - 2a_{2i}x_1p_2 + a_{3r}(x_1^3 - 3x_1p_2^2) - a_{3i}(3x_1^2p_2 - p_2^3) + a_{4r}(x_1^4 + p_2^4 - 6x_1^2p_2^2) + 4a_{4i}(x_1p_2^3 - x_1^3p_2)] - \dot{\alpha}_1x_1 + \dot{\alpha}_2p_2 + \beta, \quad (77)$$

$$f_{0i} = \ddot{f}_2x_1p_2 + 2f_2[a_{1i}x_1 + a_{1r}p_2 + a_{2i}(x_1^2 - p_2^2) + 2a_{2r}x_1p_2 + a_{3i}(x_1^3 - 3x_1p_2^2) + a_{3r}(3x_1^2p_2 - p_2^3) + a_{4i}(x_1^4 + p_2^4 - 6x_1^2p_2^2) - 4a_{4r}(x_1p_2^3 - x_1^3p_2)] - \dot{\alpha}_2x_1 - \dot{\alpha}_1p_2 + \gamma. \quad (78)$$

Here γ and β are again integration constants to be determined separately. Similarly, using the results of f_{1r} and f_{1i} from Eq. (76) and partial time derivatives of

Eqs. (77) and (78) in Eqs. (74) and (75), we get the following set of third-order differential equations for $f_2(t)$ as

$$\begin{aligned}
&\frac{\dddot{f}_2}{2}(x_1^2-p_2^2)+\dot{f}_2[3a_{1r}x_1-3a_{1i}p_2+4a_{2r}(x_1^2-p_2^2)-8a_{2i}x_1p_2+5a_{3r}(x_1^3-3x_1p_2^2)\\
&\quad-5a_{3i}(3x_1^2p_2-p_2^3)+6a_{4r}(x_1^4+p_2^4-6x_1^2p_2^2)+24a_{4i}(x_1p_2^3-x_1^3p_2)]\\
&\quad+2f_2[\dot{a}_{1r}x_1-\dot{a}_{1i}p_2+\dot{a}_{2r}(x_1^2-p_2^2)-2\dot{a}_{2i}x_1p_2+\dot{a}_{3r}(x_1^3-3x_1p_2^2)-\dot{a}_{3i}(3x_1^2p_2-p_2^3)\\
&\quad+\dot{a}_{4r}(x_1^4+p_2^4-6x_1^2p_2^2)+4\dot{a}_{4i}(x_1p_2^3-x_1^3p_2)]-\alpha_1(a_{1r}+2a_{2r}x_1-2a_{2i}p_2+3a_{3r}x_1^2\\
&\quad-3a_{3r}p_2^2-6a_{3i}x_1p_2+4a_{4r}x_1^3-12a_{4r}x_1p_2^2+4a_{4i}p_2^3-12a_{4i}x_1^2p_2)\\
&\quad+\alpha_2(a_{1i}+2a_{2r}p_2+2a_{2i}x_1+3a_{3i}x_1^2-3a_{3i}p_2^2+6a_{3r}x_1p_2-4a_{4r}p_2^3\\
&\quad+12a_{4r}x_1^2p_2+4a_{4i}x_1^3-12a_{4i}x_1p_2^2)-\ddot{\alpha}_1x_1+\ddot{\alpha}_2p_2+\dot{\beta}=0, \qquad (79)\\
&\ddot{f}_2x_1p_2+\dot{f}_2[3a_{1i}x_1+3a_{1r}p_2+4a_{2i}(x_1^2-p_2^2)+8a_{2r}x_1p_2+5a_{3i}(x_1^3-3x_1p_2^2)\\
&\qquad+5a_{3r}(3x_1^2p_2-p_2^3)+6a_{4i}(x_1^4+p_2^4-6x_1^2p_2^2)-24a_{4r}(x_1p_2^3-x_1^3p_2)]\\
&\qquad+2f_2[\dot{a}_{1i}x_1+\dot{a}_{1r}p_2+\dot{a}_{2i}(x_1^2-p_2^2)+2\dot{a}_{2r}x_1p_2+\dot{a}_{3i}(x_1^3-3x_1p_2^2)\\
&\qquad+\dot{a}_{3r}(3x_1^2p_2-p_2^3)+\dot{a}_{4i}(x_1^4+p_2^4-6x_1^2p_2^2)-4\dot{a}_{4r}(x_1p_2^3-x_1^3p_2)]\\
&\qquad-\alpha_2(a_{1r}+2a_{2r}x_1-2a_{2i}p_2+3a_{3r}x_1^2-3a_{3r}p_2^2-6a_{3i}x_1p_2+4a_{4r}x_1^3\\
&\qquad-12a_{4r}x_1p_2^2+4a_{4i}p_2^3-12a_{4i}x_1^2p_2)-\alpha_1(a_{1i}+2a_{2r}p_2+2a_{2i}x_1+3a_{3i}x_1^2\\
&\qquad-3a_{3i}p_2^2+6a_{3r}x_1p_2-4a_{4r}p_2^3+12a_{4r}x_1^2p_2+4a_{4i}x_1^3-12a_{4i}x_1p_2^2)\\
&\qquad-\ddot{\alpha}_2x_1-\ddot{\alpha}_1p_2+\dot{\gamma}=0. \qquad (80)
\end{aligned}$$

Now, inserting the different solution functions from Eqs. (76)–(78) in Eqs. (59) and (60), the real and imaginary parts of invariant (57) are obtained as

$$\begin{aligned}
I_1&=f_2(p_1^2-x_2^2)-\dot{f}_2(x_1p_1-p_2x_2)+\frac{\ddot{f}_2}{2}(x_1^2-p_2^2)+2f_2[a_{1r}x_1-a_{1i}p_2+a_{2r}(x_1^2-p_2^2)\\
&\quad-2a_{2i}x_1p_2+a_{3r}(x_1^3-3x_1p_2^2)-a_{3i}(3x_1^2p_2-p_2^3)+a_{4r}(x_1^4+p_2^4-6x_1^2p_2^2)\\
&\quad+4a_{4i}(x_1p_2^3-x_1^3p_2)]-\dot{\alpha}_1x_1+\dot{\alpha}_2p_2+\beta, \qquad (81)\\
I_2&=2f_2p_1x_2-\dot{f}_2(x_1x_2+p_1p_2)+\ddot{f}_2x_1p_2+2f_2[a_{1i}x_1+a_{1r}p_2+a_{2i}(x_1^2-p_2^2)\\
&\quad+2a_{2r}x_1p_2+a_{3i}(x_1^3-3x_1p_2^2)+a_{3r}(3x_1^2p_2-p_2^3)+a_{4i}(x_1^4+p_2^4-6x_1^2p_2^2)\\
&\quad-4a_{4r}(x_1p_2^3-x_1^3p_2)]-\dot{\alpha}_2x_1-\dot{\alpha}_1p_2+\gamma. \qquad (82)
\end{aligned}$$

Here one can easily verify that the third-order differential equations (79) and (80) are merely total time derivatives of Eqs. (81) and (82), respectively, and provide solution function f_2. Further, using the definition given in Eq. (57), a final form of the complex SR invariant is given as

$$\begin{aligned}
I&=f_2(p_1^2-x_2^2+2ip_1x_2)-\dot{f}_2(x_1+ip_2)(p_1+ix_2)+2f_2[(a_{1r}+ia_{1i})(x_1+ip_2)\\
&\quad+(a_{2r}+ia_{2i})(x_1+ip_2)^2+(a_{3r}+ia_{3i})(x_1+ip_2)^3+(a_{4r}+ia_{4i})(x_1+ip_2)^4]\\
&\quad+\frac{\ddot{f}_2}{2}(x_1+ip_2)^2+(\alpha_1+i\alpha_2)(p_1+ix_2)-(\dot{\alpha}_1+i\dot{\alpha}_2)(x_1+ip_2)+(\beta+i\gamma). \qquad (83)
\end{aligned}$$

The above equation can further be written in a compact form as

$$I = 2f_2H - \dot{f}_2(x_1 + ip_2)(p_1 + ix_2) + \frac{\ddot{f}_2}{2}(x_1 + ip_2)^2 + (\alpha_1 + i\alpha_2)(p_1 + ix_2) - (\dot{\alpha}_1 + i\dot{\alpha}_2)(x_1 + ip_2) + (\beta + i\gamma). \tag{84}$$

Here, function f_2 is given as a solution of the following third-order equation

$$\dot{f}_2[3(a_{1r} + ia_{1i})(x_1 + ip_2) + 4(a_{2r} + ia_{2i})(x_1 + ip_2)^2 + 5(a_{3r} + ia_{3i})(x_1 + ip_2)^3 + 6(a_{4r} + ia_{4i})(x_1 + ip_2)^4] + 2f_2[(\dot{a}_{1r} + i\dot{a}_{1i})(x_1 + ip_2) + (\dot{a}_{2r} + i\dot{a}_{2i})(x_1 + ip_2)^2 + (\dot{a}_{3r} + i\dot{a}_{3i})(x_1 + ip_2)^3 + (\dot{a}_{4r} + i\dot{a}_{4i})(x_1 + ip_2)^4] + \frac{\dddot{f}_2}{2}(x_1 + ip_2)^2 - (\alpha_1 + i\alpha_2)[(a_{1r} + ia_{1i}) + 2(a_{2r} + ia_{2i})(x_1 + ip_2) + 3(a_{3r} + ia_{3i})(x_1 + ip_2)^2 + 4(a_{4r} + ia_{4i})(x_1 + ip_2)^3] - (\ddot{\alpha}_1 + i\ddot{\alpha}_2)(x_1 + ip_2) + (\dot{\beta} + i\dot{\gamma}) = 0, \tag{85}$$

which is obtained by adding iota times of Eq. (80) to Eq. (79). It should be noted, that if the function f_2 is assumed to be constant and different integration constants are set to zero then $I \propto H$ where H, the total energy, itself is a well known invariant. Again, it is important to note that the quantity obtained in Eq. (84), for the real case, turns out to be $I = 2f_2H - \dot{f}_2xp + \frac{\ddot{f}_2}{2}x^2 + \alpha p - \dot{\alpha}x + \beta$ which in turn matches the invariant obtained earlier in [10, 11] for $\alpha = b_x$ and $\beta = 0$.

4. Concluding remarks

Here, complex quadratic invariants have been investigated for both TID and TD Hamiltonian systems in an extended complex phase space. In case of TID Hamiltonian systems, complex invariants for quartic, odd power quintic and even power sextic one-dimensional polynomial potentials are constructed by employing the widely used rationalization method. We further extended the ECPS for TD systems. Here the form of TD complex invariant has been taken that of SR invariant which is being utilized for the accuracy check of numerical simulation of TD Hamiltonian systems. The rationalization method is again used to isolate complex SR invariant for a general TD quartic potential. This invariant, just like that of real systems, is found to be proportional to Hamiltonian of the concerned system and reduces to its real counterpart [10, 11] under certain restriction on arbitrary parameters. We hope this particular study of complex SR invariants may have some bearings on simulating trajectories of a system of particles under the influence of complex potentials. Through this study we expanded the scope of the rationalization method in ECPS to find complex SR invariant for TD Hamiltonian systems. We plan to extend the presented studies in our future research.

REFERENCES

[1] R. S. Kaushal, S. C. Mishra and K. C. Tripathy: Construction of the second constant of motion for two-dimensional classical systems, *J. Math. Phys.* **26**, 420 (1985).

[2] J. Hietarnita: New integrable Hamiltonians with transcendental invariants, *Phys. Rev. Lett.* **52**, 1057 (1984).
[3] L. S. Hall: Invariants polynomial in momenta for integrable Hamiltonians, *Phys. Rev. Lett.* **54**, 614 (1985). 3487
[4] M. Tabor: *Chaos and Integrability in Nonlinear Dynamics*, Wiley, New York, 1989.
[5] M. Lakshmanan and S. Rajasekar: *Nonlinear Dynamics: Integrability, Chaos and Patterns*, Springer, Berlin Heideberg, 2003.
[6] M. Maamache, O. K. Djeghiour, N. Mana and W. Koussa: Pseudo-invariants theory and real phases for systems with non-Hermitian time-dependent Hamiltonians, *Eur. Phys. J. Plus* **132**, 383 (2017).
[7] R. S. Kaushal: *Classical and Quantum Mechanics of Noncentral Potentials: A Survey of Two-Dimensional Systems*, Narosa Publishing House, New Delhi, 1998.
[8] R. K. Colegrave, P. Croxson and M. A. Mannon, Complex invariants for the time-dependent harmonic oscillator, *Phys. Lett. A* **131**, 407 (1988).
[9] A. L. Xavier Jr. and M. A. M. de Aguiar: Phase space approach to the tunnel effect : A new semiclassical traversal time, *Phys. Rev. Lett.* **79**, 3323 (1997).
[10] J. Struckmeier and C. Reidel: Exact invariants for a class of three-dimensional time-dependent classical Hamiltonians, *Phys. Rev. Lett.* **85**, 3830 (2000).
[11] J. Struckmeier and C. Reidel: Invariants for time-dependent Hamiltonian systems, *Phys. Rev. E* **64**, 026503 (2001).
[12] K. J. Whiteman: Invariants and stability in classical mechanics, *Rep. Prog. Phys.* **40**, 1033 (1977).
[13] X. Xue-Jun and M. Feng-Xiang: First integrals and stability of second-order differential equations, *Chin. Phys.* **15**, 1134 (2006).
[14] S. C. Mishra and D. Parashar: Integrable classical systems in higher dimensions, *Int. J. Theor. Phys.* **29**, 299 (1990).
[15] R. Rajaraman and E. J. Weinberg: Internal symmetry and the semiclassical method in quantum field theory, *Phys. Rev. D* **11**, 2950 (1975).
[16] N. N. Rao, B. Buti and S. B. Khadkikar: Hamiltonian systems with indefinite kinetic energy, *Pramana J. Phys.* **27**, 497 (1986).
[17] R. M. Singh: Exact solutions of the Schrödinger equation for an anharmonic potential in two dimensions, *Appl. Math. Comput.* **218**, 6439 (2012).
[18] D. R. Nelson and N. M. Snerb: Non-hermitian localization and population biology, *Phys. Rev. E* **58**, 1383 (1998).
[19] N. Hatano and D. R. Nelson: Vortex pinning and non-hermitian quantum mechanics, *Phys. Rev. B* **56**, 8651 (1997).
[20] T. J. Hollowood: Solitons in affine Toda field theories, *Nucl. Phys. B* **386**, 166 (1992).
[21] F. Verhest: Nonlinear wave interactions in a complex Hamiltonian formalism, *J. Phys. A: Math. Gen* **20**, 103 (1987).
[22] H. Goldstain: *Classical Mechanics*, 2nd ed. p.435, Addison Wesley, Reading MA, 1981.
[23] A. L. Xavier Jr. and M. A. M. de Aguiar: Complex trajectories in the quartic oscillator and its semiclassical coherent state, *Ann. Phys.(N.Y.)* **252**, 458 (1996).
[24] N. Moiseyev: Quantum theory of resonances: calculating energies, widths and cross-sections by complex scaling, *Phys. Rep.* **302**, 212 (1998).
[25] R. S. Kaushal and H. J. Korsch: Some remarks on complex Hamiltonian, *Phys. Lett. A* **276**, 47 (2000).
[26] Parthasarathi and R. S. Kaushal: Quantum mechanics of complex sextic potentials in one dimension, *Phys. Scr.* **68**, 115 (2003).
[27] R. M. Singh, F. Chand and S. C. Mishra: Solution of Schrödinger equation for two-dimensional complex quartic potentials, *Comm. Theor. Phys.* **51**, 397 (2009).
[28] S. B. Bhardwaj, R. M. Singh and S. C. Mishra: Quantum mechanics of $\mathcal{PT}$ and non $\mathcal{PT}$-symmetric potentials in three dimensions, *Pramana J. Phys.* **87**, 1 (2016).
[29] S. B. Bhardwaj, R. M. Singh and S. C. Mishra: Eigenspectra of a complex coupled harmonic potential in three dimensions, *Comput. Math. Appl.* **68**, 2068 (2014).
[30] R. M. Singh, S. B. Bhardwaj and S. C. Mishra: Closed-form solutions of the Schrödinger equation for a coupled harmonic potential in three dimensions, *Comput. Math. Appl.* **66**, 537 (2013).

[31] S. Singh and R. S. Kaushal: Complex dynamical invariants for one-dimensional classical systems, *Phys. Scr.* **67**, 181 (2003).
[32] R. S. Kaushal and S. Singh: Construction of complex invariants for classical dynamical systems, *Ann. Phys.* **288**, 253 (2001).
[33] H. R. Lewis: Classical and quantum systems with time-dependent harmonic-oscillator-type Hamiltonians, *Phys. Rev. Lett.* **18**, 510 (1967);
H. R. Lewis Jr.: Class of exact invariants for classical and quantum time-dependent harmonic oscillators, *J. Math. Phys.* **9**, 1976 (1968).
[34] I. Marquette and P. Winternitz: Superintegrable systems with a third order integrals of motion, *J. Phys. A: Math. Theor.* **41**, 304031 (2008).
[35] A. Mitsopoulos, M. Tsamparlis and A. Paliathanasis: Integrable and superintegrable potentials of 2d autonomous conservative dynamical systems, *Symmetry* **12**, 1655 (2020).
[36] S. B. Bhardwaj, R. M. Singh and K. Sharma: Complex dynamical invariant for a $\mathcal{PT}$- symmetric Hamiltonian system in higher dimensions, *Chin. J. Phys.* **55**, 533 (2017).
[37] S. B. Bhardwaj, R. M. Singh, K. Sharma, R. Rani and F. Chand: Complex Integrals for 3-dimensional non-hermitian Hamiltonian systems, *Chin. J. Phys.* **55**, 1170 (2017).
[38] R. M. Singh, S. B. Bhardwaj, K. Sharma, R. Rani, F. Chand and A. Malik: Integrability of a Time Dependent Coupled Harmonic Oscillator in Higher Dimensions, *Disc. Non. Comp.* **7**, 81 (2018).
[39] N. Kumar, F. Chand and S. C. Mishra: Exact fourth order invariants for one-dimensional time-dependent Hamiltonian systems, *Indian J. Phys.* **89**, 709 (2015).
[40] F. Chand: Fourth-order constants of motion for time independent classical and quantum systems in three dimensions, *Can. J. Phys.* **88**, 165 (2010).
[41] F. Chand and S. C. Mishra: Construction of exact complex dynamical invariant of a two-dimensional classical system, *Pramana-J Phys.* **67**, 999 (2006).
[42] M. Tsamparlis and A. Mitsopoulos: Quadratic first integrals of autonomous conservative dynamical systems, *J. Math. Phys.* **61**, 072703 (2020);
M. Tsamparlis and A. Mitsopoulos: First integrals of holonomic systems without Noether symmetries, *J. Math. Phys.* **61**, 122701 (2020).
[43] H. R. Lewis and W. B. Riesenfield: An exact quantum theory of the time-dependent harmonic oscillator and of a charged particle in a time-dependent electromagnetic field, *J. Math. Phys.* **10**, 1458 (1969).
[44] N. Kumar, S. B. Bhardwaj, V. Kumar, R. M. Singh and F. Chand: Dynamical invariants for time-dependent real and complex Hamiltonian systems, *J. Math. Phys.* **62**, 112705 (2021).
[45] N. Kumar, S. B. Bhardwaj, D. Bhardwaj, R. M. Singh and F. Chand: Complex invariants for some time-independent and time-dependent classical systems, *Rep. Math. Phys.* **88**, 399 (2021).

J Opt
https://doi.org/10.1007/s12596-023-01307-6

RESEARCH ARTICLE

Self-focusing of rippled *q*-Gaussian laser beams in plasmas: effect of relativistic nonlinearity

Naveen Gupta[1] · S. B. Bhardwaj[2] · Rohit Johari[1] · A. K. Alex[1] · Suman Choudhry[1] · Devinder Singh[3]

Received: 4 May 2023 / Accepted: 8 July 2023

Abstract Theoretical investigation on self-focusing of *q*-Gaussian laser beam propagating through underdense plasma has been presented. The optical nonlinearity of plasma has been modeled by the relativistic mass nonlinearity of plasma electrons in the field of laser beam. Using variational theory approach, semi-analytical solutions of the wave equations for the fields of main beam and that of ripple have been obtained. Emphasis has been put on the evolutions of the intensities of main beam and that of ripple.

Keywords *q*-Gaussian · Laser ripple · Variational theory · Clean energy · Self-focusing

Introduction

Since the 1930s, when scientists began to realize that the sun and other stars are powered by nuclear fusion, their thoughts turned toward recreating this process in the laboratory for the viable energy production. Because fusion can use atoms present in ordinary water as a fuel, harnessing the process could assure future generations of adequate electric power [1]. The ultimate stakes are so high, fusion will produce no harmful emissions—no sooty pollutants, no nuclear waste and no greenhouse gases. All the stars and the sun use their strong gravitational pull to compress nuclei to high densities. In addition, temperatures in the sun are extremely high, so that the positively charged nuclei have enough kinetic energy to overcome their mutual electrostatic repulsion and draw near enough to fuse. However, such resources are not readily available on the earth. The particles that fuse most easily are the nuclei of deuterium and tritium. To fuse even deuterium and tritium, hydrogen gas has to be heated intensely and also has to be confined long enough that the particle density multiplied by the confinement time exceeds 10^{14} seconds per cubic centimeter. Since the 1950s, fusion research has focused on two ways of achieving this number: inertial confinement and magnetic confinement.

The strategy of inertial confinement fusion (ICF) is to shine a symmetrical array of powerful laser beams onto a spherical capsule containing a D-T mixture. The laser beams vaporize the surface of the pellet that explodes outward. To conserve momentum, the inner sphere of fuel simultaneously shoots inward just like the recoil of a gun when the bullet is fired. Although the fuel is compressed for only a brief moment (about 10^{-10} second), extremely high densities of almost 10^{25} particles per cubic centimeter can be obtained [2, 3].

For the successful realization of ICF, it is highly necessary that the fuel pellet should be heated uniformly. However, due to the nonuniform irradiance (intensity ripples) over the cross sections of the laser beams, the pellet is not heated uniformly that derives an instability known as Rayleigh–Taylor (RT) instability [4–6]: Whenever a not-very-dense fluid (like air) pushes on a denser fluid (like water), the situation is inherently unstable. If the interface between the two fluids is having any imperfection like bumps or divots, then these imperfections will immediately grow with time.

This fundamental instability can even be observed in everyday kitchen scenarios. It may be difficult to imagine an instability in the kitchen, but consider the following question: Why does not the water stay in a glass when you invert it? At first glance, the answer may seem obvious:

✉ Naveen Gupta
naveens222@rediffmail.com

[1] Lovely Professional University, Phagwara, India

[2] S U S Govt. College, Indri, Karnal, India

[3] Dyal Singh College, Karnal, India

Published online: 06 August 2023

Gravity pulls the water down and causes it to spill onto the floor. However, upon closer examination, the answer is not as straightforward. Atmospheric pressure adds complexity to the question. Every exposed surface in contact with air experiences pressure. The weight of the atmosphere exerts pressure from all directions, compressing us. Every square inch of our skin is subjected to 14.7 pounds of air pressure pushing against us. We may not notice it because our bodies are accustomed to it, but this force is significant, capable of crushing a steel can under suitable conditions. It is also more than enough to support a glass filled with water and prevent the liquid from pouring out. You can try a simple experiment yourself (over a sink, of course). Fill a glass to the brim with water. Place a smooth, rigid piece of cardboard over the mouth of the glass and invert it. Carefully release the cardboard. If done gently enough, you will observe that the water remains inside the glass. The cardboard is not holding the water in place. It is not tightly sealed to the glass; even a slight touch will dislodge the cardboard and cause the water to escape. Moreover, the water is not defying gravity by some miraculous means. It is supported by the air pressure. The upward force of the atmosphere, at 14.7 pounds per square inch, is significantly stronger than the downward force exerted by the water in the glass, which amounts to only a few ounces per square inch. When these two forces clash, the upward push of the atmosphere prevails, and the water stays put. Surprisingly, the forces are so imbalanced that you would need an exceptionally tall glass of water, around thirty feet high, for the downward weight of the water to equal the upward pressure from the atmosphere. With such a substantial discrepancy between forces, the question becomes far less trivial: Why does not water remain in a glass when it is turned upside down? The water spills out due to an effect called the Rayleigh–Taylor instability. Whenever a less dense fluid (such as air) pushes against a denser fluid (such as water), it creates an intrinsically unstable situation. If the interface between the two fluids contains any imperfections, such as bumps or divots, those imperfections rapidly grow larger. When you invert a glass of water, even if you do so carefully, the liquid's surface exhibits a few crests and troughs. In a fraction of a second, these crests expand, transforming into large drooping tendrils of water hanging down from the surface, while the troughs deepen and allow significant pockets of air to penetrate the glass. The tendrils break, the air pockets detach, and the entire glass of water spills out onto the floor. This phenomenon exemplifies the Rayleigh–Taylor instability in action.

It is almost as if the laser scientists are trying to invert a glass so carefully that the surface of the water inside would not ripple at all. In ICF as the fuel pellet is compressed, it becomes denser and denser. Long before it is hot and dense enough to fuse, it will be much denser than whatever mean is being used to compress it. A less dense substance, i.e., laser beams are being used to squash and contain a much denser one, and hence, the situation will get prone to Rayleigh–Taylor instabilities. Any tiny imperfections on the interface between the plasma and the laser beams pushing on the plasma will grow with time. Even an almost perfectly spherical pellet of deuterium–tritium will quickly become distorted, squirting tendrils in all directions (Fig. 1). Just as RT instability ruins any attempt to keep water in an inverted glass by means of air pressure, it seriously damages ICF machine's ability to compress and contain fusion plasma by means of laser beams. Thus, it becomes essential to investigate the behavior of intensity ripples over the cross section of laser beams during their propagation through plasmas.

Intensity ripples in a laser system are due to spontaneous emissions [7, 8]. Each spontaneously emitted photon adds to the coherent field (established by stimulated emissions) a small field component whose phase is random, and thus perturbs both amplitude and phase in a random manner. The net result is that the intensity profile of the laser beam exhibits fluctuations in the form of ripples (Fig. 2).

An extended physical analogy can be helpful in comprehending the involved mechanisms. The oscillations of the electromagnetic field bear resemblance to the movements of a playground swing. Similar to the motion of a light wave, the swing's oscillation exhibits a specific frequency (the number of cycles or round trips the swing completes within a given time frame) and amplitude (the height reached by the swing in each cycle). The relative motion of two children on swings, like that of two light waves, is described in terms of their relative phase: If both children reach the highest point of their swing simultaneously in each cycle, they are swinging in phase. On the other hand, if they reach the peak at different times, they are said to be out of phase to some extent.

Let's consider a scenario where a child on a playground decides to operate a swing in a slightly unconventional manner. Instead of following the conventional method of leaning back and then forward once in each cycle, the child chooses to either stand on the seat or squat down at different moments during the swing's cycle. If the child squats as the swing approaches the highest point of its motion and stands up when the swing is closest to the ground (thus exerting effort against the centrifugal force), they will be injecting additional energy into the swing's motion, thereby amplifying it. Consequently, the swing will reach greater heights in every cycle. Conversely, if the child squats when the swing is nearest to the ground and stands up as it rises, they will diminish the swing's motion, resulting in reduced height in each subsequent cycle.

In our analogy, the pumping motion performed by the child exhibits two significant characteristics. Firstly, the child stands and squats twice during each round trip of the swing. In more technical terms, the frequency of the pumping action is twice the frequency of the swing's motion.

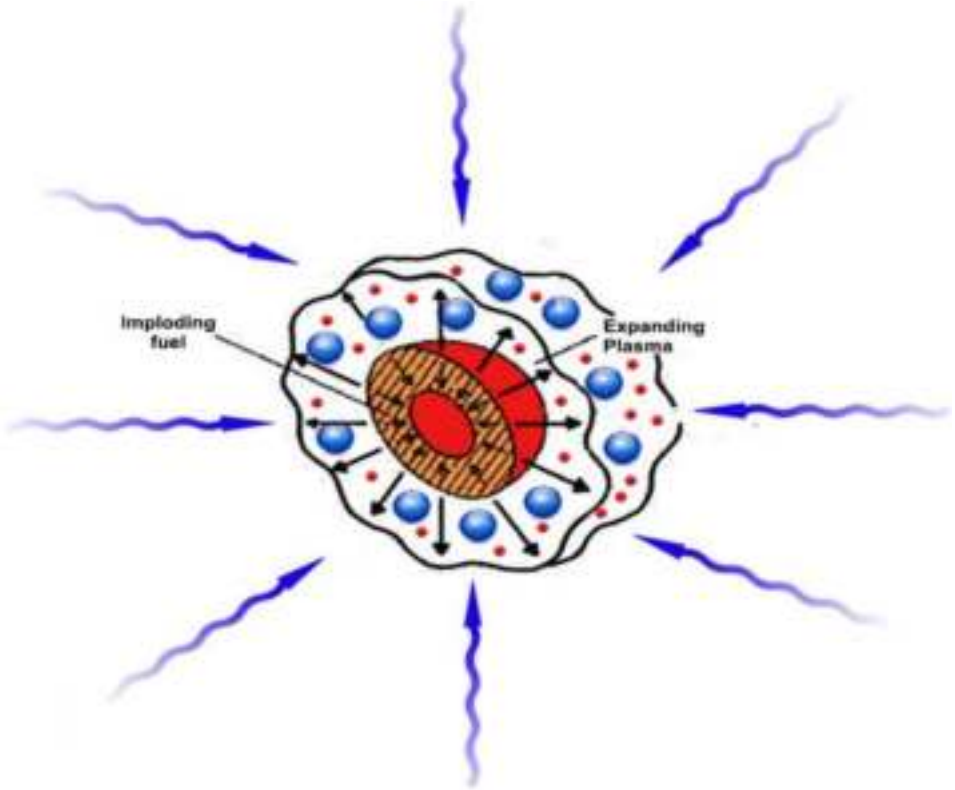

Fig. 1 Rayleigh–Taylor instability in ICF

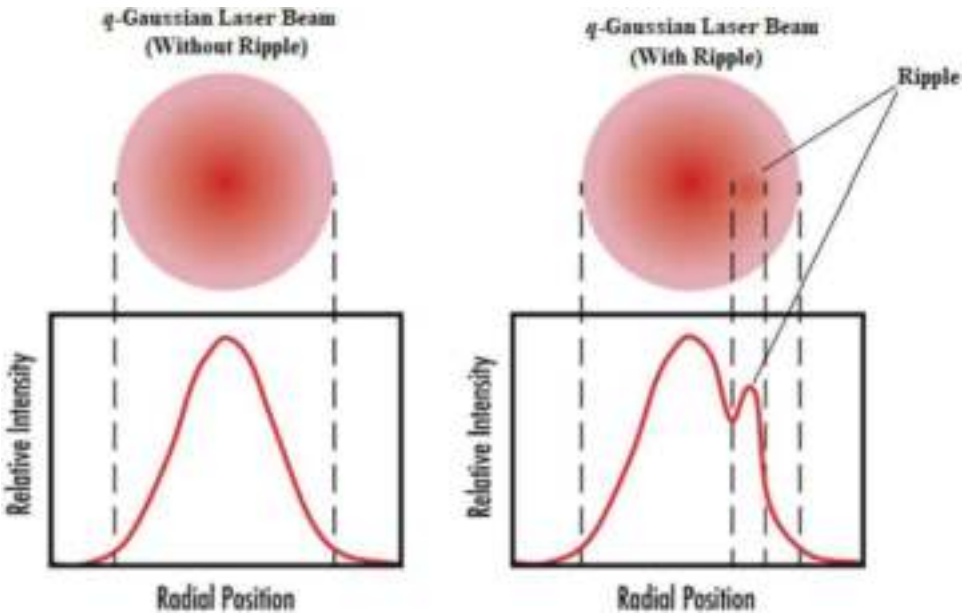

Fig. 2 Intensity ripple on laser beam

Secondly, the swing's motion can be either amplified or diminished based on the relative phase of the child's standing and squatting positions, specifically whether the child stands or squats at the highest point of the swing's cycle.

Similarly, a comparable pumping action can be applied to a light wave that is confined within an elongated cavity equipped with mirrors at both ends. Assuming the length of the cavity precisely matches a whole number of wavelengths of the light, the confined wave undergoes interference with itself upon reflection from each end of the cavity. Consequently, the wave resonates as a standing wave, akin to how a sound wave resonates within an organ pipe.

Let's consider a scenario where it becomes feasible to oscillate the mirror at one end of the cavity back and forth, thus altering the cavity's length at precisely twice the frequency of the light wave. By consistently modifying the cavity's length in this manner, energy would be either added to or subtracted from the light wave as it reflects off the mirror. Similar to the child's pumping motion, the mirror's vibration would either amplify or diminish the light wave's intensity, depending on the relative phase between the mirror's vibration and the oscillation of the light wave. If the mirror's motion aligns with the appropriate phase of the light wave's oscillation, the wave is amplified, resulting in a strengthened oscillating electromagnetic field. Conversely, if the mirror's motion aligns with the complementary phase, the wave is de-amplified, causing the oscillating electromagnetic field to weaken.

Returning to our analogy, envision an entire playground filled with children, each on their respective swings. They are all swinging at the same frequency but are not synchronized in phase. At any given moment, some children may be near the top of their swing cycle while others are closer to the ground. Now, suppose a teacher enters the playground and uses a megaphone to shout "Stand… squat… stand… squat…" at exactly twice the frequency of the children's swinging. When the teacher shouts "Stand," some children will be near or at the bottom of their swing cycle, while others will be near or at the top. Those who stand near the bottom during the teacher's command will amplify the motion of their swings, whereas those who stand near the top will de-amplify the motion of their swings.

Gradually, the children who stand near the bottom of their swing cycle will start swinging with significantly greater amplitude than before, while those who stand near the top will experience minimal swinging. Consequently, the playground will feature a group of children swinging at much higher heights, almost perfectly in phase with one another and synchronized with the teacher's commands. Meanwhile, there will be another group of children who essentially cease swinging, despite continuing to stand and squat. In our analogy, these children correspond to spontaneously emitted photons those add up to stimulatedly emitted photons in the form of intensity ripples.

It is well known fact that laser beams differing in intensity profiles behave differently in plasmas [9–12]. However, the literature review reveals the fact that most of the earlier investigations on self-focusing of rippled laser beams in plasmas have been carried out for ideal Gaussian laser beams [13–18]. In contrast with this picture, the experimental investigations on the irradiance profile of Vulcan petawatt laser at Rutherford Appleton laboratory [19] reveal that the actual irradiance over the cross section of the laser beam is not ideally Gaussian. A significant amount of laser energy was found to be lying outside the half-width full maximum of the laser beam. The best irradiance profile that fits into the experimental data [20] is Tsallis q-Gaussian distribution [21]. To best of author's knowledge to earlier investigation on self-focusing of rippled laser beams in plasmas has been reported for q-Gaussian laser beams. Thus, the aim of this paper is to give first theoretical investigation on self-focusing of rippled q-Gaussian laser beams in plasmas with relativistic optical nonlinearity.

Relativistic nonlinearity of plasma

Consider the propagation of a laser beam with angular frequency ω_0 and wave number k_0 through a plasma with equilibrium electron density n_0. The dielectric function of such a plasma can be written as

$$\epsilon = 1 - \frac{\omega_p^2}{\omega_0^2}$$

where

$$\omega_p^2 = \frac{4\pi e^2}{m_e} n_0 \tag{1}$$

is the equilibrium plasma frequency, (m_e, e) being the electronic mass and charge, respectively.

The laser beam is having sharp intensity ripples over its cross section. The electric filed vector of such a laser beam can be written as

$$\boldsymbol{E} = (A_0 + A_r) e^{\imath(k_0 z - \omega_0 t)} \boldsymbol{e_x} \tag{2}$$

where A_0 is the amplitude of the field of main beam, and A_r is that of intensity ripple. Under the intense field of the laser beam, the oscillations of the plasma electrons become relativistic, and the mass m_e of the electron in Eq. (1) needs to be replaced by $m_0\gamma$, where m_0 is the rest mass of electron, and γ is the relativistic Lorentz factor and is related to laser field amplitude as [22]

$$\gamma = \sqrt{1 + \beta E E^\star} \tag{3}$$

where $\beta = \frac{e^2}{m_0^2 \omega_0^2 c^2}$ is the coefficient of relativistic nonlinearity and

$$EE^\star = A_0 A_0^\star + A_r A_r^\star + 2A_0 A_r \cos(\theta_p) \tag{4}$$

θ_p being the phase difference between the fields of main beam and intensity ripple.

Thus, in the presence of laser beam, the dielectric function of plasma gets modified as

$$\epsilon = 1 - \frac{\omega_{p0}^2}{\omega_0^2}\left(1 + \beta A_0 A_0^\star\right)^{-\frac{1}{2}} \tag{5}$$

where

$$\omega_{p0}^2 = \frac{4\pi e^2}{m_0} n_0$$

is the equilibrium plasma frequency. Thus, the relativistic effects make the index of refraction of plasma intensity dependent which, in turn, due to the spatial dependence of the amplitude structure of the laser beam, resembles to that of graded index fiber. Separating the dielectric function of plasma into linear (ϵ_0) and nonlinear (ϕ) parts as

$$\epsilon = \epsilon_0 + \phi\left(EE^\star\right) \tag{6}$$

we get

$$\epsilon_0 = 1 - \frac{\omega_{p0}^2}{\omega_0^2} \tag{7}$$

and

$$\phi\left(EE^\star\right) = \frac{\omega_{p0}^2}{\omega_0^2}\left\{1 - \frac{1}{(1 + \beta EE^\star)^{\frac{1}{2}}}\right\} \tag{8}$$

Evolution of beam widths of laser beam

The wave equation governing the evolution of amplitude A of the main beam is

$$\iota\frac{\partial A_0}{\partial z} = \frac{1}{2k_0}\nabla_\perp^2 A_0 + \frac{k_0}{2\epsilon_0}\phi\left(A_0 A_0^\star\right)A_0 \tag{9}$$

Being nonlinear in nature, linear combination of two solutions is not a solution of this equation. In other words, superposition principle does not apply to Eq. (9). Due to the non-applicability of superposition principle, Eq. (9) does not possess any closed form analytical solution. The only way to get physical insight is to use numerical methods or semi-analytical methods. In the present investigation, we have used a semi-analytical technique known as variational method [23–27] to obtain the solution of Eq. (9). This method converts the problem of solving a partial differential equation to that of solving a set of coupled ordinary differential equations. These ordinary differential equations govern the evolution of the various parameters of interest. In case of self-focusing of laser beam, the parameter of interest is the beam width of the laser beam. According to this method, Eq. (9) is a variational problem for action principle based on Lagrangian density

$$\begin{aligned}\mathcal{L}_M =& \iota\left(A_0\frac{\partial A_0^\star}{\partial z} - A_0^\star\frac{\partial A_0}{\partial z}\right) + \left|\nabla_\perp A_0\right|^2 \\ &- \frac{\omega_{p0}^2}{c^2}\int^{A_0A_0^\star}\left\{1 - \frac{1}{\left(1 + \beta AA_0^\star\right)^{\frac{1}{2}}}\right\}d\left(A_0A_0^\star\right)\end{aligned} \tag{10}$$

In the present investigation, we have considered the trial function of the form

$$A_0(x, y, z) = \frac{E_{00}}{f}\left\{1 + \frac{r^2}{qr_0^2f^2}\right\}^{-\frac{q}{2}} \tag{11}$$

Here E_{00} is the axial amplitude of the field of the laser beam, and r_0 is the initial beam width of the main laser beam. The phenomenological parameter q is related to the deviation of amplitude structure from ideal Gaussian profile and is termed as deviation parameter. The value of deviation parameter q varies from laser to laser and can be obtained by fitting into the experimental data for a given laser system. f is the currently undetermined, real function of longitudinal coordinate z. Upon multiplication with r_0, it gives the instantaneous spot size of the laser beam. Thus, the function f is termed as dimensionless beam width parameter.

Substituting the trial function given by Eq. (11) in Lagrangian density and integrating over the entire cross section of the laser beam, we get the reduced Lagrangian as $L_M = \int \mathcal{L}_M d^2r$. The corresponding Euler–Lagrange equation

$$\frac{\mathrm{d}}{\mathrm{d}z}\left(\frac{\partial L_M}{\partial\left(\frac{\partial f}{\partial z}\right)}\right) - \frac{\partial L_M}{\partial f} = 0 \tag{12}$$

gives

$$\begin{aligned}\frac{\mathrm{d}^2 f}{\mathrm{d}z^2} =& \frac{1}{2\mathrm{k}_0^2\mathrm{r}_0^4}\frac{1}{f^3}\left(1 - \frac{1}{\mathrm{q}}\right)\left(1 - \frac{2}{\mathrm{q}}\right) \\ &\left[\left(1 + \frac{1}{\mathrm{q}}\right)^{-1} + \left(< \mathrm{L}_1 > \frac{< L_1 >}{E_{00}^2}f^2 + 2\frac{\mathrm{E}_{00}^2}{f^3}\frac{\partial < \mathrm{L}_1 >}{\partial f}\right)\right]\end{aligned} \tag{13}$$

where

$$< L_1 \geq \frac{\omega_{p0}^2}{c^2} \int \left(\int_0^{A_0 A_0^\star} \left\{ 1 - \frac{1}{\left(1 + \frac{\beta E_{00}^2}{f^2}\left(1 + \frac{r^2}{q r_0^2 f^2}\right)^{-q}\right)^{\frac{1}{2}}} \right\} \mathrm{d}\left(A_0 A_0^\star\right) \right) \mathrm{d}^2 r$$

Equation (13) can be written as

$$\frac{d^2 f}{d\xi^2} = \frac{\left(1 - \frac{1}{q}\right)\left(1 - \frac{2}{q}\right)}{\left(1 + \frac{1}{q}\right)} \frac{1}{f^3} - \left(1 - \frac{1}{q}\right)\left(1 - \frac{2}{q}\right)\left(\frac{\omega_{p0}^2 r_0^2}{c^2}\right)\frac{\beta E_{00}^2}{f^3} I \tag{14}$$

where

$$I = \int_0^\infty u^3 \left(1 + \frac{u^2}{q}\right)^{-2q-1} \left(1 + \frac{\beta E_{00}^2}{f^2}\left(1 + \frac{u^2}{q}\right)^{-q}\right)^{-\frac{3}{2}} du$$

$$\mathrm{d}\prime = \mathrm{d}k_0 r_0^2$$

$$\xi = \frac{z}{k_0 r_0^2}$$

Equation (14) is the differential equation governing the evolution of beam width of the q-Gaussian laser beam during its journey through the plasma. The first terms on the right hand side of this equation correspond to the linear propagation of the laser beam, i.e., its propagation through vacuum or through the media whose index of refraction is independent of the intensity of the laser beam. The second terms on the R.H.S of this equation correspond to the nonlinear response of the medium.

Evolution of beam width of intensity ripple

Wave equation for the intensity ripple over the cross section for the laser beam is given by

$$\iota \frac{\partial A_r}{\partial z} = \frac{1}{2k_0}\nabla_\perp^2 A_r + \frac{k_0}{2\epsilon_0}\phi\left(EE^\star\right)A_r + \frac{k_0}{2\epsilon_0}\left[\phi\left(EE^\star\right) - \phi\left(A_0 A_0^\star\right)\right]A_0 \tag{15}$$

The Lagrangian density corresponding to this equation can be written as

$$\mathcal{L}_M = \iota\left(A_r \frac{\partial A_r^\star}{\partial z} - A_r^\star \frac{\partial A_r}{\partial z}\right) + \left|\nabla_\perp A_r\right|^2 - \frac{\omega_{p0}^2}{c^2}\int^{A_r A_r^\star} \left\{1 - \frac{1}{(1 + \beta EE^\star)^{\frac{1}{2}}}\right\} d\left(A_r A_r^\star\right) - \frac{\omega_{p0}^2}{c^2}\int^{A_0 A_0^\star} \left(\left\{1 - \frac{1}{(1 + \beta EE^\star)^{\frac{1}{2}}}\right\} - \left\{1 - \frac{1}{\left(1 + \beta A_0 A_0^\star\right)^{\frac{1}{2}}}\right\}\right) d\left(A_0 A_0^\star\right) \tag{16}$$

In the present investigation, we have assumed Gaussian irradiance profile of the intensity ripple riding over the cross section of the laser beam. Such an intensity ripple can be modeled as

$$E_r E_r^\star = \frac{E_{r00}^2}{g^2} e^{-\left(\frac{r^2}{r_r^2 g^2}\right)} \left(\frac{r}{r_r g}\right)^{2n} \tag{17}$$

Here r_r is the initial width of the ripple, *andg* is the dimensionless beam width parameter of the ripple. The constant n gives the position of intensity ripple from the axis of the main beam. As the value of n increases, the intensity ripple shifts away from the beam axis.

Using the same procedure as that of Sect. "Relativistic nonlinearity of plasma", we get the following equation for the evolution of beam width of the intensity ripple

$$\begin{aligned} \frac{d^2 g}{d\xi^2} = {} & \left(\frac{r_0}{r_r}\right)^4 \frac{1}{(n+1)g^3} - \left(\frac{\omega_{p0} r_0}{c}\right)^2 \left(\frac{r_0}{r_r}\right)^4 \\ & \frac{1}{g\Gamma(n+1)}\left(2\beta E_{00}^2 \left(\frac{r_0}{r_r}\right)^{2n}\left(\frac{f}{g}\right)^{2n+2} R_1 \right. \\ & + \beta E_{00} E_{r00}\left(\frac{r_0}{r_r}\right)^n \left(\frac{f}{g}\right)^{n+1} \cos\theta_p R_2 \\ & \left. - \beta E_{00} E_{r00}\left(\frac{r_0}{r_r}\right)^n \left(\frac{f}{g}\right)^{n+1} \cos\theta_p R_3 \right) \end{aligned} \tag{18}$$

where

$$R_1 = \int_0^\infty u^{2n+1} G\left(E_{00}, E_{r00}\right) e^{-\frac{1}{2}\left(\frac{r_0^2 f^2}{r_r^2 g^2}\right)u^2} \left[n + 1 - \frac{r_0^2 f^2}{r_r^2 g^2} u^2\right] \mathrm{d}u \qquad G\left(E_{00}, E_{r00}\right) = \left[1 - \frac{1}{(1 + X(f,g))^{\frac{1}{2}}}\right]$$

$$R_2 = \int_0^\infty u^{n+1} G\left(E_{00}, E_{r00}\right) e^{-\frac{1}{2}\left(\frac{r_0^2 f^2}{r_r^2 g^2}\right)u^2} \left(1 + \frac{u^2}{q}\right)^{-\frac{q}{2}} \left[n + 2 - \left(1 + \frac{r_0^2 f^2}{r_r^2 g^2}\right)u^2\right] \mathrm{d}u$$

$$X(f,g) = \frac{\beta E_{00}^2}{f^2}\left(1 + \frac{u^2}{q}\right)^{-q} + \frac{\beta E_{r00}^2}{g^2}\left(\frac{r_0 f}{r_r g}\right)^{2n} u^{2n} e^{-\left(\frac{r_0^2 f^2}{r_r^2 g^2}\right)u^2} + 2\frac{\beta E_{00} E_{r00}}{fg}\cos\theta_p \left(\frac{r_0 f}{r_r g}\right)^n u^n e^{-\frac{1}{2}\left(\frac{r_0^2 f^2}{r_r^2 g^2}\right)u^2} \left(1 + \frac{u^2}{q}\right)^{-\frac{q}{2}}$$

$$R_3 = \int_0^\infty u^{n+1} e^{-\frac{1}{2}\left(\frac{r_0^2 f^2}{r_r^2 g^2}\right)u^2} \left(1 + \frac{u^2}{q}\right)^{-\frac{q}{2}} \left[1 - \frac{1}{\left(1 + \frac{\beta E_{00}^2}{f^2}\left(1 + \frac{u^2}{q}\right)\right)^{\frac{1}{2}}}\right] \left[n + 2 - \left(1 + \frac{r_0^2 f^2}{r_r^2 g^2}\right)u^2\right] \mathrm{d}u$$

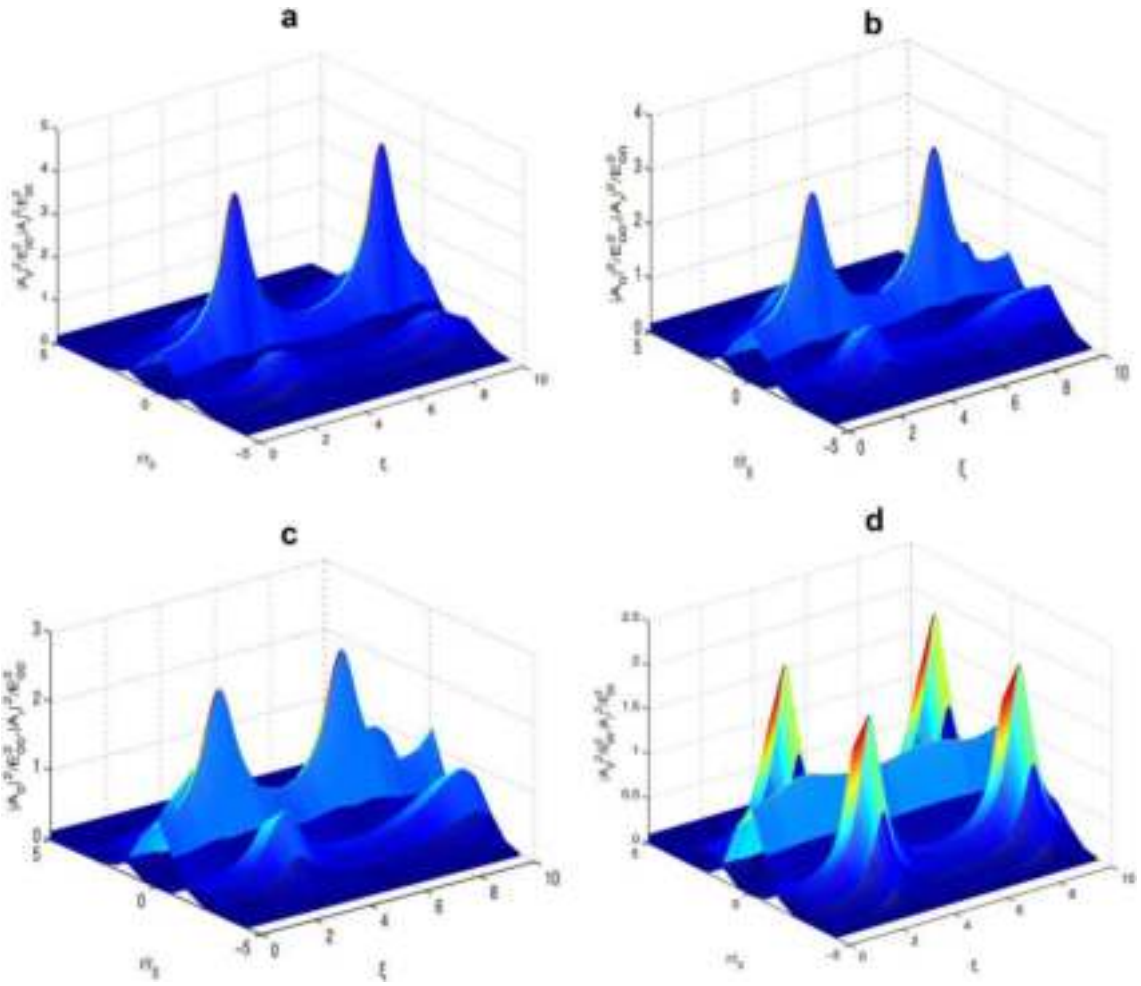

Fig. 3 Evolution of intensities of laser beam and ripple with distance of propagation for $q = (3, 4, 5, \infty)$, $\beta E_{00}^2 = 2$, $\beta E_{r00}^2 = 0.15$, $\frac{\omega_{p0}^2 r_0^2}{c^2} = 6$ and $n = 1$

Equation 18 governs the evolution of beam width of intensity ripple with distance of propagation, during the propagation of laser beam through plasma. It can be seen that the behavior of beam width of the intensity ripple is highly dependent on the propagation characteristics of the main beam. This is due to the fact that due to the laser-induced relativistic nonlinearity in the optical properties of plasma, the intensity ripple gets coupled to the main beam and is thus, strongly influenced by it. But as the overall power of ripple is quite less than that of main beam, it cannot affect the propagation of main beam but the main beam affects the propagation characteristics of the ripple.

Results and discussion

In the present investigation, Eqs. (14) and (18) have been solved numerically for following set of laser plasma parameters:

$$\omega_0 = 1.78 \times 10^{15} \frac{\text{rad}}{\text{sec}}, r_0 = 10\,\mu m, \frac{r_r}{r_0} = 0.1, \theta_p = \frac{\pi}{6}$$

and

$$q = (3, 4, 5, \infty),$$
$$\beta E_{00}^2 = (1, 1.5, 2, 2.5),$$
$$\frac{\omega_{p0}^2 r_0^2}{c^2} = (6, 9, 12, 15),$$
$$\beta E_{r00}^2 = (0.15, 0.20, 0.25, 0.30),$$
$$n = (0, 1, 2, 3)$$

Under the boundary condition that at the plane of incidence, the laser beam is collimated, i.e., it is having plane wave front. Mathematically, this condition can be expressed as

$$\frac{\mathrm{d}f}{\mathrm{d}\xi}|_{\xi=0} = \frac{\mathrm{d}g}{\mathrm{d}\xi}|_{\xi=0} = 0; f(\xi = 0) = g(\xi = 0) = 1$$

Figure 3 illustrates the effect of deviation parameter q of the main laser beam on evolution of normalized intensities of the main laser beam and that of ripple during the propagation of laser beam through the plasma. Here, the central lobes represents the intensity of the main beam, and the surrounding lobes represent that of ripple riding over the cross section of main beam. It can be seen that intensities of the main beam as well as that of ripple evolve in an oscillatory manner during the propagation of the laser beam through the plasma. These oscillations in their intensities are due to their periodic focusing/defocusing arising as a consequence of saturation nature of relativistic nonlinearity. Initially due to laser-induced relativistic nonlinearity, the beam widths of the laser beam and that of ripple start decreasing and hence their intensities start increasing that further enhances the relativistic nonlinearity. When the intensities of the laser beam and ripple becomes too high, the mass of plasma electrons in the illuminated portion of plasma gets saturated. Hence, now the laser beam propagates as if it is propagating through vacuum. Hence, after attaining minimum possible beam widths, the spot size of the main beam and that of ripple bounces back. These processes keep on repeating themselves giving an oscillatory behavior to the intensities of the laser beam and that of ripple.

The plots in Fig. 3 indicate that with increase in the value of deviation parameter q of the main laser beam, there is decrease in the extent of self-focusing of the main laser beam but along with that there is increase in the extent of self-focusing of ripple. This is due to the fact that most of the energy of laser beams with larger value of q is concentrated around a narrow region around the beam axis. Hence, off-axial rays of these beams give a little contribution to the optical nonlinearity of plasma. As the self-focusing of the laser beam is a consequence of the optical nonlinearity of plasma, increase in deviation parameter q reduces the extent of self-focusing of the main beam. The increase in the extent of self-focusing of ripple with increase in the deviation parameter q of the main beam is due to the fact that as the value of deviation parameter q increases, the intensity of the main beam converges toward the beam axis that makes the axial part of the ripple stronger. Thus, increase in deviation parameter q of the main laser beam leads to the enhancement of self-focusing of the ripple.

The plots in Fig. 4 illustrate the effect of intensity of the main beam on evolution of the intensities of main beam and that of ripple during the propagation of the laser beam through plasma. It can be seen that with increase in the intensity of main beam, the extent of self-focusing of laser beam as well as that of ripple gets increased. This is due to the fact that increase in intensity of main beam enhances the relativistic nonlinearity of plasma that, in turn, results in deeper focusing of laser beam and ripple riding over its cross section.

The plots in Fig. 5 depict the effect of plasma density on the self-focusing of main beam and intensity ripple. It can be seen that the effect of increase in plasma density is to increase the extent of self-focusing of laser beam as well as of intensity ripple. The underlying physics behind this effect is that increase in plasma density means increase in number of electrons contributing to the relativistic nonlinearity of plasma. Thus, increase in plasma density enhances the self-focusing of main beam and that of ripple.

Figure 6 illustrates the effect of initial intensity of laser ripple on self-focusing of both the ripple and laser beam. It

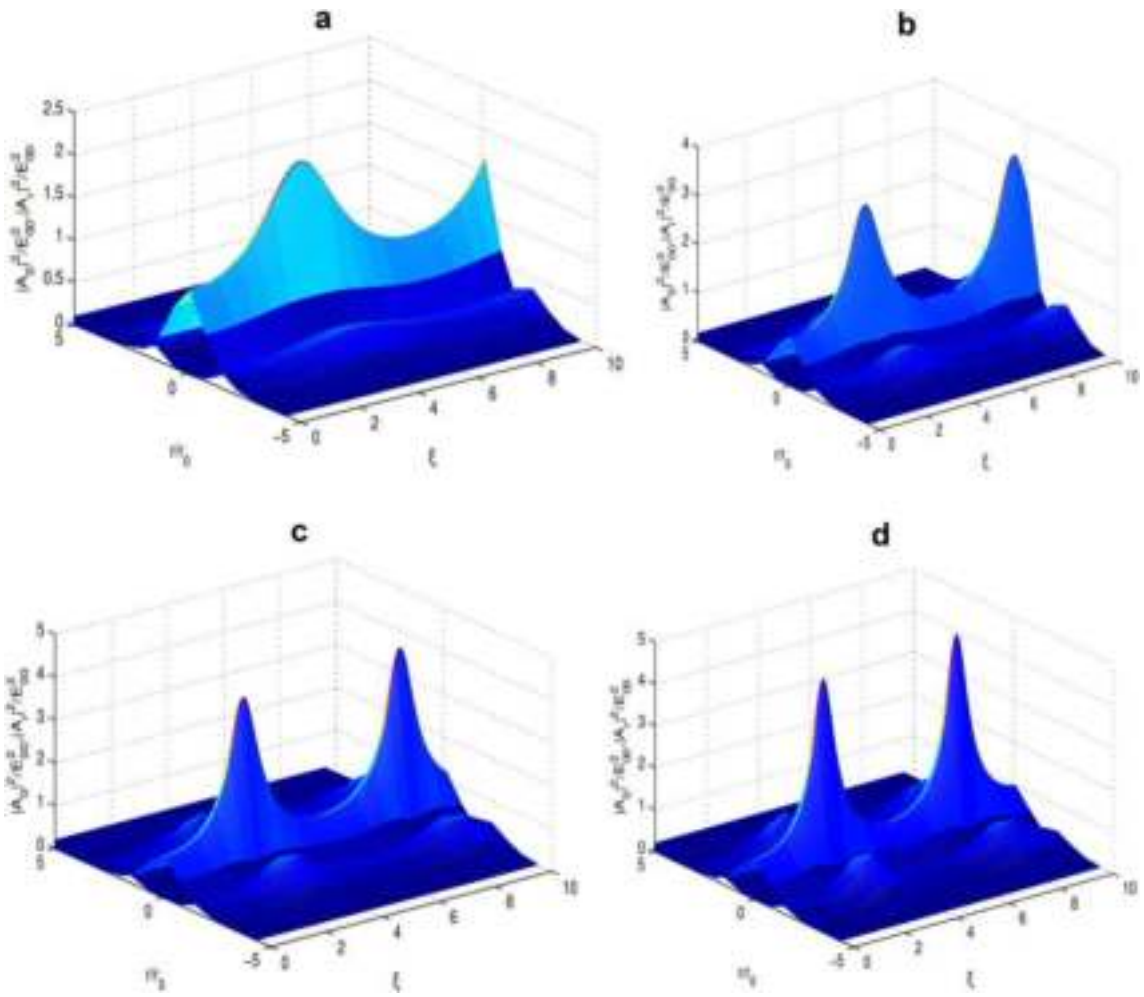

Fig. 4 Evolution of intensities of laser beam and ripple with distance of propagation for $q = 3$, $\beta E_{00}^2 = (1, 1.5, 2, 2.5)$, $\beta E_{r00}^2 = 0.15$, $\frac{\omega_{p0}^2 r_0^2}{c^2} = 6$ and $n = 1$

can be seen that with increase in initial intensity of the ripple, the extent of self-focusing of ripple increases, but there is no extent on self-focusing of main beam. The underlying physics behind this fact is that ripples with higher initial intensity produce more relativistic nonlinearity in the optical properties of plasmas, and thus, they get focused more. But, overall being very much weaker than the main beam, the propagation characteristics of ripple do not affect that of main beam, i.e., main beam can influence the intensity ripple due to its nonlinear coupling with the ripple, but being very much stronger than ripple main beam is not influenced by the ripple. Thus, increase in initial intensity of ripple has no effect on the self-focusing of the main beam.

Figure 7 depicts the effect of position of intensity ripple from the beam axis on extent of self-focusing of main beam and that of ripple. It can be seen that as the ripple shifts away from the beam axis, extent of its self-focusing increases; however, there is no effect on self-focusing of the main beam. This is due to the fact that as the position of peak intensity of ripple shifts away from the beam axis, the intensity gradient between the beam axis and position of intensity maximum of the ripple increases. This forms graded index fiber kind of structure into the plasma for the propagation of ripple. Due to the formation of this plasma channel, the extent of self-focusing of ripple increases, as the ripple shifts away from beam axis.

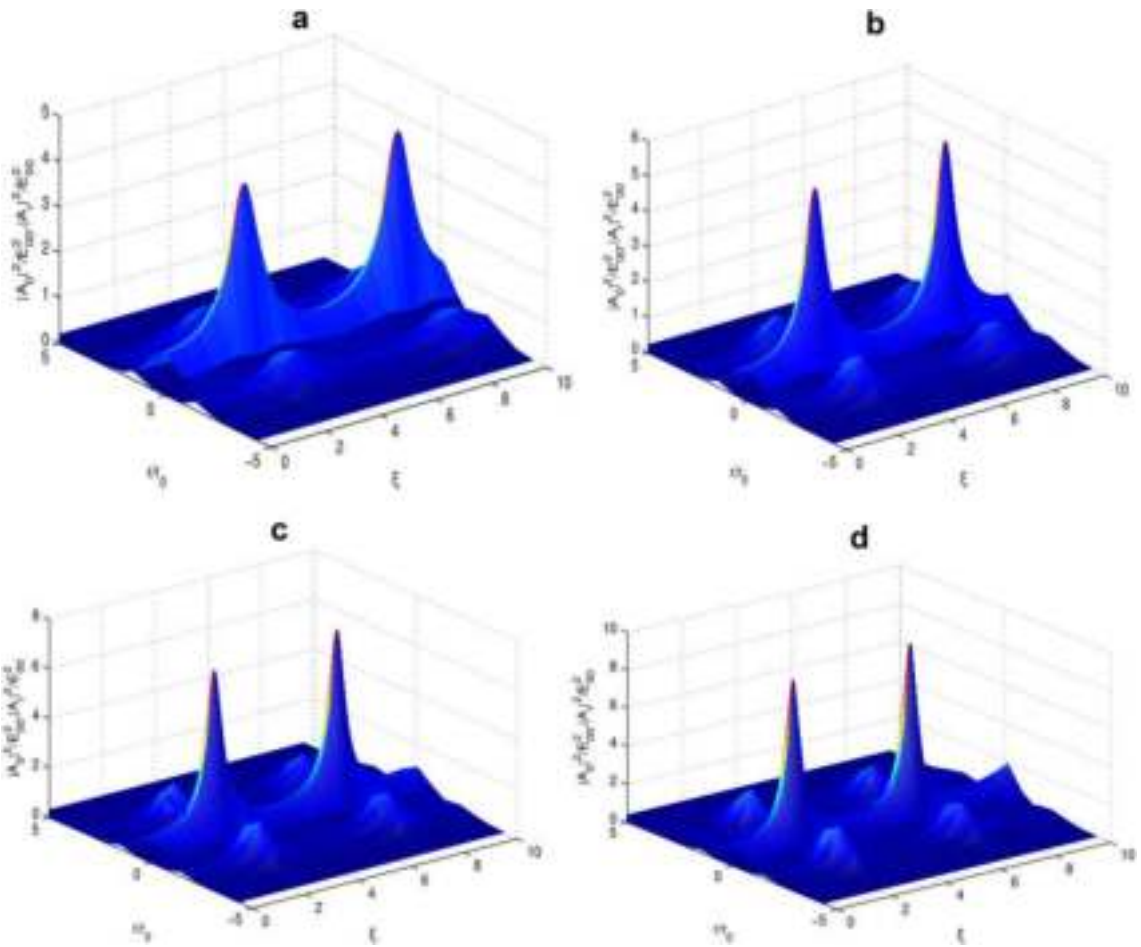

Fig. 5 Evolution of intensities of laser beam and ripple with distance of propagation for $q = 3$, $\beta E_{00}^2 = 2$, $\beta E_{r00}^2 = 0.15$, $\frac{\omega_{p0}^2 r_0^2}{c^2} = (6, 9, 12, 15)$ and $n = 1$

Conclusions

In conclusion, we have investigated the dynamics of rippled q-Gaussian laser beam propagating through under dense plasma. Effect of self-focusing of the main beam on the growth of intensity ripple riding over the cross section of the laser beam has been investigated in detail. It has been observed that the growth of intensity ripple is significantly affected by the irradiance profile of the laser beam. As the irradiance over the cross section of the main beam converges toward ideal Gaussian profile, the extent of its self-focusing gets reduced but the intensity ripple gets amplified. Hence, it can be concluded that ideal Gaussian laser beams are less suitable for ICF as they possess lesser focusing behavior as well as they amplify any perturbation in their irradiance profile. Thus, these beams will enhance the Rayleigh–Taylor instabilities during ICF.

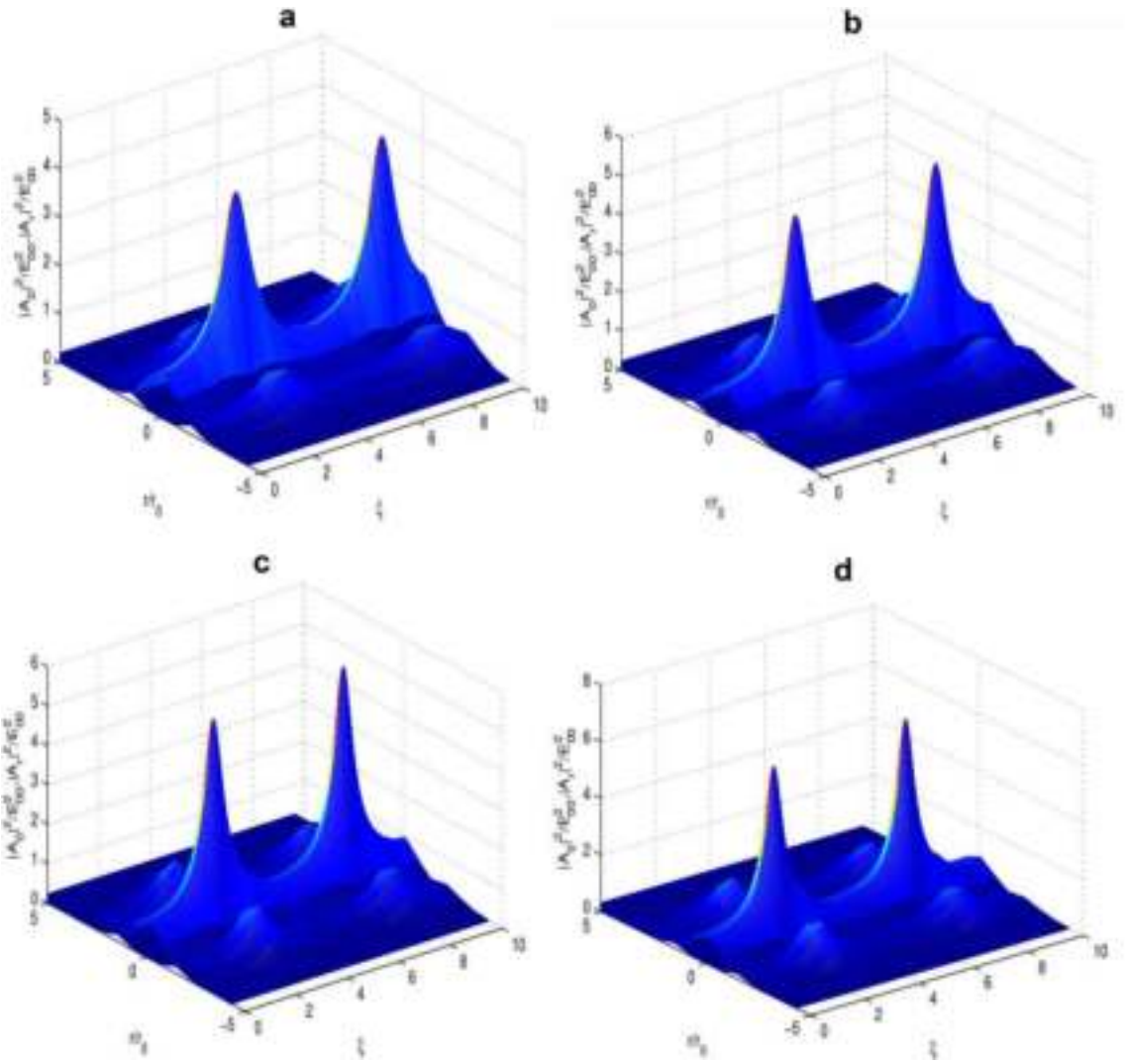

Fig. 6 Evolution of intensities of laser beam and ripple with distance of propagation for $q = 3$, $\beta E_{00}^2 = 2$, $\beta E_{r00}^2 = (0.15, 0.20, 0.25, 0.30)$, $\frac{\omega_{p0}^2 r_0^2}{c^2} = 6$ and $n = 1$

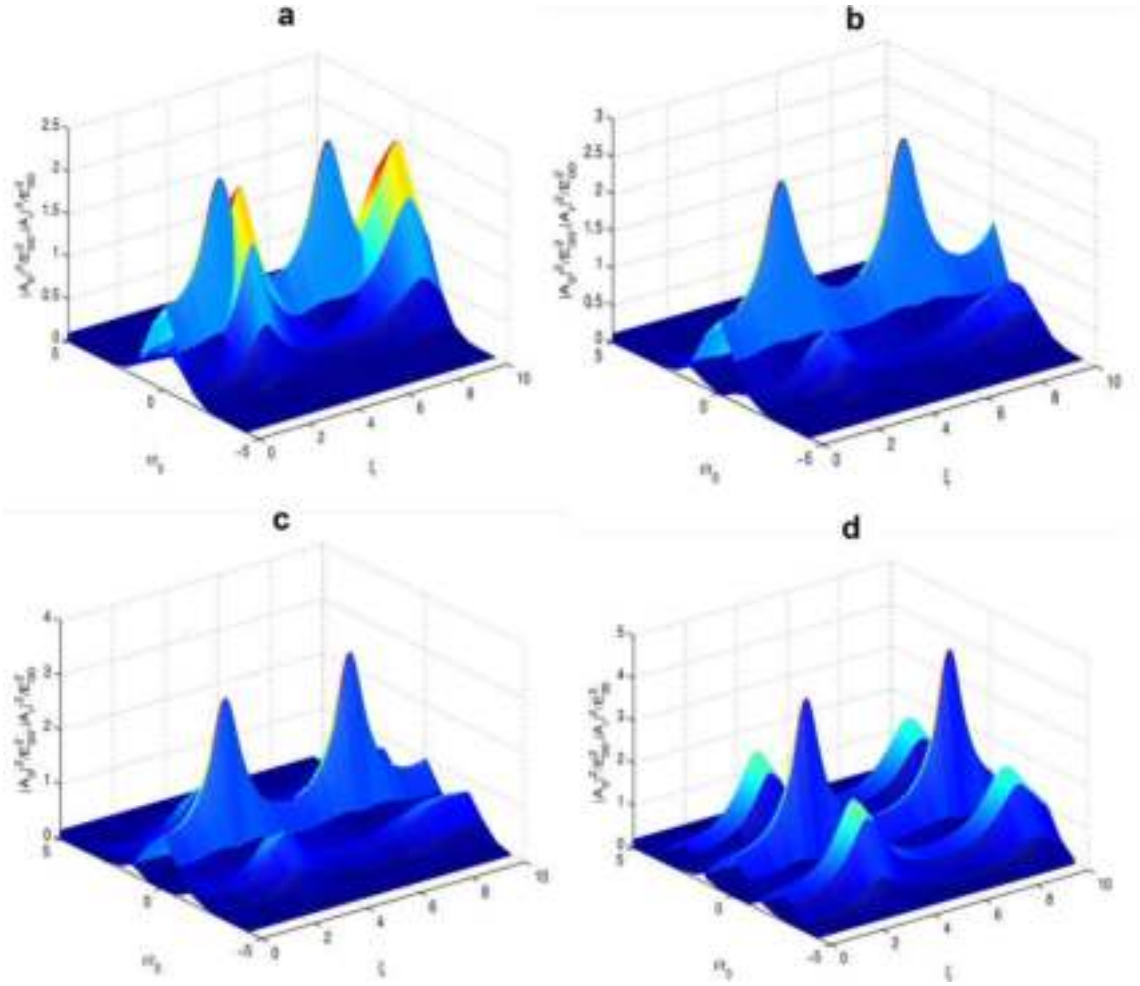

Fig.7 Evolution of intensities of laser beam and ripple with distance of propagation for $q = 3$, $\beta E_{00}^2 = 2$, $\beta E_{r00}^2 = 0.15$, $\frac{\omega_{p0}^2 r_0^2}{c^2} = 6$ and $n = (0, 1, 2, 3)$

Data availability The data that support the findings of this study are available within the article.

References

1. R.S. Craxton, K.S. Anderson, T.R. Boehly, V.N. Goncharov, D.R. Harding, J.P. Knauer, R.L. McCrory, P.W. McKenty, D.D. Meyerhofer, J.F. Myatt, A.J. Schmitt, J.D. Sethian, R.W. Short, S. Skupsky, W. Theobald, W.L. Kruer, K. Tanaka, R. Betti, T.J.B. Collins, J.A. Delettrez, S.X. Hu, J.A. Marozas, A.V. Maximov, D.T. Michel, P.B. Radha, S.P. Regan, T.C. Sangster, W. Seka, A.A. Solodov, J.M. Soures, C. Stoeckl, J.D. Zuegel, Direct-drive inertial confinement fusion: a review. Phys. Plasmas **22**, 110501 (2015)
2. M. Tabak, J. Hammer, M.E. Glinsky, W.L. Kruer, S.C. Wilks, J. Woodworth, E.M. Campbell, M.D. Perry, Ignition and high gain with ultrapowerful lasers. Phys. Plasmas **1**, 1626 (1994)
3. N. Gupta, Hot electron generation by self focused quadruple gaussian laser beams during inertial confinement fusion. Nonlinear Optics, Quantum Optics **55**, 63 (2022)
4. J.R. Freeman, M.J. Clauser, S.L. Thompson, Rayleigh-Taylor instabilities in inertial-confinement fusion targets. Nucl. Fusion **17**, 223 (1977)
5. J.D. Kilkenny, S.G. Glendinning, S.W. Haan, B.A. Hammel, J.D. Lindl, D. Munro, B.A. Remington, S.V. Weber, J.P. Knauer, C.P. Verdon, A review of the ablative stabilization of the Rayleigh-Taylor instability in regimes relevant to inertial confinement fusion. Phys. Plasmas **1**, 1379 (1994)
6. J. Sanz, Self-consistent analytical model of the Rayleigh-Taylor instability in inertial confinement fusion. Phys. Rev. Lett. **73**, 2700 (1994)
7. L. Videau, C. Rouyer, J. Garnier, A. Migus, Motion of hot spots in smoothed beams. J. Opt. Soc. Am. A **16**, 1672 (1999)
8. R. Kumar, K. Singh, T. Singh, Growth and stabilization of a laser ripple on laser beam in a collisionless unmagnetized plasma. Il Nuovo Cimento D **12**, 323 (1990)
9. N. Gupta, S. Kumar, Self-action effects of quadruple-Gaussian laser beams in collisional plasmas and their resemblance to Kepler's central force problem. Pramana **95**, 53 (2021)

10. N. Gupta, S. Kumar, S. Chaudhry, S.B. Bhardwaj, S. Kumar, Potential well dynamics of self focusing of quadruple gaussian laser beams in thermal quantum plasma. Nonlinear Optics Quantum Optics **55**, 281 (2022)
11. A. Singh, N. Gupta, Second harmonic generation of self-focused Cosh-Gaussian laser beam in collisional plasma. Optik **127**, 5452 (2016)
12. A. Singh, N. Gupta, Beat wave excitation of electron plasma wave by relativistic cross focusing of cosh-Gaussian laser beams in plasma. Phys. Plasmas **22**, 062115 (2015)
13. G. Purohit, P.K. Chuhan, R.P. Sharma, H.D. Pandey, Effect of relativistic mutual interaction of two laser beams on the growth of laser ripple in plasma. Laser Part. Beams **23**, 69 (2005)
14. R. Gauniyal, P. Chauhan, P. Rawat, G. Purohit, Effect of self-focused rippled laser beam on the excitation of ion acoustic wave in relativistic ponderomotive regime. Laser Part. Beams **32**, 557 (2014)
15. M. Moshkelgosha, The effects of ripple characteristics on the simultaneous relativistic-ponderomotive self-focusing. Acta Phys. Pol. A **136**, 957 (2019)
16. M.S. Sodha, A. Sharma, G. Prakash, M.P. Verma, Growth of a ring ripple on a Gaussian beam in a plasma. Phys. Plasmas **11**, 3023 (2004)
17. S. Misra, S.K. Mishra, On focusing of a ring ripple on a Gaussian electromagnetic beam in a plasma. Phys. Plasmas **15**, 092307 (2008)
18. G. Purohit, P. Rawat, P. Chauhan, S.T. Mahmoud, Higher-order paraxial theory of the propagation of ring rippled laser beam in plasma: Relativistic ponderomotive regime. Phys. Plasmas **22**, 052116 (2015)
19. P.K. Patel, M.H. Key, A.J. Mackinnon, R. Berry, M. Borghesi, D.M. Chambers, H. Chen, R. Clarke, C. Damian, R. Eagleton, R. Freeman, S. Glenzer, G. Gregori, R. Heathcote, D. Hey, N. Izumi, S. Kar, J. King, A. Nikroo, A. Niles, H.S. Park, J. Pasley, N. Patel, R. Shepherd, R.A. Snavely, D. Steinman, C. Stoeckl, M. Storm, W. Theobald, R. Town, R. Van Maren, S.C. Wilks, B. Zhang, Integrated laser-target interaction experiments on the RAL petawatt laser. Plasma Phys. Controll. Fusion **47**, B833 (2005)
20. M. Nakatsutsumi, J.R. Davies, R. Kodama, J.S. Green, K.L. Lancaster, K.U. Akli, F.N. Beg, S.N. Chen, D. Clark, R.R. Freeman, C.D. Gregory, H. Habara, R. Heathcote, D.S. Hey, K. Highbarger, P. Jaanimagi, M.H. Key, K. Krushelnick, T. Ma, A. MacPhee, A.J. MacKinnon, H. Nakamura, R.B. Stephens, M. Storm, M. Tampo, W. Theobald, L. Van Woerkom, R.L. Weber, M.S. Wei, N.C. Woolsey, P.A. Norreys, Space and time resolved measurements of the heating of solids to ten million kelvin by a petawatt laser. New J. Phys. **10**, 043046 (2008)
21. C. Tsallis, Nonadditive entropy and nonextensive statistical mechanics-an overview after 20 years. Braz. J. Phys. **39**, 337 (2009)
22. A.I. Akhiezer, R.V. Polovin, Theory of wave motion of an electron plasma. Sov. Phys. JETP **3**, 696 (1956)
23. D. Anderson, M. Bonnedal, M. Lisak, Nonlinear propagation of elliptically shaped Gaussian laser beams. J. Plasma Phys. **23**, 115 (1980)
24. D. Anderson, M. Bonnedal, Variational approach to nonlinear self-focusing of Gaussian laser beams. Phys. Fluids **22**, 105 (1979)
25. S. Wang, Novel soliton solution of (3+1)-dimensional perturbed Burgers equation. Phys. A **622**, 128808 (2023)
26. S. Wang, Novel complex *N*-soliton and lump solutions for nonlocal breaking equation. Results Phys. **40**, 105839 (2022)
27. S. Wang, Novel multi-soliton solutions in (2+1)-dimensional PT-symmetric couplers with varying coefficients. Optik **252**, 168495 (2022)

J Opt
https://doi.org/10.1007/s12596-023-01201-1

RESEARCH ARTICLE

Stimulated Raman scattering of self-focused Laguerre–Gaussian laser beams in axially inhomogeneous plasma

Naveen Gupta[1] · Alex AK[1] · Rohit Johari[1] · Sanjeev Kumar[1,2] · S. B. Bhardwaj[3] · A. Saini[4]

Received: 12 February 2023 / Accepted: 23 April 2023

Abstract This paper presents a theoretical investigation on stimulated Raman scattering (SRS) of intense Laguerre–Gaussian (LG) laser beams propagating through plasma with axial density ramp. The optical nonlinearity of the plasma has been considered to be originating due the ponderomotive force acting on the plasma electrons due to intensity gradient over the cross section of laser beam. An intense laser beam with frequency ω_0 propagating through plasma gets coupled with a preexisting electron plasma wave (EPW) at frequency ω_{ep} and produces a back scattered wave at frequency $\omega_s = \omega_0 - \omega_{ep}$. Using variational theory semi-analytical solution of the set of coupled wave equations for the pump, EPW and scattered wave has been obtained under W.K.B approximation. It has been observed that power of the scattered wave is significantly affected by the self-focusing effect of pump beam.

Keywords Self-focusing · Stimulated Raman scattering · Laguerre–Gaussian · Clean energy · Ponderomotive force

Introduction

The invention of the laser led to a renaissance in the field of light matter interactions by giving birth to an entirely new area of research known as laser plasma interactions. Since the past few decades, this new field is at vanguard of research due to its importance in many potent applications [1–8]. The impetus was built by the proposal of initiating thermonuclear fusion [1, 3] for viable energy production by using intense laser beams.

Both the allure and the challenges of fusion arise from the nature of the fusion process itself. Fusion fuel is abundant and cheap. The major advantages are: (1). The abundance of fuel—the most easily exploitable fuels are deuterium and tritium. Deuterium occurs naturally in all sources of water specially sea water. Tritium, however, is not readily available naturally, it can easily be manufactured inside the fusion reactor by the bombardment of neutrons with lithium, which also abundant in nature. (2). Cleanest source of energy—Fusion does not produce nuclear waste directly. In laser driven fusion, the goal is to deposit laser energy at a particular density in the plasma in order to derive the compression and subsequent heating of the fuel pellet. If the pellet is compressed sufficiently, it may undergo fusion, leaving to the release of a large amount of energy. It's as if there is a tiny hunk of the sun on Earth.

The successful implosion of the fuel pellet depends on the efficiency of laser plasma coupling which is decided by several nonlinear processes [9–11] ranging from collisional absorption to excitation of several laser driven instabilities [12–15]. In laser plasma instabilities, the pump beam (incident laser beam) splits into two daughter waves. If there is no external magnetic field, these daughter waves will be a scattered electromagnetic wave along with an electron plasma wave (EPW) or ion acoustic waves (IAW).

For laser driven fusion, these instabilities are of serious concern because if they are operative to a significant extent, they make it difficult to achieve high gain. In this context, SRS [16, 17], in which the incident laser beam decays into an EPW and a scattered electromagnetic wave, is of more

✉ Naveen Gupta
naveens222@rediffmail.com

[1] Lovely Professional University, Phagwara, Punjab, India

[2] Government College for Women, Karnal, Haryana, India

[3] SUS Govt College, Matak-Majri, Indri, Karnal, Haryana, India

[4] M. D. Govt. Girls College, Dadupur Roran, Karnal, India

Published online: 08 May 2023

serious concern because it occurs at a density much less than the critical density ($\sim \frac{1}{4}n_{cr}$). It reflects back a significant amount of laser energy that, otherwise, has to be deposited to the fusion plasma.

SRS is a two-edged sword. On the one hand, it degrades the efficiency of laser plasma coupling, and on the other hand, the excited EPW through SRS leads to the generation of superthermal electrons in laser-driven fusion. The electrons that happen to be moving in the same direction as the excited plasma wave and at roughly the same speed become trapped in the plasma wave. The high electric field of the EPW accelerates these trapped electrons to superthermal velocities. These highly penetrating superthermal electrons lead to premature burning of the pellet before the pellet gets compressed to critical density. This process is known as preheating. The attractive force between the superthermal electrons and the ions in the corona can also lead to loss of energetic ions from the ablation layer. These outward accelerated energetic ions further drain away laser energy being deposited to imploding pellet.

When these SRS was predicted and observed experimentally, it appeared that nonlinear optics could be treated in a reasonable way. However, it turns out to be much more complicated than was thought. One another nonlinear optical effect of self-focusing significantly affects SRS [18]. Because of the ponderomotive force effect, the refractive index of irradiated portion of plasma is greater where light is intense than elsewhere. This results in a gradient of index of refraction at the beam edges leading to a graded index fiber-like structure which focuses the outer portion of the beam inward. The result is that the beam gets shrinked to a very narrow diameter, of the order of a few microns. This makes the propagation dynamics of laser beam rather more complex. Self-focusing of the laser beam results in its filamentation in which a large initial beam breaks up into a number of filaments, and these filaments can further contain still finer filaments within them. In these filaments, the light intensity is very much higher than the average intensity over the cross section of the beam. Thus, all sorts of nonlinear optical effects such as SRS and SBS take place primarily in these filaments. Thus, in the investigation of SRS of laser beams in plasmas, it becomes vital to incorporate the effect of self-focusing of the laser beam [19].

Most laser beams have a Gaussian irradiance profile, although it can be beneficial to use a non-Gaussian beam in certain applications [20, 21]. The irradiance cross section of Gaussian beams decreases symmetrically with increasing distance from the center. Gaussian laser profiles have several disadvantages, such as the low-intensity portions on either side of the usable central region of the beam, known as "wings." These wings typically contain energy that is wasted because it is at a lower intensity than the threshold required for the given application, whether it is materials processing, laser surgery, laser-driven fusion or another application where an intensity above a given value is needed. In contrast with Gaussian laser beams, a new class of laser beams those carry angular momentum has gained a significant interest among researchers working on laser plasma interactions. With a suitable choice of parameters, the wings of these laser beams contain a significant amount of energy in comparison with the Gaussian laser beams [22]. Also due to vortex structure at the beam center, such laser beams can be used to trap neutral particles and thus can serve as a promising tool as optical spanners or optical tweezers. Mathematically, these laser beams are modeled by Laguerre–Gaussian functions. The literature review reveals the fact that no earlier investigation on stimulated Raman scattering (SRS) of Laguerre–Gaussian (LG) laser beams propagating through plasmas has been reported in the past. The aim of this article is to give first theoretical investigation on SRS of LG laser beams in plasmas with density ramp by incorporating the effect of self-focusing.

Ponderomotive nonlinearity of plasma

Consider the propagation of a linearly polarized Laguerre–Gaussian laser beam through a collisionless plasma, whose electron density is an increasing function of distance of propagation and is modeled by[23, 24]

$$n_0(z) = n_0^0(1 + \tan(dz)) \tag{1}$$

Here n_0^0 is the electron density at $z = 0$, i.e., the density at the plane of incidence and the constant d gives the measure of rate of increase in electron density with distance. Such a density profile is known as density ramp, and hence, the parameter d gives the measure of slope of density ramp. The electric filed vector of the laser beam is given by

$$\boldsymbol{E}(r,t) = A_0(r,z)e^{-\imath(k_0 z-\omega_0 t)}\boldsymbol{e_x} \tag{2}$$

The nonuniform irradiance over the cross section of the laser beam makes the dc component of ponderomotive force $F_p = -\frac{e^2}{4m\omega_0^2}\nabla\left(A_0A_0^*\right)$ operative. This force results in migration of electrons from high-intensity regions toward low-intensity regions of the illuminated portion of plasma. The resulting electron density of plasma is given by

$$n(r,z) = n_0(z)e^{-\frac{e^2}{8m\omega_0^2 T_0 K_0}A_0A_0^*} \tag{3}$$

where T_0 is the temperature of plasma electrons, and K_0 is the Boltzmann constant. Due to the dependence of dielectric properties of plasm $\varepsilon = 1 - \frac{4\pi e^2 n}{m\omega_0^2}$ on electron density, the

modification of electron density, in turn, alters the dielectric function of plasma. The intensity-dependent dielectric function of plasma is given by

$$\varepsilon = 1 - \frac{\omega_{p0}^2}{\omega_0^2}(1 + \tan(dz))e^{-\frac{e^2}{8m\omega_0^2 T_0 K_0}A_0 A_0^*} \tag{4}$$

Here $\omega_{p0}^2 = \frac{4\pi e^2}{m} n_0^0$ corresponds to the equilibrium plasma frequency, i.e., plasma frequency in the absence of laser beam.

Thus, the ponderomotive force on the plasma electrons produced by the laser beam, makes the index of refraction of plasma intensity dependent which, in turn, due to spatial dependence of the amplitude structure of the laser beam, resembles to that of graded index fiber. Separating the dielectric function of plasma into linear ε_0 and nonlinear $\phi(A_0 A_0^*)$ parts aswe get

$$\varepsilon = \varepsilon_0 + \phi(A_0 A_0^*)$$

$$\varepsilon_0 = 1 - \frac{\omega_{p0}^2}{\omega_0^2} \tag{5}$$

$$\phi(A_0 A_0^*) = \frac{\omega_{p0}^2}{\omega_0^2}\left\{1 - [1 + \tan(dz)]e^{-\frac{e^2}{8m\omega_0^2 T_0 K_0}A_0 A_0^*}\right\} \tag{6}$$

Self-focusing of LG laser beam

The model equation governing the evolution of a laser beam through a nonlinear medium characterized by dielectric function of the form given by Eq. (6) is

$$2\iota k_0 \frac{\partial A_0}{\partial z} = \nabla_\perp^2 A_0 + \frac{\omega_{p0}^2}{c^2}\left\{1 - (1 + \tan(dz))e^{-\frac{e^2}{8m\omega_0^2 T_0 K_0}A_0 A_0^*}\right\}A_0 \tag{7}$$

In the present investigation, we have used a semi-analytical technique known as variational method [24, 25] to solve Eq. (7). This method allows one to obtain approximate solution of a nonlinear partial differential equation by converting it to a set of coupled differential equations for the parameters of interest. According to this method, Eq. (7) is a variational problem for action principle based on Lagrangian density

$$\mathcal{L} = \iota\left(A_0\frac{\partial A_0^*}{\partial z} - A_0^*\frac{\partial A_0}{\partial z}\right) + |\nabla_\perp A_0|^2 - \frac{\omega_{p0}^2}{c^2} \int\left\{1 - (1 + \tan(dz))e^{-\frac{e^2}{8m\omega_0^2 T_0 K_0}A_0 A_0^*}\right\} d(A_0 A_0^*) \tag{8}$$

In the present investigation, we have considered the trial function of the form [26]

$$A_0(r, z) = \frac{E_{00}}{f}\left(\frac{r}{r_0 f}\right)^l e^{-\frac{r^2}{2r_0^2 f^2}} L_p^l\left(\frac{r^2}{r_0^2 f^2}\right) \tag{9}$$

where r_0 is the spot size of the laser beam at the plane of incidence, i.e., at $z = 0$, and the parameter f that depends on the longitudinal distance z is known as dimensionless beam width parameter that upon multiplication with r_0 gives the instantaneous spot size of the laser beam in plasma. The integers p and l describe the mode structure of the beam, where l denotes the number 2π phase cycles around the circumference, and $(p + 1)$ denotes the number of radial nodes in the mode profile. For $l \neq 0$, LG_p^l beam carries an orbital angular momentum $l\hbar$ per photon.

Light carrying orbital angular momentum looks very different from that emitted by common laser systems. When it hits a surface, it produces a ring-shaped irradiance pattern instead of disk-shaped pattern. The ring-shaped intensity is the result of the beam's particular phase profile. All around the ring of light, the light waves are arriving at slightly different times relative to each other. The phase fronts cannot be twisted at any arbitrary angle of steepness, because at any point of a light wave, its phase must be uniquely defined; mathematically speaking, the phase at any given angle must be the same as that after a full rotation by 360°. This means that after one wavelength, the phase front can wind around the center of the beam once clockwise, or once counterclockwise, or twice in either direction and so forth. The associated orbital angular momentum per photon turns out to be based on the number of twists of the phase fronts per wavelength of the light.

Because of their ring-like appearance, Laguerre–Gauss modes are sometimes also called "donut" modes. At the center of these light beams, the phase is not defined, and the beam contains a singularity or vortex around which the helical phase fronts swirl with ever-increasing velocity toward the core region. Physics does not allow undefined phases or infinite velocities, so the intensity of any physical light beam with orbital angular momentum vanishes at the center. At the dark core, all waves with different phases overlap and cancel each other out.

Substituting the trial function given by Eq. (9) in Lagrangian density and integrating over the entire cross section of the laser beam, we get the reduced Lagrangian as follows:

$$L = \int \mathcal{L}\left(A_0, A_0^*, \phi\right) d^2 r$$

The corresponding Euler–Lagrange equation

$$\frac{d}{dz}\left(\frac{\partial L}{\partial(\partial f/\partial z)}\right) - \frac{\partial L}{\partial f} = 0 \tag{10}$$

gives the differential equation for the evolution of beam width of the laser beam as follows:

$$\begin{aligned}(2p+l+1)r_0^2 f\frac{d^2 f}{dz^2} \\ = \frac{4\pi}{I_0 k_0^2}\int_0^\infty r|\nabla_\perp A_0|^2 dr + \frac{2\pi}{\varepsilon_0 I_0}\int_0^\infty r^2 |A_0|^2 \frac{\partial\phi}{\partial r} dr\end{aligned} \tag{11}$$

where

$$I_0 = 2\pi\int_0^\infty A_0 A_0^* r dr$$

Using Eqs. (6) and (9) in (11), we get

$$\begin{aligned}\frac{d^2 f}{d\xi^2} =& \frac{p!}{(2p+l+1)\Gamma(p+l+1)}\frac{I_{pl}}{f^3} - 2\frac{p!}{(p+l)!}\frac{1}{(2p+l+1)} \\ & \left(\frac{\omega_{p0}^2 r_0^2}{c^2}\right)\left(1+\tan\left(d'\xi\right)\right)\frac{\beta E_{00}^2}{f^3} I\end{aligned} \tag{12}$$

where

$$I_{pl} = \int_0^\infty e^{-x} x^l \left[L_p^l(x)\right]^2 \left[l - x\left(1 + 2\frac{L_{p-1}^{l+1}(x)}{L_p^l(x)}\right)\right]^2 dx$$

$$I = \int_0^\infty e^{-2x} e^{-\frac{\beta E_{00}^2}{f^2} e^{-x} x^l \left[L_p^l(x)\right]^2} \left[L_p^l(x)\right]^4 x^{2l}\left[x\left(1 + \frac{L_{p-1}^{l+1}(x)}{L_p^l(x)}\right) - l\right] dx$$

$$\xi = \frac{z}{k_0 r_0^2}$$

$$x = \frac{r^2}{r_0^2 f^2}$$

$$\beta = \frac{e^2}{8m\omega_0^2 T_0 K_0}$$

Equation (12) can be written as

$$\frac{d^2 f}{d\xi^2} + \frac{\partial V(f)}{\partial f} = 0 \tag{13}$$

where

$$V(f) = -\int^f F(f) df$$

$$\begin{aligned}F(f) =& \frac{p!}{(2p+l+1)\Gamma(p+l+1)}\frac{I_{pl}}{f^3} - 2\frac{p!}{(p+l)!}\frac{1}{(2p+l+1)} \\ & \left(\frac{\omega_{p0}^2 r_0^2}{c^2}\right)\left(1+\tan\left(d'\xi\right)\right)\frac{\beta E_{00}^2}{f^3} I\end{aligned}$$

Hence, Eq. (13) is clear that variational theory has reduced the problem of solving a nonlinear partial differential equation to that of a simple dynamical problem of a driven oscillator with unit mass. Here, the role of displacement of the oscillator tis played by the beam width parameter f and that of time is played by longitudinal distance ξ. Thus, it can be predicted that during the propagation of laser beam through the plasma, its beam width will evolve in an oscillatory manner over the distance of propagation.

Excitation of electron plasma wave

Due to their remarkable properties of quasi-neutrality and collective behavior, plasmas can support a number of wave modes. The negatively charged electrons are attracted by positively charged nuclei, but they are not bound together. This gives plasma some unusual properties—the freely floating electrons and ions are strongly affected by electric and magnetic fields. Plasma as a whole is quasi-neutral, but as the electrons and positively charged ions are separated, a disturbance can create regions of net negative and net positive charges. Such an uneven distribution of charges results in an electric field directed from positive to negative regions. This electric field pulls the electrons and ions toward each other with equal forces. But being very heavy the ions essentially remain at rest and the electrons move toward the ions. As the electrons move toward the ions, they steadily gain velocity and momentum. Due to this gain in momentum, the electrons overshoot their equilibrium positions and thereby reversing the direction of electric field. Now, the reversed electric field opposes the electron motion, slow them down and then pulling them back again. The process repeats itself, establishing an electron oscillator. In the presence of thermal velocity, these electron oscillators result in a longitudinal wave of electron density compressions and rarefactions propagating through the plasma. The propagation of excited EPW is governed by the wave equation[11]:

$$2\imath k_{ep}\frac{\partial n_{ep}}{\partial z} = \nabla_\perp^2 n_{ep} + \frac{\omega_{ep}^2}{v_{th}^2}(1+\tan(dz))\left\{1 - e^{-\beta A_0 A_0^*}\right\} n_{ep} \tag{14}$$

where $v_{th} = \sqrt{\frac{2KT_0}{m}}$ is the thermal velocity of plasma electrons. This equation can be obtained by linearizing equation of continuity, Poisson's equation and equation of motion of electron fluid. Considering the Gaussian ansatz for the EPW as

$$n_{ep} = \frac{n_{00}}{f_{ep}} e^{-r/2r_0^2 f_{ep}^2} \tag{15}$$

and using the procedure of Sect. 3, we get the equations for the evolution of beam widths of the EPW as follows:

$$\frac{d^2 f_{ep}}{d\xi^2} = \frac{1}{f^3} - \left(\frac{\omega_{ep}^2 r_0^2}{v_{th}^2}\right)\left(1 + \tan\left(d'\xi\right)\right)\frac{1}{f_{ep}^3} T \tag{16}$$

where

$$T = \int_0^\infty e^{-x} e^{-f^2/f_{ep}^2 x} e^{-\beta E_{00}^2/f^2 e^{-x} x^l} \left[L_p^l(x)\right]^2 \left[L_p^l(x)\right]^4 x^{2l} \left[x\left(1 + \frac{L_{p-1}^{l+1}(x)}{L_p^l(x)}\right) - l\right] dx$$

Equation (16) shows the coupling of EPW with pump beam, i.e., LG laser beam. It can be seen that the density perturbation associated with EPW is very sensitive to the self-focusing of the laser beam. Using Poisson's equation, the electric field of the excited EPW can be obtained as follows:

$$\boldsymbol{E_{ep}} = E_{ep} e^{\iota\left(k_{ep} z - \omega_{ep} t\right)}$$

$$E_{ep} = \frac{\iota m \omega_{ep}^2}{c k_{ep} f_{ep}} e^{-r/2r_0^2 f_{ep}^2} \tag{17}$$

Evolution of scattered beam

To understand the physics of stimulated Raman scattering in plasmas consider the propagation of an intense laser beam with amplitude E_0 through a plasma, whose density is rippled along the direction of wave vector k_0 of the incident laser beams. These density ripples of the plasma are due to the propagation of an electron plasma wave through the plasma. In the presence of the laser beam, the plasma electrons start oscillating under the effect of the field of the laser beam and thus generate a transverse electric current J_{NL}. Under proper matching of the wave vectors and frequencies, the transverse current generates a scattered wave with amplitude E_S. The scattered wave then beats with the incident laser beam and thus produces variations in wave pressure. These variations in wave pressure lead to migration of plasma electrons from the regions of high pressure to the regions of low pressure. The resulting density perturbation reinforces the initial density fluctuations associated with electron plasma wave, i.e., the plasma wave gets amplified. The presence of this feedback loop leads to the Raman instability or stimulated Raman scattering[26, 27].

Under the proper phase matching conditions

$$\boldsymbol{k_0} = \boldsymbol{k_{ep}} + \boldsymbol{k_s}$$

$$\omega_0 = \omega_{ep} + \omega_s$$

The nonlinear coupling of pump beam with EPW generates a nonlinear current density J_{NL} at frequency $\omega_s = \omega_0 - \omega_{ep}$ given by[17]

$$J_{NL} = \left(\frac{e^2 n_0}{m_0 \omega_s}\right)\frac{n_{ep}}{n_0} e^{\iota\left(\omega_s t - k_s z\right)} E_0(r, z) \tag{18}$$

This nonlinear current density leads to a scattered wave whose evolution is governed by wave equation

$$\nabla^2 E_s = \frac{1}{c^2}\frac{\partial^2 E_s}{\partial t^2} + \frac{4\pi}{c^2}\frac{\partial J_{NL}}{\partial t} \tag{19}$$

This equation gives the magnitude of electric field of scattered radiation as follows:

$$E_s = \iota \frac{\left(\omega_{p0}^2/c^2\right)}{\left(\omega_S^2/c^2 - k_s^2\right)}\frac{n_{ep}}{n_0^0} A_0(r, z) \tag{20}$$

Defining the normalized power P_S of scattered beam as

$$P_S = \frac{\int E_s E_s^* d^2 r}{\int A_0 A_0^* d^2 r} \tag{21}$$

we get

$$P_S = \frac{\left(\omega_{p0}^2/c^2\right)^2}{\left(\omega_S^2/c^2 - k_s^2\right)^2}\frac{\int \left(n_{ep}/n_0^0\right)^2 A_0 A_0^* d^2 r}{\int A_0 A_0^* d^2 r} \tag{22}$$

Equation (22) gives the power of scattered beam.

Results and discussion

In the present investigation, Eqs. (12), (16) and (20) have been solved numerically for the following set of laser and plasma parameters.

$\omega_0 = 1.78 \times 10^{15} rad/\sec; r_0 = 15\mu m; \beta E_{00}^2 = 3; \left(\frac{\omega_{p0} r_0}{c}\right)^2 = 9; T_0 = 10^6 K; \omega_{ep} = 1.48 \times 10^{14}$ rad/sec and $\frac{n_{ep}}{n_0^0} = 0.0001$

.and for different values of p, l, d', i.e.,$p = (0, 1, 2)$, $l = (0, 1, 2)$ and $d' = (0.025, 0.035, 0.045)$

In order to see the effect of orbital angular momentum of the photons on propagation dynamics of the laser beam, Eq. (14) has been solved for different values of l keeping other parametes fixed. The resulting behavior of the beam width is depicted in Fig. 1. It can be seen that the spot size of the laser beam evolves in an oscillatory fashion during its propagation through the plasma. These oscillations of the spot size are a signature of the saturation nature of ponderomotive nonlinearity. Due to the intensity gradient over the cross section of the laser beam, the plasma electrons experience ponderomotive force that expels them from the regions of high intensity toward the low-intensity regions. As the plasma index of refraction is higher for lower electron density and vice versa, the central part of the laser beam moves with lesser velocity through the plasma compared to its wings. The result is focusing of the laser beam as if it is passing through a convex lens. As the laser beam becomes more and more focused, more and more electrons are expelled from the irradiated region of plasma and ultimately the irradiated region of plasma gets completely evacuated from the electrons and thus the plasma index of refraction gets saturated. Now, the laser beam propagates as if it is propagating through vacuum and thus its beam width bounces back toward its original value. Periodic interplay between these phenomena results in oscillatory behavior of the beam width of the laser beam.

Further, it has been observed that after every focal spot, the maximum as well as the minimum of the beam width shift downwards. This is owing to the fact that the equilibrium electron density is an increasing function of longitudinal distance. Hence, the plasma index of refraction keeps on decreasing with the penetration of laser beam into the plasma. Consequently, the self-focusing effect gets enhanced and the maximum as well as minimum of the beam width go on shifting downwards after every focal spot. It is also seen that the frequency of oscillations of beam width increases with distance. The physics behind this fact is that denser is the plasma, higher will be the phase velocity of laser beam through it. Hence, in denser plasma, laser beam takes less duration to get self-focused.

It can also be seen that with increase in orbital angular momentum l, there is decrease in extent of self-focusing of the laser beam. This is due to the fact that the photons of laser beam carrying orbital angular momentum experience a centrifugal force due to which the intensity maximum of the irradiance profile gets shifted away from the beam axis. Thus, the laser beams with higher value of l get little contribution form the axial part of the beam toward nonlinear refraction. As self-focusing of the laser beam is a homeostasis of nonlinear refraction, increase in the value of l results in reduced focusing of the laser beam.

Now, in order to see the effect of radial index p on the evolution of the beam width of the laser beam, Eq. (14) has been solved for different values of p while keeping other laser plasma parameters fixed. The resulting behavior of the beam width parameter is shown in Fig. 2. It can be seen that with increase in the value of p, there is increase in the extent of self-focusing of the laser beam. This is due to the fact that with increase in value of p, the number of bright rings in the off-axial part of the laser beam increases. Thus, the laser beam with higher value of p gets additional contribution from the off-axial parts toward nonlinear refraction. Thus, increase in the value of p results in enhancement of self-focusing of the laser beam.

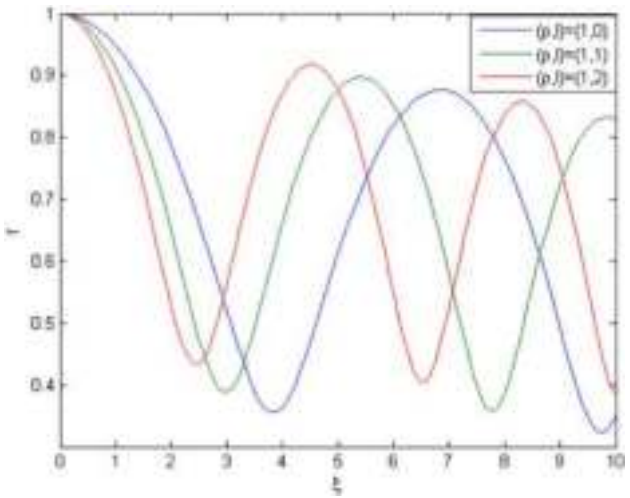

Fig. 1 Effect of orbital angular momentum l on extent of self-focusing of the laser beam

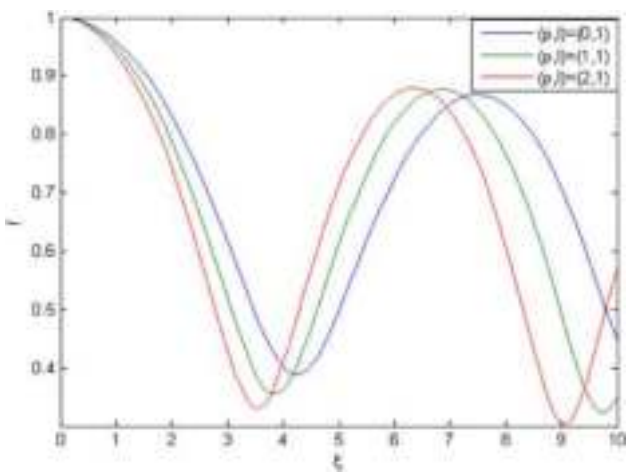

Fig. 2 Effect of radial mode index p on extent of self-focusing of the laser beam

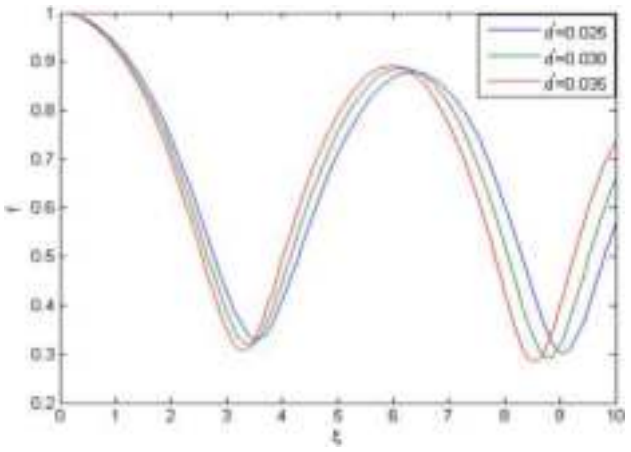

Fig. 3 Effect of slope $d^{'}$ of density ramp on extent of self-focusing of the laser beam

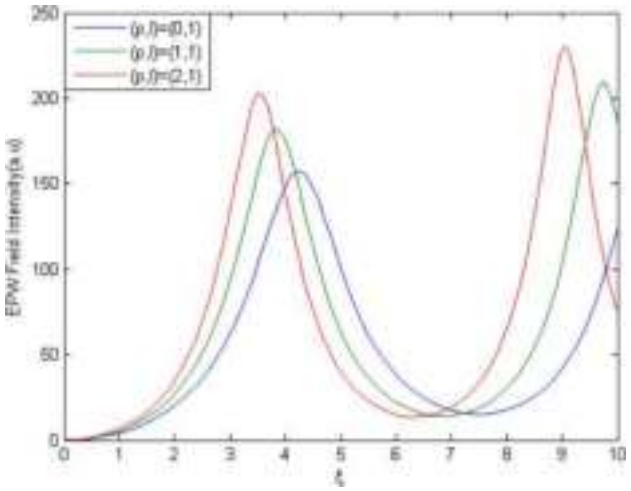

Fig.5 Effect of radial mode index p on strength of EPW

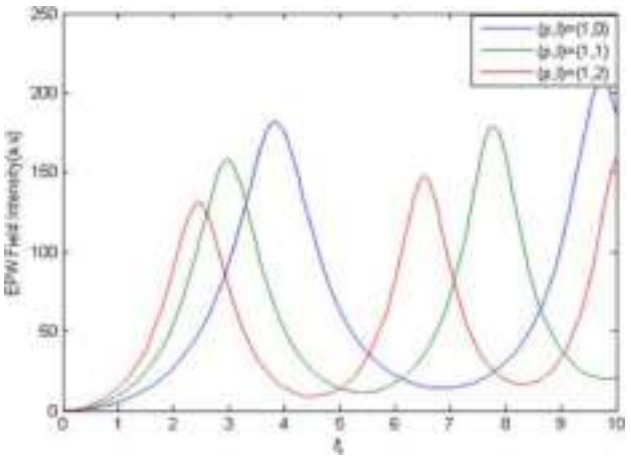

Fig. 4 Effect of orbital angular momentum l on strength of EPW

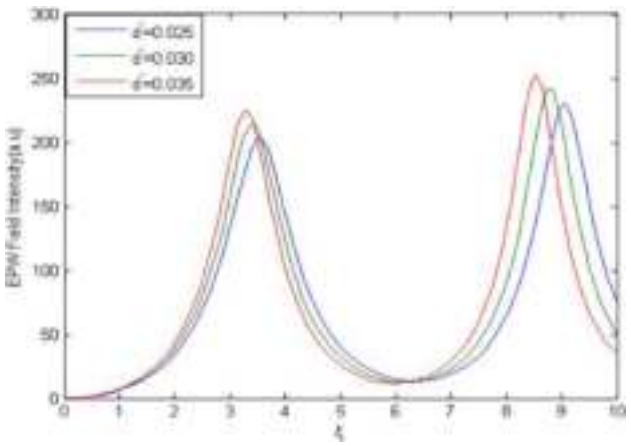

Fig. 6 Effect of slope d' of density ramp on strength of EPW

Figure 3 illustrates the effect of slope of the density ramp on self-focusing of the laser beam. It can be seen that with increase in the slope of density ramp, there is enhancement in the extent of self-focusing of the laser beam. This occurs because with increase in the slope of the density ramp, in the deeper regions of the plasma, the laser beam sees lesser index of refraction. Thus, increase in the slope of density ramp enhances the extent of focusing of the laser beam.

Figure 4 illustrates the effect of orbital angular momentum l of the laser beam on strength of excited EPW. It can be seen that the strength of the electric field of the excited EPW varies in an oscillatory manner with distance of propagation with maximum field occurring at the locations of the focal spots of the laser beam. This is due to the fact that the amplitude of the EPW is very sensitive to the extent of self-focusing of the laser beam. As the pump beam gets self-focused, its intensity increases and consequently the oscillation amplitude of the plasma electrons also increases. This, in turn, increases the amplitude of EPW. As the beam width of the pump beam evolves in an oscillatory manner, the strength of the excited EPW also shows the similar behavior with maximum field occurring at the location of minimum beam width of the pump.

It can also be seen that with increase in orbital angular momentum of the laser beam, the strength of excited EPW gets reduced. This is due to reduced self-focusing of the laser beam with increase in its orbital angular momentum.

Figures 5 and 6 illustrate the effect of radial mode index of laser beam and slope of density ramp on strength of excited EPW. It can be seen that with increase in either of radial mode index p of the laser beam or of slope $d^{'}$ of the density ramp, there is increase in strength of excited EPW. This is again due to enhanced self-focusing of the laser beam with increase in either of radial mode index of the laser beam or of slope of the density ramp.

Figures 7, 8 and 9 illustrate the effect of orbital angular momentum l, radial mode index p of the laser beam and slope d' of density ramp on power of scattered beam, respectively. It has been observed that the SRS reflectivity of plasma is a monotonically increasing function of propagation distance, showing step-like behavior. Each step occurs at the position of the minimum beam width. This is because as the pump beam gets self-focused, its intensity increases and consequently the oscillation amplitude of the plasma electrons also increases which, in turn, increases the amplitude of the generated EPW. As the density modulation of electrons due to EPW is the case of SRS, the resulting in a reflected electromagnetic beam. Increase in the amplitude of EPW means the increase in the reflectivity of these partially induced mirrors. Thus, the amplitude of the scattered wave keeps on increasing with the longitudinal distance making SRS reflectivity a monotonically increasing function of distance of propagation.

The step-like behavior of SRS reflectivity at the positions of the minimum beam width of the pump beam is owing to the fact that these are the regions of highest intensity, and hence, the current density for scattered radiation is maximum there or we can say that the reflectivity of the partially reflecting mirrors corresponding to the EPW is maximum at the focal spots of the laser beam. Hence, after attaining its local maximum value at the first focal spot, the scattered radiation again gets a sudden amplification at next focal spot. These sudden amplifications of the scattered radiation at focal spots of the pump beam give SRS reflectivity a step-like behavior.

It can also be seen that with increase in orbital angular momentum of the laser beam, the power of scattered beam gets reduced; however, with increase in radial mode index of the laser beam or slope of density ramp, the power of scattered beam increases. This is due to the fact that increase in orbital angular momentum of the laser beam makes the excited EPW weaker; however, increase in radial mode index of the laser beam or slope of density ramp makes the EPW stronger. The another reason for the decrease in the power of scattered radiation with increase in orbital angular momentum of the incident beam is that the orbital angular momentum of the incident beam reduces the coupling between the pump and scattered beam.

The plots in Fig. 9 indicate that with increase in slope of density ramp, there is increase in the power of scattered wave. This is due to increase in the extent of self-focusing of the pump beam with increase in slope of density ramp.

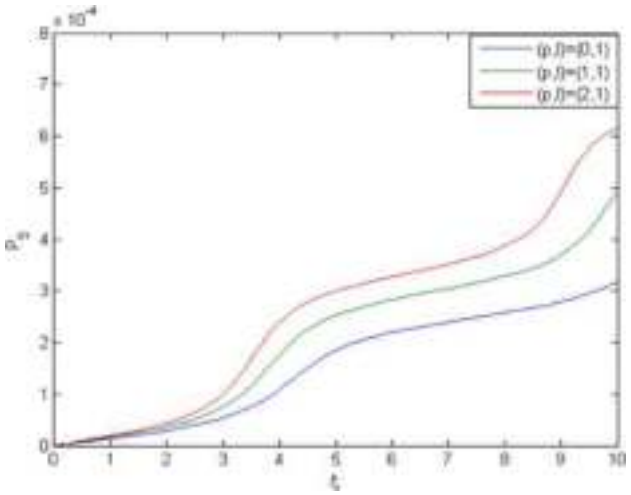

Fig. 8 Effect of radial mode index p on power of scattered beam

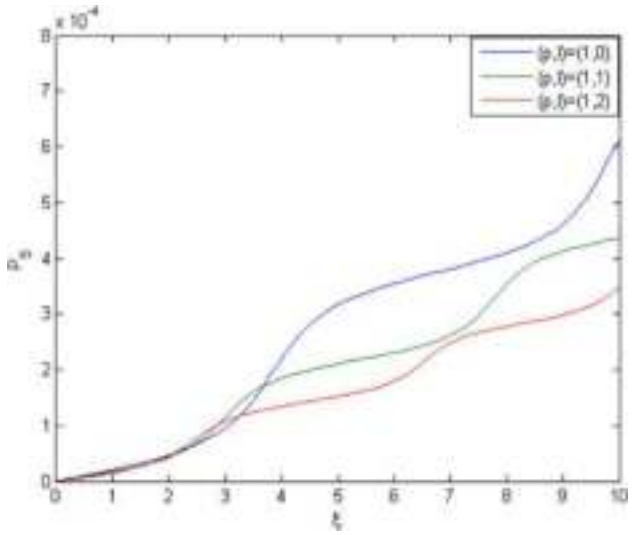

Fig.7 Effect of orbital angular momentum l on power of scattered beam

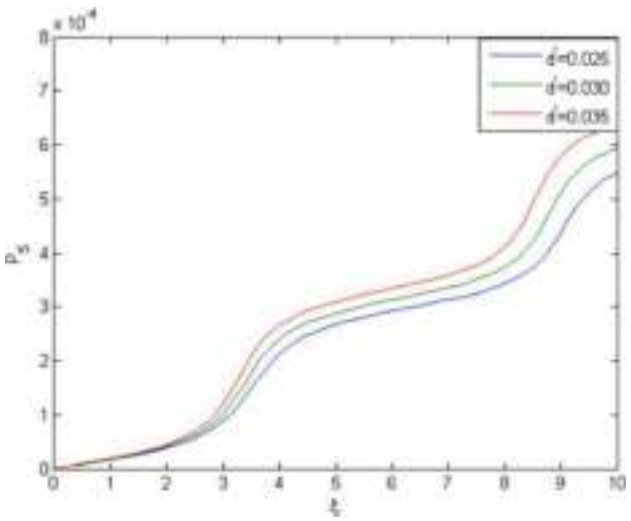

Fig. 9 Effect of slope d' of density ramp on power of scattered beam

Conclusions

In conclusion, we have investigated effect of self-focusing of Laguerre–Gaussian laser beams on SRS in collisionless plasmas. Following conclusions can be drawn from the results of present investigation:

1. There is one to one correspondence between the extent of self-focusing of the laser beam and SRS reflectivity of plasma.
2. The orbital angular momentum of the laser beam reduces the extent of its self-focusing that, in turn, reduces the SRS reflectivity of plasma. Thus laser beams with orbital angular momentum are more suitable for the applications where self-focusing and SRS are serious problems.
3. With increase in radial mode index ,p the extent of self-focusing as well as SRS reflectivity increases. Thus, it can be concluded that for applications like Raman lasers, where SRS amplification is required, laser beams with zero angular momentum but higher mode index should be preferred.

The results of the present investigation may serve as a guide for the experimentalists working in laser plasma interactions.

References

1. R.S. Craxton et al, Direct-drive inertial confinement fusion: a review. Phys. Plasmas **22**, 110501 (2015)
2. R. Betti, O.A. Hurricane, Inertial-confinement fusion with lasers. Nature Phys. **12**, 435 (2016)
3. J. Nuckolls, L. Wood, A. Thiessen, G. Zimmerman, Laser Compression of Matter to Super-High Densities: Thermonuclear (CTR) Applications. Nature **239**, 139 (1972)
4. E. Gschwendtner, P. Muggli, Plasma wakefield accelerators. Nat Rev Phys **1**, 246 (2019)
5. E. Esarey, C.B. Schroeder, W. Leemans, Physics of laser-driven plasma-based electron accelerators. Rev. Mod. Phys. **81**, 1229 (2009)
6. A. Reagan, M. Berrill, K.A. Wernsing, C. Baumgarten, M. Woolston, J.J. Rocca, High-average-power, 100-Hz-repetition-rate, tabletop soft-x-ray lasers at sub-15-nm wavelengths. Phys. Rev. A. **89**, 053820 (2014)
7. N. Lemos et al., X-ray sources using a picosecond laser driven plasma accelerator. Phys. Plasmas **26**, 083110 (2019)
8. M. Kumar, V.K. Tripathi, Y.U. Jeong, Laser driven terahertz generation in hot plasma with step density profile. Phys. Plasmas **22**, 063016 (2015)
9. C. Joshi, The nonlinear optics of plasmas. Phys. Scr. **30**, 94 (1990)
10. Q. Feng, L. Cao, Z. Liu, C. Zheng, X. He, Stimulated Brillouin scattering of backward stimulated Raman scattering. Sci. Rep. **10**, 3492 (2020)
11. N. Gupta, Self focusing and axial phase modulation of laser beams carrying orbital angular momentum in collisionless plasmas. J. Opt. Quant. Electron. **53**, 608 (2021)
12. S. Weber, C. Riconda, V.T. Tikhonchuk, Strong kinetic effects in cavity-induced low-level saturation of stimulated brillouin backscattering for high-intensity laser-plasma interaction. Phys. Plasmas **12**, 043101 (2005)
13. B.J. Albright, L. Yin, K.J. Bowers, B. Bergen, Multi-dimensional dynamics of stimulated Brillouin scattering in a laser speckle: Ion acoustic wave bowing, breakup, and laser-seeded two-ion- wave decay. Phys. Plasmas **23**, 032703 (2016)
14. C.J. Randall, J.J. Thomson, K.G. Estabrook, Enhancement of stimulated Brillouin scattering due to reflection of light from plasma critical surface. Phys. Rev. Lett. **43**, 924 (1979)
15. R.Y. Chiao, C.H. Townes, B.P. Stoicheff, Stimulated Brillouin scattering and generation of intense hypersonic waves. Phys. Rev. Lett. **12**, 592 (1964)
16. VYu. Bychenkov, W. Rozmus, V.T. Tikhonchuk, Stimulated Raman scattering in non-Maxwellian plasmas. Phys. Plasmas **4**, 1481 (1997)
17. H.A. Salih, S.T. Mahmoud, R.P. Sharma, M. Rafat, Stimulated Raman scattering of relativistic laser beam in plasmas. Phys. Plasmas **12**, 042302 (2005)
18. D. Biskamp, H. Welter, Stimulated Raman scattering from plasmas irradiated by normally and obliquely incident laser Light. Phys. Rev. Lett. **34**, 312 (1975)
19. H.A. Salih, S.T. Mahmoud, R.P. Sharma, Stimulated Raman scattering of relativistic laser beam in plasmas. Phys. Plasmas **12**, 042302 (2005)
20. R. Nuter, Ph. Korneev, V.T. Tikhonchuk, Raman scattering of a laser beam carrying an orbital angular momentum. Phys. Plasmas **29**, 062101 (2022)
21. B. Gaur, P. Rawat, G. Purohit, Mitigation of stimulated Raman backscattering by elliptical laser beam in collisionless plasma. Optik **157**, 99 (2018)
22. P. Sharma, Stimulated Raman scattering of ultra intense hollow Gaussian beam in relativistic plasma. Laser and Part. Beams **33**, 489 (2015)
23. P. Rawat, R. Gauniyal, G. Purohit, Growth of ring ripple in a collisionless plasma in relativistic-ponderomotive regime and its effect on stimulated Raman backscattering process. Phys. Plasmas **21**, 062109 (2014)
24. D. Anderson, M. Bonnedal, M. Lisak, Nonlinear propagation of elliptically shaped Gaussian laser beams. J. Plasma Phys. **23**, 115 (1980)
25. D. Anderson, M. Bonnedal, Variational approach to nonlinear self-focusing of Gaussian laser beams. Phys. Fluids **22**, 105 (1979)
26. N. Gupta, Self focusing and axial phase modulation of laser beams carrying orbital angular momentum in collisionless plasmas. Opt. and Quant. Electron **53**, 121 (2021)
27. L. Sa, J. Vieira, Self-focusing of multiple interacting Laguerre-Gauss beams in Kerr media. Phys. Rev. A **100**, 013836 (2019)

J Opt
https://doi.org/10.1007/s12596-023-01349-w

RESEARCH ARTICLE

Formation of elliptical *q*-Gaussian breather solitons in diffraction managed nonlinear optical media: effect of cubic quintic nonlinearity

Naveen Gupta[1] · A. K. Alex[1] · Rohit Johari[1] · Suman Choudhry[1] · Sanjeev Kumar[1] · Aatif Ahmad[1] · S. B. Bhardwaj[2]

Received: 3 June 2023 / Accepted: 30 July 2023

Abstract This paper presents theoretical investigation on the formation of elliptical *q*-Gaussian breather solitons in diffraction managed optical media. The optical nonlinearity of the medium has been modeled by cubic–quintic nonlinearity. To obtain the physical insight into the propagation dynamics of the laser beam, semi-analytical solution of the wave equation for the laser beam has been obtained by using variational theory approach in W.K.B approximation. Emphasis is put on investigating evolutions of transverse dimensions and axial phase of the optical beam.

Keywords Soliton · Clean Energy · Self Focusing · Variational Theory · Breather

Introduction

Since the debut of quantum mechanics in the 1920s, the two different aspects of physical quantities, i.e., waves and particles, have been intimately related in physical theories. Although both the aspects appear to be physically different, there are a number of experimental evidences that show correlation among both. In the past few years, solutions of certain wave equations have revealed another correlation between waves and particles. The surprising fact is that these wave equations are not the part of quantum mechanics but instead have been derived from classical physics [1]. Solutions to these equations describe waves those neither spread in space (i.e., those do not diffract) nor disperse in time. Diffraction and dispersion (Fig. 1) are the inherent properties of all kind of waves whether it is electromagnetic wave, mechanical wave (sound wave) or even matter wave.

However, these new kinds of waves retain their size and shape indefinitely (Fig. 2). These waves can be regarded as a quantity of energy localized permanently to a definite region of space. It can be set in motion but it cannot dissipate by spreading out. When two such waves collide, each comes away from the encounter with its identity intact (Fig. 3). If a wave meets an "anti-wave," both can be annihilated. This kind of behavior is extraordinary in waves, but it is familiar in another context, i.e., with particles. Thus, such waves can be considered as particles and are termed as "solitons."

The first recorded observation of a soliton was made almost 200 years ago by Russell [2], an engineer and naval architect. He reported to the British Association for the Advancement of Science: "I was observing the motion of a boat which was rapidly drawn along a narrow channel by a pair of horses. When the boat suddenly stopped-not so the mass of water in the channel which it had put in motion; it accumulated round the prow of the vessel in a state of violent agitation then suddenly leaving it behind rolled forward with great velocity assuming the form of a large solitary elevation a rounded smooth and well-defined heap of water which continued its course along the channel apparently without change of form or diminution of speed. I followed it on horseback and overtook it still rolling on at a rate of some eight or nine miles per hour preserving its original figure some 30 feet long and a foot to a foot and a half in height. Its height gradually diminished and after a chase of one or two miles I lost it in the windings of the channel."

Our topic of investigation, i.e., spatial optical solitons, arises due to dynamical balance of diffraction with induced focusing of the optical beam in a nonlinear medium. By nonlinear medium, it is meant by a medium whose index

✉ Naveen Gupta
naveens222@rediffmail.com

[1] Lovely Professional University, Phagwara, India

[2] SUS Govt College, Matak-Majri, Indri, Karnal, India

Published online: 18 August 2023

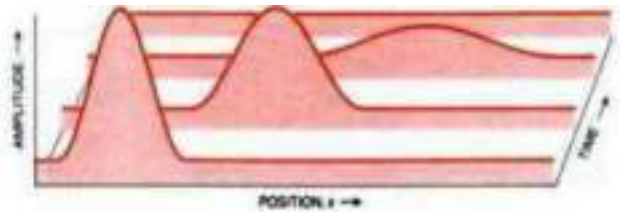

Fig. 1 Behavior of normal wave

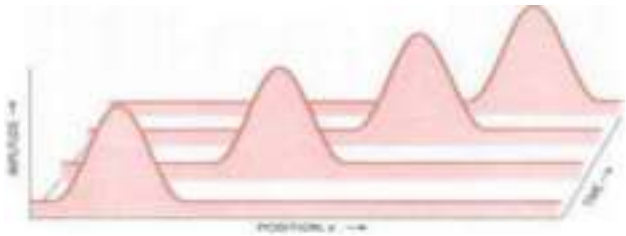

Fig. 2 Propagation of solitons

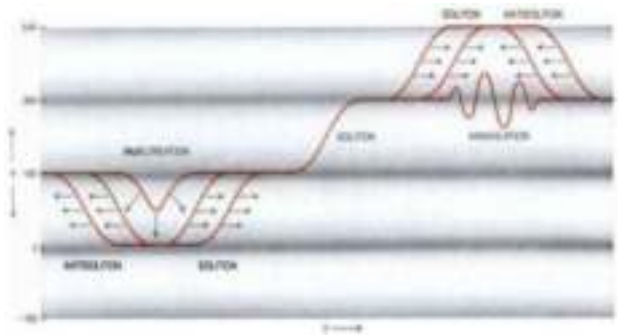

Fig. 3 Particle type behavior of solitons

of refraction is a function of beam intensity. When a narrow optical beam (i.e., a beam with finite transverse extent) propagates through vacuum or through a medium without affecting the optical properties of the medium, it undergoes diffraction and thus broadens with distance. Such a broadening of an optical beam is an inherent property of light that originates at a fundamental level form position momentum uncertainty of photons.

The narrower will be the initial beam, faster it will diverge. However, in nonlinear materials, the electrons of the medium respond to the field of the optical beam in such a way that its index of refraction does not remain constant but becomes a function of intensity of the beam. The change in index of refraction follows the intensity profile of the optical beam. As a function beam intensity, the index of refraction becomes maximum where the beam is most intense. Thus, the optical beams with bell-shaped irradiance see maximum opposition from the medium for their propagation and

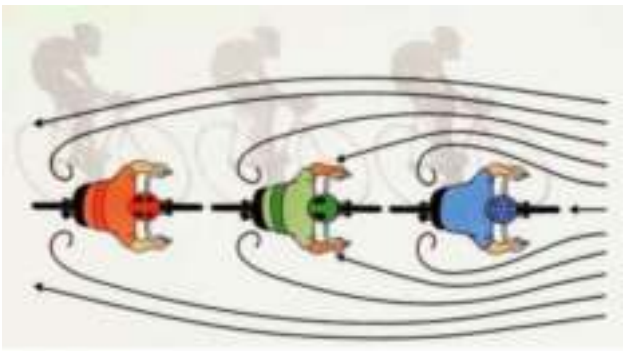

Fig. 4 Analogy of soliton formation with drafting cyclists

minimum opposition for their wings, thereby inducing a convex lens-like structure into the medium. This induced lens focuses the beam, a phenomenon called self-focusing that is a precursor of spatial solitons. When self-focusing exactly balances beam divergence, the beam become self-trapped at a very narrow width and is called an optical spatial soliton. This effect was discovered in 1964 by Chiao et al. [3].

To understand intuitively soliton formation in nonlinear optical media, consider a group of cyclists traveling into the wind and drafting off one another (that is, riding close together to cut wind resistance for those behind the leader) as depicted in Fig. 4. In the absence of wind, the cyclists would spread apart because of their different cycling speeds. However, the wind resistance impedes the stronger cyclists, who break the headwind for the weaker cyclists. Consequently, they all travel together as a packet. The different cycling speeds are like the diffraction effect of optical beam, and the wind resistance is like the nonlinearity.

Most of the earlier investigations on breather solitons in nonlinear media have taken into consideration the effect only of Kerr nonlinearity [4–8]. However, at higher intensities of the optical beams higher-order nonlinearities also come into picture those sometimes oppose the effect of Kerr nonlinearity. In other words, in nonlinear media at high input intensities there originate higher-order nonlinearities those favor the diffraction effect of light. Such an optical nonlinearity can be modeled as [9, 10]

$$n = n_0 + n_2|A_0|^2 - n_4|A_0|^4 \tag{1}$$

where A_0 is the amplitude of laser beam, n_0 is the linear refractive index of the medium, while n_2 and n_4 are, respectively, the third- and fifth-order nonlinear coefficients; n_2 is also known as Kerr coefficient. Nonlinear coefficients n_2 and n_4 are, respectively, related to third-order susceptibility $\chi^{(3)}$ and fifth-order susceptibility $\chi^{(5)}$ through $n_2 = \frac{3\chi^{(3)}}{8n_0}$ and $n_4 = \frac{5\chi^{(5)}}{16n_0}$. Due to its negative sign, the quintic nonlinearity opposes the Kerr nonlinearity of the medium and thus prevents the beam collapse.

Optical beams differing in intensity profile behave differently in nonlinear media [11–14]. From literature review, it has been seen that most of the investigations on breather solitons in nonlinear media were focused on propagation characteristics of Gaussian optical beams [15–19]. However, experimental investigations reveal that due to cavity imperfections like misalignment of end mirrors, the presence of impurities in the gain medium, etc., the irradiance over the cross section the beam is not having ideal Gaussian profile [20]. Due to these cavity imperfections, the wings of the intensity profile are slightly expanded as compared to ideal Gaussian profile. The actual profile for the irradiance over the cross section of the laser beam can be characterized by a class of distribution functions known as q-Gaussian distribution [21]. This paper aims to present for the first time, a theoretical investigation on the effect of self-focusing of elliptical q-Gaussian laser beams on the formation of breather solitons in nonlinear media possessing cubic–quintic optical nonlinearity.

Formation of breather soliton

The propagation of an optical beam in a nonlinear medium with periodically varying diffraction is governed by the wave equation [22]

$$2\imath\frac{\partial A_0}{\partial z} = \frac{1}{k_0}\left(d_0 + d_1\sin(\Omega z)\right)\left(\frac{\partial^2 A_0}{\partial x^2} + \frac{\partial^2 A_0}{\partial y^2}\right) + \frac{k_0}{n_0^2}\phi\left(A_0, A_0^\star\right)A_0 \tag{2}$$

where the constants d_0 and d_1 are associated with the amplitude of the periodic modulation of the diffraction phenomenon, Ω is the spatial frequency of the diffraction modulation, and

$$\phi\left(A_0, A_0^\star\right) = 2n_2\left|A_0\right|^2 + 2n_4\left|A_0\right|^4 \tag{3}$$

is the nonlinear dielectric function of the medium.

Before attempting to solve Eq. (2), it is important to understand the physical mechanism and the role being played by the various terms contained in it. The first term on the right hand side (R.H.S) models the diffraction broadening of the laser beam, and the second term arises due to the nonlinear response of the medium to the pump beam. Depending on its sign, this term increases or decreases the diffraction broadening of the laser beam. Therefore, this term is called nonlinear refractive term. By comparing Eq. (2) with standard Schrodinger equation of quantum mechanics, one can easily recognize that the first term is analogous to the kinetic energy of a particle of unit mass and the second term is analogous to potential energy of the particle in given force filed. Like Schrodinger equation is a statement of conservation of energy as it describes the inter conversion of kinetic energy to potential energy and vice versa. Similarly, Eq. (2) is a mathematical rule describing the interplay of diffraction and nonlinear refraction.

For the index of refraction modeled by Eq. (3), the wave equation governing the beam propagation, i.e., Eq. (2), becomes nonlinear in nature. Thus, the superposition principle will not hold for this equation and hence its closed-form solution cannot be obtained by conventional methods of solving partial differential equations (PDEs). In order to obtain physical insight into the dynamics of the optical beam, we have used a semi-analytical technique known as variational theory [23, 24]. Although numerical methods, e.g., the split-step-Fourier method and FDTD method, have been developed for solving NLSE, variational method has its own advantage as it explicitly confers the evolution equations of the beam parameters, which can be further investigated to get the insight about the beam propagation. Variational method that uses Rayleigh–Ritz optimization is also better choice for solving NLSE whose exact solution is either unavailable or may be too complicated to provide the proper physical insight. However, it fails if the beam or pulse transforms its profile or shape. This is the main drawback of this otherwise strong analytical tool. In our case, i.e., in cubic–quintic medium, elliptical q-Gaussian beam profile has been taken as it shows self-similar structure in cubic medium. The success of this approximate analytical method crucially depends on the choice of the trial function. When this choice of the trial function is appropriate, the method predicts results with very good accuracy. The heart of this method lies in the choice of this trail function, which is elliptical q-Gaussian in our case and is given by [21, 25]

$$A_0(x,y,z) = \frac{E_{00}}{\sqrt{f_x f_y}}\left\{1 + \frac{1}{q}\left(\frac{x^2}{a^2 f_x^2} + \frac{y^2}{b^2 f_y^2}\right)\right\}^{-\frac{q}{2}} \tag{4}$$

where E_{00} is the axial amplitude of the laser beam, and af_x and bf_y are the beam widths of the laser beam along x axis and y axis, respectively. Here, a and b are the respective equilibrium beam widths of the laser beam, i.e., the beam widths at the plane of entrance ($z = 0$). Hence, the parameters f_x and f_y are known as dimensionless beam width parameters. The phenomenological parameter q is the key parameter that describes the deviation of the amplitude structure of the laser beam from ideal Gaussian profile. As the value of q increases the amplitude structure converges toward the ideal Gaussian profile. For $q = 0$, the beam profile is pure flat-top profile with an infinite plane wavefront and for $q \to \infty$, i.e.,

$$\lim_{q\to\infty} A_0(r,z) = \frac{E_{00}}{\sqrt{f_x f_y}} e^{-\left(\frac{x^2}{2a^2 f_x^2} + \frac{y^2}{2b^2 f_y^2}\right)}$$

the beam profile is that of a TEM_{00} Gaussian beam. For $q > 0$ as the value of q increases, the effect on the beam waist profile is to increase the rate of change of intensity in the offaxial regions of the cross section of the laser beam.

There are many reasons for choosing this beam profile. Firstly, since our objective is to study the breathing dynamics of elliptical q Gaussian beams, the same must be taken as a trial function. Moreover, marked difference in beam propagation is observed with this type of beam profile. Secondly and more importantly, both the deviation parameter q and the beam ellipticity provide a control on diffraction, self-focusing and self-phase modulation of the beam. Thus, by varying the beam geometry the propagation dynamics of the laser beam can be controlled. Besides fundamental research interest, this beam has potential importance in realizing tunable all-optical devices.

The essential stage of variational method is to find the Lagrangian density and hence reduced Lagrangian for the system. For our model, the Lagrangian density $\mathcal{L}$ is given by

$$\mathcal{L} = i\left(A_0\frac{\partial A_0^\star}{\partial z} - A_0^\star\frac{\partial A_0}{\partial z}\right) + \left(d_0 + d_1\sin(\Omega z)\right)\left(\left|\frac{\partial A_0}{\partial x}\right|^2 + \left|\frac{\partial A_0}{\partial y}\right|^2\right) - \frac{k_0^2}{2n_0^2}\int_0^{A_0A_0^\star}\phi(A_0A_0^\star)\mathrm{d}(A_0A_0^\star) \tag{5}$$

Using Eqs. (3) and (4) in Eq. (5) and then integrating over the cross section of the laser beam, we get reduced Lagrangian as

$$< L >= \int_{-\infty}^{\infty}\int_{-\infty}^{\infty}\mathcal{L}\mathrm{d}x\mathrm{d}y \tag{6}$$

Now using corresponding Lagrangian equations of motion

$$\frac{\mathrm{d}}{\mathrm{d}z}\left(\frac{\partial}{\partial\left(\frac{\partial f_{x,y}}{\partial z}\right)} < L >\right) - \frac{\partial}{\partial f_{x,y}} < L >= 0$$

, we get the equation of motion of beam widths of the laser beam.

$$\frac{\mathrm{d}^2 f_x}{\mathrm{d}\xi^2} = \frac{\left(d_0 + d_1\sin(\Omega\prime\xi)\right)^2}{f_x^3}\frac{\left(1-\frac{1}{q}\right)\left(1-\frac{2}{q}\right)}{\left(1+\frac{1}{q}\right)} - \left(\frac{\omega_0 a}{c}\right)^2\left(d_0 + d_1\sin(\Omega\prime\xi)\right)\left(1-\frac{1}{q}\right)\left(1-\frac{2}{q}\right)T_1 \tag{7}$$

$$\frac{\mathrm{d}^2 f_y}{\mathrm{d}\xi^2} = \left(\frac{a}{b}\right)^4\frac{\left(d_0 + d_1\sin(\Omega\prime\xi)\right)^2}{f_x^3}\frac{\left(1-\frac{1}{q}\right)\left(1-\frac{2}{q}\right)}{\left(1+\frac{1}{q}\right)} - \left(\frac{a}{b}\right)^2\left(\frac{\omega_0 a}{c}\right)^2\left(d_0 + d_1\sin(\Omega\prime\xi)\right)\left(1-\frac{1}{q}\right)\left(1-\frac{2}{q}\right)T_2 \tag{8}$$

where

$$T_1 = \frac{n_2E_{00}^2}{f_x^2 f_y}I_1 - \frac{n_4E_{00}^4}{f_x^4 f_y}I_2$$

$$T_2 = \frac{n_2E_{00}^2}{f_y^2 f_x}I_1 - \frac{n_4E_{00}^4}{f_y^4 f_x}I_2$$

$$I_1 = \int_0^\infty t\left(1+\frac{t}{q}\right)^{-2q-1}dt$$

$$I_2 = \int_0^\infty t^2\left(1+\frac{t}{q}\right)^{-4q-1}dt$$

$$\xi = \frac{z}{k_0 a^2}$$

Equations (7) and (8) govern the evolution of beam widths of the laser beam along the transverse directions with distance of propagation. The first terms on the right hand sides of Eqs. (7) and (8) govern the evolution of beam widths of the laser beam in vacuum or linear media; however, the second terms on the right hand sides of these equations originate as a result of nonlinear response of the medium. Thus, it can be seen that the although in linearly media the beam widths of the laser beam along the two transverse directions evolve independently; however, due the laser-induced optical nonlinearity they get coupled to each other. The set of Eqs. (7) and (8) also indicates that variational theory has reduced the original problem of solving a nonlinear partial differential equation to a set of coupled ordinary differential equations. Although this reduced set of coupled differential equations is also lacking from an exact closed-form solution, its approximate solution can be easily obtained by simple numerical techniques. In the present investigation, these equations have been solved with the help of Runge–Kutta fourth-order method for following set of laser-plasma parameters:

$\omega_0 = 1.78\times10^{15}$ rad/sec, $a = 15\mu$m, $\frac{a}{b} = 1$, $d_0 = 1$, $d_1 = 2$, $\Omega\prime = 50$, $n_2 = 2.2\times10^{-3}$ cm^2/GW and for different values of deviation parameter $q = (3, 4, \infty)$, beam power $n_2E_{00}^2 = (3, 3.5, 4)$ and Kerr nonlinearity $\frac{n_4}{n_2^2} = (0.01, 0.001, 0.0001)$.

under initial conditions $f_{x,y} = 1$ and $\frac{df_{x,y}}{d\xi} = 0$ at $\xi = 0$. The significance of these conditions is as follows:

(1) $f_{x,y} = 1 \text{at} \xi = 0$ implies that at the entrance of the nonlinear medium the beam widths of the laser beam along x and y axes are a and b, respectively.
(2) $\frac{df_{x,y}}{d\xi} = 0$ at $\xi = 0$ implies that initially the laser beam is collimated.

In order to see how the spatial profile of the optical beam, i.e., the value of deviation parameter q affects its propagation dynamics, Eqs. (7) and (8) have been solved for different values of q while keeping the other parameters fixed, i.e., $n_2 E_{00}^2 = 3$, $\frac{n_4}{n_2^2} = 0.01$ and the corresponding behavior of the beam widths of the laser beam is depicted in Fig. 5. It can be seen that while propagating through the nonlinear medium, the cross section of the optical beam undergoes periodical breathing with mild ripples. In other words, the beam constitutes a breather soliton. The breathing of the optical beam is due to its periodic focusing/defocusing resulting from the intensity dependence of the index of refraction of the medium. Due to intensity dependence of the index of refraction of the medium, the high intensity regions of the wavefronts of the optical beam experience higher refractive index as compared to the regions of lower intensity. The situation is just similar to the focusing of an optical beam with plane wavefronts when it passes through a convex lens. Due to its bell-shaped spatial profile, the center of q-Gaussian laser beam sees maximum index of refraction and its wings see minimum index of refraction. As a result of this, the wavefronts of the optical beam bend inwards resulting in its self-focusing. As the optical beam gets self-focused with distance of propagation, its spot size decreases and hence intensity increases. As the diffraction of an optical beam varies inversely with its transverse dimensions, the decrease in beam width due to self-focusing enhances the tendency to diffract. Also, the resulting increase of intensity increases the magnitude of quintic nonlinearity. The phenomenon of diffraction and quintic response of the medium tends to expand the transverse dimensions of the optical beam, with the focusing of beam the two opposing phenomena also come into dominance. Hence, during the journey of the optical beam through a nonlinear medium there starts a competition between the phenomenon of convergence due to Kerr nonlinearity and divergence due to the combined effects of diffraction and quintic nonlinearity. The winning phenomenon ultimately decides the behavior of the beam. Thus, there exists a minimum value of beam power above which the beam will converge and otherwise it will diverge while passing through the medium. Depending on the contribution of the Kerr nonlinearity, this divergence can be greater than or smaller than the vacuum diffraction. The threshold for convergence can be obtained by balancing the right hand sides of Eqs. (7) and (8) with zero. In the present investigation, we have taken the initial power of the optical beam to be greater than the threshold for convergence. That is why immediately entering into the medium the beam undergoes convergence along both the transverse directions. When with increase in the intensity due to Kerr effect, the quintic nonlinearity starts dominating then the beam again starts to increase in its beam widths. Thus, after attaining minimum possible values the beam widths of the optical beam bounce back toward their original values. These processes

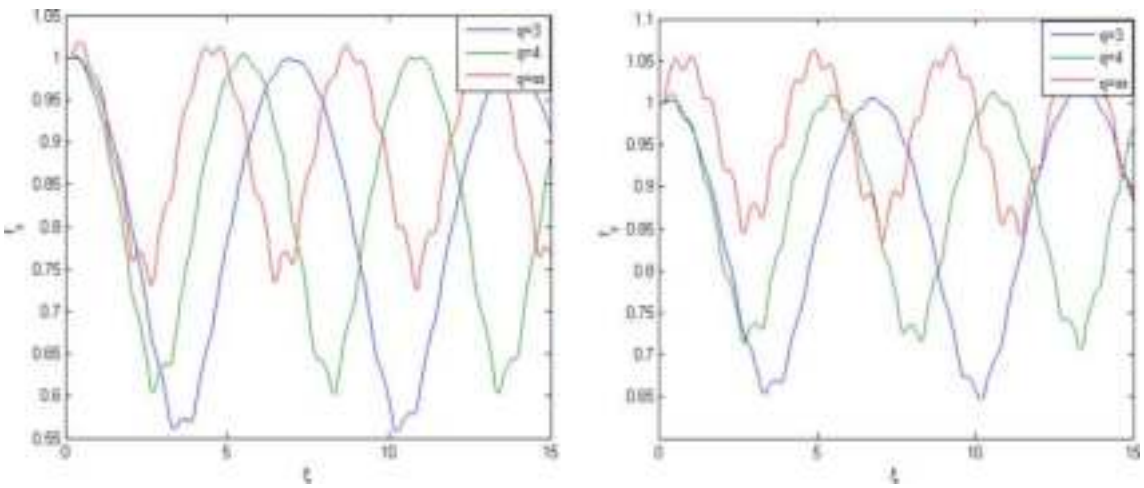

Fig. 5 Evolution of beam widths of the laser beam for different values of deviation parameter at fixed values of beam power $n_2 E_{00}^2 = 3$ and Kerr nonlinearity $\frac{n_4}{n_2^2} = 0.01$

keep on repeating during the journey of the beam through the nonlinear beam establishing a breather soliton.

The mild ripples in the breathing of the soliton are due to the periodical variations of the diffraction due to diffraction management of the medium. The physical explanation of these ripples can be obtained by comparing the evolution equations of the breather, i.e., Eqs. (7) and (8) with the equation of motion of an inverted pendulum with oscillating support. A pendulum with an oscillating support can be in a state of stable equilibrium with its bob situated above the support. The inverted pendulum establishes a stable configuration due to the net stabilizing force produced by stabilizing and destabilizing forces acting at a frequency much larger compared to the natural frequency of the pendulum with fixed support. Similar mechanism also stabilizes a Bose–Einstein condensate trapped in double-well potential with oscillating interaction and an optical beam propagating in a medium with oscillating nonlinearity.

Figure 6 shows the relative behavior of the beam widths $f_{x,y}$ for the three cases shown in Fig. 5. It can be seen that the cross section of the elliptical beam varies from elliptical to circular and then back to elliptical. Thus, the shape of the elliptical laser beam varies in an oscillatory fashion which is in agreement with the results of Fig. 5. It can also be seen that with increase in the value of deviation parameter q, the oscillations in the shape of beam from horizontal ellipse to vertical ellipse and vice versa become faster. This is again in agreement with the results in Fig. 5.

At this point, it is worthy to discuss the propagation dynamics of laser beam with the help of phase space plots (Figs. 7, 8). These are the plots of the history of the changing variables that in present care are $f_{x,y}$, $\frac{df_{x,y}}{d\xi}$. Phase space trajectories are a useful concept for visualizing the behavior of a dynamical system. For an oscillatory system like a simple pendulum, the circular closed phase space trajectories indicate purely simple harmonic oscillations and the circular spiraling trajectories indicate damped oscillations. Similarly,

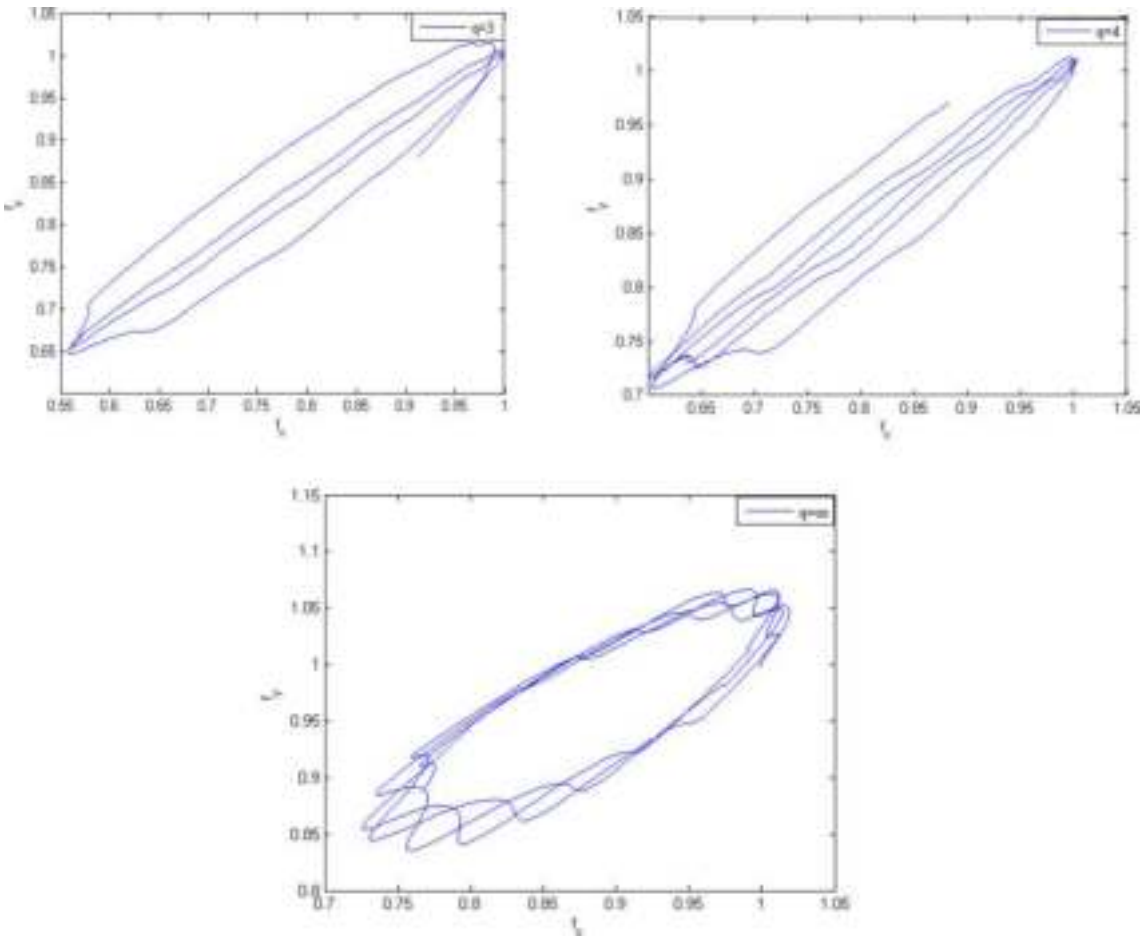

Fig. 6 Relative behavior of beam widths f_x and f_y for different values of deviation parameter q at fixed values of beam power $n_2E_{00}^2 = 3$ and Kerr nonlinearity $\frac{n_4}{n_2^2} = 0.01$

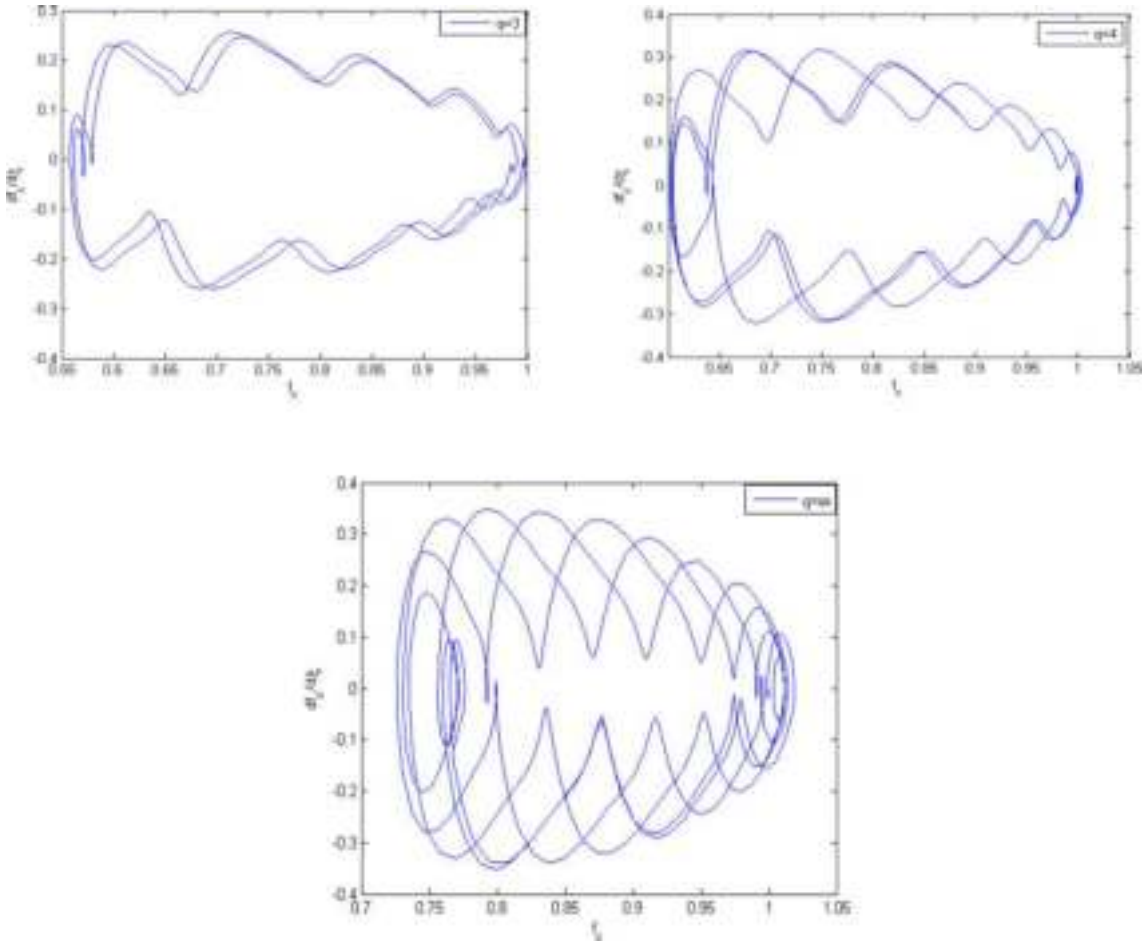

Fig. 7 Phase space plots of beam width of the laser beam along x-axis for different values of deviation parameter at fixed values of beam power $n_2 E_{00}^2 = 3$ and Kerr nonlinearity $\frac{n_4}{n_2^2} = 0.01$

the distorted phase space trajectories indicate chaotic nature of the oscillations, i.e., the oscillations containing several frequency components. As in present case also the phase space trajectories are spiraling and are distorted, this indicates that the beam widths of the laser beam are breathing in a chaotic fashion with several frequencies. It can also be seen that with increase in the value of deviation parameter q of the laser beam, the area of the phase space trajectories of both the transverse beam widths reduces. This is due to reduced extent of self-focusing along both the transverse directions with increase in deviation parameter q of the laser beam.

Figure 9 depicts the effect of intensity of the laser beam on breathing of the beam widths of the laser beam. It can be seen that with increase in intensity of the laser beam breathing of beam widths along both the transverse directions becomes deeper. This is due to the fact that as discussed above the breathing of the beam widths is due to periodic focusing/defocusing of the laser beam and with increase in the intensity of the laser beam, the focus of laser beam along both the transverse directions gets enhanced.

Figure 10 shows the effect of relative strength of the Kerr nonlinearity compared to quintic nonlinearity on breathing of the laser beam. It can be seen that as the Kerr nonlinearity becomes more and more dominating on the quintic nonlinearity, the breathing of the optical beam keeps on increasing. This is due to the reason that Kerr nonlinearity is focusing in nature and quintic nonlinearity is defocusing in nature.

Axial phase shift of the breather soliton

The self-phase modulation of the laser beam results from its longitudinal phase shift that originates from the transverse spatial confinement, which through the uncertainty principle, introduces a spread in the transverse momenta and hence a shift in the expectation value of the axial propagation constant.

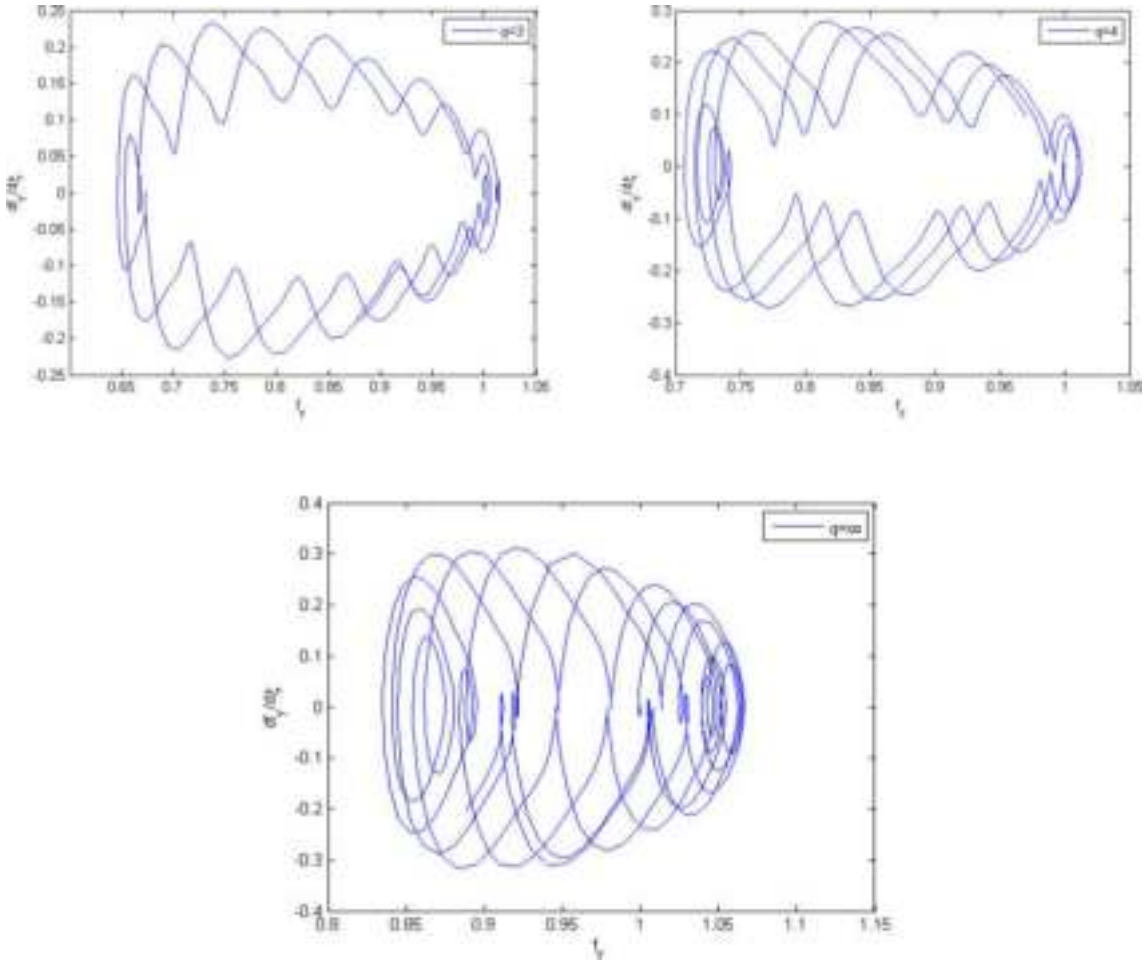

Fig. 8 Phase space plots of beam width of the laser beam along y-axis for different values of deviation parameter at fixed values of beam power $n_2E_{00}^2 = 3$and Kerr nonlinearity $\frac{n_4}{n_2^2} = 0.01$

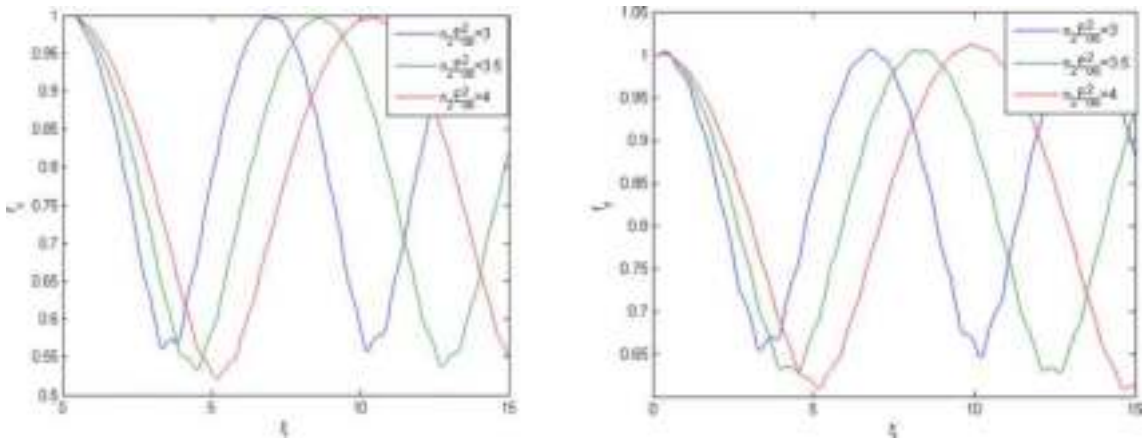

Fig. 9 Evolution of beam widths of the laser beam for different values of beam power $n_2E_{00}^2$ at fixed values of deviation parameter $q = 3$ and Kerr nonlinearity $\frac{n_4}{n_2^2} = 0.01$

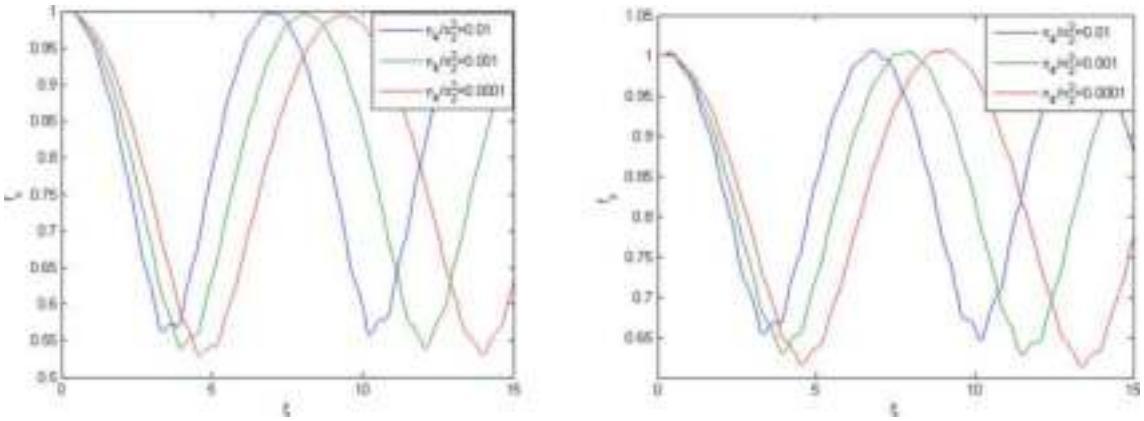

Fig. 10 Evolution of beam widths of the laser beam for different values of Kerr nonlinearity $\frac{n_4}{n_2^2}$ at fixed values of beam power $n_2E_{00}^2 = 3$ at fixed values of deviation parameter $q = 3$

A finite laser beam is having a spread in its transverse momentum because it is made up of angular spectrum of plane waves obtained by means of Fourier transformation. The r.m.s spectral width σ_k of the laser beam is defined as [26]

$$\sigma_k = \sqrt{< k_x^2 > + < k_y^2 >} \tag{9}$$

where

$$< k_x^2 >= \frac{\int_{-\infty}^{\infty}\int_{-\infty}^{\infty} k_x^2 S(k_x,k_y) S^*(k_x,k_y)\mathrm{d}k_x\mathrm{d}k_y}{\int_{-\infty}^{\infty}\int_{-\infty}^{\infty} S(k_x,k_y) S^*(k_x,k_y) dk_x dk_y}$$

$$< k_y^2 >= \frac{\int_{-\infty}^{\infty}\int_{-\infty}^{\infty} k_y^2 S(k_x,k_y) S^*(k_x,k_y)\mathrm{d}k_x\mathrm{d}k_y}{\int_{-\infty}^{\infty}\int_{-\infty}^{\infty} S(k_x,k_y) S^*(k_x,k_y) dk_x dk_y}$$

$$S(k_x,k_y) = \frac{1}{2\pi}\int_{-\infty}^{\infty}\int_{-\infty}^{\infty} A_0(x,y,z) e^{-i(k_x x + k_y y)}\mathrm{d}x\mathrm{d}y$$

The wave number k_0 of the laser beam is related to transverse and longitudinal components through

$$k_0^2 = k_x^2 + k_y^2 + k_z^2 \tag{10}$$

where k_z is the axial wave number, and k_x and k_y are the transverse wave numbers, respectively. The effective axial propagation constant of an optical beam is defined in r.m.s sense as

$$\bar{k}_z = \frac{\langle k_z^2\rangle}{k_0} = k_0 - \frac{\langle k_x^2\rangle}{k_0} - \frac{\langle k_y^2\rangle}{k_0} \tag{11}$$

The overall on axis phase $\theta(z)$ is related to effective propagation constant as

$$\bar{k}_z = \frac{\partial\theta}{\partial z} \tag{12}$$

The first term in Eq. (11) gives the phase k_0 of an infinite plane wave propagating along z-axis. The second term represents a phase shift of finite beam in comparison with infinite plane wave.

$$\frac{d\theta_\mathrm{p}}{dz} = -\frac{1}{k_0}\left(\langle k_x^2\rangle + \langle k_y^2\rangle\right) \tag{13}$$

In present investigation, Eq. (13) has been solved numerically in association with Eqs. (7) and (8) and the corresponding evolution of axial phase of the breather soliton for

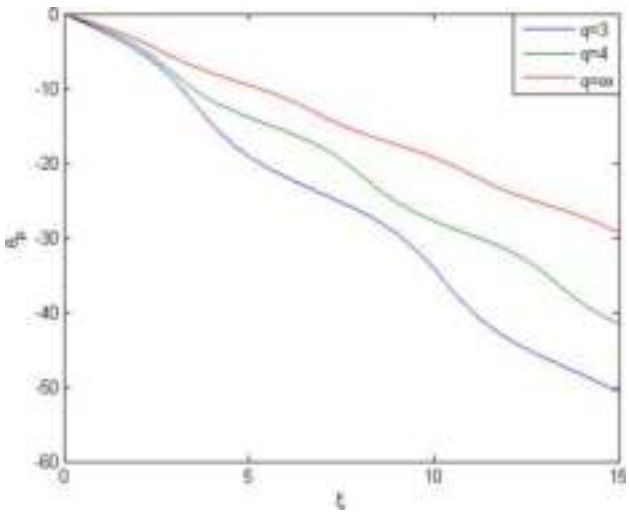

Fig. 11 Evolution of axial phase of breather soliton for different values of deviation parameter at fixed values of beam power $n_2E_{00}^2 = 3$ and Kerr nonlinearity $\frac{n_4}{n_2^2} = 0.01$

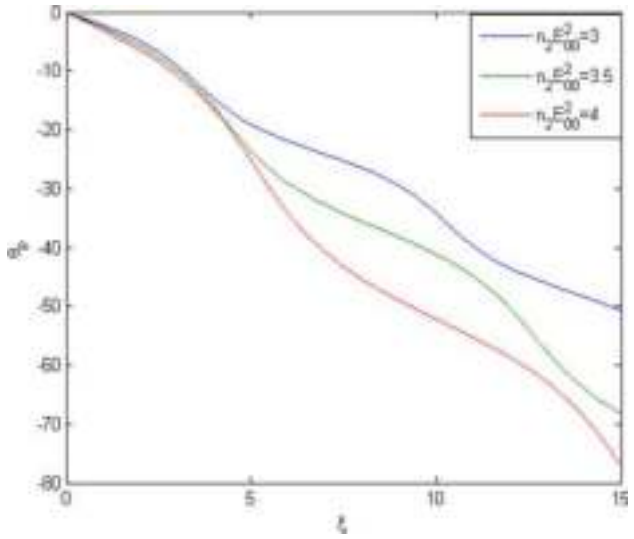

Fig. 12 Evolution of axial phase of breather soliton for different values of beam power $n_2E_{00}^2$ at fixed values of deviation parameter $q = 3$ and Kerr nonlinearity $\frac{n_4}{n_2^2} = 0.01$

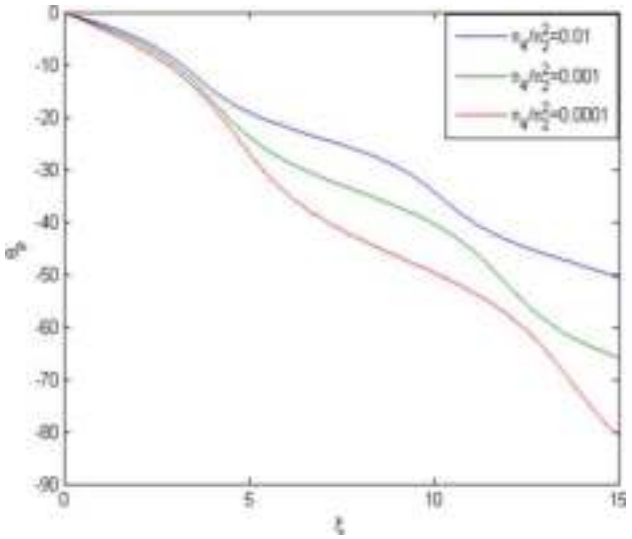

Fig. 13 Evolution of axial phase of breather soliton for different values of Kerr nonlinearity $\frac{n_4}{n_2^2}$ at fixed values of beam power $n_2E_{00}^2 = 3$ at fixed values of deviation parameter $q = 3$

different values of deviation parameter, beam intensity and Kerr nonlinearity is depicted in Figs. 11 and 12.

It can be seen that axial phase θ_p of the breather soliton decreases monotonically with distance of propagation, showing abrupt jumps at the periodic positions of the minimum beam widths. These jumps of axial phase at the focal positions of the laser beam give it a step-like behavior. The monotonic decrease in axial phase with distance is due to the fact that the self-focusing of the laser beams with distance of propagation leads to reduction in volume of space available for its propagation. This in turn through position momentum uncertainty along the transverse directions

$$\Delta x \Delta p_x = \text{constant}$$

$$\Delta y \Delta p_y = \text{constant}$$

results in increase in the transverse momentum of the photons of the laser beam. This situation is similar to that observed for a quantum particle trapped in a tube or a photon confined in a waveguide. However, the interesting fact is that in the present case there is no physical boundary to confine the photons. Now, as the overall momentum should remain conserved, the increase in transverse momentum results in reduction in the longitudinal momentum of the photons. This reduction in the longitudinal momentum is the consequence of monotonic decrease in the axial phase of the laser beam.

Step-like behavior of the axial phase, with each step occurring at positions of minimum beam width, indicates that there is slowest decrement in θ_p at points of minimum beam width. This is opposite to the behavior of phase in graded index fibers, where phase decreases slowest in the positions of minimum intensity, i.e., maximum beam width. This difference in the behavior of axial phase in plasmas and that in graded index fibers is due to the fact that due to their optical nonlinearity, plasmas behave as oscillating linear wave guides. In linear wave guides, the growth rate of axial phase is inversely proportional to the square of beam width.

The step-like behavior observed in the axial phase can be explained by its connection to Berry's phase, also known as the geometric phase. Berry's phase is an additional topological phase that a system acquires after going through a cyclic adiabatic evolution in parameter space. To better grasp the physical significance of this geometric phase, consider the following illustration:

Imagine placing the tip of a pencil at the North Pole of a globe, aligned with one of the meridians (lines of longitude) originating from the pole. Now, move the pencil downward along the meridian until it reaches the equator while keeping it perpendicular to the equator. Next, slide the pencil to another meridian and move it back to the North Pole along this new meridian. Interestingly, you will observe that although the pencil has returned to its original position without any rotations, it no longer points to the original meridian but rather to a new longitude.

This simple exercise demonstrates the concept of "parallel transport" of a vector (a quantity with both length and direction) around a circuit on a curved surface, resulting in what is known as an anholonomy. Anholonomy refers to the failure of certain variables describing the system to return to their original values. In this example, the anholonomy arises

because the pencil was forced to trace a circuit on the surface of a sphere while remaining parallel to the meridians at all times. It is purely a geometric phenomenon, independent of the pencil's energy, mass or initial direction. The extent of anholonomy depends solely on the area and curvature of the surface enclosed by the circuit. In the case of waves, this anholonomy is known as the geometric phase, which manifests as a shift in the wave's phase—the quantity describing the wave's position within its oscillatory cycle at any given time and place.

Such phase shifts originate from the dynamical phase inherent in any wave, be it quantum or classical. To understand this dynamical phase, consider the example of a traveling wave produced by jiggling a long rope fixed at one end. A series of photographs capturing the wave would reveal that points on the rope that were at the wave's crests in one picture would no longer be at the crests in another picture (unless the photographs were synchronized with the wave). In other words, the phase of the wave changes from one picture to another. The rate at which the wave's phase changes corresponds to the wave's instantaneous frequency, which, for a stationary quantum state, is proportional to the state's energy. However, since the dynamical phase does not affect the energy or spatial extent of a quantum system's wave function, it does not influence the system while it is in a stationary state.

To determine the geometric phase of a system undergoing a cyclic adiabatic change in its environment, one can plot all possible environments of the system in a parameter space. The parameter space consists of axes representing the physical variables describing the environment. A cyclic adiabatic change is then represented as a closed curve in this parameter space. In the simplest case, the geometric phase is determined by the area enclosed by the curve, which is equivalent to the solid angle subtended by the curve if it forms a spherical surface. For parameter spaces with more than three dimensions, the geometric phase can be more conveniently generalized by expressing it in terms of a mathematical quantity called a two-form. A two-form represents the flux or flow of a quantity through space. The geometric phase can be calculated by integrating or summing the two-form over any surface that captures all the flux through the circuit.

Regarding the axial phase of an optical beam, the parameter undergoing cycling is the curvature of the wavefronts of the laser beam. As the laser beam undergoes self-focusing, the radius of curvature of its wavefronts decreases, causing them to become more convex. Consequently, the axial phase of the laser beam experiences a discontinuity at the focus.

The concept of a two-form based on geometric phase finds utility in describing quantum mechanical phenomena that are unfamiliar in our everyday experiences. However, it can also be extended to describe the mechanics of familiar systems like springs and pendulums. John H. Hannay of Bristol has explored the classical counterpart of the quantum–mechanical geometric phase. He examined macroscopic systems consisting of oscillating bodies whose configuration is defined by one or more angular variables. The system's environment changes gradually, starting and ending at the same set of parameters. After completing the cycle, the oscillations retain their original amplitude, but the angles have altered.

Hannay identified that the angular shifts can be divided into dynamical and geometric components, similar to phase shifts in quantum mechanics. The dynamical part corresponds to what would be calculated assuming the angle increases at a rate equivalent to the instantaneous frequency of oscillation. Hannay's achievement was recognizing the geometric contribution, now referred to as Hannay's angle, and deriving a formula to calculate it as the flux of a two-form through a closed circuit in parameter space. However, it is important to note that the analogy with quantum mechanics is not entirely complete, as classical motions often exhibit chaotic behavior instead of simple oscillation. In chaotic systems, angle variables cannot be defined, and Hannay angles do not exist.

In one of Hannay's examples, he envisioned a bead sliding without friction at a constant speed on a noncircular wire loop while the loop is slowly rotated within its plane. In this scenario, the angle variable corresponds to the distance around the loop from a specific point. Hannay's angle indicates the position of the bead after the loop's rotation relative to where it would be if the loop had remained stationary. This angle is solely a geometric combination of the loop's perimeter and the area it encloses. It is significant for elongated, narrow loops and becomes negligible for circular ones.

Another example provided by Hannay illustrates the classical analogue of the quantum geometric phase for spins that are gradually turned. Consider a pendulum bob moving in a circular path. In this case, gravity establishes the symmetry direction, which is a vertical line passing through the center of the Earth. As the Earth rotates, the symmetry direction rotates in space (unless the experiment takes place at one of the poles). Consequently, after one day, the position of the pendulum bob in its circular orbit will be shifted by an angle—Hannay's angle—equal to the solid angle subtended by the symmetry direction.

When the pendulum bob oscillates along a linear path rather than a circular trajectory, the displacement from its original position becomes more prominent. This back-and-forth motion can be understood as a combination of two circular motions in opposite directions, akin to how linearly polarized light can be interpreted as a superposition

of two circularly polarized states. Over the course of a complete day of swinging, the two circular motions of the pendulum will have experienced opposing angular shifts. These shifts manifest as a rotation of the plane in which the pendulum bob swings, thus becoming noticeable.

The plots in Fig. 11 depict that with increase in the value of deviation parameter q there is decrease in the rate of change of axial phase with distance. This is due to the fact that as the spatial profile of the laser beam converges toward ideal Gaussian profile the transverse confinement of the laser beam due to self-focusing decreases. As spatial confinement of the laser beam is homeostasis for the axial phase shift, the reduction of self-focusing with increase in deviation parameter q results in reduction in the rate of change of axial phase with distance.

The plots in Figs. 12 and 13 indicate that with increase in either beam power or Kerr nonlinearity of the medium the rate of decrease of axial phase of the breather soliton increases. This is due to enhancement of the depth of breathing (i.e., extent of self-focusing) of the breather soliton.

Conclusions

In conclusion, we have investigated the formation of breather elliptical q-Gaussian optical solitons in cubic quintic nonlinear media. In can be concluded from the results of present investigation that irradiance profile of the optical beam plays a significant role in the breathing of the spatial soliton. For q-Gaussian laser beams q parameter acts as a control parameter to control the extent of breathing of the beam. The results of present investigation may serve as guide for the experimentalists working in the area of optical communication and sensors.

References

1. N. Gupta, Multi Gaussian breather solitons in diffraction managed nonlinear optical media. Nonlinear Opt. Quant. Opt. **55**, 309 (2022)
2. J.S. Russell, "Report on Waves, 14th Mtg. of the British Assoc. for the Advance of Science," **311**, (1844).
3. R.Y. Chiao, E. Garmire, C.H. Townes, Self-trapping of optical beams. Phys. Rev. Lett. **13**, 479 (1960)
4. M. Karlsson, D. Anderson, M. Desaix, Dynamics of self-focusing and self-phase modulation in a parabolic index optical fiber. Opt. Lett. **17**, 22 (1992)
5. P.L. Kelley, Self-focusing of optical beams. Phys. Rev. Lett. **15**, 1005 (1965)
6. R.R. Alfano, S.L. Shapiro, Observation of self-phase modulation and small-scale filaments in crystals and glasses. Phys. Rev. Lett. **24**, 592 (1970)
7. A. Biswas, Quasi-stationary optical solitons with parabolic law nonlinearity. Opt. Commun. **216**, 427 (2003)
8. J.T. Manassah, P.L. Baldeck, R.R. Alfano, Self-focusing and self-phase modulation in a parabolic graded-index optical fiber. Opt. Lett. **13**, 589 (1988)
9. D. Pushkarov, S. Tanev, Bright and dark solitary wave propagation and bistability in the anomalous dispersion region of optical waveguides with third-and fifth-order nonlinearities. Opt. Commun. **124**, 354 (1996)
10. N. Gupta, S. Kumar, Self-focusing of multi-Gaussian laser beams in nonlinear optical media as a Kepler's central force problem. Opt. Quant. Electron. **52**, 178 (2020)
11. A. Singh, N. Gupta, Self-focusing of multi-Gaussian laser beams in nonlinear optical media as a Kepler's central force problem. Optik **127**, 2432 (2016)
12. N. Singh, N. Gupta, A. Singh, Second harmonic generation of Cosh-Gaussian laser beam in collisional plasma with nonlinear absorption. Opt. Commun. **381**, 180 (2016)
13. A. Singh, N. Gupta, Second harmonic generation of self-focused Cosh-Gaussian laser beam in collisional plasma. Optik **127**, 5452 (2016)
14. S. Jana, A. Singh, K. Porsezian, T. Mithun, Self-trapped elliptical super-Gaussian beam in cubic–quintic media. Opt. Commun. **332**, 311 (2014)
15. E.M.E. Zayed, R.M.A. Shohib, M.E.M. Alngar, A. Biswas, M. Ekici, S. Khan, A.K. Alzahrani, M.R. Belic, Optical solitons and conservation laws associated with Kudryashov's sextic power-law nonlinearity of refractive index. Ukr. J. Phys. Opt. **22**, 38 (2021)
16. Y. Yildrim, A. Biswas, A. Dakova, P. Guggilla, S. Khan, H.M. Alshehri, M.R. Belic, Cubic–quartic optical solitons having quadratic–cubic nonlinearity by sine–Gordon equation approach. Ukr. J. Phys. Opt. **22**, 83 (2021)
17. A. Biswas, J. Edoki, P. Guggilla, S. Khan, A.K. Alzahrani, M.R. Belic, Cubic–quartic optical soliton perturbation with Lakshmanan-Porsezian-Daniel model by semi-inverse variational principle. Ukr. J. Phys. Opt. **22**, 123–127 (2021)
18. Y. Yıldırım, A. Biswas, P. Guggilla, S. Khan, H.M. Alshehri, M.R. Belic, Optical solitons in fiber Bragg gratings with third and fourth order dispersive reflectivities. Ukr. J. Phys. Opt. **22**, 239–254 (2021)
19. Y. Yıldırım, A. Biswas, A. Dakova, P. Guggilla, S. Khan, H.M. Alshehri, M.R. Belic, Cubic–quartic optical solitons having quadratic–cubic nonlinearity by sine–Gordon equation approach. Ukr. J. Phys. Opt. **22**, 255–269 (2021)
20. N. Gupta, S.B. Bhardwaj, Nonlinear interaction of Bessel–Gauss laser beams with plasmas with axial temperature ramp. J. Opt. **51**, 950 (2022)
21. N. Gupta, S. Kumar, Nonlinear interaction of elliptical q-Gaussian laser beams with plasmas with axial density ramp: effect of ponderomotive force. Opt. Quant. Electron. **53**, 253 (2021)
22. N. Gupta, "Self-action effects of quadruple-Gaussian laser beam in media possessing cubic–quintic nonlinearity." Em. Waves Appl. **32**, 2350 (2018)
23. D. Anderson, M. Bonnedal, M. Lisak, Nonlinear propagation of elliptically shaped Gaussian laser beams. J. Plasma Phys. **23**, 115 (1980)
24. D. Anderson, M. Bonnedal, Variational approach to nonlinear self-focusing of Gaussian laser beams. Phys. Fluids **22**, 105 (1979)

25. N. Gupta, S.B. Bhardwaj, Relativistic effects on electron acceleration by elliptical q-Gaussian laser beam driven electron plasma wave. Opt. Quant. Electron. **53**, 700 (2021)
26. S. Feng, H.G. Winful, Physical origin of the Gouy phase shift. Opt. Lett. **26**, 485 (2001)

J Opt
https://doi.org/10.1007/s12596-023-01390-9

RESEARCH ARTICLE

Excitation of upper hybrid wave by cross focused *q*-Gaussian laser beams in graded index plasma channel

Naveen Gupta[1] · Rohit Johari[1] · Sanjeev Kumar[1] · Suman Choudhry[1] · S. B. Bhardwaj[2] · A. K. Alex[1]

Received: 6 July 2023 / Accepted: 26 August 2023

Abstract In this paper, a method is presented for exciting an upper hybrid wave (UHW) in a preformed parabolic plasma channel. The plasma channel is magnetized perpendicular to the propagation direction of laser beams. The UHW is generated through the interaction of two *q*-Gaussian laser beams with frequencies ω_1 and ω_2, employing the ponderomotive nonlinearity. The evolution of the laser beam spot sizes along the propagation distance is described by a set of coupled differential equations derived using the moment theory approach in the W.K.B approximation. The ponderomotive nonlinearity depends on the intensities of both laser beams, resulting in a mutual influence between the two beams, leading to cross-focusing. Numerical simulations are conducted to examine the impact of laser and channel parameters on the cross-focusing of laser beams and its effect on the power of the generated UHW. The results indicate that the intensity profiles of the laser beams, channel depth, and strength of the static magnetic field significantly affect the power of the generated UHW.

Keywords q-Gaussian · Plasma Waves · Moment Theory · Clean Energy · Self Focusing

✉ Sanjeev Kumar
skpanwar82@gmail.com

Naveen Gupta
naveens222@rediffmail.com

[1] Lovely Professional University, Phagwara, India

[2] SUS Govt College, Matak-Majri, Indri, Karnal, India

Introduction

At the turn of the last century, the introduction of lasers [1] sparked a significant surge in research within the field of plasma physics. The study of plasmas began in the nineteenth century, when Michael Faraday investigated electrical discharges through gases. Modern plasma research dates from 1957 and 1958. During those years, Soviet Sputnik and American Explorer spacecrafts discovered that space near the earth is filled with plasma. At the same time, till then secret research on controlled thermonuclear fusion conducted by the USA, Soviet Union and Europe was revealed at the Atoms for Peace Conference in Geneva, greatly increasing the freely available information on plasmas. Fusion research focuses on producing extremely hot plasmas and confining them in magnetic "bottles," to create the conditions necessary for energy-producing nuclear reactions to occur.

Extensive studies, incorporating both theoretical and experimental approaches, have been conducted to enhance our understanding of this subject. These collective efforts have given rise to various potential applications, such as laser-driven particle accelerators [2–5], inertial confinement fusion [6, 7], X-ray lasers [8–10], laser plasma channeling [11, 12], and supercontinuum generation [13]. The successful realization of these applications relies heavily on the efficient coupling of laser energy with plasmas. Unfortunately, the interaction length between lasers and plasmas is inherently limited by diffraction divergence, restricting it to approximately a Rayleigh length in the absence of an optical guiding mechanism. Diffraction broadening, therefore, represents a fundamental phenomenon that hampers the efficiency of laser–plasma coupling. Consequently, there has been a renewed interest in extending the propagation distance of laser beams through

Published online: 13 September 2023

plasmas to make these applications viable. Optical fibers or plasma channels can be utilized to circumvent the issue of diffraction broadening in laser beam propagation. In applications involving laser—plasma interactions, laser beams with intensities ranging from 10^{14} to 10^{18} W/cm^2 are employed. However, traditional glass fibers experience ionization-induced breakdown at intensities of approximately 10^{12} W/cm^2. Plasma channels, composed of free electrons and ions, offer a promising solution as they are immune to ionization, providing a means to enhance the efficiency of laser–plasma coupling.

During the propagation of intense laser beams through plasma channels, various nonlinear effects occur, including stimulated Raman scattering [14, 15], excitation of electron-plasma waves [16, 17], and filamentation of the laser beam [12]. These effects contribute to anomalous heating of electrons and ions, scattering of electromagnetic energy out of the channel, and the disruption of energy deposition symmetry in the plasma. As a result, it is crucial to conduct both theoretical and experimental studies to investigate these phenomena. Such investigations are of utmost importance in the field of inertial confinement fusion and other applications that involve laser–plasma interactions.

Propagation of intense laser beams through plasma channels can stimulate natural modes of vibration of plasmas, i.e., electron plasma waves [16, 17] or ion acoustic waves [18, 19]. Ever since first proposed by Rosenbluth and Liu [20], there have been substantial efforts to excite EPW by beating two laser beams or by forward Raman scattering of a single laser beam. In former scheme two collinear laser beams of frequency difference equal to the plasma frequency, resonantly drive up a plasma wave with phase velocity approximately equal to group velocity of lasers in the plasma. The plasma wave excited through this scheme has potential applications like electron acceleration, plasma heating and current drive in tokamak, ionosphere heating, controlling ionosphere, plasma lasers. The EPW excited by beating of intense laser beams can also be used as diagnostic tool for obtaining information of plasma parameters. The excited EPW can scatter third laser beam, and, using the known frequency difference, one can accurately estimate the plasma density. Such a method of excitation and detection has the inherent advantage of not requiring that a probe be inserted in the plasma. It could thus be used in measuring the properties of space plasmas where probing is difficult and costly. Another interesting feature of the optical beating to excite EPW lies in the fact that if one uses only one laser, the plasma is heated in the portion of the laser beam where the frequency is equal to the plasma frequency. If one uses two lasers, however, there will be second stage of heating, when the plasma has expanded sufficiently so that the plasma frequency, in the volume of interaction of the two laser beams, is now equal to the difference frequency of the two laser beams. In the presence of static magnetic field, the number of natural modes of vibrations of the plasma increases and excitation of a particular mode is determined by the direction of propagation of pump laser beam with respect to the static magnetic field and by the nature of polarization of the pump beam. In case of plasma channel, magnetized in a direction perpendicular to the propagation of laser beams, the EPW is excited near the upper hybrid layer and is therefore termed as UHW [21, 22].

A number of theoretical investigations on excitation of UHW have been reported in the past. Sodha et al., reported the excitation of an UHW by an intense laser beam in ordinary mode, taking into account the ponderomotive nonlinearity, and they concluded that the focusing nature of the UHW is highly dependent on the initial power of the laser and strength of static magnetic field [23]. Liu studied the effects of self-generated magnetic field in laser produced plasma on the parametric decay of an extraordinary wave into two upper hybrid plasmons [24]. Purohit [25] investigated the excitation of an UHW by a rippled laser beam by taking into consideration the relativistic nonlinearity in electron mass.

Most of the theoretical investigations on excitation of UHW have been carried out within the frame work of near axis approximation in which dielectric function of plasma is Taylor expanded up to second power or to fourth power in r under the assumption that the intensity profile of the laser beam is perfectly Gaussian. In contrast to this picture investigations on intensity profile of Vulcan Petawatt laser at Rutherford Appleton laboratory by Patel et al. [26], and Nakatsutsumi et al. [27], suggest that the intensity profile of the laser beam is not exactly Gaussian but is having deviations from it. The suggested intensity profile that fits with experimental data is q-Gaussian of the form $f(r) = f(0)(1 + \frac{r^2}{qr_0^2})^{-q}$, where the values of relevant parameters q and r_0 can be obtained by fitting the experimental data. Small values of q are characterized by expanded wings of intensity distribution. Hence, for such laser beams it is not appropriate to use near axis approximation. Vlasov et al., have given powerful method of moments in which entire wavefront of laser beam is considered as a whole in the interaction process. A review of literature reveals the fact that no earlier theoretical investigation on excitation of UHW has been carried out with the help of moment theory approach. The aim of this article is to investigate for the first time the effect of cross-focusing of q-Gaussian laser beams on excitation of UHW in preformed collisionless plasma channel with the help of moment theory.

This paper is structured as follows:

In Sect. 2, the dielectric function of the plasma channel under the effect of ponderomotive nonlinearity is obtained. In Sect. 3, the nonlinear coupled differential equations governing the evolution of spot size of laser beams are derived

with the help of moment theory approach. The normalized power of excited UHW is obtained in Sect. 4. The detailed discussion and conclusions drawn from the results of present investigation are summarized in Sects. 5 and 6, respectively.

Characteristics of plasma channel

Consider the propagation of two coaxial, linearly polarized laser beams having electric field vectors

$$\mathbf{E_j}(r,z,t) = A_j(r,z)e^{-\imath(\omega_j t - k_j z)}\mathbf{e_x}; \quad j = 1,2 \tag{1}$$

through a plasma channel whose index of refraction resembles to that of a graded index fiber. The density profile of such a plasma channel is given by [28]

$$n_0(r) = N_e(0) + \triangle N_e \frac{r^2}{r_{ch}^2} \tag{2}$$

where $N_e(0)$ is the electron density on the axis of the channel, $\Delta N_e = N_e(r_{ch}) - N_e(0)$ is the depth of the channel and r_{ch} is the radius of channel. Thus, the electron density of the plasma in the channel increases radially, i.e., it is minimum on the axis of the channel and is maximum at the boundary. The channel is embedded in a static magnetic field $\mathbf{B} = B_0\mathbf{e_x}$ as shown in Fig. 1.

These kind of plasma channels are used to extend the propagation of the laser beams through plasmas beyond the diffraction limit.

Characteristics of *q*-Gaussian beam profile

At the plane of incidence, i.e., at $z = 0$, the transverse amplitude structure of the laser beams is given by [28]

$$A_j A_j^\star|_{z=0} = E_{j0}^2\left(1 + \frac{r^2}{q_j r_j^2}\right)^{-q_j}$$

where r_j are the initial radii of laser beams. The phenomenological parameters q_j describe the deviation of intensity distributions of the laser beams from Gaussian distribution. With the increase in the values of q_j, the intensity distributions of the laser beams converge toward the Gaussian distribution and become exactly Gaussian for $q_j = \infty$. For $z > 0$, energy conserving q-Gaussian ansatz for the laser beams are

$$A_j A_j^\star = \frac{E_{j0}^2}{f_j^2}\left(1 + \frac{r^2}{q_j r_j^2 f_j^2}\right)^{-q_j} \tag{3}$$

where $r_j f_j$ are the instantaneous radii of the laser beams. Hence, the functions f_j are termed as dimensionless beam width parameters that are measure of both axial intensity and spot size of the laser beams.

Ponderomotive nonlinearity of plasma channel

When such high-amplitude q-Gaussian laser beams propagate through the plasma, due to nonuniform intensity distribution along their wavefronts, the plasma electrons experience ponderomotive force

$$\mathbf{F_p} = -\frac{e^2}{4m}\nabla \sum_j \frac{1}{\omega_j^2} A_j A_j^\star \tag{4}$$

where e and m, respectively, are charge and mass of electrons, which result in their ambipolar diffusion from high field region to low field region. The electron density n responds to the laser electric fields according to

$$n = n_0(r)e^{-\Sigma_j \beta_j E_j E_j^\star} \tag{5}$$

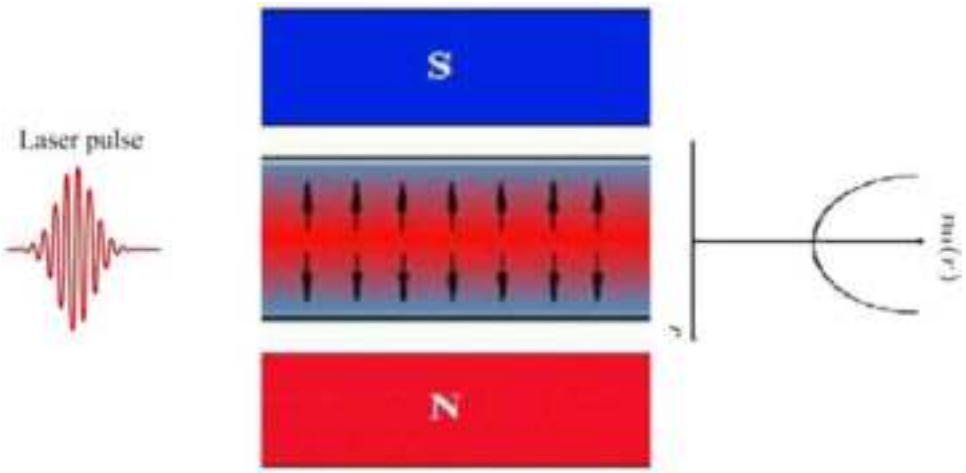

Fig. 1 Propagation of laser beam through magnetized plasma channel

where $\beta_j = \frac{e^2}{8m\omega_j^2 T_0 K_0}$ are the coefficients of ponderomotive nonlinearity, T_0 is the equilibrium temperature of plasma, K_0 is the Boltzmann constant. In this paper we shall be considering the case where laser beams vary in space, but propagate in a steady state manner in time. Consequently, ponderomotive force completely dominates ion inertia, and must be balanced by pressure forces. The formal conditions for Eq. (5) to be valid are

- macroscopic scale length L must satisfy $L >> \lambda_d$
- macroscopic velocities must be small compared with the sound speed $c_s = (\frac{T_e}{M_i})^{\frac{1}{2}}$)
- macroscopic time scales must be long compared with $(\frac{L}{c_s})$.

The redistribution of electrons results in modification of dielectric properties of plasma channel. The modified dielectric function of the plasma channel can be written as

$$\epsilon_j = 1 - \frac{\omega_p^2(r)}{\omega_j^2} e^{-\sum_j \beta_j E_j E_j^\star} \tag{6}$$

where $\omega_p^2(r) = \frac{4\pi e^2}{m} n_0(r)$ is the plasma frequency in the absence of laser beams. Using Eqs. (2–3) in Eq. (6) it can be shown that

$$\epsilon_j = \epsilon_{0j} + \phi_j(A_1 A_1^\star, A_2 A_2^\star) \tag{7}$$

where

$$\epsilon_{0j} = 1 - \frac{\omega_{p0}^2}{\omega_j^2} e^{-\sum_j \frac{\beta_j E_{jo}^2}{f_j^2}} \tag{8}$$

is the linear part of dielectric function and

$$\begin{aligned}\phi_j(A_1 A_1^\star, A_2 A_2^\star) = & \frac{\omega_{p0}^2}{\omega_j^2} e^{-\sum_j \frac{\beta_j E_{jo}^2}{f_j^2}} \\ & - \left(\frac{\omega_{p0}^2}{\omega_0^2} + \frac{\omega_{pch}^2}{\omega_0^2} \frac{r^2}{r_{ch}^2} \right) \\ & e^{-\sum_j \frac{\beta_j E_{j0}^2}{f_j^2} (1 + \frac{r^2}{q_j r_j^2 f_j^2})^{-q_j}}\end{aligned} \tag{9}$$

is the nonlinear part of dielectric function, where

$$\omega_{p0}^2 = \frac{4\pi e^2}{m} N_e(0)$$

$$\omega_{pch}^2 = \frac{4\pi e^2}{m} \triangle N_e$$

Coupled propagation of laser beams

The electric field vectors $\mathbf{E_j}(r, z, t)$ of the laser beams satisfy the wave equation

$$\nabla^2 \mathbf{E_j} - \nabla(\nabla . \mathbf{E_j}) + \frac{\omega_j^2}{c^2} \epsilon_j \mathbf{E_j} = 0 \tag{10}$$

Even if $\mathbf{E_j}$ have longitudinal components, the polarization term $\nabla(\nabla . \mathbf{E_j})$ of Eq. (10) can be neglected by assuming that the root mean square (r.m.s) radii of laser beams are much greater than their vacuum wavelengths or the laser frequencies are much greater than the plasma frequency. Under this approximation, Eq. (10) reduces to

$$\nabla^2 \mathbf{E_j} + \frac{\omega_j^2}{c^2} \epsilon_j \mathbf{E_j} = 0 \tag{11}$$

Using Eq. (1) in (11), we get

$$\iota \frac{dA_j}{dz} = \frac{1}{2k_j} \nabla_\perp^2 A_j + P_j(A_1 A_1^\star, A_2 A_2^\star) A_j \tag{12}$$

where $P_j = \frac{k_j}{2\epsilon_{0j}} \phi_j$. Equation(12) is the well-known nonlinear Schrodinger wave equation that describes stationary beam propagation in the z- direction, with the assumption that wave-amplitude scale length along z-axis is much larger as compared to characteristic scale in the transverse direction. This equation is called nonlinear Schrodinger equation because it is identical to Schrodinger equation in quantum mechanics, the only difference being that here the potential function P_j itself depends on wave-functions A_1, A_2. The term $\nabla_\perp^2 A_j$ in wave Eq. (12) represents the spatial dispersion of the laser beams and is having its origin in diffraction phenomenon, whereas the term $P_j A_j$ represents nonlinear refraction of the laser beams.

Defining total beam powers N_j as

$$N_j = \int_0^{2\pi} \int_0^{\infty} A_j A_j^\star r dr d\theta \tag{13}$$

and global Hamiltonian H_j to the wave Eqs. (12) and (9) as

$$H_j = \int_0^{2\pi} \int_0^{\infty} \frac{1}{2k_j^2} (|\nabla_\perp A_j|^2 - F_j) r dr d\theta \tag{14}$$

where

$$F_j = \frac{1}{2\epsilon_{0j}} \int_0^{A_j A_j^\star} \phi_j(A_1 A_1^\star, A_2 A_2^\star) d(A_j A_j^\star) \tag{15}$$

one can show that $\frac{\partial N_j}{\partial z} = \frac{\partial H_j}{\partial z} = 0$, i.e., H_j and N_j are invariants of wave Eq. (12). The first invariant N_j is merely a statement of the conservation of energy of the laser beams and second

invariant H_j relates the wavefront curvature of laser beams to the plasma nonlinearity. These invariants are based on the symmetry of Schrodinger wave equation under gauge transformation and transformation along z-axis and may be derived from Lagrangian density for Eq. (12). It is important to note that H_j need not be positive definite, and is in fact negative when the nonlinear refraction term dominates the dispersion term.

Defining mean square radii $< a_j^2(z) >$ of the laser beams by

$$< a_j^2(z) >= \frac{1}{N_j}\int_0^{2\pi}\int_0^{\infty} r^2 A_j A_j^{\star} r dr d\theta \tag{16}$$

one can show that

$$\frac{d^2}{dz^2} < a_j^2(z) >= 4\frac{H_j}{N_j} - \frac{4}{N_j}\int_0^{2\pi}\int_0^{\infty} Q_j r dr d\theta \tag{17}$$

where

$$Q_j = \frac{1}{2\epsilon_{0j}} A_j A_j^{\star}\phi_j - 2F_j \tag{18}$$

This can be obtained either directly by taking spatial moments of the envelope Eq. (12) or via standard conservation laws of classical field theory.

Using Eq. (3) in (13) and (16), it can be shown that

$$N_j = \pi r_j^2 E_{0j}^2 \left(1 - \frac{1}{q_j}\right)^{-1} \tag{19}$$

$$< a_j^2 >= r_j^2 f_j^2 \left(1 - \frac{2}{q_j}\right)^{-1} \tag{20}$$

Using Eqs. (9), (18–21), we get following coupled differential equations governing the propagation dynamics of laser beams under the combined effect of ponderomotive nonlinearity and radial inhomogeneity of the plasma channel.

$$\frac{d^2 f_1}{d\xi^2} + \frac{1}{f_1}\left(\frac{df_1}{d\xi}\right)^2 = \frac{\left(1-\frac{1}{q_1}\right)\left(1-\frac{2}{q_1}\right)}{\left(1+\frac{1}{q_1}\right)}\frac{1}{f_1^3} - \left(1-\frac{1}{q_1}\right)\left(1-\frac{2}{q_1}\right)\{\alpha_2 K_1 + \alpha_1 J_1 + \alpha_2 J_2\} \tag{21}$$

$$\frac{d^2 f_2}{d\xi^2} + \frac{1}{f_2}\left(\frac{df_2}{d\xi}\right)^2 = \left(\frac{r_1}{r_2}\right)^4\left(\frac{\omega_1}{\omega_2}\right)^2\left(\frac{\epsilon_{01}}{\epsilon_{02}}\right)\left[\frac{\left(1-\frac{1}{q_2}\right)\left(1-\frac{2}{q_2}\right)}{\left(1+\frac{1}{q_2}\right)}\frac{1}{f_2^3} - \left(1-\frac{1}{q_2}\right)\left(1-\frac{2}{q_2}\right)\{\alpha_2 K_6 + \alpha_1 J_3 + \alpha_2 J_4\}\right] \tag{22}$$

where

$$\alpha_1 = \frac{\omega_{p0}^2 r_1^2}{c^2}$$

$$\alpha_2 = \left(\frac{\omega_{pch}^2 r_1^2}{c^2}\right)\left(\frac{r_1^2}{r_{ch}^2}\right)$$

$$J_1 = \frac{\beta_1 E_{10}^2}{f_1^3}K_2 + \frac{\beta_2 E_{20}^2}{f_1^3}\left(\frac{r_1}{r_2}\right)^2\left(\frac{f_1}{f_2}\right)^4 K_3$$

$$J_2 = \frac{\beta_1 E_{10}^2}{f_1^3}K_4 + \frac{\beta_2 E_{20}^2}{f_1^3}\left(\frac{r_1}{r_2}\right)^2\left(\frac{f_1}{f_2}\right)^4 K_5$$

$$J_3 = \frac{\beta_1 E_{10}^2}{f_2^3}K_7 + \frac{\beta_2 E_{20}^2}{f_2^3}\left(\frac{r_1}{r_2}\right)^2\left(\frac{f_1}{f_2}\right)^4 K_8$$

$$J_4 = \frac{\beta_1 E_{10}^2}{f_2^3}f_1^2 K_9 + \frac{\beta_2 E_{20}^2}{f_2^3}f_1^2\left(\frac{r_1}{r_2}\right)^2\left(\frac{f_1}{f_2}\right)^4 K_1 0$$

$$K_1 = \int_0^{\infty} t\left(1+\frac{t}{q_1}\right)^{-q_1} G(t)dt$$

$$K_2 = \int_0^{\infty} t\left(1+\frac{t}{q_1}\right)^{-2q_1-1} G(t)dt$$

$$K_3 = \int_0^{\infty} t\left(1+\frac{t}{q_1}\right)^{-q_1}\left(1+\left(\frac{r_1 f_1}{r_2 f_2}\right)^2\frac{t}{q_2}\right)^{-q_2-1} G(t)dt$$

$$K_4 = \int_0^{\infty} t^2\left(1+\frac{t}{q_1}\right)^{-2q_1-1} G(t)dt$$

$$K_5 = \int_0^{\infty} t^2\left(1+\frac{t}{q_1}\right)^{-q_1}\left(1+\left(\frac{r_1 f_1}{r_2 f_2}\right)^2\frac{t}{q_2}\right)^{-q_2-1} G(t)dt$$

$$K_6 = \int_0^{\infty} t\left(1+\left(\frac{r_1 f_1}{r_2 f_2}\right)^2\frac{t}{q_2}\right)^{-q_2} G(t)dt$$

$$K_7 = \int_0^{\infty} t\left(1+\frac{t}{q_1}\right)^{-q_1-1}\left(1+\left(\frac{r_1 f_1}{r_2 f_2}\right)^2\frac{t}{q_2}\right)^{-q_2} G(t)dt$$

$$K_8 = \int_0^{\infty} t\left(1+\left(\frac{r_1 f_1}{r_2 f_2}\right)^2\frac{t}{q_2}\right)^{-2q_2-1} G(t)dt$$

$$K_9 = \int_0^{\infty} t^2\left(1+\frac{t}{q_1}\right)^{-q_1-1}\left(1+\left(\frac{r_1 f_1}{r_2 f_2}\right)^2\frac{t}{q_2}\right)^{-q_2} G(t)dt$$

$$K_{10} = \int_0^{\infty} t^2\left(1+\left(\frac{r_1 f_1}{r_2 f_2}\right)^2\frac{t}{q_2}\right)^{-2q_2-1} G(t)dt$$

$$G(t) = e^{-\left\{\frac{\beta_1 E_{10}^2}{f_1^2}\left(1+\frac{t}{q_1}\right)^{-q_1} + \frac{\beta_2 E_{20}^2}{f_2^2}\left(1+\frac{t}{q_2}\left(\frac{r_1^2 f_1^2}{r_2^2 f_2^2}\right)^2\right)^{-q_2}\right\}}$$

$$t = \frac{r^2}{r_1^2 f_1^2}$$

$$\xi = \frac{z}{k_1 r_1^2}$$

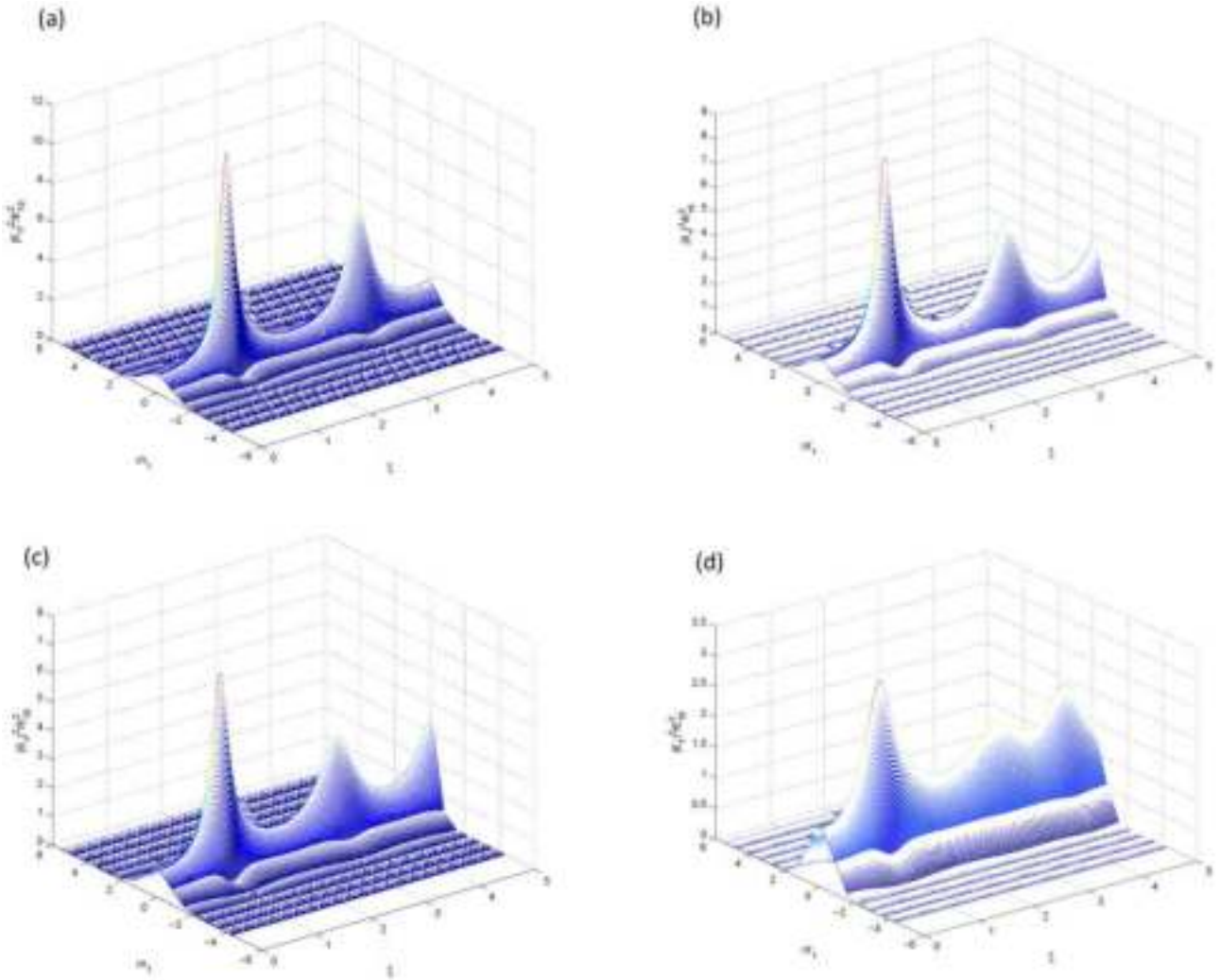

Fig. 2 Variation of normalized intensity of first beam with normalized distance of propagation ξ and radial distance $\frac{r}{r_1}$, keeping $\alpha_1 = 6$, $\alpha_2 = 1.2$, $\frac{\omega_c}{\omega_1} = 0.1$, $\beta E_{10}^2 = 1.0$, $\beta E_{20}^2 = 1.50$, $q_2 = 4$ fixed and at different values of q_1, (**a**) $q_1 = 4$, (**b**) $q_1 = 5$, (**c**) $q_1 = 6$, (**d**) $q_1 = \infty$, respectively

Excitation of upper hybrid wave

Due to ponderomotive nonlinearity, the q-Gaussian laser beams get cross-focused and hence produce sharp density gradients in the transverse direction. The generated density gradients in turn produce plasma wave at frequency $\omega = \omega_1 - \omega_2$ (Fig. 10). Upper hybrid waves can be imagined as energetic surfers riding the crests and troughs of a vast plasma sea, where the plasma's charged particles represent the water molecules. The Earth's magnetic field acts like the ocean's currents, influencing the movement of these surfing waves. The key characteristics and properties of upper hybrid waves include [29–34]:

- *Frequency range* Upper hybrid waves typically occur in the frequency range between the ion and electron plasma frequencies. They can bridge the gap between these two frequencies.
- *Origin* Upper hybrid waves result from the combined effects of the ion and electron motion within the plasma. They involve a balance between the inertia of ions and the thermal pressure of electrons.
- *Propagation* These waves propagate obliquely to the magnetic field direction, meaning they are not restricted to moving along magnetic field lines. Their direction of propagation is influenced by the angle between the wave vector and the magnetic field lines.
- *Wave structure* Upper hybrid waves have a complex wave structure that can exhibit both electrostatic and electromagnetic characteristics. They involve oscillations of the charged particles in response to the electric and magnetic fields.

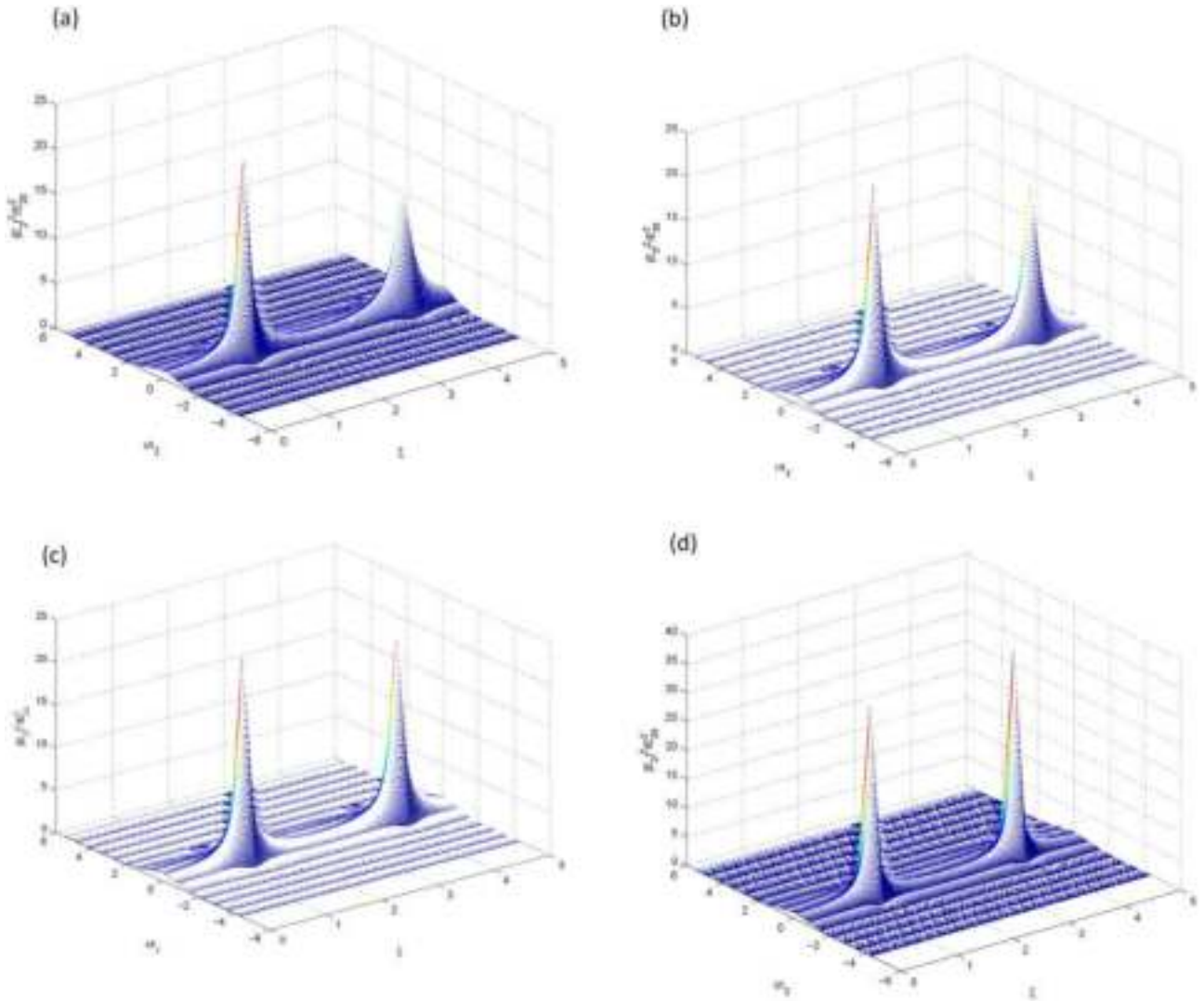

Fig. 3 Variation of normalized intensity of second beam with normalized distance of propagation ξ and radial distance $\frac{r}{r_2}$, keeping $\alpha_1 = 6$, $\alpha_2 = 1.2$, $\frac{\omega_c}{\omega_1}$= 0.1, βE_{10}^2= 1.0, βE_{20}^2= 1.50, q_2= 4 fixed and at different values of q_1, (**a**) q_1= 4, (**b**) q_1= 5, (**c**) q_1= 6, (**d**) q_1= ∞, respectively

Magnetic fields that thread through plasmas make them behave somewhat like such a fluid. A magnetic field exerts a force (the Lorentz force) on a moving electrically charged particle. The field can be thought of as a series of magnetic lines through the plasma, like the field lines around a bar magnet that can be made visible with iron filings. The Lorentz force always acts perpendicular both to the direction of the magnetic field line and to the direction in which a particle is moving. If the particle moves perpendicular to the field, the force acts like a rubber band, pulling the particle back and constraining it to move in small circles about the magnetic field line. The particle can, however, move freely in the direction of the magnetic field line. The combination of the free motion along and constrained, circular rotation across the magnetic field shapes the particle's trajectory into a helix that winds around magnetic field line. The Lorentz force makes it difficult to disperse the plasma in the direction perpendicular to the magnetic field. The maximum distance over which particles can move away from the field, called the Larmor radius, is inversely proportional to the field strength. The collective motion of plasma particles across the magnetic field actually drags the field lines along with it. The magnetic field thus becomes "frozen" into the plasma. In short, a magnetic field endows collisionless plasmas with elastic properties analogous to those of a dense gas, and so a plasma wave crossing a magnetic field behaves somewhat like an ordinary sound wave.

The dynamics of generated plasma wave is governed by

- Equation of continuity:

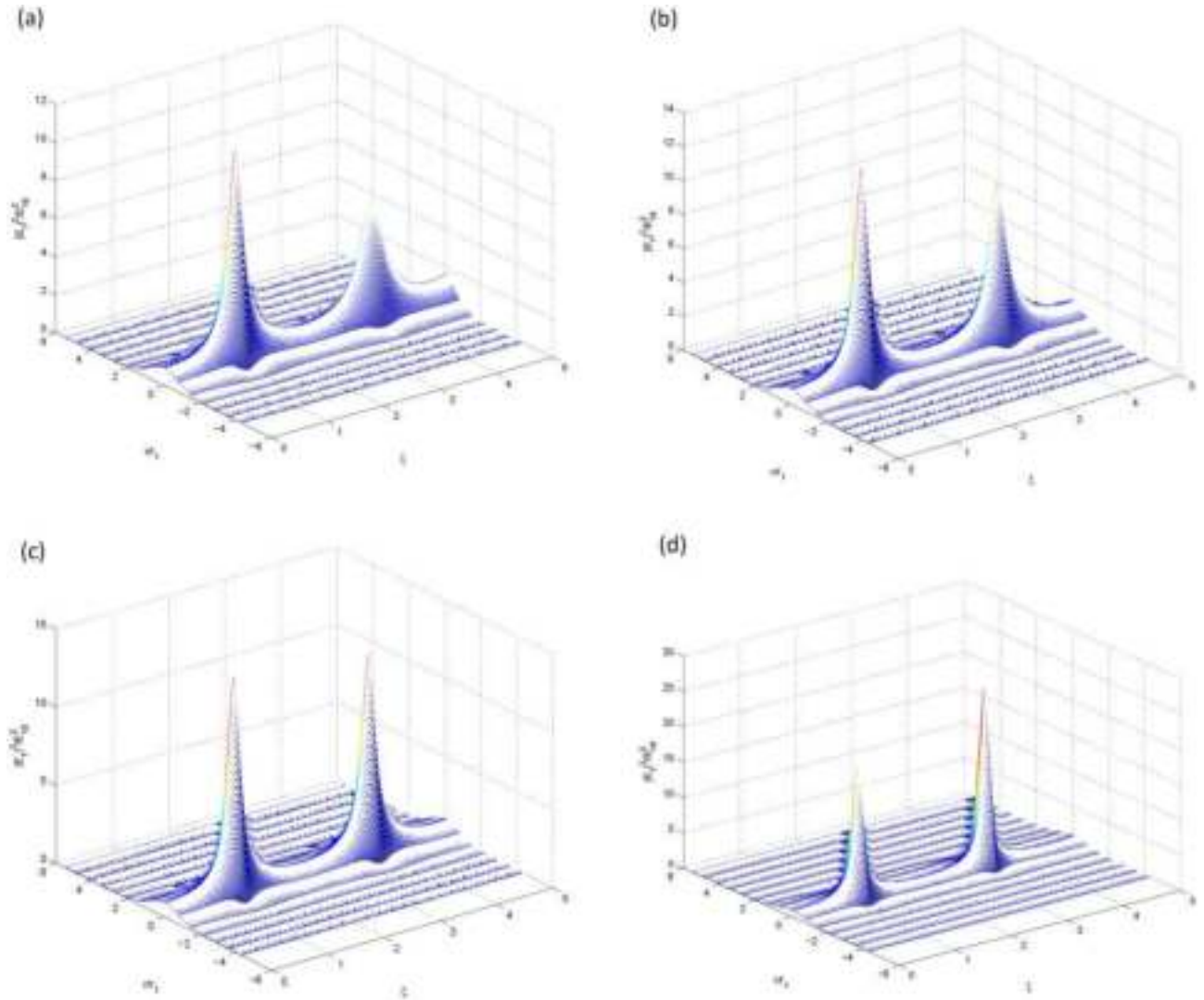

Fig. 4 Variation of normalized intensity of first beam with normalized distance of propagation ξ and radial distance $\frac{r}{r_1}$, keeping $\alpha_1 = 6$, $\alpha_2 = 1.2$, $\frac{\omega_c}{\omega_1} = 0.1$, $\beta E_{10}^2 = 1.0$, $\beta E_{20}^2 = 1.50$, $q_1 = 4$ fixed and at different values of q_2, (**a**) $q_2 = 4$, (**b**) $q_2 = 5$, (**c**) $q_2 = 6$, (**d**) $q_2 = \infty$, respectively

$$\frac{\partial N}{\partial t} + \nabla(N\mathbf{v}) = 0 \tag{23}$$

- Equation of motion

$$m\frac{d\mathbf{v}}{dt} = -e\mathbf{E} - 3\frac{K_0 T_0}{N}\nabla N - e\frac{\mathbf{v}\times\mathbf{B_0}}{c} \tag{24}$$

- Poisson's Equation

$$\nabla.\mathbf{E} = -4\pi eN \tag{25}$$

where N is the total electron density, $\mathbf{E}$ is the sum of electric fields of laser beams and UHW

$$N = n_0(r) + n'$$
$$E = \sum_j \mathbf{E_j} + \mathbf{E}'$$

$\mathbf{v} = \mathbf{v_e}$ = oscillatory velocity of electrons Using linear perturbation theory, Eqs.(23–25) reduce to

$$\frac{\partial n'}{\partial t} + \nabla(n_0\mathbf{v_e}) = 0 \tag{26}$$

$$m\frac{\partial \mathbf{v_e}}{\partial t} = -e\mathbf{E}' - 3\frac{K_0 T_0}{m}\nabla n' - e\frac{\mathbf{v}\times\mathbf{B_0}}{c} \tag{27}$$

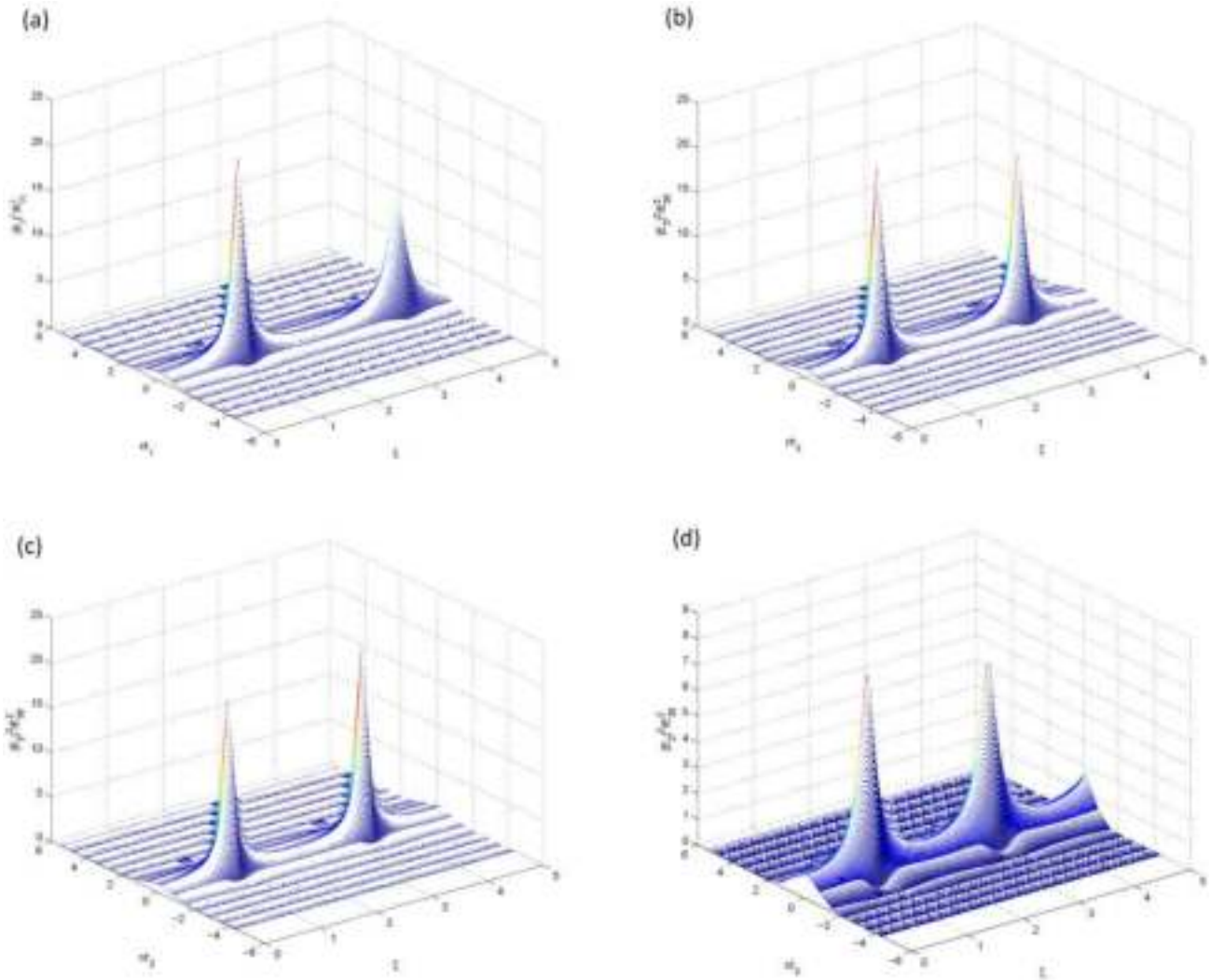

Fig. 5 Variation of normalized intensity of second beam with normalized distance of propagation ξ and radial distance $\frac{r}{r_2}$, keeping $\alpha_1 = 6$, $\alpha_2 = 1.2$, $\frac{\omega_c}{\omega_1} = 0.1$, $\beta E_{10}^2 = 1.0$, $\beta E_{20}^2 = 1.50$, $q_1 = 4$ fixed and at different values of q_2, (**a**) $q_2 = 4$, (**b**) $q_2 = 5$, (**c**) $q_2 = 6$, (**d**) $q_2 = \infty$, respectively

$$\nabla.\mathbf{E}^{'} = -4\pi e n^{'} \tag{28}$$

Using Eqs.(27–29) we get, wave equation for UHW

$$\frac{\partial^2 n^{'}}{\partial t^2} - v_{th}^2 \nabla^2 n^{'} + \left(\omega_{p0}^2 + \omega_{pch}^2 \frac{r^2}{r_{ch}^2}\right) e^{-\sum_j \beta_j A_j A_j^{\star}} \frac{n^{'}}{\left(1 - \frac{\omega_c^2}{\omega^2}\right)} = \frac{e}{m} n_0 \nabla \sum_j E_j \tag{29}$$

Taking

$$n^{'} = n_1 e^{\iota(\omega t - kz)}$$

where $\omega = \omega_2 - \omega_1$ and $k = k_2 - k_1$, we get density perturbation associated with UHW

$$n_1 = \frac{en_0}{m} \frac{1}{\left\{\omega^2 - k^2 v_{th}^2 - \frac{(\omega_{p0}^2 + \omega_{pch}^2 \frac{r^2}{r_{ch}^2})}{(1 - \frac{\omega_c^2}{\omega^2})} e^{-\sum_j \beta_j A_j A_j^{\star}}\right\}} \sum_j F_j(f_j) \tag{30}$$

where

$$F_j(f_j) = -\frac{E_{j0}}{r_j^2 f_j^3} \left(1 + \frac{r^2}{q_j r_j^2 f_j^2}\right)^{-\frac{q_j}{2}-1} r$$

Using Poisson's equation

$$\nabla \mathbf{E}^{'} = -4\pi e n^{'}$$

$$E^{'} = E_{e.p} e^{\iota(\omega t - kz)}$$

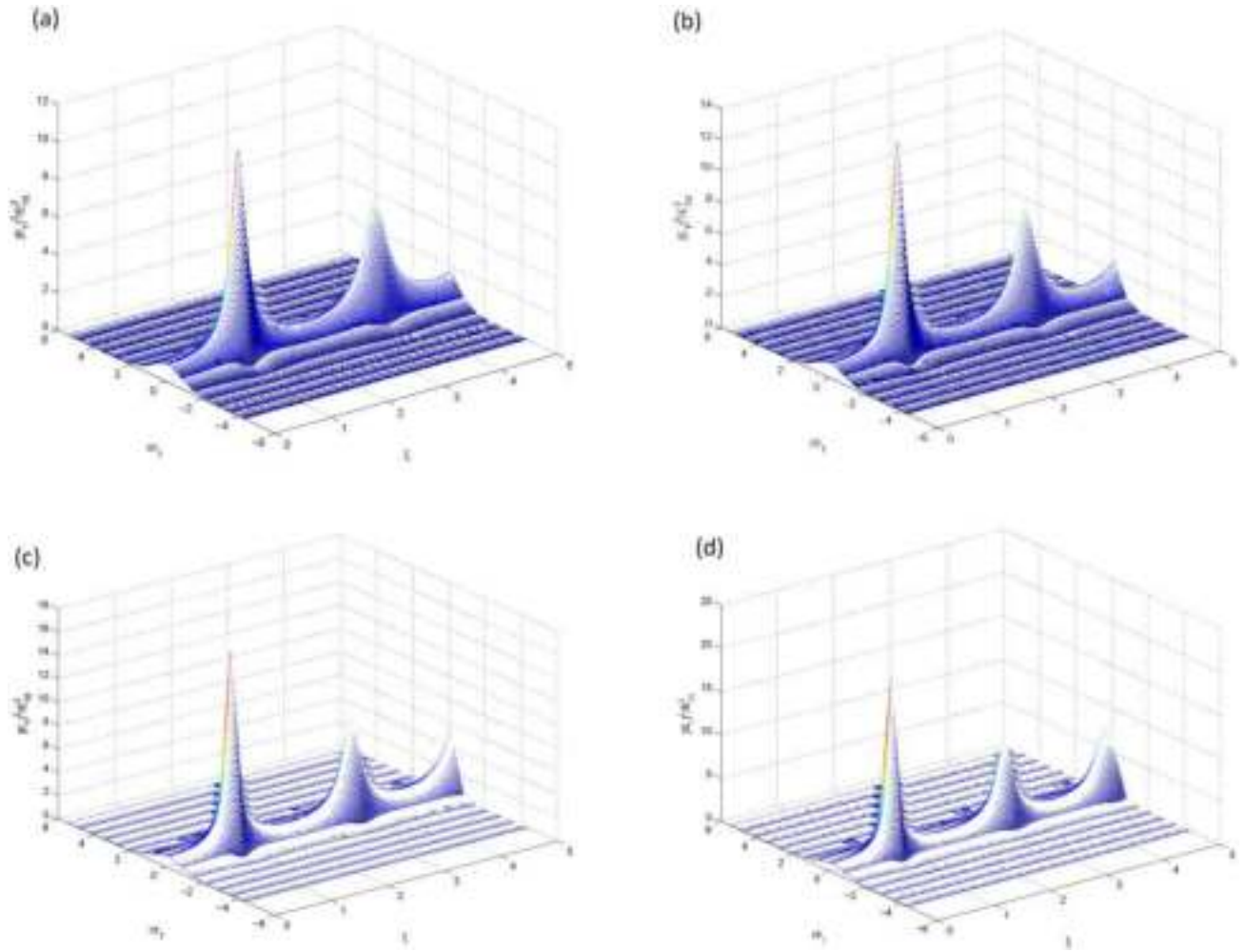

Fig. 6 Variation of normalized intensity of first beam with normalized distance of propagation ξ and radial distance $\frac{r}{r_1}$, keeping $q_1 = 4, q_2 = 4$, $\alpha_2 = 1.2$, $\frac{\omega_c}{\omega_1} = 0.1$, $\beta E_{10}^2 = 1.0$, $\beta E_{20}^2 = 1.50$ fixed and at different values of α_1, (**a**) α_1=6, (**b**) α_1=7, (**c**) α_1=8, (**d**) α_1= 9, respectively

we get

$$E_{e.p} = \frac{\iota}{k}\frac{4\pi e^2 n_0(r)}{m} \frac{1}{\left\{\omega^2 - k^2 v_{th} r - \frac{(\omega_{p0}^2 + \omega_{pch}^2 \frac{r^2}{r_{ch}^2})}{(1-\frac{\omega_c^2}{\omega^2})} e^{-\sum_j A_j A_j^\star}\right\}} \sum_j F_j \quad (31)$$

Defining normalized power of UHW as

$$\eta = \frac{P_{e.p}}{P_1}$$

where

$$P_{e.p} = \int_0^\infty E_{e.p} E_{e.p}^\star 2\pi r dr$$

$$P_1 = \int_0^\infty E_1 E_1^\star 2\pi r dr$$

we get

$$\eta = \frac{\omega_{p0}^4}{k^2\omega^4 r_1^2}\left(1 - \frac{1}{q_1}\right)^{-1} \int_0^\infty t \frac{\left(1 + \frac{alpha_2}{\alpha_1} f_1^2 t\right)^2}{D(\omega_1, \omega_2)} X(E_{10}, E_{20}) dt \quad (32)$$

where

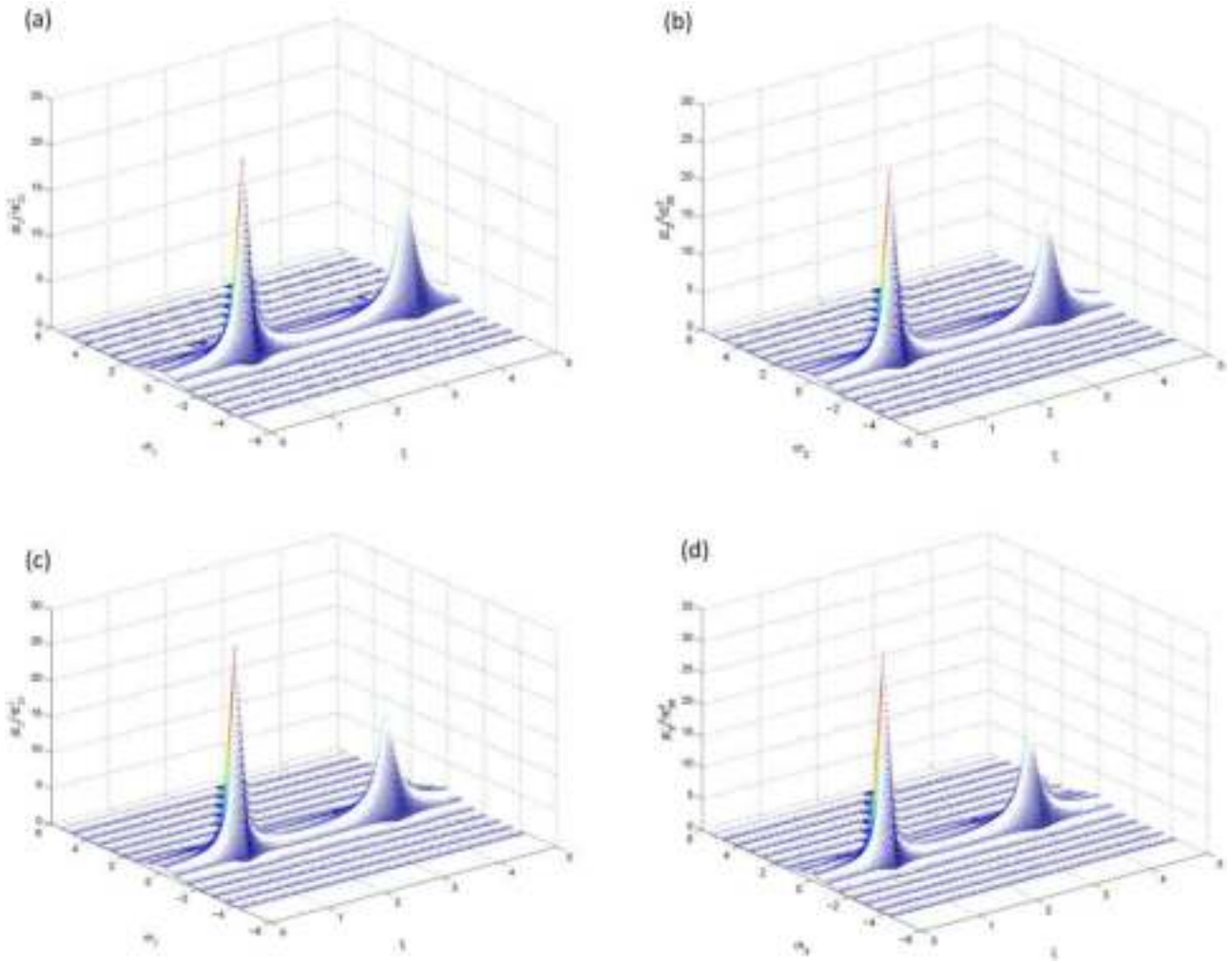

Fig. 7 Variation of normalized intensity of second beam with normalized distance of propagation ξ and radial distance $\frac{r}{r_2}$, keeping $q_1 = 4$, $q_2 = 4$, $\alpha_2 = 1.2$, $\frac{\omega_c}{\omega_1} = 0.1$=0.1, βE_{10}^2=1.0, βE_{20}^2=1.50 fixed and at different values of α_1, (**a**) α_1=6, (**b**) α_1=7, (**c**) α_1=8, (**d**) α_1= 9, respectively

$$D(\omega_1,\omega_2) = \left\{1 - \frac{k^2 v_{th}^2}{\omega^2} - \frac{\omega_{p0}^2}{\omega^2}\frac{(1+\frac{\omega_{ch}^2}{\omega_{p0}^2}\frac{r^2}{r_{ch}^2}f_1^2 t)}{(1-\frac{\omega_c^2}{\omega^2})}G(t)\right\}^2$$

$$X(E_{10},E_{20}) = \left\{\left(1+\frac{t}{q_1}\right)^{-\frac{-q_1}{2}-1} + \frac{\omega_1}{\omega_2}\sqrt{\frac{\beta_2 E_{20}^2}{\beta_1 E_{10}^2}\frac{r_1^2 f_1^3}{r_2^2 f_2^3}}\left(1+\frac{r_1^2 f_1^2}{r_2^2 f_2^2}\frac{t}{q_2}\right)^{-\frac{q_2}{2}-1}\right\}^2$$

Discussion

Equations (22) and (23) are the coupled nonlinear differential equations governing the cross-focusing of two coaxial q-Gaussian laser beams in collisionless plasma. Equation (30) gives the normalized power of electron plasma wave generated as a result of beating of the two laser beams. Numerical computational techniques are used to investigate the beam dynamics as analytic solutions of these equations are not possible. It is worth noting to understand the physical mechanisms of various terms on the right hand sides of Eqs. (22) and (23). The first terms on R.H.S of Eqs.(22) and (23) are responsible for diffraction divergence of the laser beams and have their origin in the Laplacian $\nabla_\perp^2$, appearing in nonlinear wave Eq. (13). The second terms on R.H.S of these equations arise due to the combined effect of ponderomotive nonlinearity and nonlinear coupling between the two laser beams. These terms are responsible for nonlinear refraction

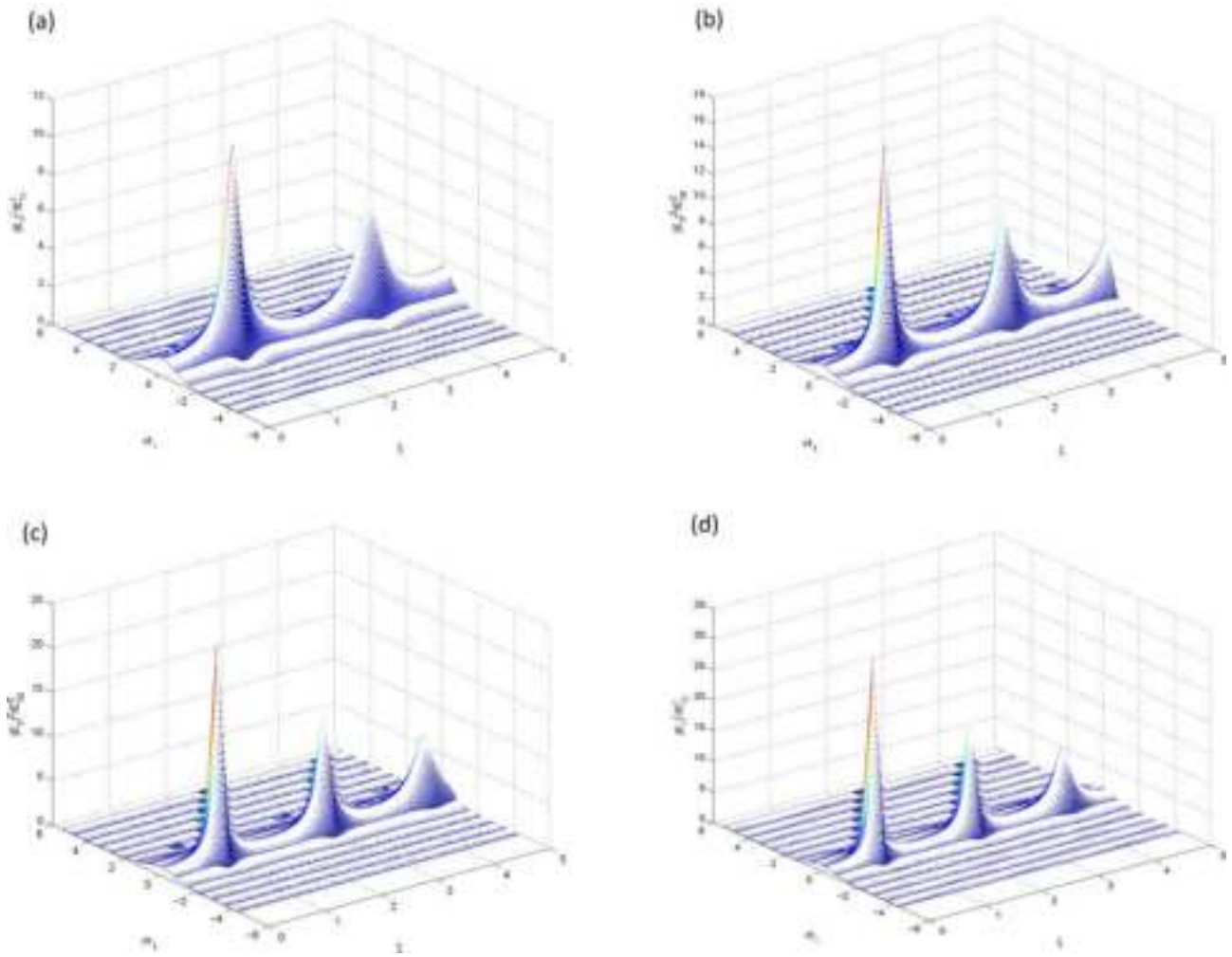

Fig. 8 Variation of normalized intensity of first beam with normalized distance of propagation ξ and radial distance $\frac{r}{r_1}$, keeping $q_1 = 4$, $q_2 = 4$, $\alpha_1 = 6$, $\frac{\omega_c}{\omega_1} = 0.1$, βE_{10}^2=1.0, βE_{20}^2=1.50 fixed and at different values of α_2, (**a**) α_2=1.2, (**b**) α_2=1.8, (**c**) α_2=2.4, (**d**) α_2= 3, respectively

of the laser beams. It is the relative competition between the diffractive and refractive terms that determine the focusing/defocusing of the laser beams in plasma.

To analyze the effect of deviation of intensity distribution of laser beams from Gaussian distribution and plasma density on cross-focusing of the laser beams as well as beat wave excitation of electron plasma wave, Eqs. (22–23) and (33) have been solved for following set of laser–plasma parameters

$\omega_1 = 1.78 \times 10^{15}$];rad/sec;$\omega_2 = 1.98 \times 10^{15}$];rad/sec

$r_1 = 15\ \mu$m;$r_2 = 16.67\ \mu$m

$T_0 = 10^6$ K

Figures2 and 3 illustrate the effect of q_1 i.e., deviation of intensity distribution of first laser beam from Gaussian distribution on focusing/defocusing of the two laser beams. The plots in Fig. 1 depict that increase in the value of q_1 leads to decrease in the extent of self-focusing of first laser beam. This is due to the fact that as the value of q_1 increases toward higher values, the intensity of the first laser beam shifts toward the axial region of the wavefront and the diffraction divergence of axial rays is stronger as compared to off axial rays. It is also observed from Fig. 1 that the laser beams with higher q values possess faster focusing. The underlying physics behind this fact is the slower focusing character of the off axial rays.

The plots in Fig. 3 depict that increase in the value of q_1 leads to increase in the extent of self-focusing of the second laser beam. This is due to the fact that increase in the value of q_1 leads to increase in the magnitude of refractive term as compared to diffractive term in Eq. 23.

The plots in Figs. 4 and 5 also depict the same result that increase in the value of q_2 leads to increase in the extent of self-focusing of first laser beam and decrease in that of second laser beam.

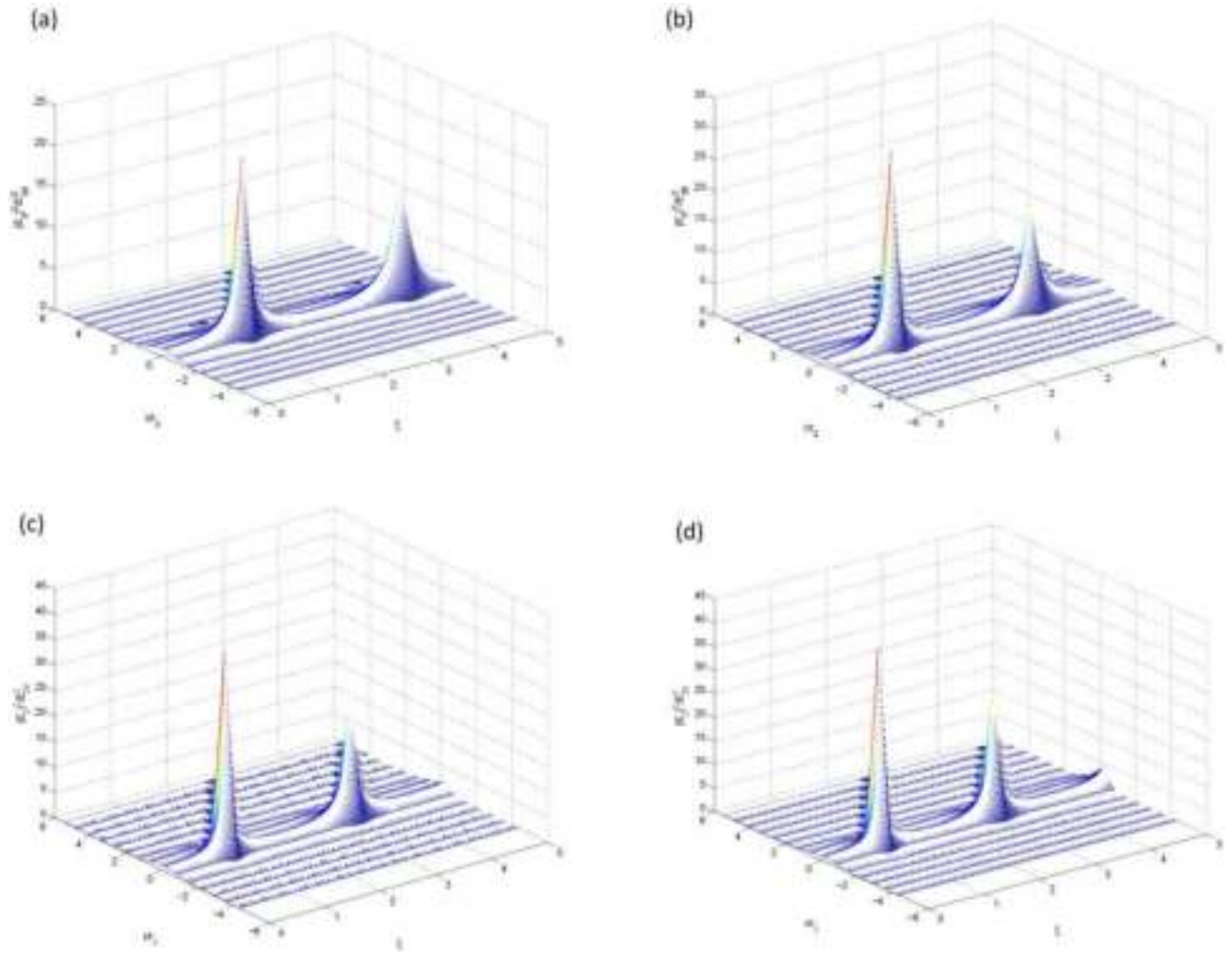

Fig. 9 Variation of normalized intensity of second beam with normalized distance of propagation ξ and radial distance $\frac{r}{r_2}$, keeping $q_1 = 4$, $q_2 = 4$, $\alpha_1 = 6$, $\frac{\omega_c}{\omega_1} = 0.1$, βE_{10}^2=1.0, βE_{20}^2=1.50 fixed and at different values of α_2, (**a**) α_2=1.2, (**b**) α_2=1.8, (**c**) α_2=2.4, (**d**) α_2= 3, respectively

Figures 6 and 7 describe the effect of plasma density on focusing/defocusing of the two laser beams. It is observed that increase in plasma density leads to increase in extent of self-focusing of both the laser beams. This is due to the fact that increase in plasma density leads to increase in number of electrons contributing to ponderomotive nonlinearity.

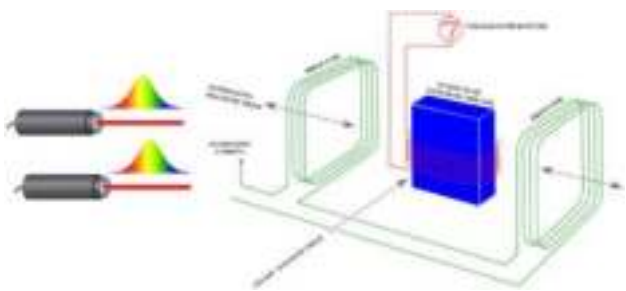

Fig. 10 Excitation of UHW

Figures 8 and 9 depict the effect of depth of plasma channel on focusing/defocusing of the two laser beams. It can be seen that more is the depth of plasma channel more is the extent of self-focusing of the two laser beams. This is due to the fact that radial plasma density gradient favors the nonlinear refraction of the two laser beams.

Figures 11 and 12 illustrate the effect of deviation of intensity distributions of the laser beams from Gaussian distribution on power of generated plasma wave. It is observed that amplitude of the generated plasma wave is maximum at the focal spots of the two laser beams. This is due to the fact that focal spots of the laser beams are the regions of very high intensity and hence act as source for plasma wave generation. It is observed form Fig. 10 that increase in the value of q_1 leads to decrease in the amplitude of plasma wave at the focal spots of first laser beam whereas there is increase in amplitude of plasma wave at the focal spots of the second laser beam. This is due to the fact that increase in the value

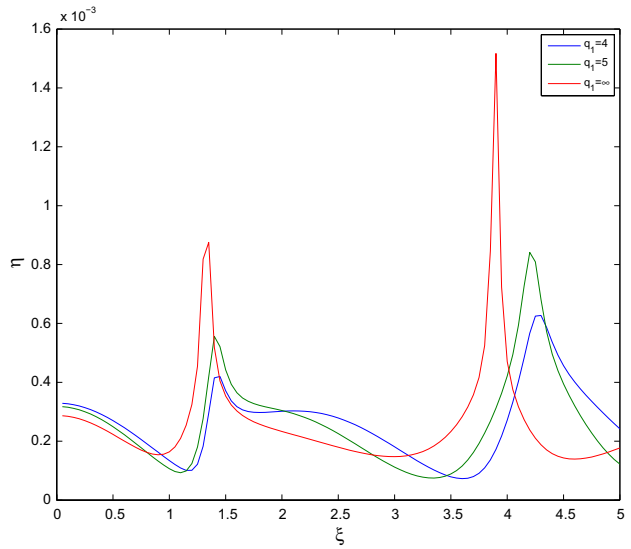

Fig. 11 Variation of normalized power η of UHW with normalized distance of propagation ξ for different values of q_1 viz., q_1=4, 5, ∞ at fixed q_2=4, α_1=6, α_2=1.2, βE_{10}^2=1.0, βE_{20}^2=1.50, $\frac{\omega_c}{\omega_1} = 0.1$, respectively

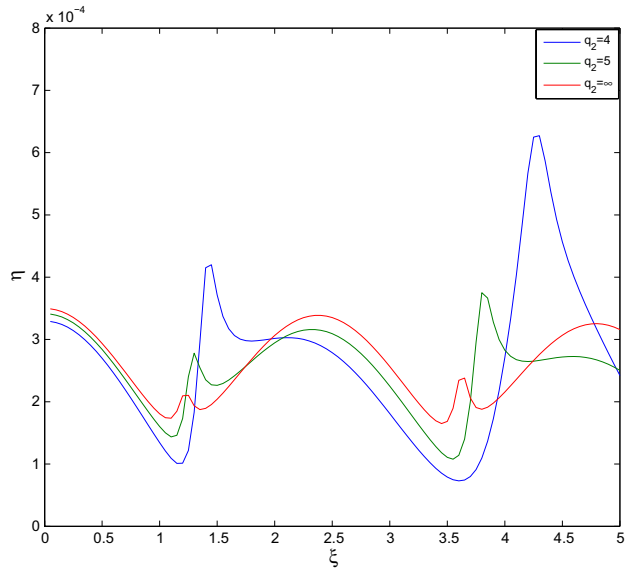

Fig. 12 Variation of normalized power η of UHW with normalized distance of propagation ξ for different values of q_2 viz., q_2=4, 5, ∞ at fixed q_1=4, α_1=6, α_2=1.2, βE_{10}^2=1.0, βE_{20}^2=1.50, $\frac{\omega_c}{\omega_1} = 0.1$, respectively

of q_1 leads to decrease in the extent of self-focusing of first laser beam and to increase in that of second laser beam. Similarly, the plots in Fig. 11 depict that increase in the value of q_2 leads to increase in the amplitude of plasma wave at the focal spots of first laser beam and decrease in amplitude of plasma wave at the focal spots of the second laser beam.

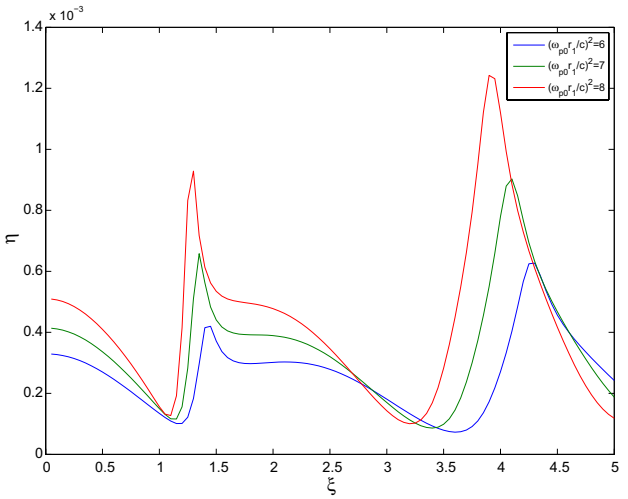

Fig. 13 Variation of normalized power η of UHW with normalized distance of propagation ξ for different values of α_1 viz., α_1=6, 7, 8 at fixed q_1=4, q_2=4, α_2=1.2, βE_{10}^2=1.0, βE_{20}^2=1.50, $\frac{\omega_c}{\omega_1} = 0.1$, respectively

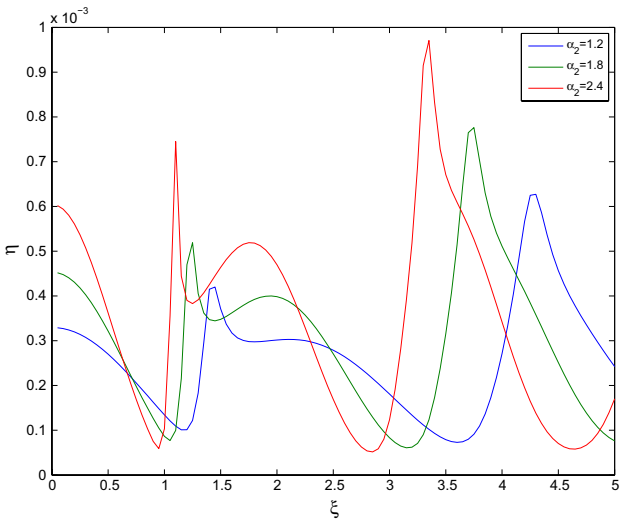

Fig. 14 Variation of normalized power η of UHW with normalized distance of propagation ξ for different values of α_2 viz., α_2=1.2, 1.8, 2.4 at fixed q_1=4, q_2=4, α_2=1.2, βE_{10}^2=1.0, βE_{20}^2=1.50, $\frac{\omega_c}{\omega_1} = 0.1$, respectively

Figures 13 and 14 illustrate the effect of plasma density and depth of plasma channel on power of excited UHW. It can be seen that both plasma density and depth of plasma channel help to enhance the power of excited UHW. This is due to the enhancement of extent of self-focusing of both the laser beams with increase in these parameters of the plasma channel.

Conclusions

In this paper, authors have investigated the cross-focusing of two intense coaxial q-Gaussian laser beams in collisionless plasma and subsequently its effect on beat wave excitation of UHW. The following important conclusions have been drawn from the present analysis:

- Greater is the extent of deviation of intensity distribution of one laser beam from Gaussian distribution, greater is the extent of its self- focusing, and lesser is the extent of self-focusing of other laser beam.
- Increase in plasma density enhances the extent of self-focusing of both the laser beams as well as the amplitude of generated plasma wave.
- Amplitude of generated plasma wave is maximum at the focal spots of the two laser beams.
- Increase in the q value of one laser beam leads to decrease in the amplitude of generated plasma wave at its focal spots while there is an increase in the amplitude of generated plasma wave at the focal spots of the other laser beam.

The results of present analysis may be of importance in various contexts of laser plasma physics. Besides its obvious relevance to inertial confinement fusion and beat wave accelerators, these results can also be helpful in other applications requiring laser beams with localized energy. The present investigation may be useful for experimentalists working in the area of laser plasma interactions.

References

1. T.H. Maiman, Stimulated optical radiation in Ruby. Nature **187**, 493 (1960)
2. T. Tajima, J.M. Dawson, Laser electron accelerator. Phys. Rev. Lett. **43**, 267 (1979)
3. S.P.D. Mangles, C.D. Murphy, Z. Najmudin, A.G.R. Thomas, J.L. Collier, A.E. Dangor, E.J. Divall, P.S. Foster, J.G. Gallacher, C.J. Hooker, D.A. Jaroszynski, A.J. Langley, W.B. Mori, P.A. Norreys, F.S. Tsung, R. Viskup, B.R. Walton, K. Krushelnick, Monoenergetic beams of relativistic electrons from intense laser-plasma interactions. Nature **431**, 535 (2004)
4. C.G.R. Geddes, Cs. Toth, J. van Tilborg, E. Esarey, C.B. Schroeder, D. Bruhwiler, C. Nieter, J. Cary, W.P. Leemans, High-quality electron beams from a laser wakefield accelerator using plasma-channel guiding, Nature **431** 538 (2004)
5. J. Faure, Y. Glinec, A. Pukhov, S. Kiselev, S. Gordienko, E. Lefebvre, J.-P. Rousseau, F. Burgy, V. Malka, A laser-plasma accelerator producing monoenergetic electron beams. Nature **431**, 541 (2004)
6. C. Deutsch, H. Furukawa, K. Mima, M. Murakami, K. Nishihara, Interaction physics of the fast ignitor concept. Phys. Rev. Lett. **77**, 2483 (1996)
7. H. Hora, New aspects for fusion energy using inertial confinement. Laser Part. Beams **25**, 37 (2007)
8. P. Amendt, D.C. Eder, S.C. Wilks, X-ray lasing by optical-field-induced ionization. Phys. Rev. Lett. **66**, 2589 (1991)
9. D.C. Eder, P. Amendt, L.B. DaSilva, R.A. London, B.J. MacGowan, D.L. Matthews, B.M. Penetrante, M.D. Rosen, S.C. Wilks, T.D. Donnelly, R.W. Falcone, G.L. Strobel, Tabletop x-ray lasers. Phys. Plasmas **1**, 1744 (1994)
10. A.Y. Faenov, A.I. Magunov, T.A. Pikuz, I.Y. Skobelev, S.V. Gasilov, S. Stagira, F. Calegari, M. Nisoli, S. Silvestri, L. Poletto, P. Villoresi, A.A. Andreev, X-ray spectroscopy observation of fast ions generation in plasma produced by short low-contrast laser pulse irradiation of solid targets. Laser Part. Beams **25**, 267 (2007)
11. A. Singh, K. Walia, Relativistic self-focusing and self-channeling of Gaussian laser beam in plasma. Appl. Phys. B **101**, 617 (2010)
12. P. Kaw, G. Schmidt, T. Wilcox, Filamentation and trapping of electromagnetic radiation in plasmas. Phys. Fluids **16**, 1522 (1973)
13. A. Ting, K. Krushelnick, H.R. Burris, A. Fisher, C. Manka, C.I. Moore, Backscattered super-continuum emission from high-intensity laserplasma interactions. Opt. Lett. **21**, 1096 (1996)
14. N. Gupta, S. Kumar, S.B. Bhardwaj, Stimulated Raman scattering of self focused elliptical q-Gaussian laser beam in plasma with axial temperture ramp: effect of ponderomotive force. J. Em. Waves Appl. **36**, 767 (2021)
15. N. Gupta, S. Kumar, S.B. Bhardwaj, Stimulated Raman scattering of Cosh-Gaussian laser beams in plasma with axial density ramp: effect of self-focusing. J. Russ. Laser Res. **43**, 667 (2022)
16. A. Singh, N. Gupta, Electron plasma wave excitation by beating of two q-Gaussian laser beams in collisionless plasma. Laser Part. Beams **34**, 230 (2016)
17. N. Gupta, S. Kumar, S.B. Bhardwaj, Excitation of electron plasma wave by self focused Cosh-Gaussian laser beams in collisionless plasma: effect of density ramp. J. Appl. Spec. **90**, 120 (2023)
18. N. Gupta, S. Choudhry, S. Kumar, S.B. Bhardwaj, Self-focusing of laser-driven ion acoustic waves in plasma with axial density ramp. J. Opt. (2022). https://doi.org/10.1007/s12596-022-00955-4
19. N. Gupta, S. Choudhry, S.B. Bhardwaj, S. Kumar, Excitation of ion acoustic waves by self-focused q-Gaussian laser beam in plasma with axial density ramp. J. Opt. (2022). https://doi.org/10.1007/s12596-022-00873-5
20. M.N. Rosenbluth, C.S. Liu, Excitation of plasma waves by two laser beams. Phys. Rev. Lett. **29**, 701 (1972)
21. I. Stenflo, P.K. Shukla, Generation of radiation by upper-hybrid waves in non-uniform plasmas. Planet. Space Sci. **40**, 473 (1992)
22. S.M. Grach, Yu.E. Men'kova, P. Stubbe, On the penetration of upper hybrid waves into a plasma depletion. Adv. Space Res. **11**, 2428 (2004)
23. M.S. Sodha, K.P. Maheshwari, R.P. Sharma, S.C. Kaushik, Resonant excitation of the upper hybrid wave by two em beams. J. Appl. Phys. **50**, 1256 (1979)
24. C. Grebogi, C.S. Liu, Parametric decay of extraordinary electromagnetic waves into two upper hybrid plasmons. J. Plasma Phys. **23**, 147 (1980)
25. G. Purohit, Upper hybrid wave excitation and particle acceleration by resonant beating of two hollow Gaussian laser beams in magnetized plasma. J. Opt. Soc. Am. B **39**, 2066 (2022)
26. P.K. Patel, M.H. Key, A.J. Mackinnon, R. Berry, M. Borghesi, D.M. Chambers, H. Chen, R. Clarke, C. Damian, R. Eagleton, R. Freeman, S. Glenzer, G. Gregori, R. Heathcote, D. Hey, N. Izumi, S. Kar, J. King, A. Nikroo, A. Niles, H.S. Park, J. Pasley, N. Patel, R. Shepherd, R.A. Snavely, D. Steinman, C. Stoeckl, M. Storm, W. Theobald, R. Town, R.V. Maren, S.C. Wilks, B. Zhang, Integrated laser-target interaction experiments on the RAL petawatt laser. Plasma Phys. Control. Fusion **47**, B833 (2005)

27. M. Nakatsutsumi, J.R. Davies, R. Kodama, J.S. Green, K.L. Lancaster, K.U. Akli, F.N. Beg, S.N. Chen, D. Clark, R.R. Freeman, C.D. Gregory, H. Habara, R. Heathcote, D.S. Hey, K. Highbarger, P. Jaanimagi, M.H. Key, K. Krushelnick, T. Ma, A. Macphee, A.J. MacKinnon, H. Nakamura, R.B. Stephens, M. Storm, M. Tampo, W. Theobald, L.V. Woerkom, R.L. Weber, M.S. Wei, N.C. Woolsey, P.A. Norreys, Space and time resolved measurements of the heating of solids to ten million kelvin by a petawatt laser. New J. Phys. **10**, 043046 (2008)
28. A. Singh, N. Gupta, Higher harmonic generation by self-focused q-Gaussian laser beam in preformed collisionless plasma channel. Laser Part. Beams **32**, 621 (2014)
29. H. Akou, Excitation of upper-hybrid plasma wake wave by a low-frequency extraordinary electromagnetic wave. Contrib. Plasma Phys. **61**, e202000149 (2021)
30. G. Purohit, P. Sharma, R.P. Sharma, Excitation of an upper hybrid wave by two intense laser beams and particle acceleration. Phys. Lett. A **374**, 866 (2010)
31. G. Purohit, P. Chauhan, R.P. Sharma, Resonant excitation of the upper hybrid wave by relativistic cross focusing of two laser beams. Laser Part. Beams **27**, 429 (2009)
32. G. Purohit, P.K. Chauha, R.P. Sharma, Excitation of an upper hybrid wave by a high power laser beam in plasma. Laser Part. Beams **26**, 61–68 (2008)
33. T. Singh, N. Saini, Nonlinear interaction of a rippled laser beam with an electrostatic upper hybrid wave in collisional plasma. Laser Part. Beams **25**, 283 (2007)
34. G. Purohit, P.K. Chauhan, R.P. Sharma, Dynamics of the excitation of an upper hybrid wave by a rippled laser beam in magnetoplasma. Phys. Plasmas **15**, 052101 (2008)

J Opt
https://doi.org/10.1007/s12596-023-01537-8

RESEARCH ARTICLE

Spatial frequency chirping of *q*-Gaussian laser beams in graded index plasma channel with ponderomotive nonlinearity

Naveen Gupta[1] · Rohit Johari[1] · A. K. Alex[1] · Suman Choudhry[1] · Sanjeev Kumar[1] · S. B. Bhardwaj[2]

Received: 15 August 2023 / Accepted: 11 November 2023

Abstract Chirping of spatial frequency of *q*-Gaussian laser beams interacting nonlinearly with plasmas with radially inhomogeneous electron density has been investigated theoretically. Due to the radial nonuniformity of the electron density, the index of refraction of the plasma channel resembles to that of a graded index fiber. Chirping or modulation of spatial frequency also known as phase anomaly occurs due to position momentum uncertainty of photons. Due to intensity gradient over the laser cross section, the transverse component of ponderomotive force becomes finite. This results in redistribution of carriers in the irradiated potion of the channel. This results in the enhancement of the radial gradient of the density profile that stimulates the laser beam to get self-focused. The reduction in transverse dimensions of the laser beam in turn leads to spread in transverse momentum of its photons. This transverse momentum spread then modifies the axial phase of the laser beam. Following Virial theory, equations of motion for radius and spatial frequency of the laser beam have been obtained. The equations so obtained have been solved numerically to envision the effect of various laser and plasma parameters on the evolution of beam envelope. Manifestation of axial phase to Berry phase has also been explained.

Keywords *q*-Gaussian · Virial theory · Self-focusing · Gouy phase

Introduction

The additional accumulation of axial phase of a converging beam in comparison with an infinite plane wave is known as modulation of spatial frequency or Gouy phase shift [1]. In his experiment, Gouy reflected a beam of light emerging from a pin hole, from both a curved and flat mirror. The focusing beam over lapped with the nonfocusing beam in a region near the focus and created a circular diffraction pattern. Gouy then looked at the circular diffraction pattern at several different locations, both before and after the focus. He observed that the central region of the diffraction pattern changed from bright to dark, indicating an axial phase jump of the focusing beam—the Gouy phase shift.

Observing Gouy phase shift is relatively easy, but explaining it is not. Since its discovery, the Gouy phase shift has remained a matter of debate. Curiosity about its origin and physical meaning is still at the vanguard of investigations. Various theories [2, 3] (ranging from classical to quantum) have been used to explain its origin. Classically the phase shift of an optical beam arises due to the contribution of an additional phase in the neighborhood of the beam focal spot arising from the second-order derivative of field amplitude with respect to transverse coordinates. However, in quantum mechanical terms the Gouy phase shift is considered to be originating as a consequence of modification of its transverse dimensions. Converging beams going through focus have finite spatial extent in the transverse plane. The uncertainty relation then induces some distribution over the transverse and consequently longitudinal wave vectors. The net effect of this distribution over wave vectors is an overall phase shift.

Since the discovery of lasers [4], the anomalous behavior of the spatial frequency also known as axial phase or wave number of the optical beams has been drawing attention of

✉ Naveen Gupta
naveens222@rediffmail.com

[1] Lovely Professional University, Phagwara, India

[2] SUS Govt College, Matak-Majri, Indri, Karnal, India

Published online: 02 December 2023

the researchers due to its relevance in a number of applications and physical problems. In wave optics, it explains the phase shift obtained by the secondary wavelets emerging from primary wave front. In the working of lasers, it decides the resonant frequencies of various transverse modes in laser cavity. Axial phase jump of optical beams also play a significant role in applied physics problems. A potential example is optical trapping of particles where it produces lateral trapping force [5] and also provides a mechanism for the tracking of trapped particles [6, 7]. Moreover, a number of schemes for higher harmonic generation [8, 9] of optical beams use the concept of longitudinal phase shift to meet the phase matching condition.

Over past few decades, a number of theoretical and experimental investigation on Gouy phase shift of laser beams have been reported by various researchers. Erden and Ozaktas [10] investigated Gouy phase shift of Gaussian laser beams propagating through first-order optical systems. Andresen et al. [11] investigated similarity between spectral phase shift and the Gouy phase shift. Gordon and Barge [12] investigated the effect of axial phase shift on coherent phase control of chemical reactions. From literature review, it has been observed that in almost all the previous investigations on Gouy phase shift, the irradiance over the cross section of the laser beam has been considered to be ideally Gaussian. However, by investigating experimentally, Patel et al. [13] have shown that although the laser operates in TEM_{00} mode, the irradiance over its cross section is not ideally Gaussian. A significant amount of the laser energy was found to be present in the off-axial region of the beam cross section. The difference in the behavior of irradiance over the laser beam wave front from ideal Gaussian is due to cavity imperfections that may be inherent or accidental in nature. By fitting into the experimental data, it was shown that [14] the actual irradiance over the beam's cross section can be modeled by a set of distribution functions known as q-Gaussian distribution given by Tsalli [15]. Till date, no experimental or theoretical investigation on Gouy phase shift of q-Gaussian laser beams in nonlinear media has been reported by any researcher. Thus, this paper aims to investigate for the first time Gouy phase shift of self-focused q-Gaussian laser beams in preformed plasma channels.

Index of refraction of plasma channel under ponderomotive nonlinearity

Consider the interaction of an intense laser beam with a preformed plasma channel. The axis of the plasma channel is along the z axis, and the laser beam axis is coinciding with the channel axis. The electron density of the plasma channel varies parabolically with radial coordinate as [16]

$$n(r) = n_0 + \Delta n \frac{r^2}{r_{\mathrm{ch}}^2} \tag{1}$$

where n_0 is the axial electron density of the channel, Δn is the difference in the electron density at the edge of the channel and that at the axis and r_{ch} is the radius of the plasma channel. Due to the transverse intensity gradient over the laser beam, the free carriers in plasma experience a radial force

$$\boldsymbol{F}_p = \frac{e^2}{4m\omega_0^2}\nabla(AA^*)$$

known as ponderomotive force. Due to this ponderomotive force, the plasma electrons migrate from high intensity region of the illuminated portion of the channel toward its edges. This migration of electrons, thus, increases the depth of the channel. The modified electron density is given by [17]

$$n_e = n(r)e^{-\beta AA^*} \tag{2}$$

where $\beta = \frac{e^2}{(8K_0T_0m\omega_0^2)}$ is the constant associated with the strength of ponderomotive force. Hence, in the presence of laser beam the dielectric function

$$\epsilon = 1 - \frac{4\pi e^2}{m\omega_0^2}n_e$$

of the channel gets altered as

$$\epsilon = 1 - \left(\frac{\omega_{p0}^2}{\omega_0^2} + \frac{\omega_{p\mathrm{ch}}^2}{\omega_0^2 r_{\mathrm{ch}}^2}r^2\right)e^{-\beta AA^*} \tag{3}$$

where

$$\omega_{p0}^2 = \frac{4\pi e^2}{m}n_0$$

and

$$\omega_{p\mathrm{ch}}^2 = \frac{4\pi e^2}{m}\Delta n$$

Splitting the dielectric function of the plasma channel into linear and nonlinear parts as , we can write

$$\epsilon = \epsilon_0 + \phi(AA^*)$$

$$\epsilon_0 = 1 - \frac{\omega_{p0}^2}{\omega_0^2}e^{-\beta AA^*|_{r=0}} \tag{4}$$

and

$$\phi(AA^*) = \frac{\omega_{p0}^2}{\omega_0^2} e^{-\beta AA^*|_{r=0}} - \left(\frac{\omega_{p0}^2}{\omega_0^2} + \frac{\omega_{pch}^2}{\omega_0^2 r_{ch}^2} r^2 \right) e^{-\beta AA^*} \quad (5)$$

Equation (5) gives the optical nonlinearity of plasma channel due to the ponderomotive force. Thus, it is also known as ponderomotive dielectric function of the plasma channel.

Beam width evolution

The starting point for the investigation of evolution of an optical beam through a nonlinear medium is the wave equation

$$i\frac{\partial A}{\partial z} = \frac{1}{2k_0}\nabla_\perp^2 A + \frac{k_0}{2\beta_0}\phi(AA^*)A \quad (6)$$

As the potential function ϕ is a function of filed amplitude A, Eq. (6) is nonlinear and nature, and thus, it does not follow superposition principle. Hence, conventional methods of solving partial differential equations are not applicable to Eq. (6). Thus, in order to have physical insight into the propagation dynamics of the laser beam, semi-analytical methods such as variational method, method of moments and source-dependent expansion method are used for this equation.

In the present study, we have used Virial theory [18] to obtain an approximate solution of Eq. (6). According to Virial theory, evolution of a laser beam through a nonlinear medium is a variational problem characterized by the Hamiltonian

$$H = \int \mathcal{H} r dr$$

with

$$\mathcal{H} = |\nabla_\perp A|^2 - \frac{1}{2\epsilon_0} \int \phi(AA^*) d(AA^*)$$

The basic idea of Virial theory is then the selection of a trial function containing the physical parameters of interest. This trial function characterizes the actual solution of the problem as close as possible. The Virial theory then recasts the original problem of solving a PDE into that of solving a set of ODEs governing the evolution of these parameters. In the present analysis, we assume $A(r; z)$ takes the form of the function given by [19, 20]

$$A(r,z) = \frac{E_{00}}{f}\left(1 + \frac{r^2}{q r_0^2 f^2}\right)^{-\frac{q}{2}} e^{i\theta} \quad (7)$$

where the function $f(z)$ is one of the key parameters of the present investigation. Its physical significance is twofold: (1) Upon multiplication with equilibrium beam radius, it gives the instantaneous beam waist size, i.e., radius of the laser beam at a given location inside the plasma channel, and (2) on dividing the laser amplitude, it gives the measure of axial intensity of the laser beam. Hence, in the standard literature the function $f(z)$ is referred to as dimensionless beam width parameter. The phenomenological constant q is related to the imperfections of the laser system, and its value has to be found by fitting into the experimental data. It describes how much the irradiance over the beam cross section is deviating from ideal Gaussian profile. Hence, the parameter q is termed as deviation parameter. The function $\theta(z)$ is known as longitudinal phase of the laser beam which is also known as Gouy phase. The Virial theory defines the effective beam width of an optical beam in root mean square (r.m.s) sense as

$$\langle \sigma^2 \rangle = \frac{1}{I_0} \int A r^2 A^* d^2 r \quad (8)$$

where

$$I_0 = \int AA^* d^2 r$$

and

$$d^2 r = r dr d\theta$$

Differentiating Eq. (8) twice with respect to z and making use of Eq. (6), it can be shown that the effective beam width of the beam envelope evolves according to the equation

$$\frac{d^2 f}{d\xi^2} = \frac{\left(1-\frac{1}{q}\right)\left(1-\frac{2}{q}\right)}{\left(1+\frac{1}{q}\right)} \frac{1}{f^3} - \left(1-\frac{1}{q}\right)\left(1-\frac{2}{q}\right) J - \frac{1}{f}\left(\frac{df}{d\xi}\right)^2 \quad (9)$$

where

$$J = \frac{\beta E_{00}^2}{f^3}\left(\frac{\omega_{p0}^2 r^2}{c^2} I_1 + f^2 \frac{\omega_{pch}^2 r_0^2}{c^2} \frac{r_0^2}{r_{ch}^2} I_2 \right) + \frac{\omega_{p0}^2 r_0^2}{c^2} \frac{r_0^2}{r_{ch}^2} f^2 I_3$$

$$I_1 = \int_0^\infty t\left(1+\frac{t}{q}\right)^{-2q-1} e^{-\frac{\beta E_{00}^2}{f^2}\left(1+\frac{t}{q}\right)^{-q}} dt$$

$$I_2 = \int_0^\infty t^2\left(1+\frac{t}{q}\right)^{-2q-1} e^{-\frac{\beta E_{00}^2}{f^2}\left(1+\frac{t}{q}\right)^{-q}} dt$$

$$I_3 = \int_0^\infty t\left(1+\frac{t}{q}\right)^{-q} e^{-\frac{\beta E_{00}^2}{f^2}\left(1+\frac{t}{q}\right)^{-q}} dt$$

$$t = \frac{r^2}{r_0^2 f^2}$$

$$\xi = \frac{z}{k_0 r_0^2}$$

Thus, from Eq. (9) it can be seen that the Virial theory provides a rule, expressed mathematically as an ordinary differential equation, that describes how the beam width of the laser beam evolves during its propagation through a nonlinear medium, in the present case through a plasma channel with graded index of refraction. Although Eq. (9) also cannot be integrated to get an exact analytical solution, its approximate solution can be easily obtained with the help of simple numerical techniques. Before actually attempting to solve Eq. (9), it is worth identifying the physical significance of the various terms on its right-hand side (RHS). The first term on the RHS of Eq. (9) has its origin in the light's fundamental wave nature of diffraction. Hence, the first term governs the diffraction broadening of the laser beam during its propagation. The second term on RHS of Eq. (9) originates under the combined effects of radial inhomogeneity of plasma channel and the ponderomotive nonlinearity produced by the nonuniform irradiance of the laser beam. The ultimate competition between these two terms dictates whether the beam will converge or diverge.

Spatial frequency chirp

Using Eq. (7) in (6) and equating imaginary parts, we get

$$-2k_0 \frac{d\theta_p}{dz} = \frac{r^2}{r_0^2 f^4}\left(1+\frac{2}{q}\right)\left(1+\frac{r^2}{qr_0^2 f^2}\right)^{-2} - \frac{2}{r_0^2 f^2}\left(1+\frac{r^2}{qr_0^2 f^2}\right)^{-1} + \frac{\omega_0^2}{c^2}\phi(AA^*)$$

Taking zeroth-order spatial intensity moment of this equation, we get

$$\frac{d\theta_p}{dz} = \frac{1}{f^2}\left(1-\frac{1}{q}\right) - \frac{1}{2f^2}\frac{\left(1-\frac{1}{q}\right)\left(1-\frac{2}{q}\right)}{\left(1+\frac{1}{q}\right)} - \frac{1}{2}\left(1-\frac{1}{q}\right)I_4 \tag{10}$$

where

$$I_4 = \int_0^\infty \left(1+\frac{1}{q}\right)\left\{\frac{\omega_{p0}^2 r_0^2}{c^2} e^{-\frac{\beta E_{00}^2}{f^2}} - \left[\frac{\omega_{p0}^2 r_0^2}{c^2} + \frac{\omega_{pch}^2 r_0^2}{c^2}\frac{r_0^2}{r_{ch}^2} f^2 t\right] e^{-\frac{\beta E_{00}^2}{f^2}\left(1+\frac{t}{q}\right)^{-q}}\right\} dt$$

Equation (10) is the governing equation for the evolution of spatial frequency of the laser beam along the length of the plasma channel.

Results and discussion

In solving eqs. (9) and (10), it has been assumed that while entering into the channel the laser beam is collimated and is having plane wave front. Mathematically these conditions are represented as $f=1$, $\frac{df}{d\xi} = \theta = 0$ at $\xi=0$. In the present study, eqs. (9) and (10) have been solved for a typical set of parameters: $\omega_0 = 1.78 \times 10^{14}\,\text{rad sec}^{-1}$, $r_0 = 15\,\mu\text{m}$, $n_0 = \left(1.5\times10^{18}, 2\times10^{18}, 2.5\times10^{18}\right)\text{cm}^{-3}$, $\Delta n = (0, 10, 15)\,\text{cm}^{-3}$, $E_{00} = (3\times10^9, 6\times10^9, 9\times10^9)\,\text{Vm}^{-1}$ and $q = (3, 4, \infty)$. The corresponding evolutions of beam with and axial phase of the beam are shown in the form of graphs in Figs. 1, 2, 3, 4, 5, 6, 7, 8, 9.

It can be seen that the envelope of the laser beam evolves in a sausage-like manner through the plasma channel, i.e., its beam width undergo harmonic variations in such a way that the laser beam is passing through a linear array of periodically spaced convex lenses. These harmonic variations of the beam width are due to periodic focusing/defocusing of the laser beam. As the index of refraction of the plasma channel increases with intensity of the laser beam (Eq. 5), the most intense central part of the bell-shaped beam sees a higher index of refraction than its wings. This effectively slows down the phase of the central part of the beam leading to a curved, concave wave front around beam axis, which causes focusing of the beam as it is propagating through a convex lens. As this now-focusing beam propagates, its intensity further increases, and the central part of the beam is retarded even more by the changing refractive index. This process continues till the ponderomotive nonlinearity gets saturated, i.e., almost all the illuminated region of the plasma channel gets evacuated from the electrons. The beam then propagates as if it is propagating through vacuum, i.e., it again starts diverging. Now, as the beam width of the laser beam jumps back toward its original value, the ponderomotive force again comes into picture and starts opposing diffraction. Hence, during the journey of the laser beam through the plasma channel there starts a competition between the two phenomena of diffraction and nonlinear refraction due to radial inhomogeneity of the plasma channel and ponderomotive nonlinearity. The ultimate behavior of the

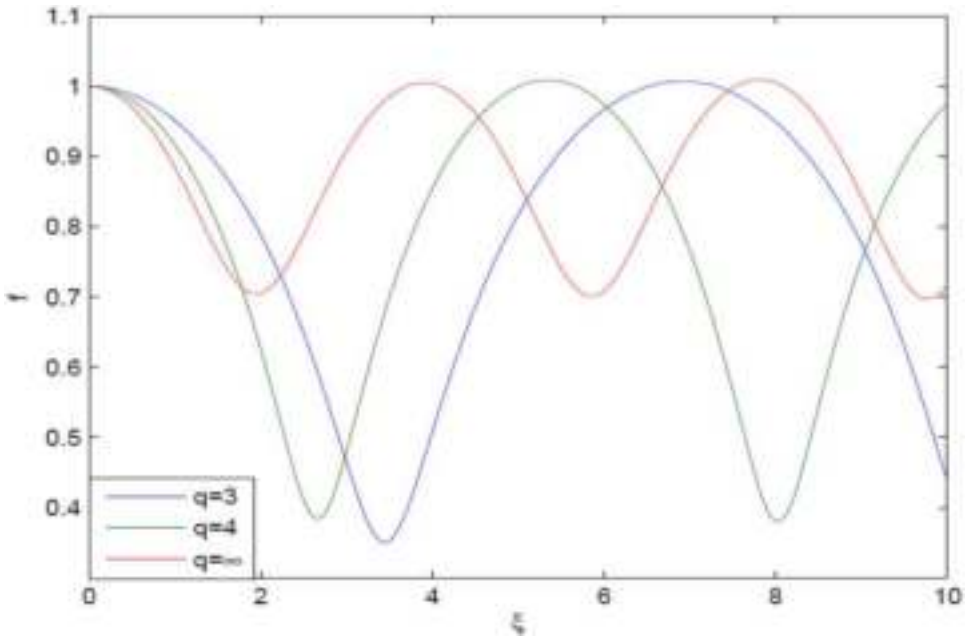

Fig. 1 Effect of deviation parameter "q" on self-focusing of laser beam

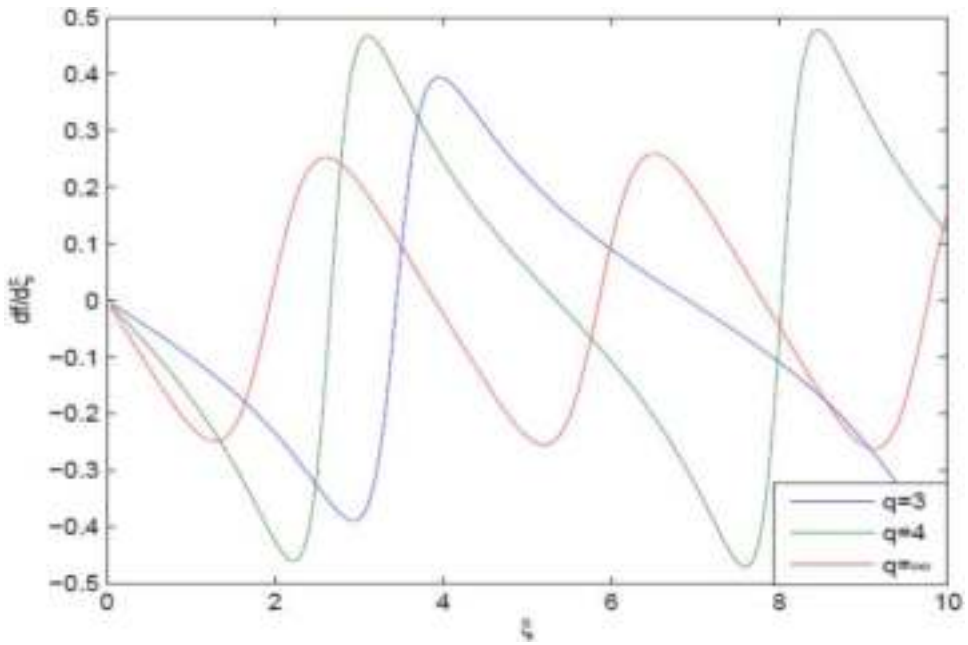

Fig. 2 Effect of "q" on laser beam wave front curvature during its propagation

beam is decided by the winning phenomenon. As the two phenomena win the competition periodically, the beam width of the laser beam evolves in an oscillatory manner.

Reduction in focusing of the laser beams with their irradiance closer to Gaussian profile is also shown in Fig. 1. This is due to localization of most of the beam power in a narrow region around the axis of the laser beam for beams with larger value of deviation parameter q. Hence, such beams get a very little contribution from the rays away from the beam axis in order to generate optical nonlinearity in the medium. As the self-focusing effect is a consequence of nonlinear refraction, laser beams with their intensity profiles closer to Gaussian profile show relatively lesser self-focusing.

The plots in Fig. 1 also indicate that instead of their reduced focusing, the laser beams with higher value of deviation parameter q possess faster focusing character. This is due to the faster focusing character of axial rays. Being away from the axis, off-axial rays take more duration to get self-focused. As there are more number of off-axial rays in laser beams with lower q values, by increasing the value of deviation parameter q, the focusing of the laser beam becomes faster. This result of faster focusing of laser

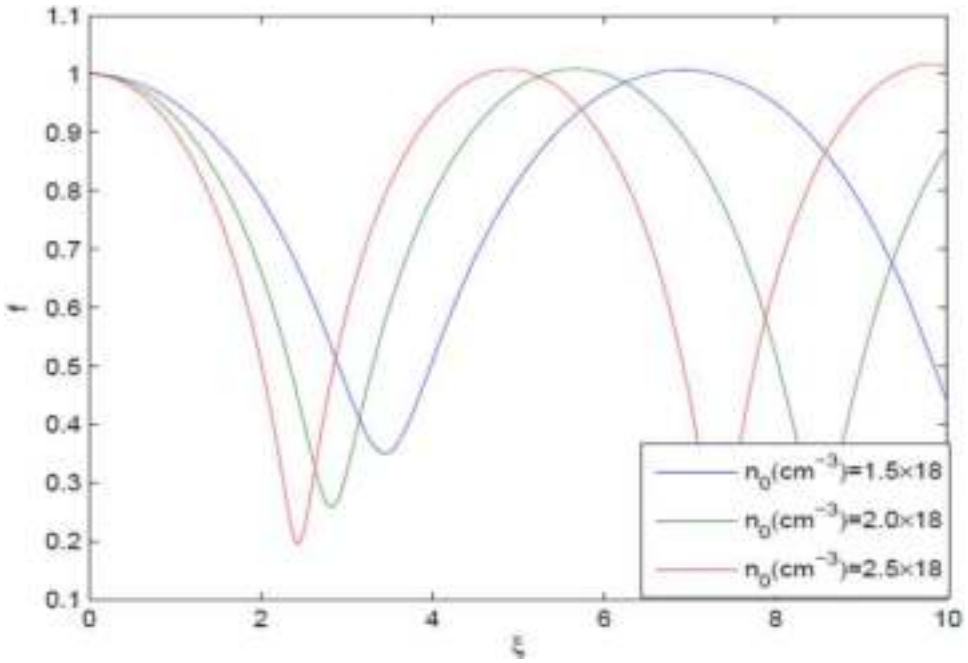

Fig. 3 Effect of plasma density on self-focusing of laser beam

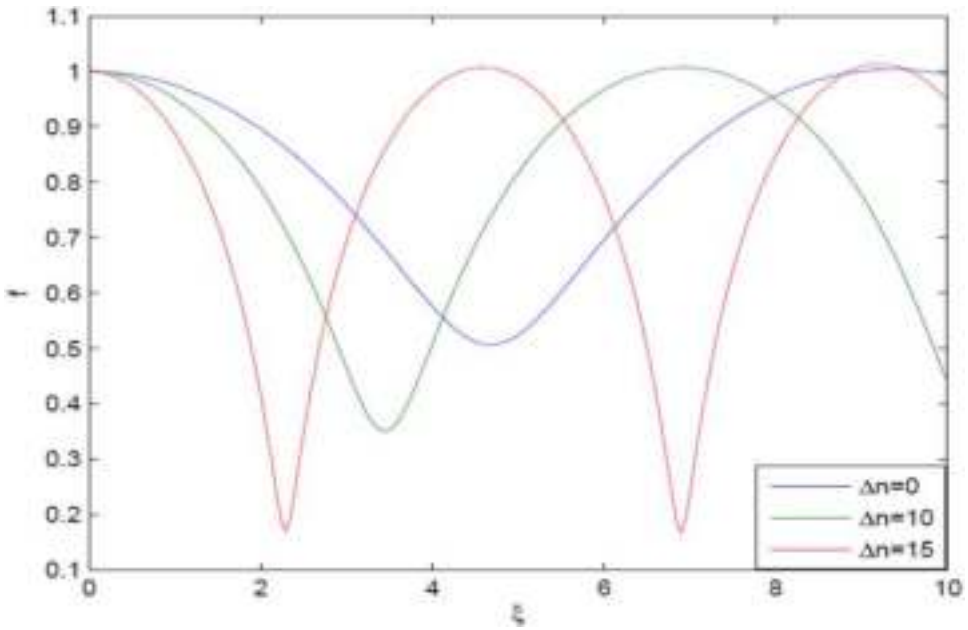

Fig. 4 Effect of channel depth on self-focusing of laser beam

beams with lower q value is contrary to that reported by Sharma and Kourakis where it was shown that laser beams with lower value of q possess slower focusing. This difference between the two results is mainly due to the reason that in their analysis Sharma and Kourakis have expanded the dielectric function of the plasma only up to r^4. However, by analyzing the q-Gaussian distribution it can be seen that change in the value of deviation parameter q is having hardly any effect on the irradiance in the regions closer to the axis. The change in the value of deviation parameter q affects the irradiance only in the regions away from the beam axis that has been eliminated in the analysis of Sharma and Kourakis. However, in our study the dielectric function of the plasma has been considered as a whole. Thus, it can be concluded that by optimizing the value of deviation parameter q, one can control focusing as well as the location of the focal spot of a laser beam.

The graphical curves in Fig. 2 depict the variations of beam wave front curvature. The periodic changes in the sign of wave front curvature indicate that during the journey of

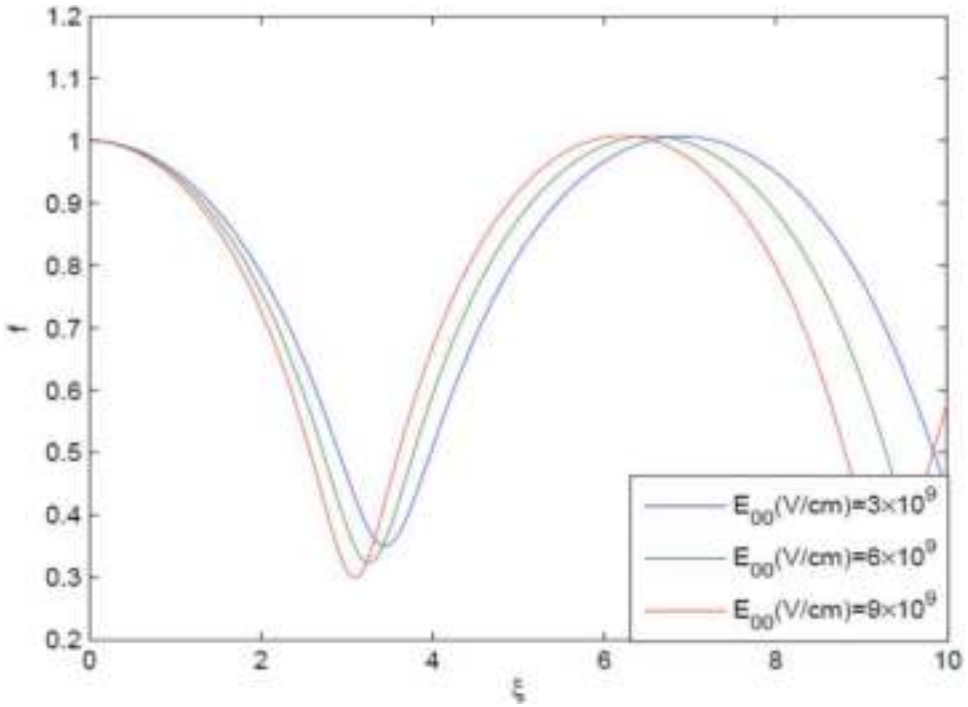

Fig. 5 Effect of laser field amplitude on its self-focusing

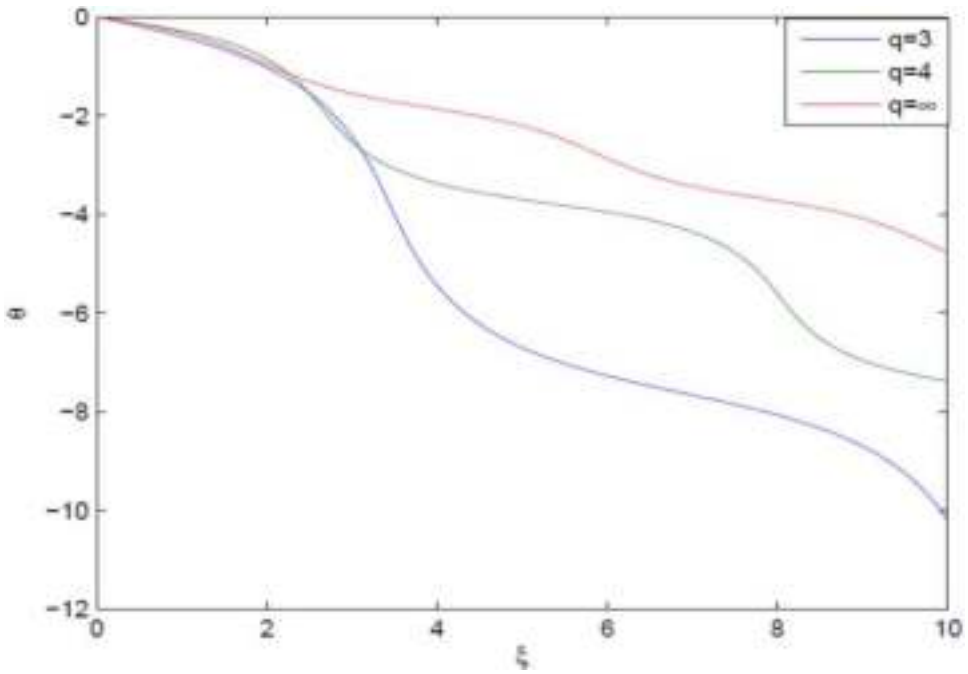

Fig. 6 Effect of deviation parameter q on axial phase shift of laser beam

the laser beam through the plasma channel, its wave front periodically changes form plane wave front to convex and then again from convex to plane and then from plane to concave. All these processes keep on repeating in an oscillatory fashion.

The curves in Fig. 3 are showing the effect of electron density on focusing of the laser beam. It can be seen that an increase in the plasma density enhances the focusing of the laser beam. This is due to the fact that the increase in the electron density makes the ponderomotive force stronger. As the focusing of the laser beam is occurring as a consequence of ponderomotive force acting on the electrons, the increase in the electron density enhances the self-focusing of the laser beam.

The graphical curves in Fig. 4 show the effect of channel depth on focusing of the laser beam. It can be seen that

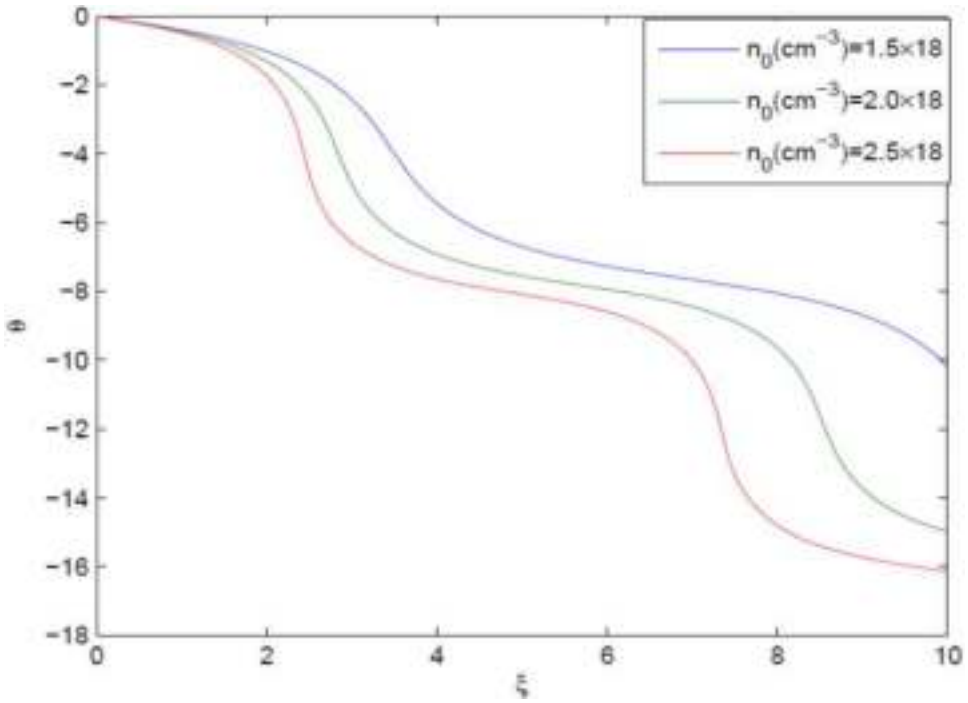

Fig. 7 Effect of plasma density on axial phase shift of laser beam

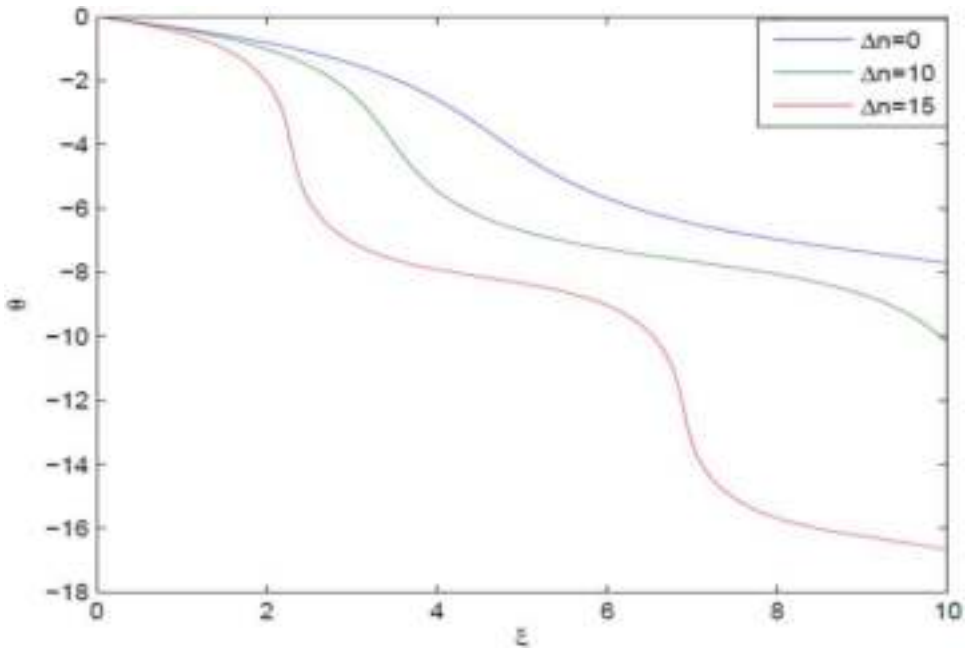

Fig. 8 Effect of channel depth on axial phase shift of laser beam

for a given set of laser and plasma parameters minimum focusing is occurring in the absence of radial inhomogeneity, i.e., for $\Delta n = 0$, and with the increasing channel depth, focusing gets enhanced and occurs earlier. This is due to the reason that the channel depth enhances the radial inhomogeneity of the index of refraction. As parabolic plasma channels are analogous to graded index fibers based on total internal reflection, the increase in the channel depth helps in improving the focusing of the laser beam. Thus, it may be concluded from the curves in Figs. 3, 4 that for a given laser beam the focusing can be controlled by optimizing the electron density or radial inhomogeneity of the channel. In applications like laser-driven plasma-based accelerators where tight focusing of the laser beams as well as low electron density of the plasma are the major prerequisites, the plasma channels with parabolic radial density profile may offer themselves as an ideal candidate.

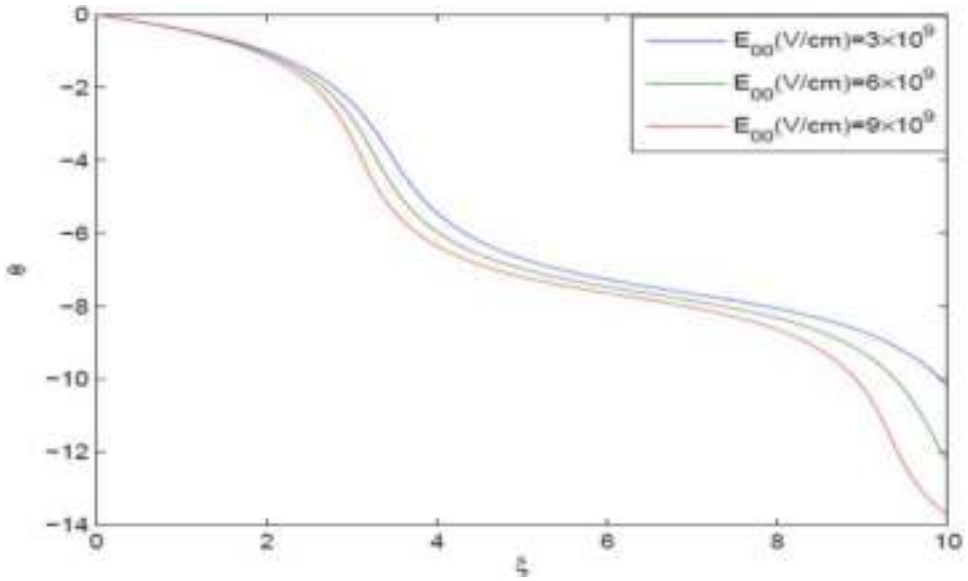

Fig. 9 Effect of laser field amplitude on its axial phase shift

The effect of initial intensity of the laser beam on its self-focusing is depicted in Fig. 5. It can be seen that laser beams with higher focusing possess higher focusing character. This is due to that fact that like the electron density, the intensity of the laser beam also makes the ponderomotive force stronger. Thus, initial laser intensity also enhances its focusing.

Figures 6, 7, 8, 9 illustrate the evolution of axial phase of the laser beam with distance along the plasma channel. It can be seen that the axial phase of the laser beam decreases monotonically with distance, showing steplike behavior. This is due to the periodical self-focusing/defocusing of the laser beam. As the laser beam undergo self-focusing, its intensity increases, and hence, the laser phase fronts start experiencing larger refractive indices. This results in decreased phase velocity of the phase fronts that leads to decreased spacing between the phase fronts. This fact can be explained in another way. The axial phase shift of the laser beam occurs due to the transverse momentum gained by the photons due to the reduction in the volume of space available for their propagation. As the transverse spatial confinement of the laser beam occurs due to self-focusing, the photons gain additional transverse momentum $(k_x;k_y)$ due to position momentum uncertainty $\Delta k_x \Delta x =$ constant and $\Delta k_y \Delta y =$ constant. As the overall momentum of the laser beam is conserved, the increase in the transverse momentum reduces the longitudinal momentum. Thus, during the propagation of laser beam its longitudinal momentum reduces as the beam keep on focusing. This results in monotonic decrease in its axial phase.

Steplike behavior of the axial phase is also shown in Figs. 6, 7, 8, 9. This indicates that while moving from one focal position to another the axial phase of the laser beam remains almost constant at the position of its focus, the axial phase takes an abrupt jump. This behavior of the axial phase can be explained through its manifestation to Berry's phase. Berry phase is an additional geometrical (topological) phase that a system acquires after a cyclic adiabatic evolution in parameter space. In case of axial phase of an optical beam, the parameter that is cycled is the wave front curvature of the laser beam. As the laser beam gets self-focused, the radius of curvature of its wave fronts decreases as the wave fronts become more and more convex due to self-focusing. Hence, the axial phase of the laser beam takes a jump the focus. As the laser beam gets maximum possible intensity, the nonlinear terms in beam width equation (Eq. 9) vanishes. Hence, the laser beam propagates as if it is propagating through vacuum, i.e., it starts diverging, and hence, the wave front curvature changes its sign, i.e., it becomes convex from concave. Now till the wave fronts again become plane when the nonlinearity of the medium comes into picture, the axial phase of the beam remains almost constant. Hence, as the wave front curvature changes periodically, the axial phase of the laser beam shows steplike behavior with abrupt jumps at the focal positions.

Figure 6 shows that with the increase in the value of deviation parameter q there is a reduction in the rate of change of axial phase of the laser beam with distance. This is due to the one to one correspondence between the extent of focusing of the laser beam and the rate of decrease in its axial phase. As with increasing q, the focusing of the laser beam gets reduced; hence, the rate of change of axial phase also reduces with an increase in the deviation parameter q.

The curves in Figs. 7, 8, 9 indicate that with the increase in either plasma density, channel depth or laser intensity, the rate of decrease in the axial phase increases. This is due to enhancement of focusing of the laser beam with an increase in these parameters.

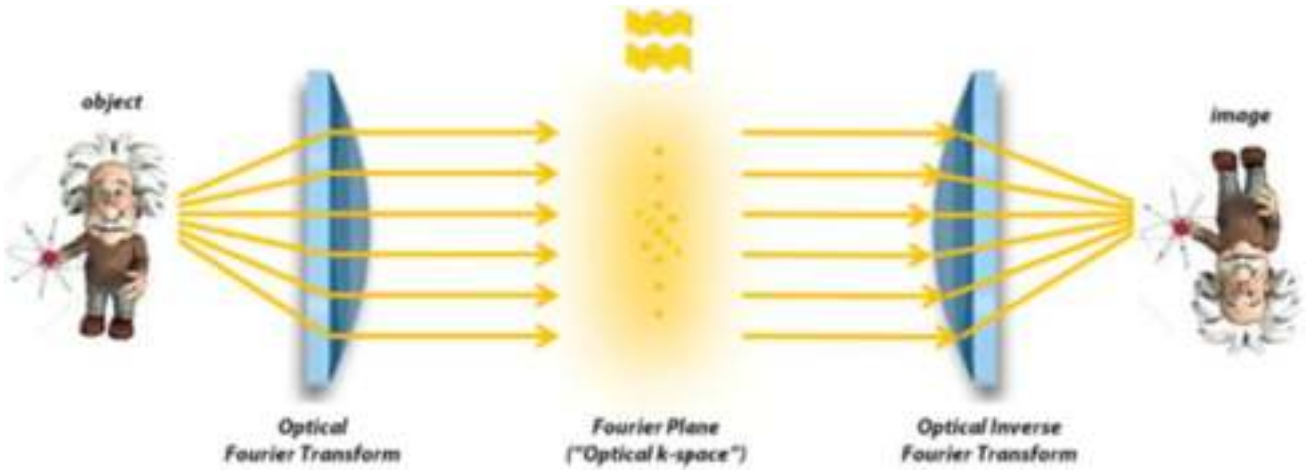

Fig. 10 Analogy for physical significance of *k*-space

Physical significance of *k*-space

To grasp the physical significance of *k*-space, imagine observing a caricature of Einstein through a pair of lenses. The light waves emanating from the artwork enter the initial lens and undergo refraction (bending) based on their spatial frequencies. Waves with lower frequencies experience minimal refraction, passing directly through the central region of the lens. On the other hand, waves with higher frequencies are refracted more noticeably at the outer edges. The outcome produced by the first lens is a sequence of indistinct wave fronts, where spatial frequencies increase toward the outer boundaries and decrease toward the center. These waves interact in ways that either reinforce or cancel each other out. In this manner, the initial lens has effectively executed an "optical" Fourier transformation of the incoming light rays.

Positioning your head at the midpoint between the two lenses, known as the Fourier plane, and gazing back toward the caricature, your sight would encounter only an indefinite, hazy radiance symbolizing the mean light intensity that enters the initial lens. The light waves lack focus and would not coalesce into an image on your retina. This state is what can be referred to as being situated in "optical" *k*-space.

The second lens undoes this process by reassembling the previously dispersed waves in optical k-space, restoring them to their original relationships. Consequently, the second lens functions as an inverse Fourier transformation, facilitating the formation of a well-defined image. Why is it that an image of the k-space "galaxy" is not observable when you position your eye at the Fourier plane? One factor is that the human eye perceives only magnitude, whereas a lens combines both phase and magnitude data. To effectively perceive the anticipated optical k-space pattern, a more sophisticated apparatus known as a "4-f" setup is required. This 4-f configuration comprises a highly focused monochromatic laser light source, a filter or screen positioned at the Fourier plane and detection through a sensitive charge-coupled device. Such 4-f experiments are commonly used in advanced physics or engineering courses focused on optics and can be procured from suppliers specializing in scientific educational equipment.

Even if the cartoon analogy did not provide clarity, the key takeaway remains unchanged: k-space serves as a deconstructed representation of the inherent spatial frequencies within the original object. In the case of light waves, the transformation from an object to optical k-space is swift and direct, achieved through the use of a lens. However, for MRI, the procedure is more intricate and time-intensive. It involves collecting signals subsequent to stimulating the object with multiple RF pulses and variable gradients. Nonetheless, the outcome is consistent: the creation of an assortment of k-space data systematically arranged based on spatial frequency. Whether in the realms of optics or MRI, a subsequent reversal of this process unfolds, culminating in the reassembly of dispersed waves to form a coherent final image (Fig. 10).

Conclusion

In the present work, the authors have investigated axial phase shift also known as Gouy phase shift, of q-Gaussian laser beams propagating through collisionless plasma channels. It has been concluded that spatial confinement of the laser beam resulting from its self-focusing due to the ponderomotive nonlinearity of the plasma channel leads to spread in the transverse momentum of the laser beam. This in turn leads to jump in the axial phase of the laser beam at its focal spots. The results of the present investigation may serve as a

guide for the researchers working in the area of laser plasma interactions and nonlinear optics.

References

1. L.G. Gouy, Sur une propriete nouvelle des ondes lumineuses. C. R. Acad. Sci. ParisSer. **110**, 1251 (1890)
2. R.W. Boyd, Intuitive explanation of the phase anomaly of focused light beams. J. Opt. Soc. Am. **70**, 877 (1980)
3. S. Feng, H.G. Winful, Physical origin of the Gouy phase shift. Opt. Lett. **26**, 485 (2001)
4. T.H. Maiman, Stimulated optical radiation in ruby. Nature **187**, 993 (1960)
5. F. Gittes, C.F. Schmidt, Interference model for back-focal-plane displacementdetection in optical tweezers. Opt. Lett. **23**, 7 (1998)
6. S.B. Pal, A. Haldar, R.K. Gupta, N. Ghosh, B. Roy, A. Banerjee, Probing the dynamics of an optically trapped particle by phase sensitive back focal plane interferometry. Opt. Express **20**, 8317 (2012)
7. L. Friedrich, A. Rohrbach, Phase anomalies in Bessel-Gauss beams. Opt. Lett. **37**, 2019 (2012)
8. B.E. Saleh, M.C. Teich, S. Carrasco, J.T. Fourkas, Second-and third-harmonic generation with vector Gaussian beams. J. Opt. Soc. Am. B **23**, 2134 (2006)
9. Y.Q. Qin, C. Zhang, Y.Y. Zhu, Perfect quasi-phase matching for the third-harmonic generation using focused Gaussian beams. Opt. Lett. **33**, 720 (2008)
10. M.F. Erden, H.M. Ozaktas, Accumulated Gouy phase shift in Gaussian beampropagation through first-order optical systems. J. Opt. Soc. Am. A **14**, 2190 (1997)
11. C. Finot, D. Oron, E.R. Andresen, H. Rigneault, Spectral analog of the Gouy phase shift. Phys. Rev. Lett. **110**, 143902 (2013)
12. R.J. Gordon, V.J. Barge, Effect of the Gouy phase on the coherent phase control of chemical reactions. J. Chem. Phys. **127**, 204302 (2007)
13. M.H. Key, A.J. Mackinnon, R. Berry, M. Borghesi, D.M. Chambers, H. Chen, C. Damian, R. Eagleton, R. Freeman, S. Glenzer, G. Gregori, R. Heathcote, D. Hey, N. Izumi, A. Nikroo, A. Niles, H.S. Park, J. Pasley, N. Patel, R. Shepherd, R.A. Snavely, D. Steinman, C. Stoeckl, M. Storm, W. Theobald, R. Town, R.V. Maren, S.C. Wilks, P.K. Patel, B. Zhang, Integrated laser–target interaction experiments on the RAL petawatt laser. Plasma Phys. Cont. Fusion **47**, B833 (2005)
14. J.R. Davies, R. Kodama, J.S. Green, K.L. Lancaster, K.U. Akli, F.N. Beg, S.N. Chen, D. Clark, R.R. Free-man, C.D. Gregory, H. Habara, R. Heathcote, D.S. Hey, K. Highbarger, Jaan-imagi, P. Key, M.H. Krushelnick, K. Ma, T. MacPhee, A. MacKinnon, A.J. Nakamura, H. Stephens, R.B. Storm, M.M. Tampo Theobald, W. Woerkom, L.V. Weber, R.L. Wei, M.S. Woolsey, N.C. Nakatsutsumi, P.A. Norreys, Space and time resolved measurements of the heating of solids to ten million kelvin by a petawatt laser. New J. Phys. **10**, 043046 (2008)
15. C.J. Tsallis, Possible generalization of Boltzmann-Gibbs statistics. Stat. Phys. **52**, 479 (1988)
16. N. Singh, N. Gupta, A. Singh, Second harmonic generation of q-Gaussian laser beam in preformed collisional plasma channel with nonlinear absorption. Phys. Plasmas **22**, 113106 (2015)
17. A. Kumar, Ponderomotive self-focusing of surface plasma wave. Plasmonics **8**, 1135 (2013)
18. B. Guo, On global solution for a class of systems of multi-dimensional generalized Zakharov type equation. Acta Math. Appl. Sin. **10**, 419 (1994)
19. A. Sharma, I. Kourakis, Spatial evolution of a q-Gaussian laser beam in relativisticplasma. Laser Part. Beams **28**, 479 (2010)
20. N. Gupta, Second harmonic generation of q-Gaussian laser beam in plasma channel created by ignitor heater technique. Laser Part. Beams **37**, 184 (2019)

J Opt
https://doi.org/10.1007/s12596-023-01541-y

RESEARCH ARTICLE

Third harmonic generation of self-focused q-Gaussian laser beams in nonlinear media: effect of cubic quintic nonlinearity

Naveen Gupta[1] · Sanjeev Kumar[1,2] · S. B. Bhardwaj[3] · Suman Choudhry[1,2] · A. K. Alex[1] · Rohit Johari[1] · Amit Bindra[1]

Received: 9 August 2023 / Accepted: 13 November 2023

Abstract This paper presents theoretical investigation on third harmonic generation (THG) in nonlinear media. Variational method has been adopted to find the semi analytical solution of the wave equation governing the evolution of slowly varying beam envelop in nonlinear medium. Emphasis is put on investigating the evolution of beam width of the laser beam with distance through the medium. When laser beam with frequency ω_0 propagates through a nonlinear medium dominated by $\chi^{(3)}$ nonlinearity, oscillations of the electrons of the medium contain a frequency component $\omega_3 = 3\omega_0$ and thus produce third harmonic of the pump beam. An equation governing the conversion efficiency of third harmonic has been derived. Deviation of intensity profile of the incident laser beam from ideal Gaussian profile has also been incorporated through q-Gaussian profile.

Keywords Self focusing · Cubic quintic · q-Gaussian · Harmonic generation

Introduction

The quest for short wavelength coherent radiation sources for medical diagnostics and treatment, homeland security, plasma diagnostics, etc. has a long history. For past few decades only two main approaches, namely free electron lasers and synchrotron had been considered for this purpose. However, involvement of large infrastructure, accelerators, beam lines and massive gantries of more than 100 tons, makes these techniques are quite expensive. As a result, access to these facilities is quite limited, specifically for less affluent institutes like universities and hospitals these facilities are not affordable and therefore the research related to them is not growing at a faster pace.

By bringing coherent short wavelength sources off the shelf, the process of laser HHG can reduce the cost of coherent radiation sources. The reduction in cost is not only due to the replacement of accelerator but also due to the fact that there will be no requirement of large building footprints and massive gantries. To understand the generation of higher harmonics in nonlinear media let us see what happens when an intense laser beam passes through a transparent optical medium. The focused light from certain lasers has an electric field as strong as 10^7 V cm^{-1}. Such optical fields are as intense as the cohesive local electric fields in the crystal. Consequently when intense laser beams enter a transparent crystal, they cause a massive redistribution of the electrons and the resulting polarization is no longer proportional to the optical electric field. In fact, at optical fields of 10^7 V cm^{-1} and higher many materials break down completely.

Figure 1 illustrates the characteristic response when an intense optical electric field travels through a nonlinear, or ionic, material. It shows that an intense field in the "right" direction is more effective in polarizing the material than a field in the "left" direction. Such a situation can occur only in a crystal that has a "one-wayness" in its structure, or, to be more precise, one that has no center of symmetry. Such crystals are called as noncentro symmetric crystals. Of the crystals found in nature only about 10% fall in this class, and they usually exhibit the phenomenon called piezoelectricity. When a piezoelectric crystal is subjected to mechanical pressure, its asymmetry leads

✉ Naveen Gupta
naveens222@rediffmail.com

[1] Lovely Professional University, Phagwara, India

[2] Government College for Women, Karnal, India

[3] SUS Government College, Matak-Majri, Indri, Karnal, India

Published online: 16 December 2023

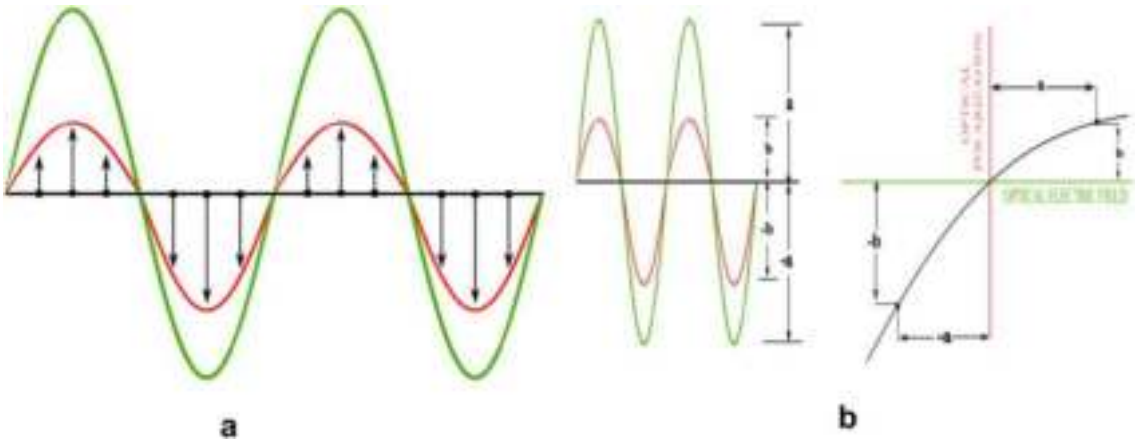

Fig. 1 **a** Nonlinear Polarization of medium. **b** Nonlinear response of crystal

to unequal distortions in the distribution of positive and negative charge and a voltage appears across the faces of the crystal.

The distorted polarization wave produced by an intense laser beam travels at the same velocity as the light wave. It can be shown by Fourier analysis that the distorted wave is the sum of three components: a wave at the fundamental frequency ω of the light wave, a wave at the second-harmonic frequency (2ω) and a third component that corresponds to a "direct current," or steady, polarization (Fig. 2).

Due to the second-harmonic polarization wave the crystal now behaves like a highly directional antenna, supporting a wave of current at frequency 2ω and thus radiates a light wave at frequency double of that of incident wave.

In case of ordinary symmetrical crystals and isotropic materials such as glass and liquids also the nonlinear phenomena can be observed. These materials become nonlinear in the presence of sufficiently intense fields, but the effects are much weaker than those found in asymmetric materials. Because symmetrical materials lack an intrinsic one-wayness, the polarization wave produced by an intense light beam is not skewed left or right as it is in asymmetric materials (Fig. 3). Instead the electronic charges in the material are displaced equally to the left and to the right.

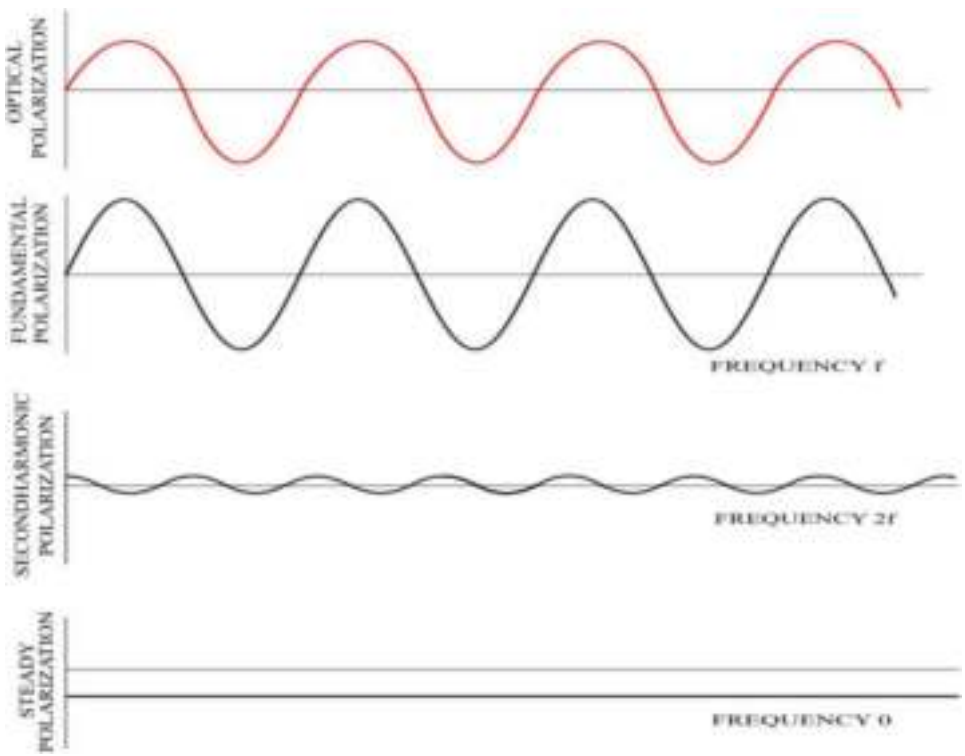

Fig. 2 Frequency components of polarization waves

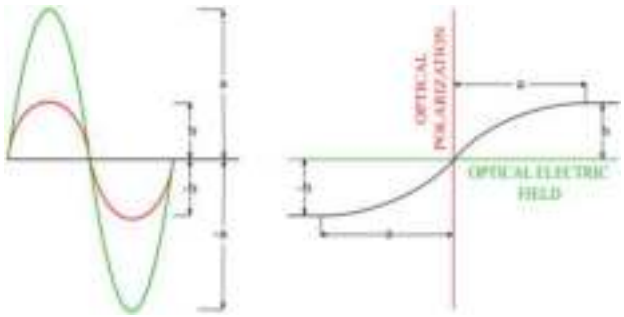

Fig. 3 Nonlinear polarization in symmetrical crystals

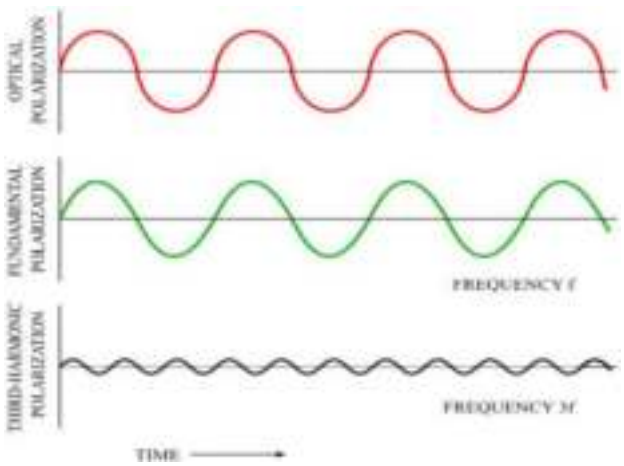

Fig. 4 Frequency components of polarization wave in symmetric crystals

The nonlinearity arises from the fact that the displacement can no longer follow in exact proportion as the electric field rises to peak intensity.

When this sort of distorted polarization wave is analyzed into its components, it is found to consist mainly of a pure wave of the fundamental frequency and a weak third-harmonic wave (Fig. 4). The third harmonic of ruby laser light (6,943 Å) occurs in the far ultraviolet at 2,314 Å. It has been produced in calcite with a conversion efficiency of three parts per million.

The interaction of laser beams with nonlinear media can stimulate several nonlinear effects [1–3] that significantly affect the process of harmonic generation. One such phenomenon is self-focusing that occurs due to the modification of optical properties of the medium by the laser beam. The presence of intense laser beams in nonlinear optical media makes their index of refraction a function of laser intensity. Hence, maximum index of refraction occurs where the intensity is highest. In other words, the beam induces a convex lens in the medium and thus its intensity gets accumulated towards the axis of the beam. The resulting increase in the intensity enhances the efficiency of its conversion to third harmonics.

Since its discovery by Franken [4] a vast literature has been reported on HHG of laser beams in nonlinear media. Literature review [5–8] indicates that the investigations reported on THG, till date, are focused on the investigation of propagation dynamics of ideal Gaussian beams. However, experimental investigations reveal that due to cavity imperfections like misalignment of end mirrors, presence of impurities in the gain medium, etc., the irradiance over the cross section the beam is not having ideal Gaussian profile. However, due to these cavity imperfections the wings of the intensity profile are slightly expanded as compared to ideal Gaussian profile. The actual profile for the irradiance over the cross section of the laser beam can be characterized by a class of distribution functions known as q-Gaussian distribution. This paper aims to present for the first time, a theoretical investigation on the effect of self-focusing of q -Gaussian laser beams on THG in media exhibiting cubic-quintic optical nonlinearity.

Dynamics of pump beam

Consider the interaction of a linearly polarized electromagnetic beam having electric field

$$\boldsymbol{E}(r,z,t) = A_0(r,z)e^{i\left(k_0 z-\omega_0 t\right)}\boldsymbol{e_x} \tag{1}$$

with a nonlinear medium characterized by higher order susceptibilities $\chi^{(3)}$, $\chi^{(5)}$,$\chi^{(7)}$, and so on. For anisotropic media these higher order susceptibilities are generally tensor in nature that can be explained as follows:

when an electron in the dielectric lattice is displaced from equilibrium, it will experience not only a restoring force, but also forces from the neighboring molecules (Fig. 5).

A field applied in the x direction may result in an electron moving in the y and z directions as well (Fig. 6).

The strength and direction of these forces depend very much on the structure of the crystal. Thus, the susceptibility of an anisotropic medium is in general a tensor of rank 2 having 9 terms (A tensor is the most general product of two or more vectors. The number of vectors multiplied equals the rank of the tensor. A tensor of rank n contains 3^n elements.). For isotropic media like glass these higher order susceptibilities are scalar in nature. The effective dielectric function of such a medium is given by

$$\epsilon = \epsilon_0 + \sum_n \frac{n!}{\left(\frac{n-1}{2}\right)!\left(\frac{n+1}{2}\right)!}2^{1-n}\chi^{(n)}\left|A_0\right|^{n-1} \tag{2}$$

where ϵ_0 is the intensity independent component of dielectric function and is related to the wave number k_0 of the laser beam as $k_0 = \frac{\omega_0\sqrt{\epsilon_0}}{c}$. Laser beam propagation through such

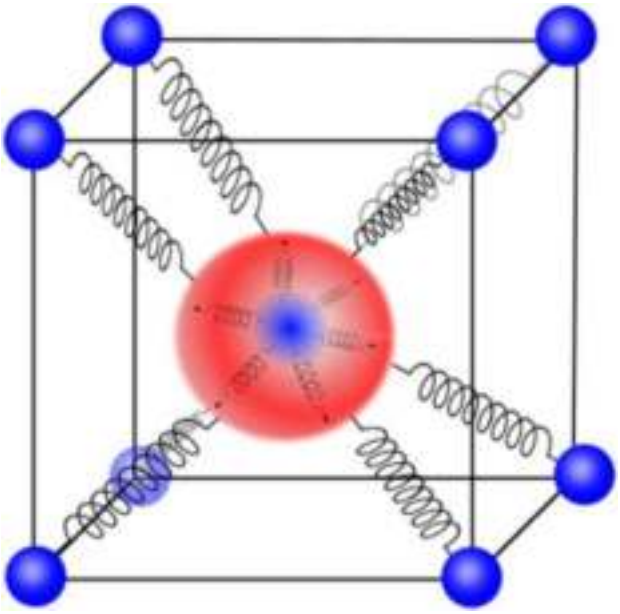

Fig. 5 Restoring force on electron cloud of an atom/molecule in a crystal lattice

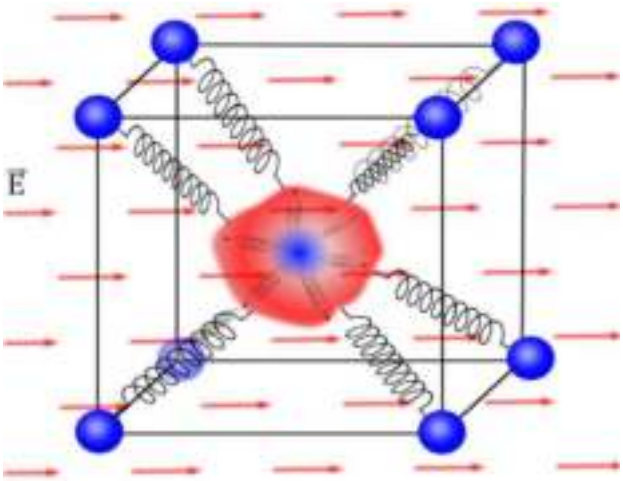

Fig. 6 Tensor nature of nonlinear susceptibility

a medium is modeled by wave equation (that can be obtained from Maxwell's equations)

$$2i\frac{\partial A_0}{\partial z} = \nabla_{\perp}^2 A_0 + 2k_0^2\frac{\omega_0^2}{c^2}\left(\sum_n \frac{n!}{\left(\frac{n-1}{2}\right)!\left(\frac{n+1}{2}\right)!}2^{1-n}\chi^{(n)}|A_0|^{n-1}\right)A_0 \tag{3}$$

Equation (3) is identical to a well-known wave equation known as nonlinear Schrodinger equation (NSE) that governs the transmission of electromagnetic waves through nonlinear media and is a statement of interplay between nonlinearity and diffraction.

Although Eq. (3) is lacking from exact analytical solutions, a physical insight into the propagation dynamics of the pump beam can be obtained by using a semi analytical approach known as variational theory [9, 10]. This method replaces a partial differential equation with a set of coupled ordinary differential equations for the coefficients of an ansatz describing the full solution of wave Eq. (3). According to this method, Eq. (3) is a variational problem for action principle based on Lagrangian density

$$\mathcal{L} = i\left(A_0\frac{\partial A_0^{\star}}{\partial z} - A_0^{\star}\frac{\partial A_0}{\partial z}\right) + \left|\nabla_{\perp}A_0\right|^2 - k_0^2\sum_n \frac{n!}{\left(\frac{n-1}{2}\right)!\left(\frac{n+1}{2}\right)!}\frac{2^{1-n}}{\left(\frac{n+1}{2}\right)}\chi^{(n)}|A_0|^{n+1} \tag{4}$$

In the present analysis, we assume $A_0(r,z)$ takes the form of the function given by [11]

$$A_0(r,z) = \frac{E_{00}}{f}\left(1+\frac{r^2}{qr_0^2f^2}\right)^{-\frac{q}{2}} \tag{5}$$

where the parameter $f(z)$ is currently undetermined and upon multiplication with initial beam width r_0 it gives the waist size of the laser beam at particular location inside the medium. Hence, the parameter $f(z)$ can be referred to as dimensionless beam width parameter. The phenomenological parameter q is related to the deviation of irradiance, over the cross section of the beam, from ideal Gaussian profile. For $q = 0$ the beam profile is pure flat-top profile with an infinite plane wavefront and for $q \to \infty$ i.e.,

$$\lim_{q\to\infty} A_0(r,z) = \frac{E_{00}}{f}e^{-\frac{r^2}{2r_0^2f^2}}$$

the beam profile is that of a TEM_{00} Gaussian beam. For $q > 0$ as the value of q increases, the effect on the beam waist profile is to increase the rate of change in intensity in the off axial regions of the cross section of the laser beam as shown in Fig. 7.

Substituting the trial function (Eq. 5) in Lagrangian density and integrating over r we get reduced Lagrangian as $L = \int_0^{\infty}\mathcal{L}rdr$. The corresponding Euler–Lagrange equation

$$\frac{d}{dz}\left(\frac{\partial L}{\partial\left(\frac{\partial f}{\partial z}\right)}\right) - \frac{\partial L}{\partial f} = 0 \tag{6}$$

gives the following ordinary differential equation describing the dynamical variations of beam width with propagation distance.

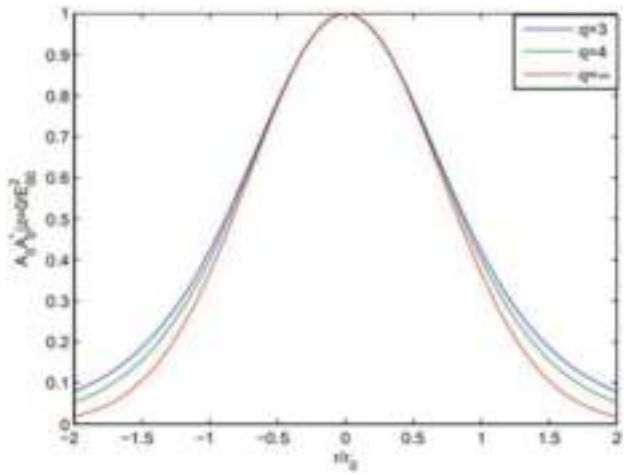

Fig. 7 Intensity profile of q-Gaussian laser beam

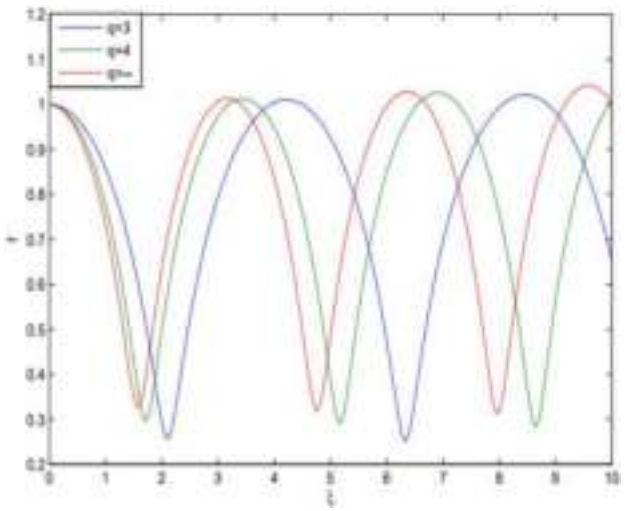

Fig. 8 Effect of deviation parameter q on evolution of beam width of the laser beam

$$\frac{d^2f}{d\xi^2} = \frac{\left(1-\frac{1}{q}\right)\left(1-\frac{2}{q}\right)}{\left(1+\frac{1}{q}\right)}\frac{1}{f^3} - \frac{1}{\epsilon_0}\left(\frac{\omega_0 r_0}{c}\right)^2 \left(1-\frac{1}{q}\right)\left(1-\frac{2}{q}\right)\sum_n \frac{\chi^{(n)}E_{00}^{n-1}}{f^n} \frac{n!}{\left(\frac{n-1}{2}\right)!\left(\frac{n+1}{2}\right)!}\frac{2^{1-n}}{(n+1)((n+1)-\frac{1}{q})} \tag{7}$$

where

$$\xi = \frac{z}{k_0 r_0^2}$$

Thus, it follows from Eq. (7) that the problem of solving a partial differential equation i.e., NSWE (Eq. 3) has reduced to that of solving an ordinary differential equation. Although this reduced equation is also lacking an exact analytical solution due to its non integrability, its approximate solution can be easily obtained with the help of simple numerical techniques. In solving Eq. (7) it has been assumed that initially the beam is collimated i.e., it satisfies the boundary conditions $f = 1$ and $\frac{df}{d\xi} = 0$ at $\xi = 0$.

Third harmonic generation

The amplitude A_3 of the third harmonic component obeys the equation

$$2i\frac{\partial A_3}{\partial z} + \nabla_\perp^2 A_3 = -\frac{\omega_3^2}{c^2}\chi^{(3)}A_0^3 e^{i\Delta k z} \tag{8}$$

where

$$\Delta k = 3k_0 - k_3$$

and

$$A_3(r,z) = E_3(z)\left(1+\frac{r^2}{qr_0^2f^2}\right)^{-\frac{q}{2}} \tag{9}$$

Using Eqs. (5) and (9) in Eq. (8), we get

$$E_3(z) = \int_0^z 3i\frac{\omega_0}{2c}\frac{\chi^{(3)}E_{00}^2}{f^3}\left(1+\frac{r^2}{qr_0^2f^2}\right)^{-\frac{(n-1)q}{2}} dz \tag{10}$$

Hence, the conversion efficiency η_3 of third harmonic can be written as

$$\eta_3 = \frac{\int_0^\infty \left|E_3 E_3^\star\right|^2 rdr}{\int_0^\infty A_0 A_0^\star rdr} \tag{11}$$

Equation (11) has been solved numerically in association with Eq. (7) to see how conversion efficiency of the harmonic power evolves with longitudinal distance.

Discussion

In the present analysis, solution of Eqs. (7) and (11) has been obtained with the help of Runge Kutta fourth-order method for the following set of laser and medium parameters:

$$\omega_0 = 1.78\times10^{15}\text{rad/sec}, r_0 = 15\mu\text{m}, n = 3,5, \quad \epsilon_0 = 3, \chi^{(3)}E_{00}^2 = 0.003, \chi^{(5)}E_{00}^4 = -0.0001 \tag{12}$$

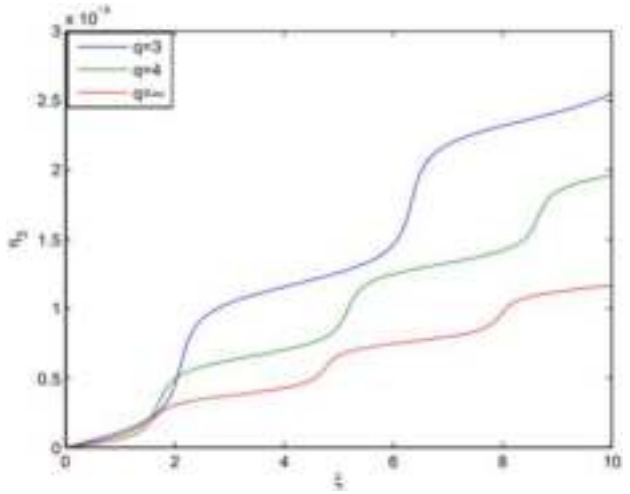

Fig. 9 Effect of deviation parameter q on conversion efficiency of THG

The corresponding evolutions of the beam width and conversion efficiency of THG are shown in Figs. 8 and 9, respectively. Breather like behavior i.e., harmonic variations in the beam width with distance of propagation through the medium, can be clearly seen from the plots in Fig. 8. These harmonic variations of the beam width can be explained by examining the role and origin of various terms contained in Eq. (7). The first term on right hand side (R.H.S), which is proportional to f^{-3}, is the spatial dispersive term, that models the spreading of the laser beam in transverse directions occurring as a consequence of diffraction divergence. The second term which is proportional to f^{-n} arises due to the optical nonlinearity of the medium resulting as a consequence of anharmonic motion of the atomic dipoles under the field of laser beam. The order of anharmonicity is described by higher order susceptibilities $\chi^{(n)}$. Depending on the sign of $\chi^{(n)}$ the second term can oppose or favor the effect of first term. In the present investigation, we have solved Eq. (7) for $\chi^{(3)}$ and $\chi^{(5)}$ by taking $\chi^{(3)}$ to be positive and $\chi^{(5)}$ to be negative. Thus, the first term along with $\chi^{(5)}$ term oppose the effect of $\chi^{(3)}$ term. The winning term ultimately decide the behavior of the laser beam i.e., whether the beam will converge or diverge. Thus, there exists a critical value of beam intensity above which the beam will converge. In the present investigation the initial beam intensity has been taken greater than the critical intensity i.e., why the spot size of the laser beam is converging initially. As the beam width decreases, the $\chi^{(5)}$ $ term start dominating $\chi^{(3)}$ term. Also, reduction in the spot size of the laser beam results in increase in its transverse momentum spread via position momentum uncertainty, which in turn leads to increase in its diffraction effect. Hence, there starts a competition between self-focusing due to $\chi^{(3)}$ $ nonlinearity and self defocusing due to natural diffraction and $\chi^{(5)}$ nonlinearity. This competition goes on till the laser beam attains minimum possible spot size. There after diffraction effects become dominant and hence the beam width of the laser beam again starts increasing. As the beam width of the laser beam starts increasing, the competition between diffraction broadening and nonlinear refraction starts again. Now, this competition lasts till maximum value of f is obtained. These processes go on repeating themselves and thus give breather like behavior to the spot size of the laser beam.

Reduction in focusing of the laser beam with increase in the value of q has also been observed from Fig. 6. The reason behind this effect is that for laser beams with higher value of q most of the intensity is concentrated in a narrow region around the axis of the beam. Hence, these beams get a get a very less contribution from the off axial part in order to produce nonlinearity in the medium. As the phenomenon of self-focusing is a homeostasis of nonlinear refraction of the laser beam due to optical nonlinearity of the medium, increase in the value of q reduces the extent of self focusing.

From the plots in Fig. 9 it can be clearly seen that the normalized power of the harmonic radiation is a monotonically increasing function of distance of propagation showing periodical step like behavior. Each step occurs at the position of the minimum beam width. This is because as the pump beam gets self-focused, its intensity increases and consequently the oscillation amplitude of the atomic dipoles also increases. These higher amplitude atomic oscillators emit radiation of relatively higher intensity. Hence, there is monotonic increase in the power of harmonic radiations with distance of propagation. The step like behavior of the power of harmonic radiation at the positions of the focal spots of the pump beam are due to the fact that being the regions of highest intensity, the amplitude of the atomic oscillators is maximum at the focal spots of the pump. Hence, after attaining its maximum value the harmonic power moves towards its next possible higher value at next focal spot. These transitions of harmonic power from one maximum value to next maximum value give it a step like behavior, each step occurring at the position of minimum beam width of the pump.

Reduction in the efficiency η_3 of conversion to third harmonics with increase in the value of q can be seen from the plots in Fig. 9. The underlying physics behind this is the one to one correspondence between the conversion to higher harmonics and the degree of self-focusing of the pump beam. Larger is the extent of focusing larger will be the efficiency of the conversion process and vice versa. Hence, decrease in the focusing of laser beam with increase in the value of q reduces the efficiency of conversion to third harmonics.

Conclusions

In conclusion, we have investigated the effect of self-focusing of a laser beam on its THG in cubic quintic optical nonlinear media. From the results of present investigation it can be concluded that irradiance profile of the laser beam plays a significant role in determining its propagation characteristics as well as the conversion efficiency of THG in nonlinear media. As the irradiance profile of the laser beam converges toward Gaussian profile, there is a significant decrease in the conversion efficiency of THG. Thus, for efficient THG laser beams with expanded wings of the irradiance profile are more suitable.

The results of present investigation may serve as a guide for the experimentalists working in the area of nonlinear optics and light matter interactions.

References

1. G.A. Askaryan, Effects of the gradient of strong electromagnetic beam on electrons and atoms. Soviet Phys. JETP **15**, 1567 (1962)
2. E. Garmire, R.Y. Chiaoand, C.H. Townes, Self-trapping of optical beams. Phys. Rev. Lett. **13**, 479 (1965)
3. P.L. Kelley, Self-focusing of optical beams. Phys. Rev. Lett. **15**, 1005 (1965)
4. P.A. Franken, Generation of optical harmonics. Phys. Rev. Lett. **7**, 118 (1961)
5. Y. Luo, S.A. Maier, T. Wu, L. We, Phase-matching and peak nonlinearity enhanced thirdharmonic generation in graphene plasmonic coupler. Phys. Rev. Appl. **11**, 014049 (2019)
6. R.S. Tasgal, Y.B. Band, Third-harmonic generation in isotropic media by focused pulses. Phys. Rev. A **70**, 053810 (2004)
7. M. Trippenbach, M. Matuszewski, R.S. Tasgal, Y.B. Band, Highly nonlinear dynamics of third harmonic generation by focused beams. Phys. Rev. A **69**, 013809 (2004)
8. U. Gubler, C. Bosshard, Optical third-harmonic generation of fused silica in gas atmosphere: absolute value of the third-order nonlinear optical susceptibility $\chi(3)$. Phys. Rev. B **61**, 10702 (2006)
9. D. Anderson, Variational approach to nonlinear pulse propagation in optical fibers. Phys. Rev. A **27**, 135 (1983)
10. Y. Kaganovskii, A.D. Wilson, D. Ianetz, M. Rosenbluth, Propagation of an asymmetric Gaussian beam in a nonlinear absorbing medium. Phys. Rev. A **81**, 053851 (2010)
11. A. Singh, N. Gupta, Second harmonic generation by relativistic self-focusing of q-Gaussian laser beam in preformed parabolic plasma channel. Phys. Plasmas **22**, 013102 (2015)

Second-harmonic generation of two cross-focused q-Gaussian laser beams by nonlinear frequency mixing in plasmas

Article *in* Journal of Optics · November 2022

DOI: 10.1007/s12596-022-00995-w

CITATION
1

READS
33

7 authors, including:

S B Bhardwaj
SUS Govt College Indri Karnal
69 PUBLICATIONS **364** CITATIONS
SEE PROFILE

Sanjeev Kumar
Government College for Women, Karnal, Haryana, India
26 PUBLICATIONS **77** CITATIONS
SEE PROFILE

Suman Choudhry
Government College for Women, Karnal, Haryana, India
22 PUBLICATIONS **46** CITATIONS
SEE PROFILE

Siddhanth Shishodia
Lovely Professional University
3 PUBLICATIONS **2** CITATIONS
SEE PROFILE

J Opt
https://doi.org/10.1007/s12596-022-00995-w

RESEARCH ARTICLE

Second-harmonic generation of two cross-focused q-Gaussian laser beams by nonlinear frequency mixing in plasmas

Naveen Gupta[1] · S. B. Bhardwaj[2] · Sanjeev Kumar[1] · Suman Choudhry[1] · Rishabh Khatri[1] · Siddhanth Shishodia[1] · Rohit Johari[1]

Received: 11 July 2022 / Accepted: 18 October 2022

Abstract A scheme for second-harmonic generation (SHG) of a pair of q-Gaussian laser beams interacting nonlinearly with underdense plasma has been proposed. Due to the relativistic increase in electron mass under the intense fields of the laser beam, the resulting optical nonlinearity of plasma leads cross-focusing of the laser beams. The resulting nonlinear coupling between the two laser beams makes the oscillations of plasma electrons to contain a frequency component equal to the sum of frequencies of the pump beams. This results in a nonlinear current density at frequency equal to the sum of frequencies of the pump beams. If the frequencies of the pump beams are equal, then the resulting nonlinear current generates a new radiation at frequency twice the frequencies of the pump beams— a phenomenon known as SHG. Starting from nonlinear Schrodinger wave equation a set of coupled differential equations governing the evolution of beam widths of the laser beams and power of generated second-harmonic radiation with longitudinal distance has been obtained with the help of variational theory. The equations so obtained have been solved numerically to envision the effect of laser as well as plasma parameters on the power of generated second-harmonic radiation.

Keywords Cosh Gaussian · Self-focusing · Nonlinear optics · Second-harmonic generation · Clean energy

✉ Naveen Gupta
naveens222@rediffmail.com

[1] Lovely Professional University, Phagwara, India

[2] SUS Govt College, Matak-Majri, Indri, Karnal, India

Introduction

The invention of the laser [1] is the most towering achievement in the long history of light. It brought an extraordinary technological leap, which has since paved the way for a startling new era in optical science and technology. For the first time, man got a remarkable tool for direct generation and manipulation of coherent light. Laser brought same revolution to optics that transistor brought to electronics and cyclotron brought to nuclear physics. The distinctive qualities of laser derive from its coherence properties, which result in a beam of light with a well-defined optical phase both in space and time. This prescribed phase generally confines the wavelength and frequency of the laser light to a restricted range, so that the beam exhibits a narrow frequency spectrum. Another unique property of laser light is its directionality, which means that the beam can propagate over great distances without significant spreading and can be readily manipulated using conventional optical elements. The phase coherence and directionality of the laser make it possible to create extremely large optical powers and focused intensities that cannot be obtained from incoherent light emitters. These characteristics also allow accurate transfer of information [2], precise calibration of time [3, 4], and measurements of many physical constants [5, 6], among numerous other applications, using laser light. Lasers are now standard components of such commonplace objects as compact-disk players and printers. The everyday presence of lasers does not mean, however, that they have been reduced to performing only pedestrian tasks. Higher-end applications like laser surgery [7], laser-driven particle accelerators [8, 9], inertial confinement fusion [10], etc., are also abound.

Success is never without limitations, and laser is also not an exception. By the virtue of its unique coherence properties, laser light contains only a confined band of frequencies

Published online: 05 November 2022

determined by the energy gap in the laser material. In this regard, the laser can be viewed as a light source with limited spectral versatility. It is possible to develop tunable lasers with more extended spectral emission using materials with broadened energy levels or energy bands). However, the maximum spectral coverage available to the most prominent tunable lasers (e.g., Ti:sapphire) is still limited to at best 300–400 nm. In addition, the restricted availability of suitable laser materials has confined the wavelength coverage of existing tunable lasers mainly to the visible and near-infrared spectrum. These limitations have left substantial portions of the optical spectrum inaccessible to lasers, and alternative methods for the generation of coherent light in these regions have had to be devised.

One of the most effective techniques to overcome the spectral limitations of lasers is to exploit nonlinear optics. The potential of nonlinear processes for the generation of tunable coherent radiation was recognized soon after the invention of the laser [11]. Nonlinear optical techniques are based on a fundamentally different principle from lasers. While the process of light emission in a laser is a direct result of the transitions between the energy levels in the laser gain medium, nonlinear optical processes rely on the alternative mechanism for light generation, namely electric dipole oscillations [12].

When light is incident on matter, the bound electrons vibrate in the electromagnetic field. While moving under the electromagnetic force, the electrons generate a synchronous polarization field, which interferes with the original field. At low amplitude, this generated field is proportional to the exciting one, and the interference between the driving field and the generated one is the origin of the linear properties of light in matter, such as those described by the optical index of refraction. On the other hand, when the input electric field is large, electron displacement becomes nonlinear at the higher field strengths. This is the regime of nonlinear optics. The exact form of nonlinear response depends on crystallographic structure of the material (Figs. 1, 2).

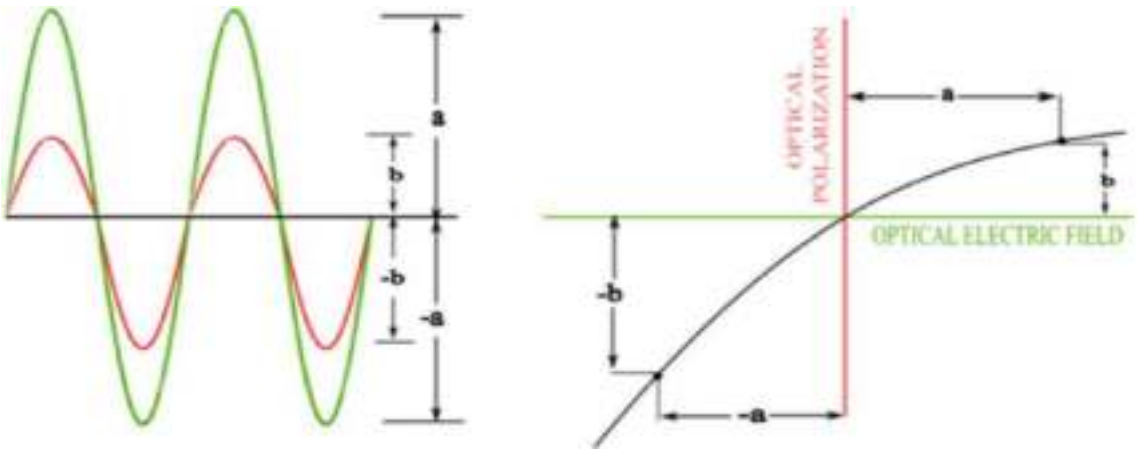

Fig. 1 Nonlinear response of noncentrosymmetric crystal

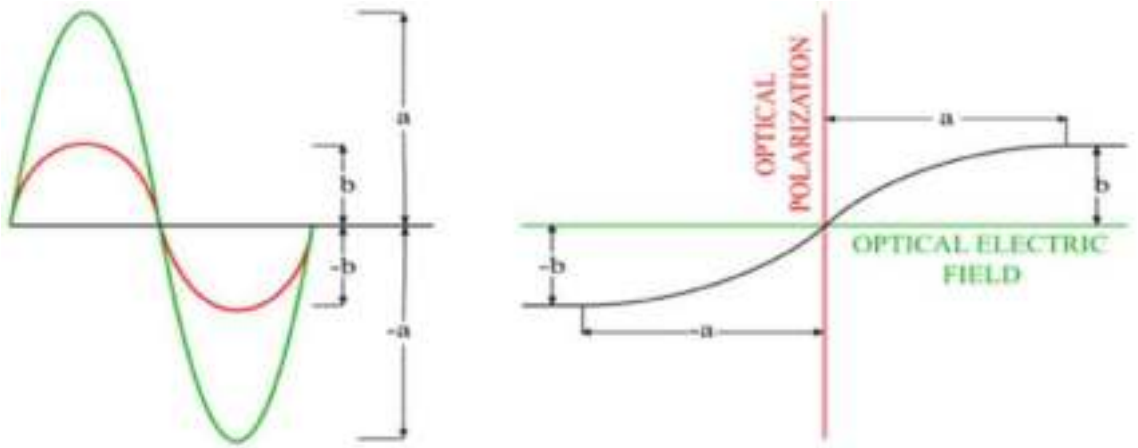

Fig. 2 Nonlinear polarization in symmetrical crystals

However, in either case, the electrons oscillate not only at the input frequency but also over an infinite range of frequencies, above and below the input frequency that can be seen from the Fourier expansion of the electron displacement. The resulting light emission from the oscillating electrons is thus also over an infinite band of frequencies. If the potential that binds the electrons in the material is asymmetric in space, the electron orbits will be distorted relative to the symmetric case, that is, elongated in the direction of the more confining part of the potential. The distorted electron orbits will then generate harmonic polarization waves. For instance, a wave at radial frequency ω will generate a wave at frequency 2ω (Fig. 3). This is called second-harmonic generation (SHG) and is widely used in the field of nonlinear optics.

A concise and clear description of the physical mechanism of SHG can also be given on the basis of quantum theory of radiations which is based on quantum electrodynamics. The main advantage of using this theory is that whenever there is an exchange of energy and momentum either among different components of optical fields or between the optical field and the medium, this theory can reveal the coherent wave property of the optical field as well as the quantum nature of the field. The starting point of this theory is to consider the optical field and the molecules of the nonlinear medium as a combined and quantized system. The interaction between the optical field and the molecule results in (i) transition of the molecule among its different energy states and (ii) a simultaneous change of distribution of photons in different modes (photon states). In order to give a rigorous and complete physical description for these processes, the key concept of intermediate state must be introduced, which is a quantum state characterizing the whole system involving both optical fields and the molecule. In such an intermediate state of the whole system, the photon number (degeneracy) in a mode has changed by $+1$ or -1, while the molecule has left its original state (mostly ground state); however, at this moment, the molecule is not certainly located in any specific excited state, but correlated with all possible excited states with a certain occupying probability for each. In this case, it is convenient to introduce a virtual energy level in the energy diagram to represent such an intermediate state. In the intermediate state represented by a virtual state level, the energy range of all molecular eigen states that may be occupied by an excited molecule is nearly unlimited; according to the uncertainty principle, the staying time of this molecule in that intermediate state is infinitely short. Relying on the concept of intermediate state and its representation of a virtual energy level, many nonlinear optical effects can be interpreted very clearly.

As an example, the schematic energy-level diagram describing SHG is shown in Fig. 4. In this case, the

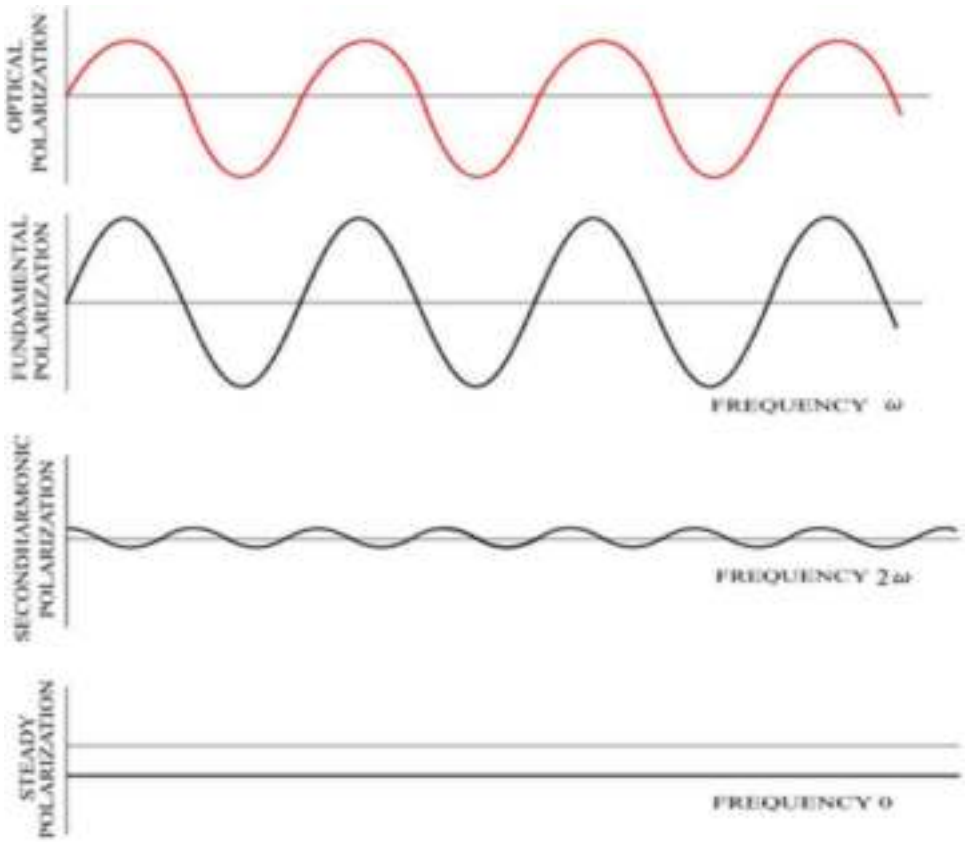

Fig. 3 Second-harmonic generation in noncentrosymmetric media

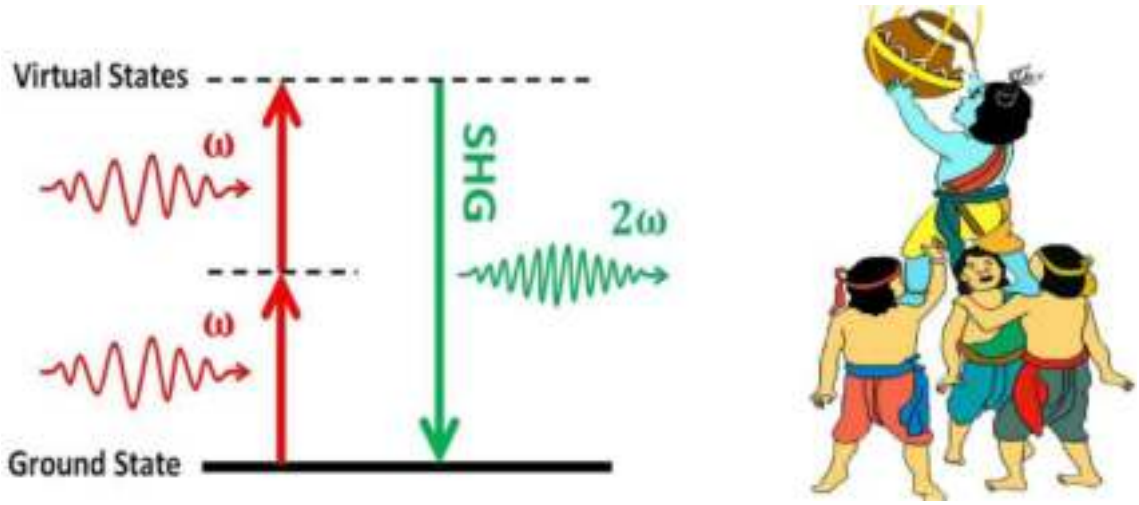

Fig. 4 QED description of SHG

elementary process of SHG occurs via multiple quantum transitions or multiple steps. In the first step, there is an annihilation of one photon from the fundamental light field, while a molecule of the medium left its initial (ground) state to an intermediate state; in the second step, there is the annihilation of another fundamental photon, while the excited molecule is situated in another intermediate state; in the final step, this excited molecule is returning to its initial state, while there is the creation of a new photon of doubled frequency. Since the staying time of the molecule in each intermediate state is extremely short (near the response time of electron-cloud distortion), the above-mentioned three steps actually occur instantaneously and simultaneously. Here, we have to visualize that the elementary SHG process undergoes three quantum transitions via two intermediate states, because in the quantum theory of radiation for each quantum transition of the whole system, the photon number in a given mode can only change either by − 1 (i.e., annihilation of a photon) or + 1 (i.e., creation of a photon). This rule holds for any types of optical processes involving emission, absorption, or molecular scattering of light. We should keep in mind that for all those phenomena (such as nonlinear frequency mixing, Raman scattering, and multi-photon absorption), the observable elementary process is actually an instantaneous single event even though which may undergo multiple quantum transitions via one or multiple intermediate states. With such an understanding, for instance, the elementary process of SHG can also be simply described as the annihilation of two fundamental photons and the simultaneous creation of one second-harmonic photon.

Similarly, if the potential that binds the electrons in the material is symmetric in space, then the wave at frequency ω will generate a new wave at frequency 3ω (Fig. 5).

If two waves of frequencies ω_1 and ω_2 propagate simultaneously through a nonlinear medium, then it may result in the generation of new waves at frequencies $2\omega_1, 2\omega_2, \omega_1 + \omega_2 \cdot \omega_1 - \omega_2$ (Fig. 6).

In case of plasmas, the role of polarization waves is played by the propagating electron plasma waves EPWs. Thus, plasmas can also lead to the generation of higher harmonics of the incident waves through the process of nonlinear frequency mixing. However, plasmas offer several advantages over the other nonlinear media for frequency mixing. The major advantage is that there is no upper threshold on the power of radiation that can be sent through them. Plasmas by definition are already ionized, and thus, they have infinite immunity against ionization-induced damages. In contrast to this, the best-known glasses get damaged by ionization only at 10 W/cm^2. Thus, second harmonics of any intensity can be produced with the help of plasmas as a nonlinear medium [13–15].

Most laser beams have a Gaussian irradiance profile, although it can be beneficial to use a non-Gaussian beam in certain applications [16, 17]. The irradiance cross section of Gaussian beams decreases symmetrically with increasing distance from the center. Gaussian laser profiles have several disadvantages, such as the low-intensity portions on either side of the usable central region of the beam, known as "wings." These wings typically contain energy that is wasted because it is at a lower intensity than the threshold required for the given application, whether it is materials processing, laser surgery, laser-driven fusion or another application where an intensity above a given value is needed. Thus, due to their expanded wings of the irradiance profile, a new class of laser beams known as q-Gaussian laser beams has gained a significant interest of researchers working in the area of laser–plasma

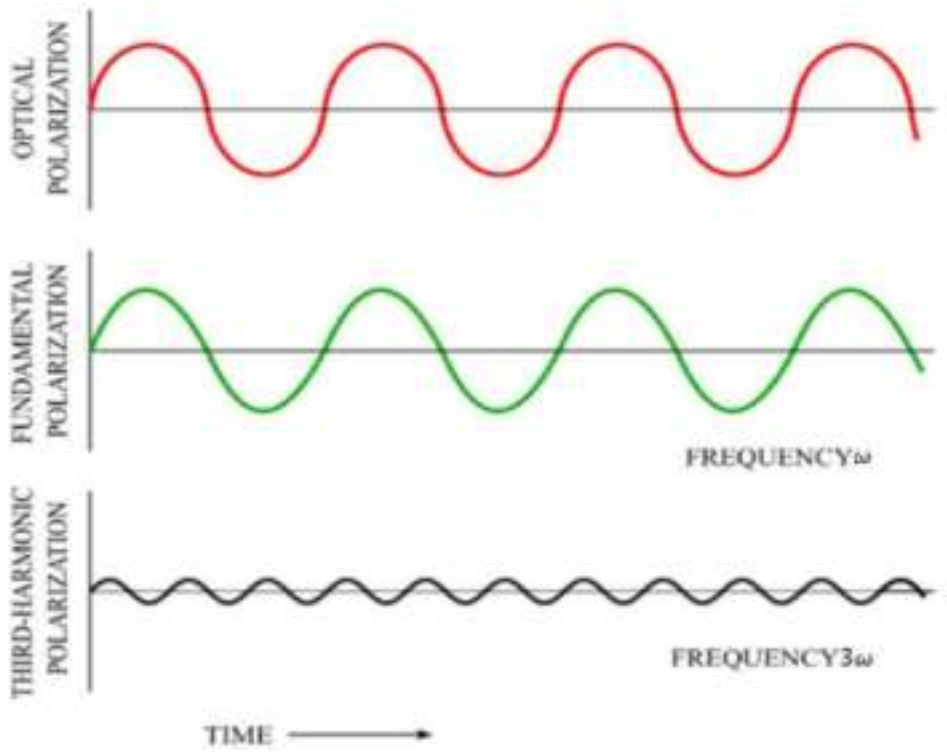

Fig. 5 Third harmonic generation in centrosymmetric media

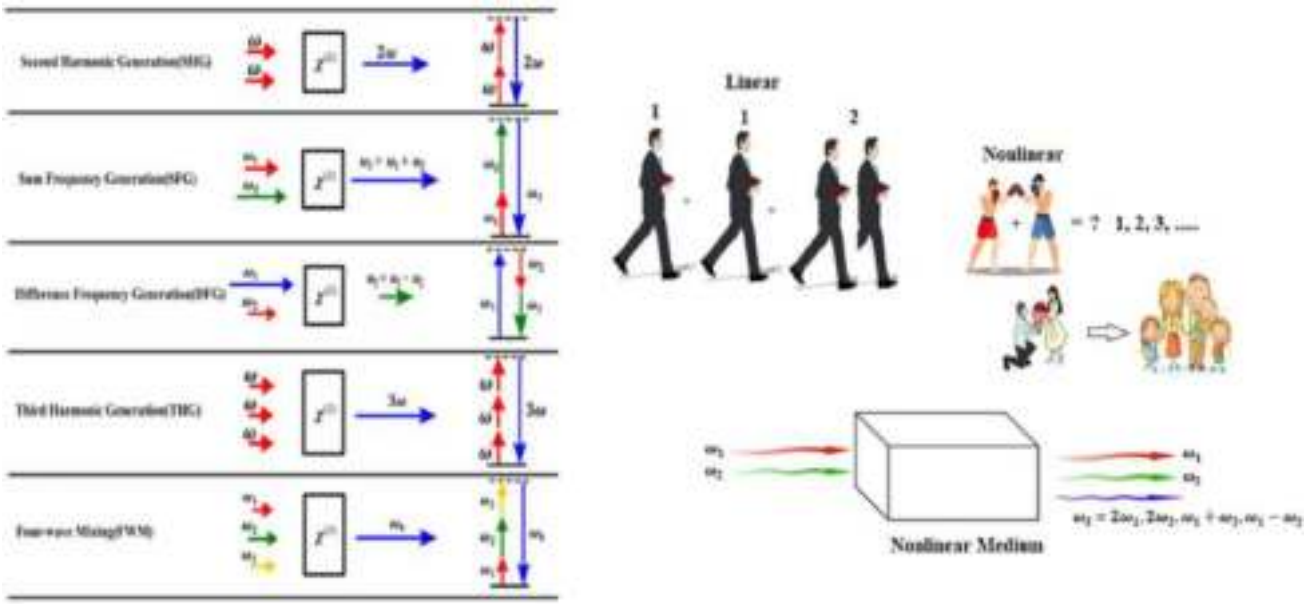

Fig. 6 Frequency mixing in nonlinear media

interactions [18, 19]. These beams contain a significant amount of energy outside the full width half maximum of their irradiance profile. The literature review reveals the fact that most of the earlier investigations on SHG of intense laser beams in plasmas have been reported for Gaussian laser beams. Thus, this article aims to give first theoretical investigation on SHG of q-Gaussian laser beams in plasma by nonlinear frequency mixing including the effect of cross-focusing of the laser beams.

Relativistic nonlinearity of plasma

Consider the propagation of two coaxial laser beams with electric field vectors

$$\boldsymbol{E}_j(r,z,t) = A_j(r,z)e^{i\left(k_j z-\omega_j t\right)}\boldsymbol{e}_x, \quad j=1,2 \tag{1}$$

Through a plasma with equilibrium electron density n_0. Here, k_j, ω_j are the wave numbers and angular frequencies of the fields of the laser beams, and $A_j(r, z)$ are their slowly varying complex amplitudes. The amplitude structure over the cross sections of the q-Gaussian laser beams is given by [19]

$$A_j(r,z) = \frac{E_{j0}}{f_j}\left(1+\frac{r^2}{qr_j^2f_j^2}\right)^{-\frac{q_j}{2}} \tag{2}$$

Here, the phenomenological constant q_j is related to deviation of amplitude structure over the cross section of laser beams form ideal Gaussian profile. Laser beams with lower values of q_j are characterized by expanded wings of the intensity distribution in comparison to the ideal Gaussian distribution. Hence, the parameter q_j is also termed as deviation parameter. As the value of q_j increases, the amplitude structure over the cross section of the laser beams converges toward the ideal Gaussian profile. The functions $f_j(z)$ are the key parameters of interest that upon multiplication with initial beam radius r_j give the instantaneous beam widths of the laser beams. Hence, f_j is called as beam width parameter.

The dielectric function of a plasma with electron density n_e for an electromagnetic beam with frequency ω_j is given by

$$\varepsilon = 1-\frac{\omega_p^2}{\omega_j^2} \tag{3}$$

where

$$\omega_p^2 = \frac{4\pi e^2 n_0}{m_e} \tag{4}$$

is the natural frequency of oscillations of plasma electrons, i.e., plasma frequency. When under the effect of intense fields of the incident laser beams the quiver velocity of plasma electrons becomes comparable to that of speed of light in vacuum; then, the effective mass m_e of electron in Eq. (4) needs to be replaced by $m_0\gamma$, where γ is the relativistic Lorentz factor, and m_0 is the rest mass of electron. Following Akhiezer and Polovin [20], the relativistic Lorentz factor can be related to the total intensity of the laser beams as

$$\gamma = \left(1+\sum_j \beta_j A_j A_j^*\right)^{\frac{1}{2}} \tag{5}$$

where $\beta_j = \frac{e^2}{m_0^2c^2\omega_j^2}$ is the coefficient of relativistic nonlinearity.

Since, the effective dielectric function of plasma depends on effective mass of plasma electrons through the plasma frequency (Eq. 4). Hence, intensity dependence of electron mass in turn affects the optical properties of plasma in a nonlinear manner. The resulting intensity dependence of dielectric function of plasma for q-Gaussian laser beams can be written as

$$\varepsilon_j = 1-\frac{\omega_{p0}^2}{\omega_j^2}\left(1+\sum_j \frac{\beta_j E_{j0}^2}{f_j^2}\left(1+\frac{r^2}{qr_j^2f_j^2}\right)^{-q_j}\right)^{-\frac{1}{2}} \tag{6}$$

where

$$\omega_{p0}^2 = \frac{4\pi e^2}{m_0}n_e$$

is the plasma frequency in the absence of laser beams. From Eq. (6), it can be seen that the dielectric function of plasma is a function of intensities of both the laser beams. Hence, during their simultaneous propagation through plasma, the two laser beams get nonlinearly coupled with each other. Equation (6) can be written as

$$\varepsilon_j = \varepsilon_{0j} +_j \left(A_1A_1^*, A_2A_2^*\right) \tag{7}$$

where

$$\varepsilon_{0j} = 1-\frac{\omega_{p0}^2}{\omega_j^2} \tag{8}$$

are the linear parts of dielectric function and

$$\Phi_j\left(A_1A_1^*, A_2A_2^*\right) = \frac{\omega_{p0}^2}{\omega_j^2}\left\{1-\left(1+\sum_j \frac{\beta_j E_{j0}^2}{f_j^2}\left(1+\frac{r^2}{q_j r_j^2 f_j^2}\right)^{-q_j}\right)^{-\frac{1}{2}}\right\} \tag{9}$$

are the nonlinear parts of dielectric function.

Cross-focusing of laser beams

The evolution of beam envelope of an optical beam through a nonlinear medium is governed by the wave equation

$$i\frac{\partial A_j}{\partial z} = \frac{1}{2k_j}\nabla_\perp^2 A_j + \frac{k_j}{2\varepsilon_{0j}}\phi_j\left(A_1A_1^*, A_2A_2^*\right)A_j \tag{10}$$

As Eq. (10) is a nonlinear partial differential equation, it does not possess any closed-form exact solution. Thus, in

order to have physical insight into the propagation dynamics of the laser beams, we have used a semi-analytical technique known as variational theory [21, 22] to solve Eq. (10). According to variational method, Eq. (10) is a variational problem for action principle based on Lagrangian density

$$
\begin{aligned}
&= i\left(A_1\frac{\partial A_1^*}{\partial z} - A_1^*\frac{\partial A_1}{\partial z}\right) + i\left(A_2\frac{\partial A_2^*}{\partial z} - A_2^*\frac{\partial A_2}{\partial z}\right)\\
&+\left|\nabla_\perp A_1\right|^2 + \left|\nabla_\perp A_1\right|^2 - \frac{\omega_1^2}{c^2}\int^{A_1A_1^*}\Phi\left(A_1A_1^*, A_2A_2^*\right)d\left(A_1A_1^*\right)\\
&-\frac{\omega_2^2}{c^2}\int^{A_2A_2^*}\Phi\left(A_1A_1^*, A_2A_2^*\right)d\left(A_2A_2^*\right)
\end{aligned}
\tag{11}
$$

Substituting the trial function for q-Gaussian beam profile in Lagrangian density and integrating over the entire cross section of the laser beam we get the reduced Lagrangian as $L = \int \pounds d^2r$. The corresponding Euler–Lagrange equations

$$
\frac{\mathrm{d}}{\mathrm{d}z}\left(\frac{\mathrm{d}L}{\partial\left(\frac{\partial f_j}{\partial z}\right)}\right) - \frac{\partial L}{\partial f_j} = 0 \tag{12}
$$

give

$$
\begin{aligned}
\frac{\mathrm{d}^2 f_j}{\mathrm{d}\xi^2} + \frac{1}{f_j}\left(\frac{\mathrm{d}f_j}{\mathrm{d}\xi}\right)^2 &= \frac{1}{k_j^2 r_j^4 f_j^3}\frac{\left(1-\frac{1}{q_j}\right)\left(1-\frac{1}{q_j}\right)}{\left(1+\frac{1}{q_j}\right)}\\
&+\frac{\left(1-\frac{2}{q_j}\right)}{r_j^2\varepsilon_{0j}I_{0j}}\int r^2 A_jA_j^*\frac{\partial\phi_j}{\partial r}\mathrm{d}^2 r
\end{aligned}
\tag{13}
$$

Using Eq. (9) in (13), the set of coupled differential equations for beam widths of the two laser beams are obtained

$$
\begin{aligned}
\frac{\mathrm{d}^2 f_1}{\mathrm{d}\xi^2} + \frac{1}{f_1}\left(\frac{\mathrm{d}f_1}{\mathrm{d}\xi}\right)^2 &= \frac{\left(1-\frac{1}{q_1}\right)\left(1-\frac{1}{q_1}\right)}{\left(1+\frac{1}{q_1}\right)}\frac{1}{f_1^3}\\
&-2\left(\frac{\omega_{p0}r_1}{c}\right)^2\left(1-\frac{1}{q_1}\right)\left(1-\frac{2}{q_1}\right)J_1
\end{aligned}
\tag{14}
$$

$$
\begin{aligned}
\frac{\mathrm{d}^2 f_2}{\mathrm{d}\xi^2} + \frac{1}{f_2}\left(\frac{\mathrm{d}f_2}{\mathrm{d}\xi}\right)^2 &= \left(\frac{r_1}{r_2}\right)^4\left(\frac{\omega_1}{\omega_2}\right)^2\left(\frac{\varepsilon_{01}}{\varepsilon_{02}}\right)\frac{\left(1-\frac{1}{q_2}\right)\left(1-\frac{1}{q_2}\right)}{\left(1+\frac{1}{q_2}\right)}\frac{1}{f_2^3}\\
&-2\left(\frac{\omega_{p0}r_1}{c}\right)^2\left(1-\frac{1}{q_2}\right)\left(1-\frac{2}{q_2}\right)J_2
\end{aligned}
\tag{15}
$$

where $\xi = \frac{z}{k_1 r_1^2}$ is the dimensionless distance of propagation, and

$$
\begin{aligned}
J_1 &= \frac{\beta_1 E_{10}^2}{f_1^3}T_1 + \frac{\beta_2 E_{20}^2}{f_1^3}\left(\frac{r_1}{r_2}\right)^2\left(\frac{f_1}{f_2}\right)^4 T_2\\
J_2 &= \frac{\beta_1 E_{10}^2}{f_2^3}T_3 + \frac{\beta_2 E_{20}^2}{f_2^3}\left(\frac{r_1}{r_2}\right)^2\left(\frac{f_1}{f_2}\right)^4 T_4\\
T_1 &= \int_0^\infty x^3\left(1+\frac{x^2}{q_1}\right)^{-2q_1-1}G(x)\mathrm{d}x\\
T_2 &= \int_0^\infty x^3\left(1+\frac{x^2}{q_1}\right)^{-q_1}\left(1+\frac{x^2}{q_2}\left(\frac{r_1f_1}{r_2f_2}\right)^2\right)^{-q_2-1}G(x)\mathrm{d}x\\
T_3 &= \int_0^\infty x^3\left(1+\frac{x^2}{q_1}\right)^{-q_1-1}\left(1+\frac{x^2}{q_2}\left(\frac{r_1f_1}{r_2f_2}\right)^2\right)^{-q_2}G(x)\mathrm{d}x\\
T_4 &= \int_0^\infty x^3\left(1+\frac{x^2}{q_2}\left(\frac{r_1f_1}{r_2f_2}\right)^2\right)^{-2q_2-1}G(x)\mathrm{d}x\\
G(x) &= e^{-\left\{\frac{\beta_1E_{10}^2}{f_1^2}\left(1+\frac{x^2}{q_1}\right)^{-q_1}+\frac{\beta_2E_{20}^2}{f_2^2}\left(1+\frac{x^2}{q_2}\left(\frac{r_1f_1}{r_2f_2}\right)^2\right)^{-q_2}\right\}}\\
x &= \frac{r}{r_1f_1}
\end{aligned}
$$

Equations (14) and (15) are the coupled nonlinear differential equations governing the cross-focusing of two coaxial q-Gaussian laser beams in collisionless plasma. For initially plane wavefronts, these equations are subjected to boundary conditions $f_j = 1$ and $\frac{\mathrm{d}f_j}{\mathrm{d}\xi} = 0$ at $\xi = 0$.

To analyze the effect of deviation of intensity distribution of laser beams from Gaussian distribution and plasma density on cross-focusing of the laser beams eqs.(14)-(15) have been solved for following set of laser-plasma parameters: $\omega_1 = \omega_2 = 1.758\times10^{14}\,\mathrm{rad\,s^{-1}}, \lambda_1 = \lambda_2 = 10.7\,\mu\mathrm{m}(\mathrm{CO_2\ laser}), r_1 = 15\,\mu\mathrm{m}, r_2 = 16\,\mu\mathrm{m}, T_0 = 10^7\,\mathrm{K}, \frac{\omega_{p0}^2 r_1^2}{c^2} = 9, \beta_1E_{10}^2 = 3, \beta_2E_{20}^2 = 1$ and for different values of q_1 and q_2 viz., $q_1 = q_2 = (3, 4, \infty)$.

Figure 7 illustrates the effect of deviation parameter q_1 of beam1 on focusing/defocusing of the two laser beams. It can be seen that during the propagation of the laser beams through plasma, their beam widths vary harmonically with distance. This behavior of the beam widths of the laser beams can be explained by examining the role and origin of various terms contained in Eqs. (14) and (15).

The first terms on the right-hand sides (R.H.S) of these equations that vary inversely with the cube of their beam widths are the spatial dispersive terms that model the spreading of the laser beams in transverse directions occurring as consequence of light's wave nature of diffraction. The second terms on the R.H.S of these equations that have complex dependence on beam widths f_1 and f_2 of the two laser beams arise as a consequence of relativistic nonlinearity of plasma and nonlinear coupling the laser beams with each other. It can be seen that although two

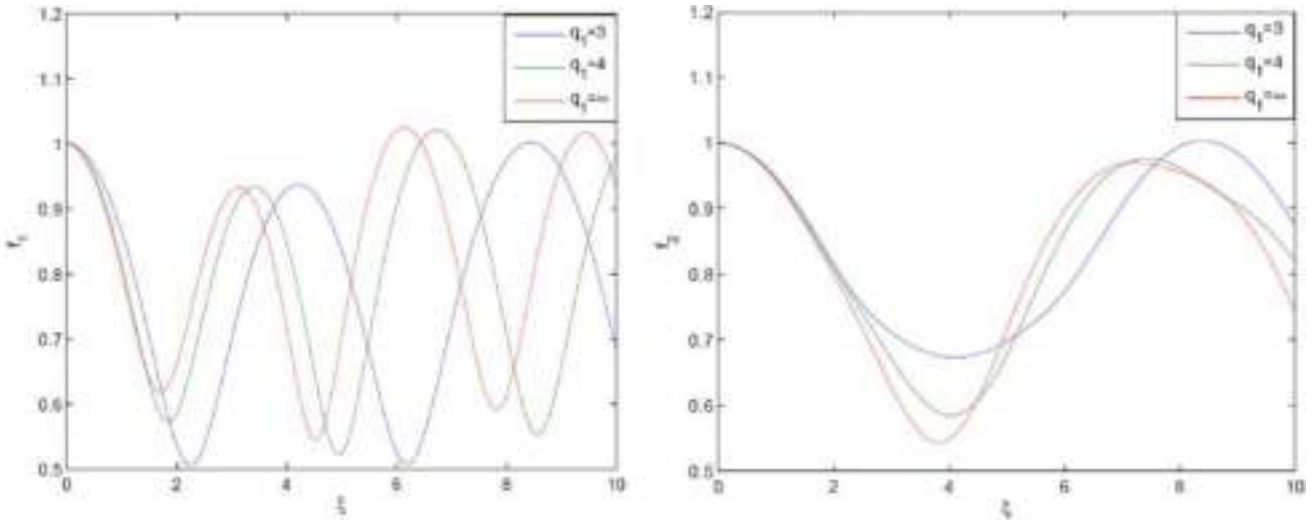

Fig. 7 Variation of beam width parameters f_1 and f_2 of laser beams with distance of propagation in plasma for different values of q_1 and at fixed values of $q_2 = 3$, $\frac{\omega_{p0}^2 r_1^2}{c^2} = 9$, $\beta_1 E_{10}^2 = 3$ and $\beta_2 E_{20}^2 = 1$

copropagating laser beams through vacuum do not interact with each other, but during their propagation through plasma medium, they get coupled with each other. As a consequence of the relativistic nonlinearity of plasma, the resulting nonlinear refraction of the laser beams tends to counterbalance the effect of diffraction by inducing a convex lens-like structure into the plasma. Thus, during the propagation of the laser beams through plasma, there starts a competition between the two phenomena of diffraction and nonlinear refraction. The winning phenomenon ultimately decides the behavior of the laser beams, i.e., whether the beams will converge or diverge. Thus, there exists a critical value of the total beam intensity above which the beams will converge.

In the present investigation, the initial beam intensity has been taken to be greater than the critical intensity, i.e., why the spot sizes of the two laser beams are converging initially. As the beam widths of the laser beams get reduced, their intensity increases. When the intensity of the laser beams become too high, the mass of plasma electrons and thus the optical nonlinearity of plasma get saturated. Thus, the laser beams propagate as if they are propagating through a linear medium. Hence, after attaining minimum possible value, the beam widths of the two laser beams bounce back to their initial values. As the beam widths of the laser beams start increasing, the competition between diffraction and nonlinear refraction starts again. Now, the competition lasts till maximum values of f_1 and f_2 are obtained. These processes go on repeating themselves and thus give breather-like behavior to the spot sizes of the laser beams.

The plots in Fig. 7 depict that increase in the value of q_1 leads to decrease in the extent of self-focusing of first laser beam. This is due to the fact that as the value of q_1 increases toward higher values, the intensity of the first laser beam shifts toward the axial region of the wavefront. As a result, laser beams with higher q value get lesser contribution from the off axial rays toward nonlinear refraction. As nonlinear refraction of the laser beam is a homeostasis for self-focusing, increase in the value of q_1 results in reduced focusing of beam 1. It is also observed from Fig. 7 that the laser beams with higher q values possess faster focusing. The underlying physics behind this fact is the slower-focusing character of the off-axial rays.

The plots in Fig. 7 also depict that increase in the value of q_1 leads to increase in the extent of self-focusing of the second laser beam. This is due to the fact that due to nonlinear coupling between the two laser beams, the increase in value of q_1 favors the nonlinear refraction of beam2.

Figure 8 depicts the effect of deviation parameter q_2 of beam 2 on evolution of the beam widths of the two laser beams. It can be seen that increase in value of q_2 decreases the self-focusing of beam 2 and increases that of beam 1.

Excitation of electron plasma wave (EPW)

EPW that results in the generation of second-harmonics radiations can be excited into the plasma due to remarkable properties of plasma. Plasma as a whole possesses quasi-neutrality, i.e., it contains almost equal number of free electrons and ions. But, as the electrons and net positively charged ions are separated, a disturbance can create regions of net negative and regions of positive charges acting like the plates of a charged parallel plate capacitor. Such an uneven

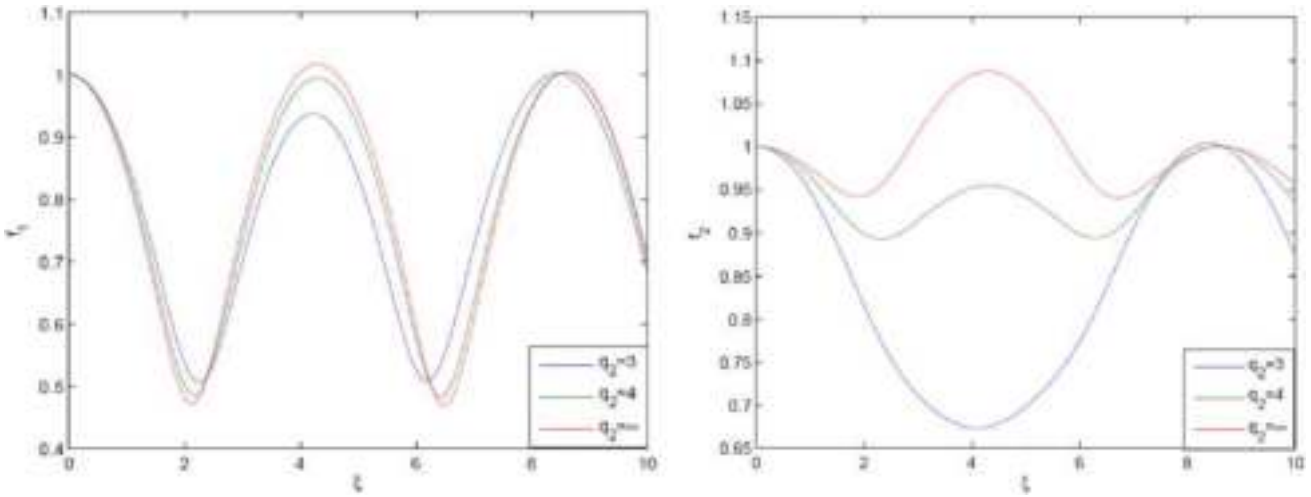

Fig. 8 Variation of beam width parameters f_1 and f_2 of the laser beams with distance of propagation in plasma for different values of q_2 and at fixed values of $q_1 = 3$, $\frac{\omega_{p0}^2 r_1^2}{c^2} = 9$, $\beta_1 E_{10}^2 = 3$ and $\beta_2 E_{20}^2 = 1$

distribution of charges results in an electric field running from positive to negative regions. This electric field pulls the electrons and ions toward each other with equal forces. Ions being much heavier than the electrons remain at rest and the electrons move toward the positive regions. As the electrons move toward the ions, they steadily gain velocity and momentum like a pendulum moving toward its mean position from an extreme position. Due to this gain in momentum, the electrons overshoot their equilibrium positions resulting in reversing the direction of electric field. Now, the reversed electric field opposes the motion of electrons and slows them down and then pulling them back again. The process repeats itself, establishing electron oscillations. In the presence of thermal velocities, these electrons oscillations form a longitudinal wave of positive and negative regions traveling through the plasma (Fig. 9).

The electron oscillators can be set in motion by intense laser beams. As the laser beams enter the plasma region, they exert pressure on plasma electrons, and hence, the plasma electrons move out of the way. As the laser beams exit, leaving a region deficient of electrons, the plasma electrons rush back to establish equilibrium. This movement of plasma electrons initiates the oscillations and results in a plasma wave.

As the two laser beams with different frequencies are propagating simultaneously through the plasma, the plasma oscillations of the plasma electrons under the fields of the two laser beams also contain a frequency component equal to the sum of the frequencies of the two laser beams. The electron density perturbation n' associated with the excited EPW evolves according to the wave equation

$$\frac{\partial^2 n'}{\partial t^2} - v_{th}^2 \nabla^2 n' + \omega_p^2 n' = \frac{e}{m} n_0 \nabla \Sigma_j E_j \tag{16}$$

Taking

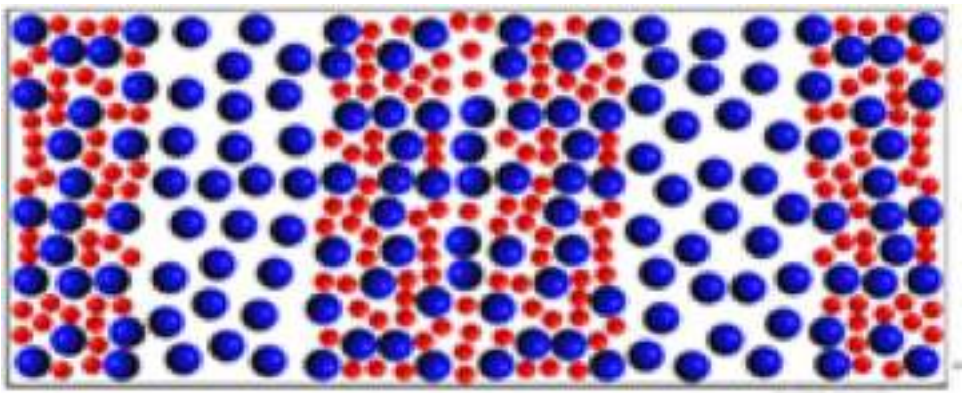

Fig. 9 Electron plasma wave

$$n' = n_1 e^{i(kz-\omega t)}$$

where $\omega = \omega_1 + \omega_2$ and $k = k_1 + k_2$, we get the amplitude of density perturbation associated with plasma wave

$$n_1 = \frac{en_0}{m}\frac{1}{\left(\omega^2 - k^2 v_{\text{th}}^2 - \omega_{\text{p}}^2\right)}\left[\frac{E_{10}}{r_{\text{I}}^2 f_1^3}\left(1+\frac{r^2}{q_1 r_{\text{I}}^2 f_1^2}\right)^{-\frac{q_1}{2}-1} + \frac{E_{20}}{r_2^2 f_2^3}\left(1+\frac{r^2}{q_2 r_2^2 f_2^2}\right)^{-\frac{q_1}{2}-1}\right] r \tag{17}$$

Second-harmonic generation

The density perturbation associated with excited EPW results in a nonlinear current density at frequency $\omega = \omega_1 + \omega_1$ that acts as source for a new radiation at frequency ω, for $\omega_1 = \omega_2$, this new radiation will be having frequency twice that of the pump beams and is thus called as second-harmonic radiation (Fig. 10).

e generated current density is given by

$$J_{\text{T}} = \frac{e^2 n_0}{m\omega}\left(\frac{n_1}{n_0}\right) e^{i(\omega t - kz)}\left(E_1 + E_2\right) \tag{18}$$

The electric field of the resulting harmonic radiation evolves according to the wave equation

$$\nabla^2 E_{\text{T}} = \frac{1}{c^2}\frac{\partial^2 E_{\text{T}}}{\partial t^2} + \frac{4\pi}{c^2}\frac{\partial J_{\text{T}}}{\partial t} \tag{19}$$

This equation gives the magnitude of electric field of second-harmonic radiation as

$$E_{\text{T}} = i\frac{\left(\frac{\omega_{\text{p0}}^2}{c^2}\right)}{\left(\frac{\omega^2}{c^2} - k^2\right)}\frac{n_1}{n_0}\left(E_1 + E_2\right) \tag{20}$$

Defining the normalized power of second-harmonic radiation as

$$P_{\text{T}} = \frac{\int_0^\infty E_{\text{T}} E_{\text{T}}^* r\text{d}r}{\int_0^\infty A_1 A_1^* r\text{d}r} \tag{21}$$

We get

$$P_{\text{T}} = \frac{\left(\frac{\omega_{\text{p0}}^2}{c^2}\right)^2}{\left(\frac{\omega^2}{c^2} - k^2\right)^2}\frac{\int\left(\frac{n_1}{n_0}\right)^2\left(E_1 + E_2\right)^2 r\text{d}r}{\int A_1 A_1^* r\text{d}r} \tag{22}$$

Equation (22) gives the normalized power of the second-harmonic radiation produced by the two laser beams while propagating through the plasma. Equation 22 has been solved numerically in association with the beam width eqs.14 and 15, and the corresponding evolutions of the normalized power with distance of propagation for different values of q_j are depicted in Fig. 11. It has been observed that the power of second-harmonic radiation is a monotonically increasing function of propagation, showing step like behavior. Each step occurs at the position of the minimum beam width of the two laser beams. This is because as the pump beams get self-focused their intensity increases and consequently the oscillation amplitude of the plasma electrons also increases which in turn increases the amplitude of the generated EPW. Since, the density perturbation associated with EPW acts as source for nonlinear current density for second-harmonic radiation, there is monotonic increase in the second-harmonic power with distance.

To understand the physics of SHG in plasmas consider the simultaneous propagation of two intense laser beams through a plasma whose density is rippled along the direction of propagation of the two laser beams. These density ripples of the plasma are due to the propagation of an electron plasma wave through the plasma. In the presence of the laser beams, the plasma electrons start oscillating under the effect of the field of the laser beams and thus generate a transverse electric current J_{T}. Under proper matching of the wave vectors and frequencies, the transverse current generates a second-harmonic wave. The generated harmonic wave then beats with the incident laser beams and thus produces variations in wave pressure. These variations in wave pressure lead to migration of plasma electrons from the regions of high pressure to the regions of low pressure. The resulting density perturbation reinforces the initial density fluctuations associated with electron plasma wave, i.e., the plasma wave gets amplified. The presence of this feedback loop (Fig. 12) leads to the amplification of the harmonic wave with distance of propagation.

The step like behavior of the power of second-harmonic radiation at the positions of the minimum beam width of the pump beams is owing to the fact that these are the regions of highest intensity, and hence, the current density for second-harmonic radiation is maximum there. Hence, after attaining its maximum value the power of second-harmonic radiation moves toward its next possible higher value at next focal spot. These transitions of second-harmonic power from one maximum value to next maximum value give it a step like behavior.

Reduction in the power P_{T} of second-harmonic radiation with increase in the value of deviation parameter q_1 of beam 1 has also been observed from the plots in Fig. 11. The underlying physics behind this is the one-to-one

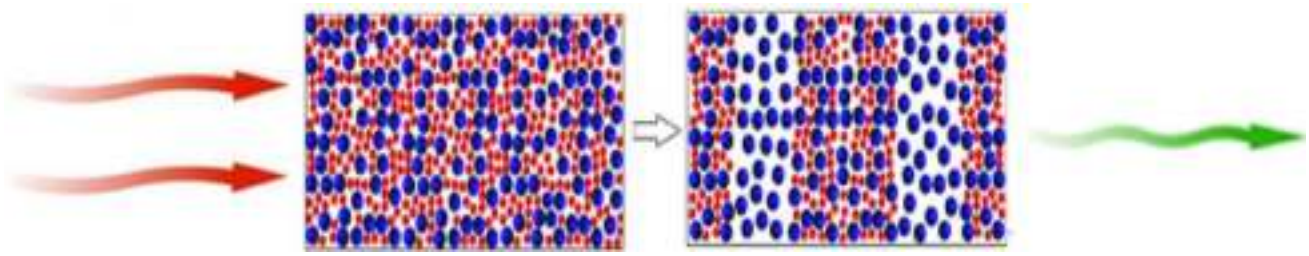

Fig. 10 Second-harmonic generation in plasma

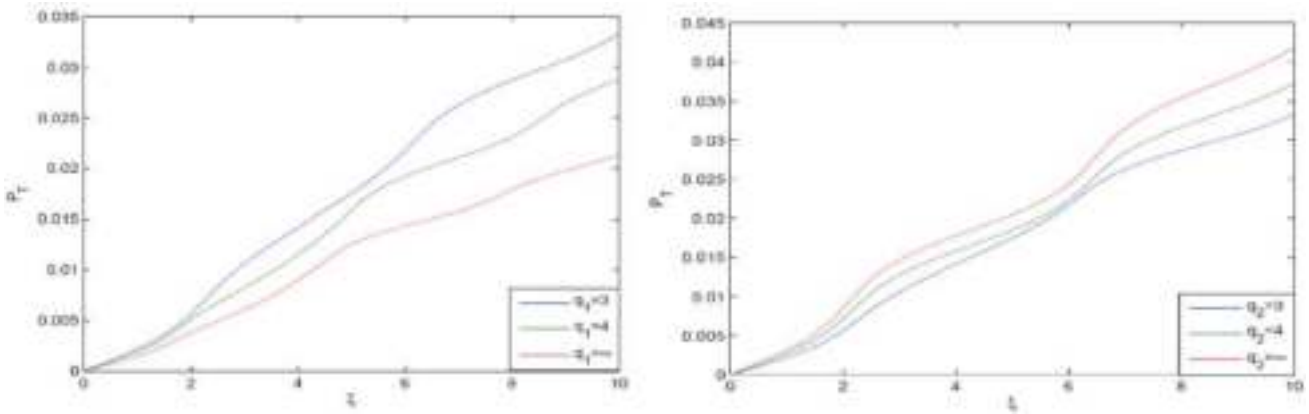

Fig. 11 Variation of normalized power P_T of second-harmonic radiation with distance of propagation in plasma for different values of deviation parameters of the laser beams and at fixed values of $q_2 = 3, \beta_1 E_{10}^2 = 3$ and $\frac{\omega_{p0}^2 r_1^2}{c^2} = 9$

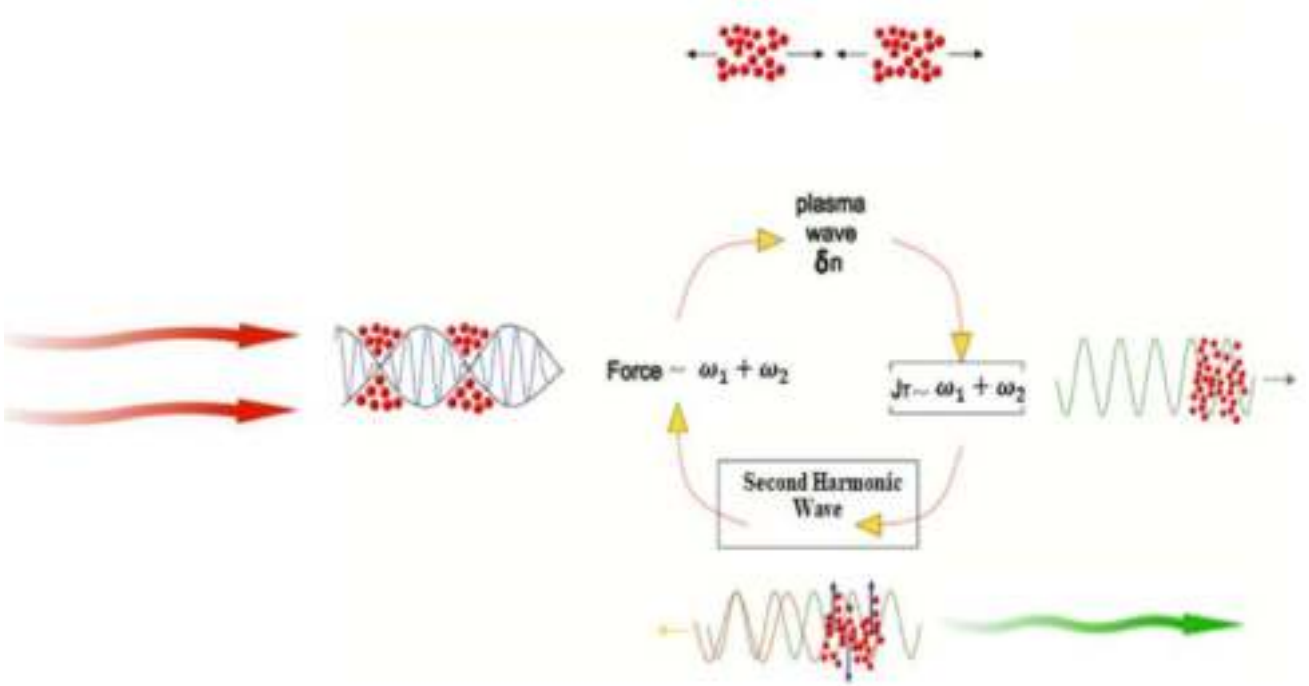

Fig. 12 Feedback loop for amplification of second-harmonic radiation

correspondence between the power of second-harmonic radiation and the degree of self-focusing of the pump beams. As increase in the value of q_1 reduces the extent of focusing of the pump beam 1 (beam with higher initial intensity) and increases the focusing of beam 2. However, in producing second-harmonic radiation, dominant role is played by beam with higher initial intensity. Hence, there is corresponding decrease in the power of second-harmonic radiation with increase in q_1. Same is the reason behind the observed increase in the power of second-harmonic radiation with increase in the value of deviation parameter q_2 of beam 2 (Fig. 11).

Conclusions

In conclusion, we have investigated the effect of cross-focusing of intense laser beams on second-harmonic generation in plasma under the effect of relativistic nonlinearity. Effect of the deviation of amplitude structure of laser beams from ideal Gaussian profile has been incorporated through q-Gaussian distribution. It has been observed that deviation parameters of the laser beams significantly affect the cross-focusing and hence the power of generated second-harmonic radiation. As the amplitude structure of laser beam with higher initial intensity (i.e., pump beam) converges toward the ideal Gaussian profile, there is decrease in the power of generated second-harmonic radiation. However, in case, the amplitude structure of laser beam with lower initial intensity (i.e., probe beam) converges toward the ideal Gaussian profile, and there is increase in the power of generated second-harmonic radiation. Thus, by controlling the deviation parameters of the pump and probe beams, one can optimize the power of second-harmonic radiation for a given set of plasma parameters. The results of present study may be helpful for the experimentalists working in the field of laser–plasma interactions.

References

1. T.H. Maiman, Stimulated optical radiation in Ruby. Nature **187**, 493 (1960)
2. S.E. Miller, Communication by laser. Sci. Am. **214**, 19 (1966)
3. T. Fortier, E. Baumann, 20 years of developments in optical frequency comb technology and applications. Commun. Phys. **2**, 153 (2019)
4. M. Giunta, W. Hansel, M. Fischer, M. Lezius, T. Udem, R. Holzwarth, Real-time phase tracking for wide-band optical frequency measurements at the 20th decimal place. Nat. Photonics **14**, 44 (2020)
5. S. Mak, D. Yip, The measurement of the speed of light using a laser pointer. Phys. Educ. **35**, 95 (2000)
6. D.K. Mao, X.B. Deng, H.Q. Luo, Y.Y. Xu, M.K. Zhou, X.C. Duan, Z.K. Hu, A dual-magneto-optical-trap atom gravity gradiometer for determining the Newtonian gravitational constant. Rev. Sci. Inst. **92**, 053202 (2021)
7. E. Khalkhal, M.R. Tavirani, M.R. Zali, Z. Akbari, The evaluation of laser application in surgery: a review article. J. lasers in med. Sci. **10**, S104 (2019)
8. E. Esarey, C.B. Schroeder, W.P. Leemans, Physics of laser-driven plasma-based electron accelerators. Rev. Mod. Phys. **81**, 1229 (2009)
9. N. Gupta, S.B. Bhardwaj, Relativistic effects on electron acceleration by elliptical q-Gaussian laser beam driven electron plasma wave. Opt. Quant. Electron. **53**, 700 (2021)
10. N. Gupta, Hot electron generation by self focused quadruple gaussian laser beams during inertial confinement fusion. Nonlinear Opt. Quan. Opt. **55**, 63 (2022)
11. P.A. Franken, A.E. Hill, C.W. Peters, G. Weinreich, Generation of optical harmonics. Phys. Rev. Lett. **7**, 118 (1961)
12. N. Gupta, Optical second and third harmonic generation of laser beams in nonlinear media: a review. Nonlinear Opt. Quant. Opt. **53**, 291 (2021)
13. A. Singh, N. Gupta, Higher harmonic generation by self-focused q-Gaussian laser beam in preformed collisionless plasma channel. Laser Part. Beams **32**, 621 (2014)
14. N. Gupta, Second harmonic generation of q-Gaussian laser beam in plasma channel created by ignitor heater technique. Laser Part. Beams **37**, 184 (2019)
15. N. Gupta, S. Kumar, Generation of second harmonics of self-focused quadruple-Gaussian laser beams in collisional plasmas with density ramp. J. Opt. **49**, 455 (2020)
16. N. Gupta, N. Singh, A. Singh, Second harmonic generation of q-Gaussian laser beam in preformed collisional plasma channel with nonlinear absorption. Phys. Plasmas **22**, 113106 (2015)
17. A. Singh, N. Gupta, Second harmonic generation by relativistic self-focusing of q-Gaussian laser beam in preformed parabolic plasma channel. Phys. Plasmas **22**, 013102 (2015)
18. A. Sharma, I. Kourakis, Spatial evolution of a q-Gaussian laser beam in relativistic plasma. Laser Part. Beams **28**, 470 (2010)
19. N. Gupta, S. Kumar, S.B. Bhardwaj, Stimulated Raman scattering of self-focused elliptical q-Gaussian laser beam in plasma with axial density ramp: effect of ponderomotive force. J. Opt. (2021). https://doi.org/10.1007/s12596-021-00822-8
20. A.I. Akhiezer, R.V. Polovin, Theory of wave motion of an electron plasma. Sov. Phys. JETP **3**, 696 (1956)
21. D. Anderson, M. Bonnedal, Variational approach to nonlinear self-focusing of Gaussian laser beams. Phys. Fluids **22**, 105 (1979)
22. D. Anderson, M. Bonnedal, M. Lisak, Self-trapped cylindrical laser beams. Phys. Fluids **22**, 1838 (1979)

Second-harmonic generation of two cross-focused q-Gaussian laser beams by nonlinear frequency mixing in plasmas

Article *in* Journal of Optics · November 2022

DOI: 10.1007/s12596-022-00995-w

CITATION
1

READS
33

7 authors, including:

S B Bhardwaj
SUS Govt College Indri Karnal
69 PUBLICATIONS **364** CITATIONS
SEE PROFILE

Sanjeev Kumar
Government College for Women, Karnal, Haryana, India
26 PUBLICATIONS **77** CITATIONS
SEE PROFILE

Suman Choudhry
Government College for Women, Karnal, Haryana, India
22 PUBLICATIONS **46** CITATIONS
SEE PROFILE

Siddhanth Shishodia
Lovely Professional University
3 PUBLICATIONS **2** CITATIONS
SEE PROFILE

J Opt
https://doi.org/10.1007/s12596-022-00995-w

RESEARCH ARTICLE

Second-harmonic generation of two cross-focused q-Gaussian laser beams by nonlinear frequency mixing in plasmas

Naveen Gupta[1] · S. B. Bhardwaj[2] · Sanjeev Kumar[1] · Suman Choudhry[1] · Rishabh Khatri[1] · Siddhanth Shishodia[1] · Rohit Johari[1]

Received: 11 July 2022 / Accepted: 18 October 2022

Abstract A scheme for second-harmonic generation (SHG) of a pair of q-Gaussian laser beams interacting nonlinearly with underdense plasma has been proposed. Due to the relativistic increase in electron mass under the intense fields of the laser beam, the resulting optical nonlinearity of plasma leads cross-focusing of the laser beams. The resulting nonlinear coupling between the two laser beams makes the oscillations of plasma electrons to contain a frequency component equal to the sum of frequencies of the pump beams. This results in a nonlinear current density at frequency equal to the sum of frequencies of the pump beams. If the frequencies of the pump beams are equal, then the resulting nonlinear current generates a new radiation at frequency twice the frequencies of the pump beams— a phenomenon known as SHG. Starting from nonlinear Schrodinger wave equation a set of coupled differential equations governing the evolution of beam widths of the laser beams and power of generated second-harmonic radiation with longitudinal distance has been obtained with the help of variational theory. The equations so obtained have been solved numerically to envision the effect of laser as well as plasma parameters on the power of generated second-harmonic radiation.

Keywords Cosh Gaussian · Self-focusing · Nonlinear optics · Second-harmonic generation · Clean energy

✉ Naveen Gupta
naveens222@rediffmail.com

[1] Lovely Professional University, Phagwara, India

[2] SUS Govt College, Matak-Majri, Indri, Karnal, India

Introduction

The invention of the laser [1] is the most towering achievement in the long history of light. It brought an extraordinary technological leap, which has since paved the way for a startling new era in optical science and technology. For the first time, man got a remarkable tool for direct generation and manipulation of coherent light. Laser brought same revolution to optics that transistor brought to electronics and cyclotron brought to nuclear physics. The distinctive qualities of laser derive from its coherence properties, which result in a beam of light with a well-defined optical phase both in space and time. This prescribed phase generally confines the wavelength and frequency of the laser light to a restricted range, so that the beam exhibits a narrow frequency spectrum. Another unique property of laser light is its directionality, which means that the beam can propagate over great distances without significant spreading and can be readily manipulated using conventional optical elements. The phase coherence and directionality of the laser make it possible to create extremely large optical powers and focused intensities that cannot be obtained from incoherent light emitters. These characteristics also allow accurate transfer of information [2], precise calibration of time [3, 4], and measurements of many physical constants [5, 6], among numerous other applications, using laser light. Lasers are now standard components of such commonplace objects as compact-disk players and printers. The everyday presence of lasers does not mean, however, that they have been reduced to performing only pedestrian tasks. Higher-end applications like laser surgery [7], laser-driven particle accelerators [8, 9], inertial confinement fusion [10], etc., are also abound.

Success is never without limitations, and laser is also not an exception. By the virtue of its unique coherence properties, laser light contains only a confined band of frequencies

Published online: 05 November 2022

determined by the energy gap in the laser material. In this regard, the laser can be viewed as a light source with limited spectral versatility. It is possible to develop tunable lasers with more extended spectral emission using materials with broadened energy levels or energy bands). However, the maximum spectral coverage available to the most prominent tunable lasers (e.g., Ti:sapphire) is still limited to at best 300–400 nm. In addition, the restricted availability of suitable laser materials has confined the wavelength coverage of existing tunable lasers mainly to the visible and near-infrared spectrum. These limitations have left substantial portions of the optical spectrum inaccessible to lasers, and alternative methods for the generation of coherent light in these regions have had to be devised.

One of the most effective techniques to overcome the spectral limitations of lasers is to exploit nonlinear optics. The potential of nonlinear processes for the generation of tunable coherent radiation was recognized soon after the invention of the laser [11]. Nonlinear optical techniques are based on a fundamentally different principle from lasers. While the process of light emission in a laser is a direct result of the transitions between the energy levels in the laser gain medium, nonlinear optical processes rely on the alternative mechanism for light generation, namely electric dipole oscillations [12].

When light is incident on matter, the bound electrons vibrate in the electromagnetic field. While moving under the electromagnetic force, the electrons generate a synchronous polarization field, which interferes with the original field. At low amplitude, this generated field is proportional to the exciting one, and the interference between the driving field and the generated one is the origin of the linear properties of light in matter, such as those described by the optical index of refraction. On the other hand, when the input electric field is large, electron displacement becomes nonlinear at the higher field strengths. This is the regime of nonlinear optics. The exact form of nonlinear response depends on crystallographic structure of the material (Figs. 1, 2).

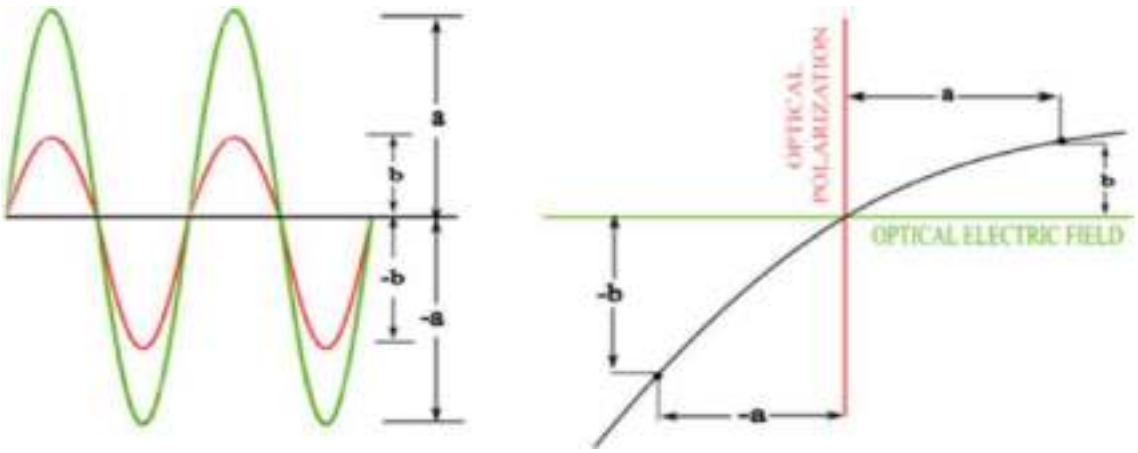

Fig. 1 Nonlinear response of noncentrosymmetric crystal

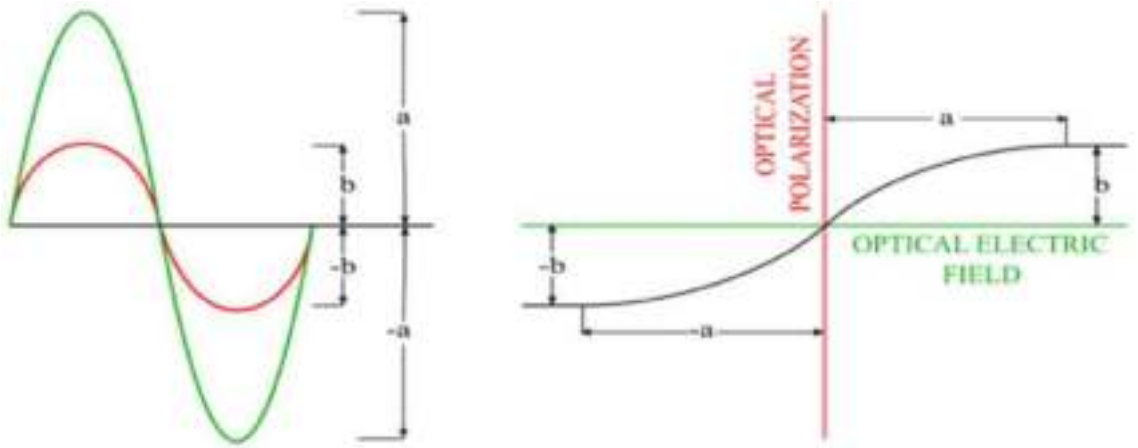

Fig. 2 Nonlinear polarization in symmetrical crystals

However, in either case, the electrons oscillate not only at the input frequency but also over an infinite range of frequencies, above and below the input frequency that can be seen from the Fourier expansion of the electron displacement. The resulting light emission from the oscillating electrons is thus also over an infinite band of frequencies. If the potential that binds the electrons in the material is asymmetric in space, the electron orbits will be distorted relative to the symmetric case, that is, elongated in the direction of the more confining part of the potential. The distorted electron orbits will then generate harmonic polarization waves. For instance, a wave at radial frequency ω will generate a wave at frequency 2ω (Fig. 3). This is called second-harmonic generation (SHG) and is widely used in the field of nonlinear optics.

A concise and clear description of the physical mechanism of SHG can also be given on the basis of quantum theory of radiations which is based on quantum electrodynamics. The main advantage of using this theory is that whenever there is an exchange of energy and momentum either among different components of optical fields or between the optical field and the medium, this theory can reveal the coherent wave property of the optical field as well as the quantum nature of the field. The starting point of this theory is to consider the optical field and the molecules of the nonlinear medium as a combined and quantized system. The interaction between the optical field and the molecule results in (i) transition of the molecule among its different energy states and (ii) a simultaneous change of distribution of photons in different modes (photon states). In order to give a rigorous and complete physical description for these processes, the key concept of intermediate state must be introduced, which is a quantum state characterizing the whole system involving both optical fields and the molecule. In such an intermediate state of the whole system, the photon number (degeneracy) in a mode has changed by $+1$ or -1, while the molecule has left its original state (mostly ground state); however, at this moment, the molecule is not certainly located in any specific excited state, but correlated with all possible excited states with a certain occupying probability for each. In this case, it is convenient to introduce a virtual energy level in the energy diagram to represent such an intermediate state. In the intermediate state represented by a virtual state level, the energy range of all molecular eigen states that may be occupied by an excited molecule is nearly unlimited; according to the uncertainty principle, the staying time of this molecule in that intermediate state is infinitely short. Relying on the concept of intermediate state and its representation of a virtual energy level, many nonlinear optical effects can be interpreted very clearly.

As an example, the schematic energy-level diagram describing SHG is shown in Fig. 4. In this case, the

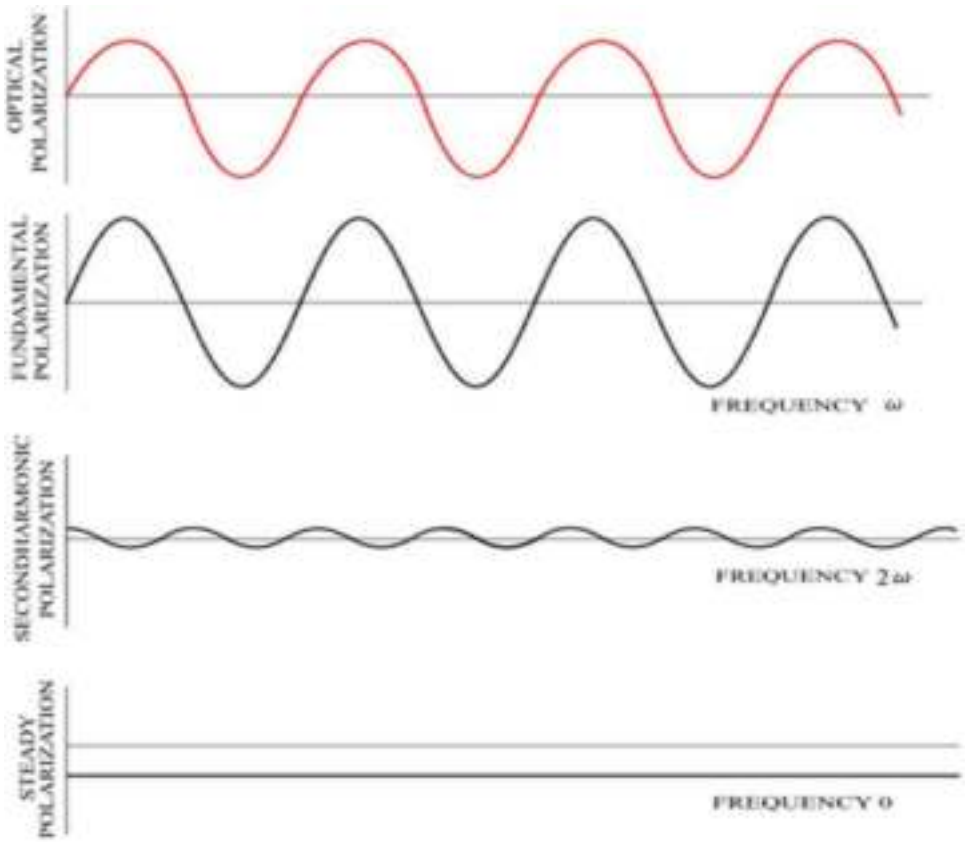

Fig. 3 Second-harmonic generation in noncentrosymmetric media

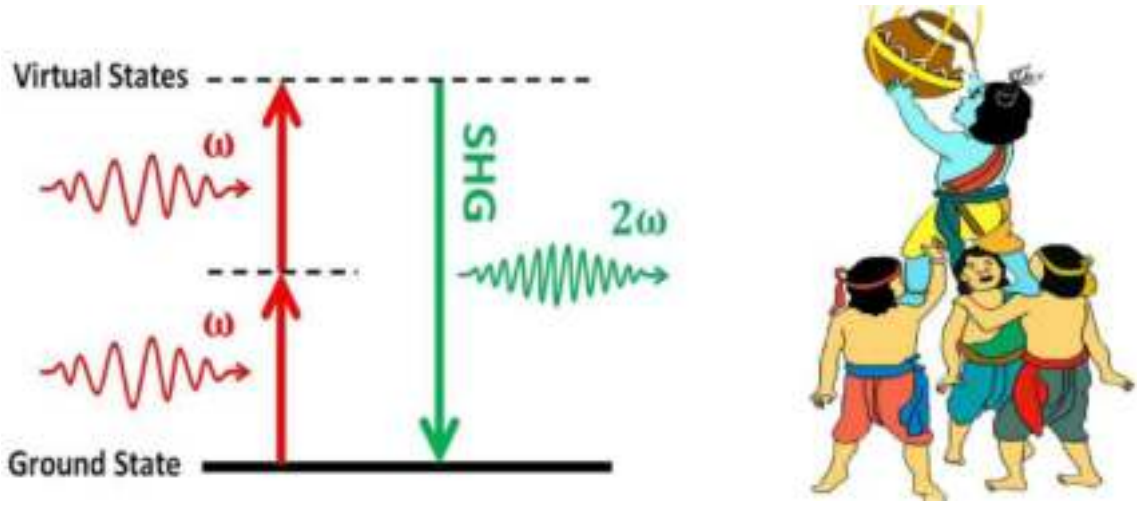

Fig. 4 QED description of SHG

elementary process of SHG occurs via multiple quantum transitions or multiple steps. In the first step, there is an annihilation of one photon from the fundamental light field, while a molecule of the medium left its initial (ground) state to an intermediate state; in the second step, there is the annihilation of another fundamental photon, while the excited molecule is situated in another intermediate state; in the final step, this excited molecule is returning to its initial state, while there is the creation of a new photon of doubled frequency. Since the staying time of the molecule in each intermediate state is extremely short (near the response time of electron-cloud distortion), the above-mentioned three steps actually occur instantaneously and simultaneously. Here, we have to visualize that the elementary SHG process undergoes three quantum transitions via two intermediate states, because in the quantum theory of radiation for each quantum transition of the whole system, the photon number in a given mode can only change either by − 1 (i.e., annihilation of a photon) or + 1 (i.e., creation of a photon). This rule holds for any types of optical processes involving emission, absorption, or molecular scattering of light. We should keep in mind that for all those phenomena (such as nonlinear frequency mixing, Raman scattering, and multi-photon absorption), the observable elementary process is actually an instantaneous single event even though which may undergo multiple quantum transitions via one or multiple intermediate states. With such an understanding, for instance, the elementary process of SHG can also be simply described as the annihilation of two fundamental photons and the simultaneous creation of one second-harmonic photon.

Similarly, if the potential that binds the electrons in the material is symmetric in space, then the wave at frequency ω will generate a new wave at frequency 3ω (Fig. 5).

If two waves of frequencies ω_1 and ω_2 propagate simultaneously through a nonlinear medium, then it may result in the generation of new waves at frequencies $2\omega_1, 2\omega_2, \omega_1 + \omega_2 \cdot \omega_1 - \omega_2$ (Fig. 6).

In case of plasmas, the role of polarization waves is played by the propagating electron plasma waves EPWs. Thus, plasmas can also lead to the generation of higher harmonics of the incident waves through the process of nonlinear frequency mixing. However, plasmas offer several advantages over the other nonlinear media for frequency mixing. The major advantage is that there is no upper threshold on the power of radiation that can be sent through them. Plasmas by definition are already ionized, and thus, they have infinite immunity against ionization-induced damages. In contrast to this, the best-known glasses get damaged by ionization only at 10 W/cm^2. Thus, second harmonics of any intensity can be produced with the help of plasmas as a nonlinear medium [13–15].

Most laser beams have a Gaussian irradiance profile, although it can be beneficial to use a non-Gaussian beam in certain applications [16, 17]. The irradiance cross section of Gaussian beams decreases symmetrically with increasing distance from the center. Gaussian laser profiles have several disadvantages, such as the low-intensity portions on either side of the usable central region of the beam, known as "wings." These wings typically contain energy that is wasted because it is at a lower intensity than the threshold required for the given application, whether it is materials processing, laser surgery, laser-driven fusion or another application where an intensity above a given value is needed. Thus, due to their expanded wings of the irradiance profile, a new class of laser beams known as q-Gaussian laser beams has gained a significant interest of researchers working in the area of laser–plasma

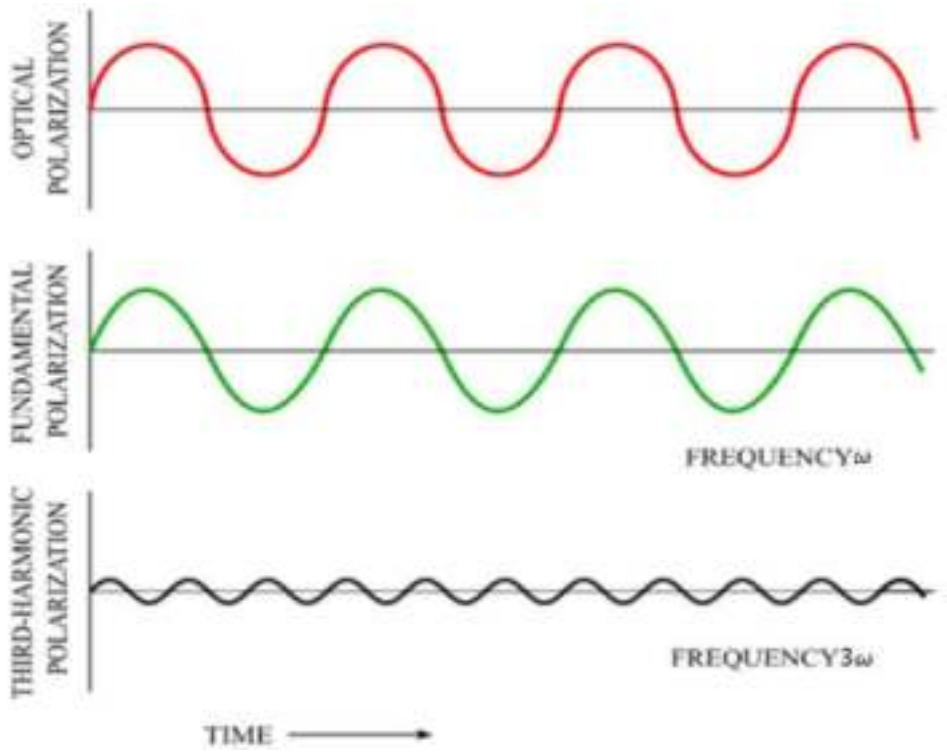

Fig. 5 Third harmonic generation in centrosymmetric media

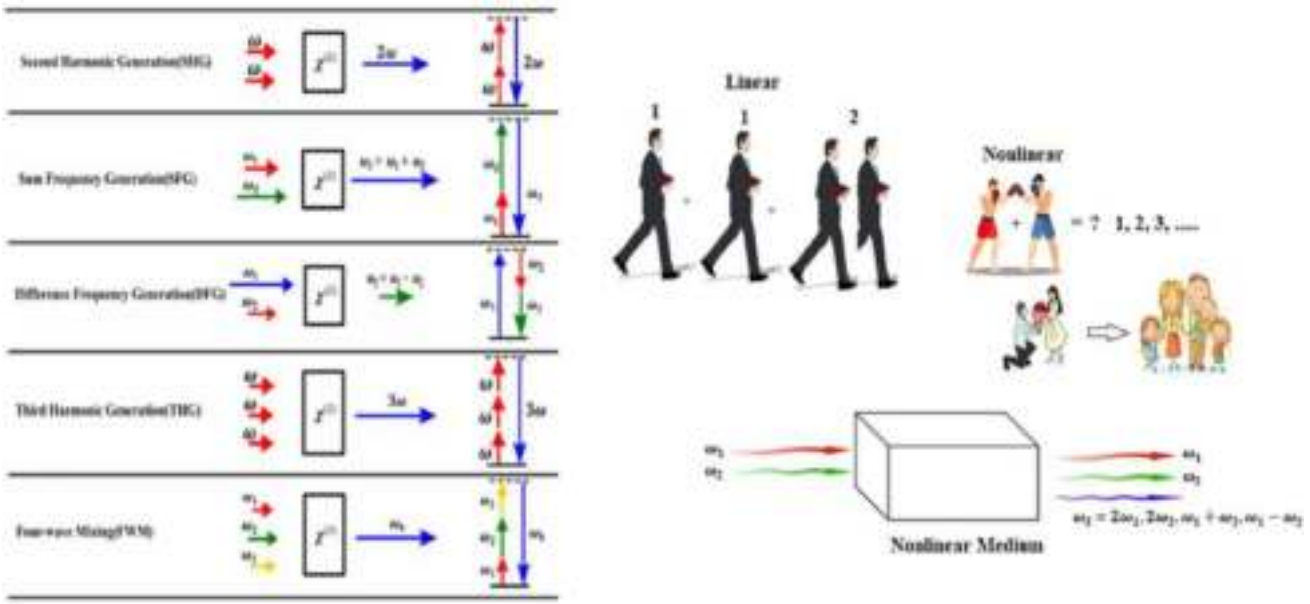

Fig. 6 Frequency mixing in nonlinear media

interactions [18, 19]. These beams contain a significant amount of energy outside the full width half maximum of their irradiance profile. The literature review reveals the fact that most of the earlier investigations on SHG of intense laser beams in plasmas have been reported for Gaussian laser beams. Thus, this article aims to give first theoretical investigation on SHG of q-Gaussian laser beams in plasma by nonlinear frequency mixing including the effect of cross-focusing of the laser beams.

Relativistic nonlinearity of plasma

Consider the propagation of two coaxial laser beams with electric field vectors

$$\boldsymbol{E}_j(r,z,t) = A_j(r,z)e^{i\left(k_j z-\omega_j t\right)}\boldsymbol{e}_x, \quad j=1,2 \tag{1}$$

Through a plasma with equilibrium electron density n_0. Here, k_j, ω_j are the wave numbers and angular frequencies of the fields of the laser beams, and $A_j(r, z)$ are their slowly varying complex amplitudes. The amplitude structure over the cross sections of the q-Gaussian laser beams is given by [19]

$$A_j(r,z) = \frac{E_{j0}}{f_j}\left(1+\frac{r^2}{qr_j^2f_j^2}\right)^{-\frac{q_j}{2}} \tag{2}$$

Here, the phenomenological constant q_j is related to deviation of amplitude structure over the cross section of laser beams form ideal Gaussian profile. Laser beams with lower values of q_j are characterized by expanded wings of the intensity distribution in comparison to the ideal Gaussian distribution. Hence, the parameter q_j is also termed as deviation parameter. As the value of q_j increases, the amplitude structure over the cross section of the laser beams converges toward the ideal Gaussian profile. The functions $f_j(z)$ are the key parameters of interest that upon multiplication with initial beam radius r_j give the instantaneous beam widths of the laser beams. Hence, f_j is called as beam width parameter.

The dielectric function of a plasma with electron density n_e for an electromagnetic beam with frequency ω_j is given by

$$\varepsilon = 1-\frac{\omega_p^2}{\omega_j^2} \tag{3}$$

where

$$\omega_p^2 = \frac{4\pi e^2 n_0}{m_e} \tag{4}$$

is the natural frequency of oscillations of plasma electrons, i.e., plasma frequency. When under the effect of intense fields of the incident laser beams the quiver velocity of plasma electrons becomes comparable to that of speed of light in vacuum; then, the effective mass m_e of electron in Eq. (4) needs to be replaced by $m_0\gamma$, where γ is the relativistic Lorentz factor, and m_0 is the rest mass of electron. Following Akhiezer and Polovin [20], the relativistic Lorentz factor can be related to the total intensity of the laser beams as

$$\gamma = \left(1+\sum_j \beta_j A_j A_j^*\right)^{\frac{1}{2}} \tag{5}$$

where $\beta_j = \frac{e^2}{m_0^2c^2\omega_j^2}$ is the coefficient of relativistic nonlinearity.

Since, the effective dielectric function of plasma depends on effective mass of plasma electrons through the plasma frequency (Eq. 4). Hence, intensity dependence of electron mass in turn affects the optical properties of plasma in a nonlinear manner. The resulting intensity dependence of dielectric function of plasma for q-Gaussian laser beams can be written as

$$\varepsilon_j = 1-\frac{\omega_{p0}^2}{\omega_j^2}\left(1+\sum_j \frac{\beta_j E_{j0}^2}{f_j^2}\left(1+\frac{r^2}{qr_j^2f_j^2}\right)^{-q_j}\right)^{-\frac{1}{2}} \tag{6}$$

where

$$\omega_{p0}^2 = \frac{4\pi e^2}{m_0}n_e$$

is the plasma frequency in the absence of laser beams. From Eq. (6), it can be seen that the dielectric function of plasma is a function of intensities of both the laser beams. Hence, during their simultaneous propagation through plasma, the two laser beams get nonlinearly coupled with each other. Equation (6) can be written as

$$\varepsilon_j = \varepsilon_{0j} +_j \left(A_1A_1^*, A_2A_2^*\right) \tag{7}$$

where

$$\varepsilon_{0j} = 1-\frac{\omega_{p0}^2}{\omega_j^2} \tag{8}$$

are the linear parts of dielectric function and

$$\Phi_j\left(A_1A_1^*, A_2A_2^*\right) = \frac{\omega_{p0}^2}{\omega_j^2}\left\{1-\left(1+\sum_j \frac{\beta_j E_{j0}^2}{f_j^2}\left(1+\frac{r^2}{q_j r_j^2 f_j^2}\right)^{-q_j}\right)^{-\frac{1}{2}}\right\} \tag{9}$$

are the nonlinear parts of dielectric function.

Cross-focusing of laser beams

The evolution of beam envelope of an optical beam through a nonlinear medium is governed by the wave equation

$$i\frac{\partial A_j}{\partial z} = \frac{1}{2k_j}\nabla_\perp^2 A_j + \frac{k_j}{2\varepsilon_{0j}}\phi_j\left(A_1A_1^*, A_2A_2^*\right)A_j \tag{10}$$

As Eq. (10) is a nonlinear partial differential equation, it does not possess any closed-form exact solution. Thus, in

order to have physical insight into the propagation dynamics of the laser beams, we have used a semi-analytical technique known as variational theory [21, 22] to solve Eq. (10). According to variational method, Eq. (10) is a variational problem for action principle based on Lagrangian density

$$
\begin{aligned}
&= i\left(A_1\frac{\partial A_1^*}{\partial z} - A_1^*\frac{\partial A_1}{\partial z}\right) + i\left(A_2\frac{\partial A_2^*}{\partial z} - A_2^*\frac{\partial A_2}{\partial z}\right)\\
&+\left|\nabla_\perp A_1\right|^2 + \left|\nabla_\perp A_1\right|^2 - \frac{\omega_1^2}{c^2}\int^{A_1A_1^*}\Phi\left(A_1A_1^*, A_2A_2^*\right)d\left(A_1A_1^*\right)\\
&-\frac{\omega_2^2}{c^2}\int^{A_2A_2^*}\Phi\left(A_1A_1^*, A_2A_2^*\right)d\left(A_2A_2^*\right)
\end{aligned}
\tag{11}
$$

Substituting the trial function for q-Gaussian beam profile in Lagrangian density and integrating over the entire cross section of the laser beam we get the reduced Lagrangian as $L = \int \pounds d^2r$. The corresponding Euler–Lagrange equations

$$
\frac{\mathrm{d}}{\mathrm{d}z}\left(\frac{\mathrm{d}L}{\partial\left(\frac{\partial f_j}{\partial z}\right)}\right) - \frac{\partial L}{\partial f_j} = 0 \tag{12}
$$

give

$$
\begin{aligned}
\frac{\mathrm{d}^2 f_j}{\mathrm{d}\xi^2} + \frac{1}{f_j}\left(\frac{\mathrm{d}f_j}{\mathrm{d}\xi}\right)^2 &= \frac{1}{k_j^2 r_j^4 f_j^3}\frac{\left(1-\frac{1}{q_j}\right)\left(1-\frac{1}{q_j}\right)}{\left(1+\frac{1}{q_j}\right)}\\
&+\frac{\left(1-\frac{2}{q_j}\right)}{r_j^2\varepsilon_{0j}I_{0j}}\int r^2 A_jA_j^*\frac{\partial\phi_j}{\partial r}\mathrm{d}^2 r
\end{aligned}
\tag{13}
$$

Using Eq. (9) in (13), the set of coupled differential equations for beam widths of the two laser beams are obtained

$$
\begin{aligned}
\frac{\mathrm{d}^2 f_1}{\mathrm{d}\xi^2} + \frac{1}{f_1}\left(\frac{\mathrm{d}f_1}{\mathrm{d}\xi}\right)^2 &= \frac{\left(1-\frac{1}{q_1}\right)\left(1-\frac{1}{q_1}\right)}{\left(1+\frac{1}{q_1}\right)}\frac{1}{f_1^3}\\
&-2\left(\frac{\omega_{p0}r_1}{c}\right)^2\left(1-\frac{1}{q_1}\right)\left(1-\frac{2}{q_1}\right)J_1
\end{aligned}
\tag{14}
$$

$$
\begin{aligned}
\frac{\mathrm{d}^2 f_2}{\mathrm{d}\xi^2} + \frac{1}{f_2}\left(\frac{\mathrm{d}f_2}{\mathrm{d}\xi}\right)^2 &= \left(\frac{r_1}{r_2}\right)^4\left(\frac{\omega_1}{\omega_2}\right)^2\left(\frac{\varepsilon_{01}}{\varepsilon_{02}}\right)\frac{\left(1-\frac{1}{q_2}\right)\left(1-\frac{1}{q_2}\right)}{\left(1+\frac{1}{q_2}\right)}\frac{1}{f_2^3}\\
&-2\left(\frac{\omega_{p0}r_1}{c}\right)^2\left(1-\frac{1}{q_2}\right)\left(1-\frac{2}{q_2}\right)J_2
\end{aligned}
\tag{15}
$$

where $\xi = \frac{z}{k_1 r_1^2}$ is the dimensionless distance of propagation, and

$$
\begin{aligned}
J_1 &= \frac{\beta_1 E_{10}^2}{f_1^3}T_1 + \frac{\beta_2 E_{20}^2}{f_1^3}\left(\frac{r_1}{r_2}\right)^2\left(\frac{f_1}{f_2}\right)^4 T_2\\
J_2 &= \frac{\beta_1 E_{10}^2}{f_2^3}T_3 + \frac{\beta_2 E_{20}^2}{f_2^3}\left(\frac{r_1}{r_2}\right)^2\left(\frac{f_1}{f_2}\right)^4 T_4\\
T_1 &= \int_0^\infty x^3\left(1+\frac{x^2}{q_1}\right)^{-2q_1-1}G(x)\mathrm{d}x\\
T_2 &= \int_0^\infty x^3\left(1+\frac{x^2}{q_1}\right)^{-q_1}\left(1+\frac{x^2}{q_2}\left(\frac{r_1f_1}{r_2f_2}\right)^2\right)^{-q_2-1}G(x)\mathrm{d}x\\
T_3 &= \int_0^\infty x^3\left(1+\frac{x^2}{q_1}\right)^{-q_1-1}\left(1+\frac{x^2}{q_2}\left(\frac{r_1f_1}{r_2f_2}\right)^2\right)^{-q_2}G(x)\mathrm{d}x\\
T_4 &= \int_0^\infty x^3\left(1+\frac{x^2}{q_2}\left(\frac{r_1f_1}{r_2f_2}\right)^2\right)^{-2q_2-1}G(x)\mathrm{d}x\\
G(x) &= e^{-\left\{\frac{\beta_1E_{10}^2}{f_1^2}\left(1+\frac{x^2}{q_1}\right)^{-q_1}+\frac{\beta_2E_{20}^2}{f_2^2}\left(1+\frac{x^2}{q_2}\left(\frac{r_1f_1}{r_2f_2}\right)^2\right)^{-q_2}\right\}}\\
x &= \frac{r}{r_1f_1}
\end{aligned}
$$

Equations (14) and (15) are the coupled nonlinear differential equations governing the cross-focusing of two coaxial q-Gaussian laser beams in collisionless plasma. For initially plane wavefronts, these equations are subjected to boundary conditions $f_j = 1$ and $\frac{\mathrm{d}f_j}{\mathrm{d}\xi} = 0$ at $\xi = 0$.

To analyze the effect of deviation of intensity distribution of laser beams from Gaussian distribution and plasma density on cross-focusing of the laser beams eqs.(14)-(15) have been solved for following set of laser-plasma parameters: $\omega_1 = \omega_2 = 1.758\times10^{14}\,\mathrm{rad\,s^{-1}}, \lambda_1 = \lambda_2 = 10.7\,\mu\mathrm{m}(\mathrm{CO_2\ laser}), r_1 = 15\,\mu\mathrm{m}, r_2 = 16\,\mu\mathrm{m}, T_0 = 10^7\,\mathrm{K}, \frac{\omega_{p0}^2 r_1^2}{c^2} = 9, \beta_1E_{10}^2 = 3, \beta_2E_{20}^2 = 1$ and for different values of q_1 and q_2 viz., $q_1 = q_2 = (3, 4, \infty)$.

Figure 7 illustrates the effect of deviation parameter q_1 of beam1 on focusing/defocusing of the two laser beams. It can be seen that during the propagation of the laser beams through plasma, their beam widths vary harmonically with distance. This behavior of the beam widths of the laser beams can be explained by examining the role and origin of various terms contained in Eqs. (14) and (15).

The first terms on the right-hand sides (R.H.S) of these equations that vary inversely with the cube of their beam widths are the spatial dispersive terms that model the spreading of the laser beams in transverse directions occurring as consequence of light's wave nature of diffraction. The second terms on the R.H.S of these equations that have complex dependence on beam widths f_1 and f_2 of the two laser beams arise as a consequence of relativistic nonlinearity of plasma and nonlinear coupling the laser beams with each other. It can be seen that although two

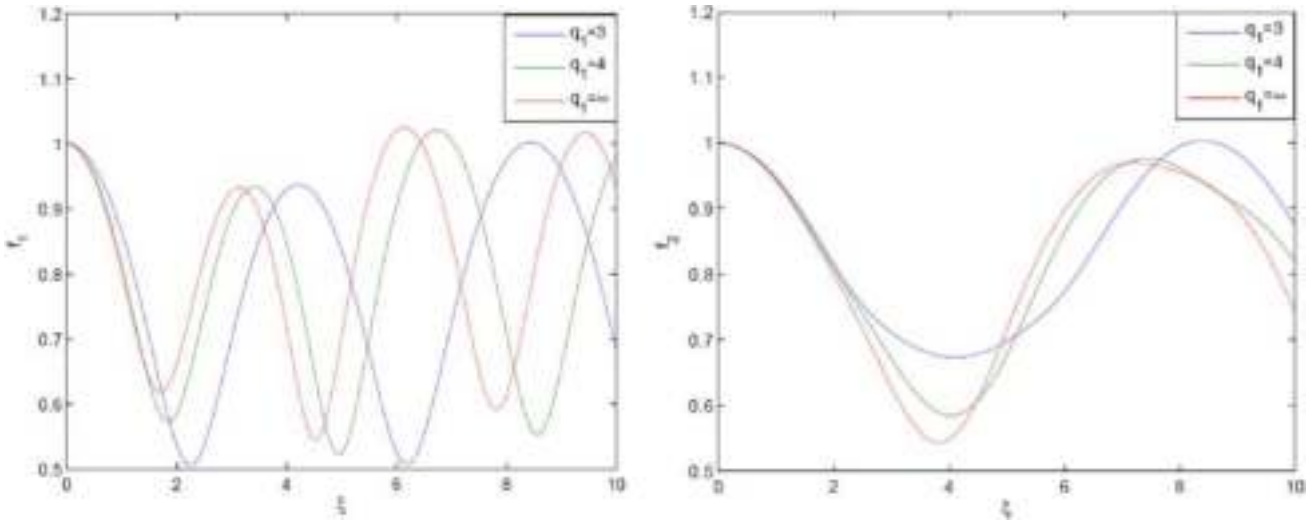

Fig. 7 Variation of beam width parameters f_1 and f_2 of laser beams with distance of propagation in plasma for different values of q_1 and at fixed values of $q_2 = 3$, $\frac{\omega_{p0}^2 r_1^2}{c^2} = 9$, $\beta_1 E_{10}^2 = 3$ and $\beta_2 E_{20}^2 = 1$

copropagating laser beams through vacuum do not interact with each other, but during their propagation through plasma medium, they get coupled with each other. As a consequence of the relativistic nonlinearity of plasma, the resulting nonlinear refraction of the laser beams tends to counterbalance the effect of diffraction by inducing a convex lens-like structure into the plasma. Thus, during the propagation of the laser beams through plasma, there starts a competition between the two phenomena of diffraction and nonlinear refraction. The winning phenomenon ultimately decides the behavior of the laser beams, i.e., whether the beams will converge or diverge. Thus, there exists a critical value of the total beam intensity above which the beams will converge.

In the present investigation, the initial beam intensity has been taken to be greater than the critical intensity, i.e., why the spot sizes of the two laser beams are converging initially. As the beam widths of the laser beams get reduced, their intensity increases. When the intensity of the laser beams become too high, the mass of plasma electrons and thus the optical nonlinearity of plasma get saturated. Thus, the laser beams propagate as if they are propagating through a linear medium. Hence, after attaining minimum possible value, the beam widths of the two laser beams bounce back to their initial values. As the beam widths of the laser beams start increasing, the competition between diffraction and nonlinear refraction starts again. Now, the competition lasts till maximum values of f_1 and f_2 are obtained. These processes go on repeating themselves and thus give breather-like behavior to the spot sizes of the laser beams.

The plots in Fig. 7 depict that increase in the value of q_1 leads to decrease in the extent of self-focusing of first laser beam. This is due to the fact that as the value of q_1 increases toward higher values, the intensity of the first laser beam shifts toward the axial region of the wavefront. As a result, laser beams with higher q value get lesser contribution from the off axial rays toward nonlinear refraction. As nonlinear refraction of the laser beam is a homeostasis for self-focusing, increase in the value of q_1 results in reduced focusing of beam 1. It is also observed from Fig. 7 that the laser beams with higher q values possess faster focusing. The underlying physics behind this fact is the slower-focusing character of the off-axial rays.

The plots in Fig. 7 also depict that increase in the value of q_1 leads to increase in the extent of self-focusing of the second laser beam. This is due to the fact that due to nonlinear coupling between the two laser beams, the increase in value of q_1 favors the nonlinear refraction of beam2.

Figure 8 depicts the effect of deviation parameter q_2 of beam 2 on evolution of the beam widths of the two laser beams. It can be seen that increase in value of q_2 decreases the self-focusing of beam 2 and increases that of beam 1.

Excitation of electron plasma wave (EPW)

EPW that results in the generation of second-harmonics radiations can be excited into the plasma due to remarkable properties of plasma. Plasma as a whole possesses quasi-neutrality, i.e., it contains almost equal number of free electrons and ions. But, as the electrons and net positively charged ions are separated, a disturbance can create regions of net negative and regions of positive charges acting like the plates of a charged parallel plate capacitor. Such an uneven

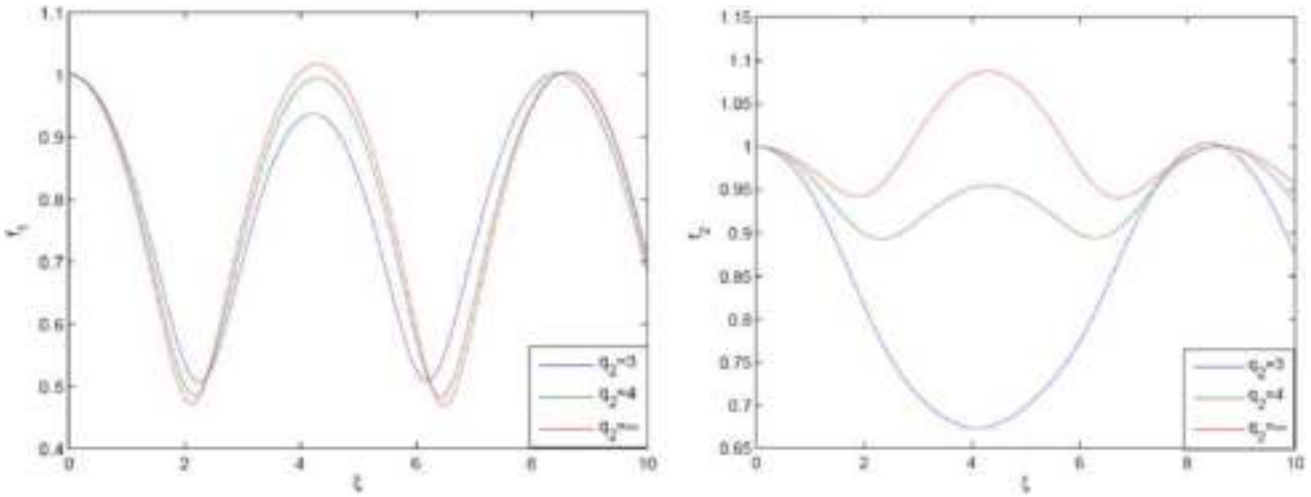

Fig. 8 Variation of beam width parameters f_1 and f_2 of the laser beams with distance of propagation in plasma for different values of q_2 and at fixed values of $q_1 = 3$, $\frac{\omega_{p0}^2 r_1^2}{c^2} = 9$, $\beta_1 E_{10}^2 = 3$ and $\beta_2 E_{20}^2 = 1$

distribution of charges results in an electric field running from positive to negative regions. This electric field pulls the electrons and ions toward each other with equal forces. Ions being much heavier than the electrons remain at rest and the electrons move toward the positive regions. As the electrons move toward the ions, they steadily gain velocity and momentum like a pendulum moving toward its mean position from an extreme position. Due to this gain in momentum, the electrons overshoot their equilibrium positions resulting in reversing the direction of electric field. Now, the reversed electric field opposes the motion of electrons and slows them down and then pulling them back again. The process repeats itself, establishing electron oscillations. In the presence of thermal velocities, these electrons oscillations form a longitudinal wave of positive and negative regions traveling through the plasma (Fig. 9).

The electron oscillators can be set in motion by intense laser beams. As the laser beams enter the plasma region, they exert pressure on plasma electrons, and hence, the plasma electrons move out of the way. As the laser beams exit, leaving a region deficient of electrons, the plasma electrons rush back to establish equilibrium. This movement of plasma electrons initiates the oscillations and results in a plasma wave.

As the two laser beams with different frequencies are propagating simultaneously through the plasma, the plasma oscillations of the plasma electrons under the fields of the two laser beams also contain a frequency component equal to the sum of the frequencies of the two laser beams. The electron density perturbation n' associated with the excited EPW evolves according to the wave equation

$$\frac{\partial^2 n'}{\partial t^2} - v_{th}^2 \nabla^2 n' + \omega_p^2 n' = \frac{e}{m} n_0 \nabla \Sigma_j E_j \tag{16}$$

Taking

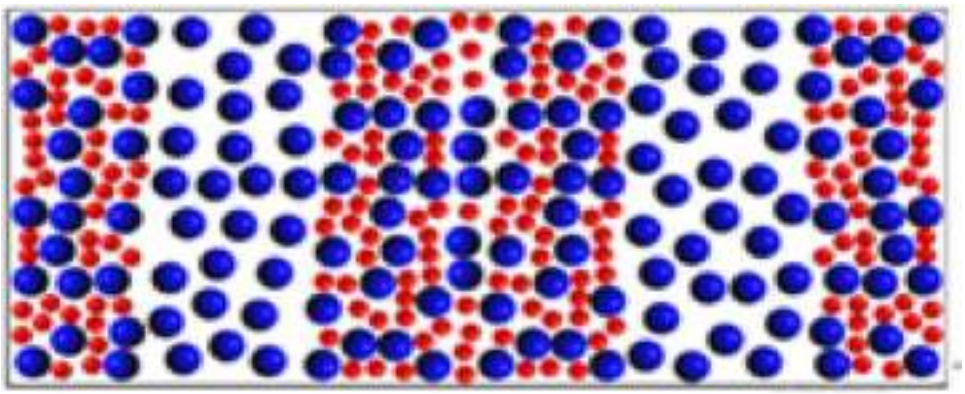

Fig. 9 Electron plasma wave

$$n' = n_1 e^{i(kz-\omega t)}$$

where $\omega = \omega_1 + \omega_2$ and $k = k_1 + k_2$, we get the amplitude of density perturbation associated with plasma wave

$$n_1 = \frac{en_0}{m}\frac{1}{\left(\omega^2 - k^2 v_{\text{th}}^2 - \omega_{\text{p}}^2\right)}\left[\frac{E_{10}}{r_{\text{I}}^2 f_1^3}\left(1+\frac{r^2}{q_1 r_{\text{I}}^2 f_1^2}\right)^{-\frac{q_1}{2}-1} + \frac{E_{20}}{r_2^2 f_2^3}\left(1+\frac{r^2}{q_2 r_2^2 f_2^2}\right)^{-\frac{q_1}{2}-1}\right] r \tag{17}$$

Second-harmonic generation

The density perturbation associated with excited EPW results in a nonlinear current density at frequency $\omega = \omega_1 + \omega_1$ that acts as source for a new radiation at frequency ω, for $\omega_1 = \omega_2$, this new radiation will be having frequency twice that of the pump beams and is thus called as second-harmonic radiation (Fig. 10).

e generated current density is given by

$$J_{\text{T}} = \frac{e^2 n_0}{m\omega}\left(\frac{n_1}{n_0}\right) e^{i(\omega t - kz)}\left(E_1 + E_2\right) \tag{18}$$

The electric field of the resulting harmonic radiation evolves according to the wave equation

$$\nabla^2 E_{\text{T}} = \frac{1}{c^2}\frac{\partial^2 E_{\text{T}}}{\partial t^2} + \frac{4\pi}{c^2}\frac{\partial J_{\text{T}}}{\partial t} \tag{19}$$

This equation gives the magnitude of electric field of second-harmonic radiation as

$$E_{\text{T}} = i\frac{\left(\frac{\omega_{\text{p0}}^2}{c^2}\right)}{\left(\frac{\omega^2}{c^2} - k^2\right)}\frac{n_1}{n_0}\left(E_1 + E_2\right) \tag{20}$$

Defining the normalized power of second-harmonic radiation as

$$P_{\text{T}} = \frac{\int_0^\infty E_{\text{T}} E_{\text{T}}^* r\text{d}r}{\int_0^\infty A_1 A_1^* r\text{d}r} \tag{21}$$

We get

$$P_{\text{T}} = \frac{\left(\frac{\omega_{\text{p0}}^2}{c^2}\right)^2}{\left(\frac{\omega^2}{c^2} - k^2\right)^2}\frac{\int\left(\frac{n_1}{n_0}\right)^2\left(E_1 + E_2\right)^2 r\text{d}r}{\int A_1 A_1^* r\text{d}r} \tag{22}$$

Equation (22) gives the normalized power of the second-harmonic radiation produced by the two laser beams while propagating through the plasma. Equation 22 has been solved numerically in association with the beam width eqs.14 and 15, and the corresponding evolutions of the normalized power with distance of propagation for different values of q_j are depicted in Fig. 11. It has been observed that the power of second-harmonic radiation is a monotonically increasing function of propagation, showing step like behavior. Each step occurs at the position of the minimum beam width of the two laser beams. This is because as the pump beams get self-focused their intensity increases and consequently the oscillation amplitude of the plasma electrons also increases which in turn increases the amplitude of the generated EPW. Since, the density perturbation associated with EPW acts as source for nonlinear current density for second-harmonic radiation, there is monotonic increase in the second-harmonic power with distance.

To understand the physics of SHG in plasmas consider the simultaneous propagation of two intense laser beams through a plasma whose density is rippled along the direction of propagation of the two laser beams. These density ripples of the plasma are due to the propagation of an electron plasma wave through the plasma. In the presence of the laser beams, the plasma electrons start oscillating under the effect of the field of the laser beams and thus generate a transverse electric current J_{T}. Under proper matching of the wave vectors and frequencies, the transverse current generates a second-harmonic wave. The generated harmonic wave then beats with the incident laser beams and thus produces variations in wave pressure. These variations in wave pressure lead to migration of plasma electrons from the regions of high pressure to the regions of low pressure. The resulting density perturbation reinforces the initial density fluctuations associated with electron plasma wave, i.e., the plasma wave gets amplified. The presence of this feedback loop (Fig. 12) leads to the amplification of the harmonic wave with distance of propagation.

The step like behavior of the power of second-harmonic radiation at the positions of the minimum beam width of the pump beams is owing to the fact that these are the regions of highest intensity, and hence, the current density for second-harmonic radiation is maximum there. Hence, after attaining its maximum value the power of second-harmonic radiation moves toward its next possible higher value at next focal spot. These transitions of second-harmonic power from one maximum value to next maximum value give it a step like behavior.

Reduction in the power P_{T} of second-harmonic radiation with increase in the value of deviation parameter q_1 of beam 1 has also been observed from the plots in Fig. 11. The underlying physics behind this is the one-to-one

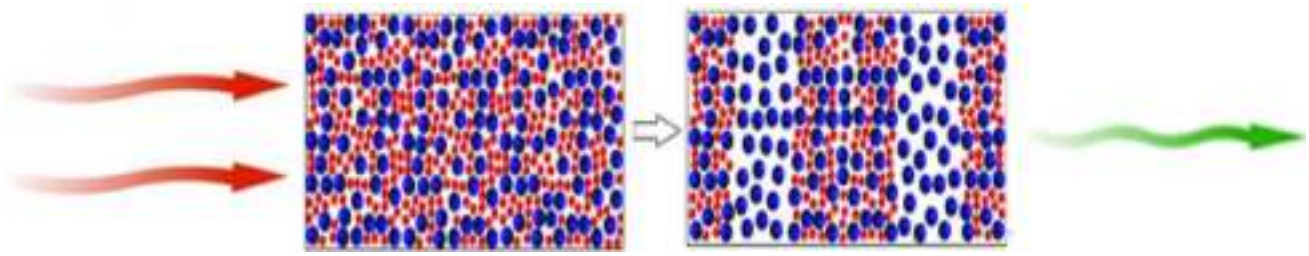

Fig. 10 Second-harmonic generation in plasma

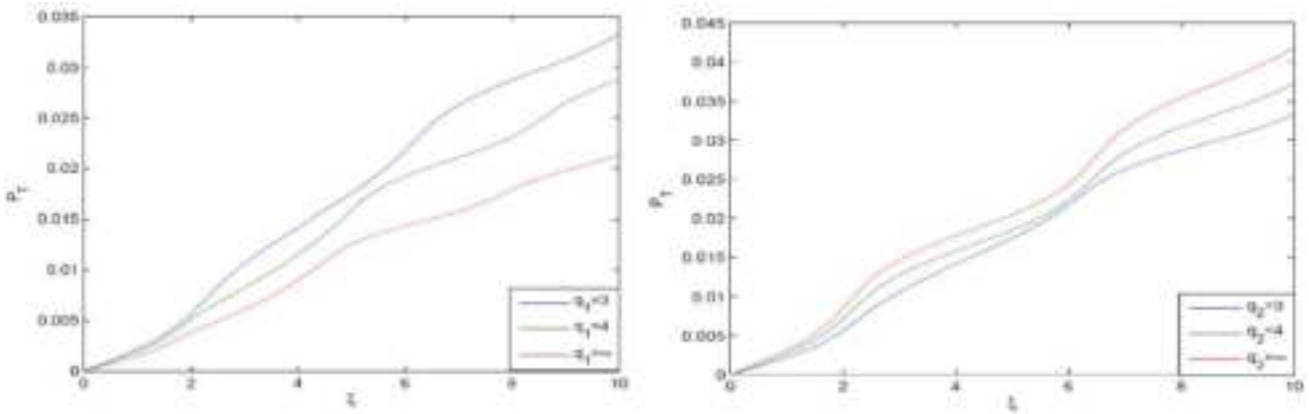

Fig. 11 Variation of normalized power P_T of second-harmonic radiation with distance of propagation in plasma for different values of deviation parameters of the laser beams and at fixed values of $q_2 = 3, \beta_1 E_{10}^2 = 3$ and $\frac{\omega_{p0}^2 r_1^2}{c^2} = 9$

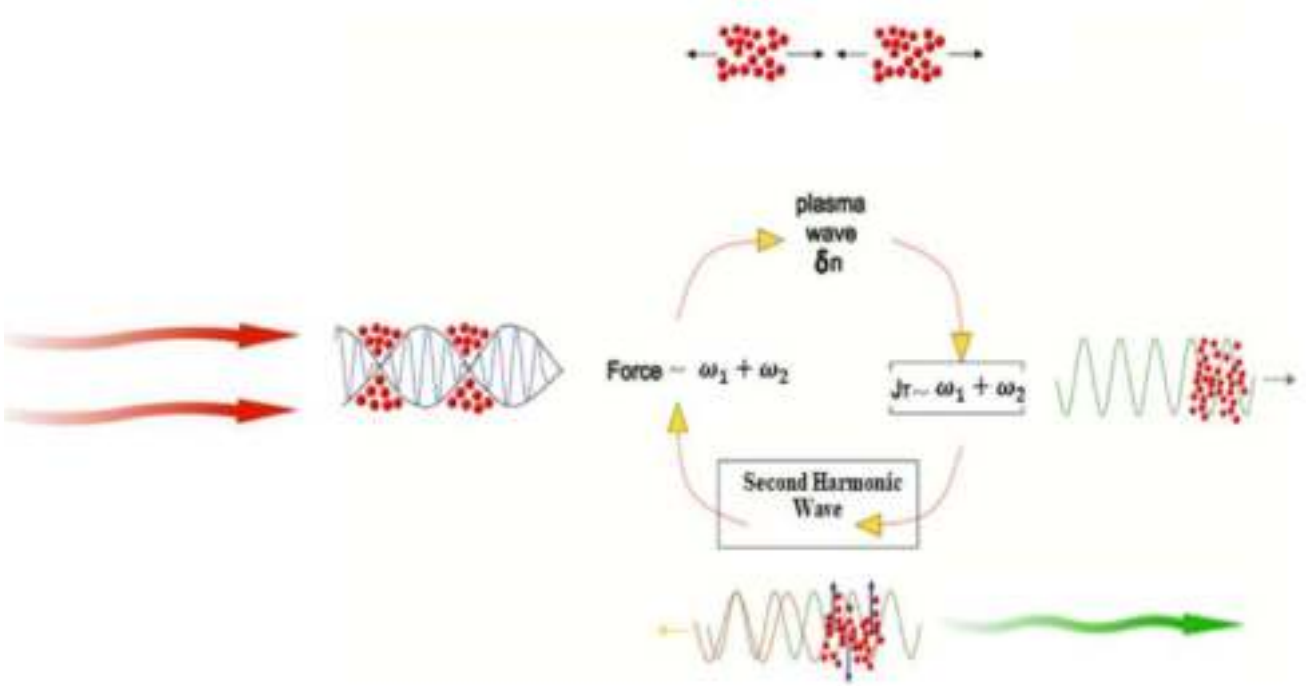

Fig. 12 Feedback loop for amplification of second-harmonic radiation

correspondence between the power of second-harmonic radiation and the degree of self-focusing of the pump beams. As increase in the value of q_1 reduces the extent of focusing of the pump beam 1 (beam with higher initial intensity) and increases the focusing of beam 2. However, in producing second-harmonic radiation, dominant role is played by beam with higher initial intensity. Hence, there is corresponding decrease in the power of second-harmonic radiation with increase in q_1. Same is the reason behind the observed increase in the power of second-harmonic radiation with increase in the value of deviation parameter q_2 of beam 2 (Fig. 11).

Conclusions

In conclusion, we have investigated the effect of cross-focusing of intense laser beams on second-harmonic generation in plasma under the effect of relativistic nonlinearity. Effect of the deviation of amplitude structure of laser beams from ideal Gaussian profile has been incorporated through q-Gaussian distribution. It has been observed that deviation parameters of the laser beams significantly affect the cross-focusing and hence the power of generated second-harmonic radiation. As the amplitude structure of laser beam with higher initial intensity (i.e., pump beam) converges toward the ideal Gaussian profile, there is decrease in the power of generated second-harmonic radiation. However, in case, the amplitude structure of laser beam with lower initial intensity (i.e., probe beam) converges toward the ideal Gaussian profile, and there is increase in the power of generated second-harmonic radiation. Thus, by controlling the deviation parameters of the pump and probe beams, one can optimize the power of second-harmonic radiation for a given set of plasma parameters. The results of present study may be helpful for the experimentalists working in the field of laser–plasma interactions.

References

1. T.H. Maiman, Stimulated optical radiation in Ruby. Nature **187**, 493 (1960)
2. S.E. Miller, Communication by laser. Sci. Am. **214**, 19 (1966)
3. T. Fortier, E. Baumann, 20 years of developments in optical frequency comb technology and applications. Commun. Phys. **2**, 153 (2019)
4. M. Giunta, W. Hansel, M. Fischer, M. Lezius, T. Udem, R. Holzwarth, Real-time phase tracking for wide-band optical frequency measurements at the 20th decimal place. Nat. Photonics **14**, 44 (2020)
5. S. Mak, D. Yip, The measurement of the speed of light using a laser pointer. Phys. Educ. **35**, 95 (2000)
6. D.K. Mao, X.B. Deng, H.Q. Luo, Y.Y. Xu, M.K. Zhou, X.C. Duan, Z.K. Hu, A dual-magneto-optical-trap atom gravity gradiometer for determining the Newtonian gravitational constant. Rev. Sci. Inst. **92**, 053202 (2021)
7. E. Khalkhal, M.R. Tavirani, M.R. Zali, Z. Akbari, The evaluation of laser application in surgery: a review article. J. lasers in med. Sci. **10**, S104 (2019)
8. E. Esarey, C.B. Schroeder, W.P. Leemans, Physics of laser-driven plasma-based electron accelerators. Rev. Mod. Phys. **81**, 1229 (2009)
9. N. Gupta, S.B. Bhardwaj, Relativistic effects on electron acceleration by elliptical q-Gaussian laser beam driven electron plasma wave. Opt. Quant. Electron. **53**, 700 (2021)
10. N. Gupta, Hot electron generation by self focused quadruple gaussian laser beams during inertial confinement fusion. Nonlinear Opt. Quan. Opt. **55**, 63 (2022)
11. P.A. Franken, A.E. Hill, C.W. Peters, G. Weinreich, Generation of optical harmonics. Phys. Rev. Lett. **7**, 118 (1961)
12. N. Gupta, Optical second and third harmonic generation of laser beams in nonlinear media: a review. Nonlinear Opt. Quant. Opt. **53**, 291 (2021)
13. A. Singh, N. Gupta, Higher harmonic generation by self-focused q-Gaussian laser beam in preformed collisionless plasma channel. Laser Part. Beams **32**, 621 (2014)
14. N. Gupta, Second harmonic generation of q-Gaussian laser beam in plasma channel created by ignitor heater technique. Laser Part. Beams **37**, 184 (2019)
15. N. Gupta, S. Kumar, Generation of second harmonics of self-focused quadruple-Gaussian laser beams in collisional plasmas with density ramp. J. Opt. **49**, 455 (2020)
16. N. Gupta, N. Singh, A. Singh, Second harmonic generation of q-Gaussian laser beam in preformed collisional plasma channel with nonlinear absorption. Phys. Plasmas **22**, 113106 (2015)
17. A. Singh, N. Gupta, Second harmonic generation by relativistic self-focusing of q-Gaussian laser beam in preformed parabolic plasma channel. Phys. Plasmas **22**, 013102 (2015)
18. A. Sharma, I. Kourakis, Spatial evolution of a q-Gaussian laser beam in relativistic plasma. Laser Part. Beams **28**, 470 (2010)
19. N. Gupta, S. Kumar, S.B. Bhardwaj, Stimulated Raman scattering of self-focused elliptical q-Gaussian laser beam in plasma with axial density ramp: effect of ponderomotive force. J. Opt. (2021). https://doi.org/10.1007/s12596-021-00822-8
20. A.I. Akhiezer, R.V. Polovin, Theory of wave motion of an electron plasma. Sov. Phys. JETP **3**, 696 (1956)
21. D. Anderson, M. Bonnedal, Variational approach to nonlinear self-focusing of Gaussian laser beams. Phys. Fluids **22**, 105 (1979)
22. D. Anderson, M. Bonnedal, M. Lisak, Self-trapped cylindrical laser beams. Phys. Fluids **22**, 1838 (1979)

JOURNAL OF THE
ASIATIC SOCIETY OF MUMBAI

1804

UGC CARE GROUP - I
JOURNAL
ISSN : 0972-0766

CERTIFICATE OF PUBLICATION

This is to certify that the article entitled

ANALYSIS OF ELECTROSTATIC AND PHYSIOCHEMICAL PROPERTIES OF 4-(4-BENZOYL-1H-1,2,3-TRIAZOL-1-YL)BENZENESULPHONAMIDE AND THEIR DERIVATIVES USING DFT AND ADME BASED APPROACHES

Authored By

Gulab Singh
Department of Chemistry, Shaheed Udham Singh Govt. College, Matak Majri, Karnal132041

Published in

JOURNAL OF THE ASIATIC SOCIETY OF MUMBAI
ISSN : 0972-0766

Vol. : XCVI, No:33, 2023

UGC CARE Approved, Peer Reviewed and Referred Journal

Editor
Parmeeta Deshpande

Shikshan Sanshodhan

Journal of Arts, Humanities and Social Sciences

ISSN (O) : 2581 - 6241

Monthly, Peer-Reviewed, Refereed, Indexed Research Journal

Certificate of Publication

IMPACT FACTOR : 6.831

PAPER ID : SS202405009

is awarded to

मंजू सैनी

For the research paper / article entitled

भरतमुनि नाट्यशास्त्र का एक व्यापक विश्लेषण

Published in Volume - 7, Issue - 5, May - 2024.

DOIs:10.2018/SS/202405009

The Managing Editor
Research Culture Society and Publication
http://shikshansanshodhan.researchculturesociety.org/
Email: shikshansanshodhan@gmail.com

Peer-to-Peer Networking and Applications
https://doi.org/10.1007/s12083-024-01695-x

Assessing the efficacy of a novel adaptive fuzzy c-means (AFCM) based clustering algorithm for mobile agent itinerary planning in wireless sensor networks using validity indices

Nidhi Kashyap[1] · Shuchita Upadhyaya[1] · Monika Poriye[1] · Sachin Lalar[1] · Shalini Aggarwal[2]

Received: 2 July 2023 / Accepted: 15 March 2024

Abstract
Wireless Sensor Networks (WSN) are composed of small sensor nodes that either transmit their sensed data to the sink node directly or transmit it to its respective cluster head, which then transmits it to the sink node. However, this consumes a lot of network bandwidth and energy from the constrained sensor nodes. To address these constraints, Mobile Agents (MA) paradigm can be used in WSNs, which may lead to better energy and bandwidth conservation. When a single mobile agent is insufficient to complete a task, multiple mobile agents can be deployed to perform in parallel and reduce network latency. The set of sensor nodes and their sequence that MAs must migrate to complete a task is called an itinerary. The planning of the itinerary is the most prominent and significant issue related to the MA-based system, including the determination of an appropriate number of MAs to be dispatched, determining the set of sensor nodes and their sequence to be visited by MAs. This paper proposes a fuzzy-based algorithm to partition Wireless Sensor Networks into a set of sensor nodes, called domains, for enhancing the efficiency of the WSN in terms of its prolonged operation. Experimental evaluations are conducted to compare the proposed algorithm with benchmarked algorithms. The paper suggests that the proposed algorithm's integration with MA-based systems can enhance their performance and prolong the WSN's lifetime.

Keywords Clustering · Fuzzy based · Itinerary planning · Mobile agent · Routing · WSN

1 Introduction

A mobile agent is a small, self-governing software program that proactively moves from one node to another to execute tasks [1]. The source code of the mobile agent is compact, allowing it to compute results from the network [2, 3]. The mobile agent is designed to operate even in situations where there is a disconnection [2, 4]. It requires a network only to move to the next node in order to complete its assigned task. As a result, it can efficiently access resources in distributed systems even with low bandwidth. Once dispatched, the mobile agent starts its itinerary from the first node. The results of the computation are stored in its data payload [5, 6]. It resumes execution at each itinerary node and gradually carries out its task [7]. To conserve energy, the processed and accumulated data are aggregated at each node. This ensures that only meaningful, significant, and relevant information is carried by the mobile agent and delivered to the designated node [8, 9].

Mobile agents (MAs) play a crucial role in enhancing the efficiency and extending the lifetime of Wireless Sensor Networks (WSNs) through various means:

- **Energy Efficiency:** MAs can carry out computations and perform tasks locally within the network, reducing the need for constant data transmission to a central

✉ Nidhi Kashyap
nidhikashyap@kuk.ac.in

Shuchita Upadhyaya
supadhyaya@kuk.ac.in

Monika Poriye
monikaporiye@kuk.ac.in

Sachin Lalar
sachin509@kuk.ac.in

Shalini Aggarwal
shaliniagg07@gmail.com

[1] Department of Computer Science and Applications, Kurukshetra University, Kurukshetra, India

[2] Department of Computer Science, S.U.S. Govt. College, Matak Majri, Indri, Karnal, India

Published online: 11 May 2024

point. This minimizes the energy expenditure associated with long-distance communication, thereby conserving the energy of individual sensor nodes. By executing tasks locally, MAs can help mitigate the energy consumption imbalance among nodes, extending the overall network lifetime.

- **Data Aggregation and Processing:** MAs can collect and aggregate data from multiple sensor nodes while in transit, consolidating information before transmitting it to the sink or base station. This aggregation reduces redundant transmissions and helps in processing data at intermediate points, lowering the volume of information sent across the network. Consequently, it reduces the amount of data traffic, conserving energy and bandwidth resources.
- **Dynamic Network Reconfiguration:** MAs facilitate dynamic reconfiguration and adaptability within WSNs. They can reprogram sensor nodes, change their functionalities, or update their operating parameters on the fly. This adaptability helps in responding to changing environmental conditions or network requirements, optimizing the network's performance and efficiency.
- **Fault Tolerance and Load Balancing:** MAs can contribute to fault tolerance by intelligently redistributing tasks among sensor nodes. In case of node failures or network congestion, MAs can redistribute tasks or reroute data flows to ensure the network's continued operation. This load balancing prevents nodes from becoming overloaded and prolongs the overall network lifetime.
- **Optimized Routing and Path Planning:** MAs can intelligently navigate through the network, selecting efficient routes to transmit data. They can employ adaptive routing algorithms, avoiding congested areas or selecting paths that require less energy consumption, which in turn reduces the overall energy expenditure of the network.

In essence, the deployment of mobile agents in WSNs introduces flexibility, adaptability, and efficiency enhancements. Their ability to perform localized computations, aggregate data, optimize routing, and dynamically manage network resources significantly contributes to improving WSN efficiency and prolonging its operational lifetime.

To complete the task, a set of sensor nodes and their visiting sequence by the mobile agents must be determined through itinerary planning. This planning significantly impacts the system's overall performance [10]. Assigning numerous large source nodes to a single itinerary can result in inflated data payloads for the mobile agents, leading to reliability issues, delays, and inefficiencies. To address this, dispatching multiple mobile agents in parallel can reduce itinerary length and resolve the aforementioned issues associated with a long itinerary.

Multiple mobile agent itinerary planning (MIP) poses various challenges, which have been addressed by several authors through the presentation of single and multiple mobile agent itinerary planning algorithms. These algorithms comprise two distinct approaches: static itinerary planning and dynamic itinerary planning [11, 12]. In static itinerary planning, the mobile agent knows its scheduled itinerary in advance and uses centralized routing. This approach is suitable for monitoring-type applications, such as measuring physical quantities like temperature, pressure, and humidity. However, it becomes invalid when a node dies or goes offline, as its itinerary is predetermined and listed in the mobile agent's data structure. In contrast, the dynamic approach is better suited for target-tracking type applications, where the trajectory root of the target is unknown, and the itinerary is decided on the fly, independent of any predetermined schedule. This reactive approach is well-suited for scenarios where the agent needs to decide its sequence of source nodes in real-time. The literature presents a range of issues related to MIP, and relevant suggestions have been incorporated into proposed algorithms by different authors.

This paper is structured as follows: Section 2 provides a concise literature review, which contextualizes clustering of Wireless Sensor Networks (WSN) for a mobile agent. Section 3 describes the proposed algorithm in detail, including corresponding pseudo code. Section 4 introduces the validation indices used to evaluate the performance of the proposed algorithm. In the next section, the results of experiment evaluations are presented, along with a detailed mathematical analysis of the proposed algorithm's execution. Finally, succinct conclusions are drawn based on the study's findings in the conclusion section.

2 Related work

A comprehensive literature review revealed that clustering networks for multi-mobile agent itinerary planning (MIP) follow specific criteria. The proposed algorithms, as surveyed in literature, employ diverse techniques, including k-means, x-means, tree-based, genetic algorithm-based, center locations-based, or directional-based approaches, to partition the network.

The research gaps and the strengths of the reviewed algorithms have been discussed in Table 1.

After a review, it was discovered that various criteria are used to partition networks for multiple mobile agent itinerary planning (MIP). Proposed algorithms in the literature use different methods to partition networks, including:

- **k and x-means:** Greatest Information with Greatest Memory Mobile agent (GIGM-MIP) [1], Chen et al.

Table 1 A succinct description of related approaches with their subsequent investigations

Algorithms with sources	Strategy used	Research objectives	Research gap for the related approach	Findings or inferences	Limitations or Weaknesses	How the proposed study overcomes the addressed gap
GIGM-MIP [1], Chen et al. [2], SMIP [3], Pourroostaei Ardakani [4]	k-means and x-means	Distributing whole network into disjoint clusters with less distant sensor nodes together	Difficult to identify k or x value	GIGM reduces latency for collecting information as it distributes network into equal sized clusters	Strenuous to recognize the value of k or x	No need to identify or assume a c value, the proposed algorithm takes itself
MST-MIP [5], TBID [6], MINDS [7], NOID [8], ILS [9], Disjoint MIP [10], CBID [11], SNOID [12]	Tree structured	Distributing network into clusters such that single MA is dedicated to each stemmed branch	Not suited to time based applications as MA has to traverse each node twice by reverse mapping	Well suited for WSNs due to reduced computational complexity	Slow and can't be used in real time based applications	No need to traverse each node twice
CSA-MIP [13], Aloui et al. [14], Wu et al. [15], Qadori et al. [16], GA-MIP [17]	GA based	Grouping of source nodes by representing them as genes and other array represents the number of source nodes to each MA	Initialization has been done using random selection	Very effective for the object tracking and detection problems	Ineffectual for time constraint applications Initialization must be done with an effective selection operator instead of random selection	All the sensor nodes have been associated with the respective domain initially by using the largest membership values
CL-MIP [18], EMIP [19], OM-MIP [20], MAEF [21]	VCL based	Distributing network into circular or elliptical regions around the center of the dense area	Seems to encourage exploitation since all VCLs belong to most dense region in the network	VCLs are chosen so that more dense region will become the center of the cluster	Iteratively VCL should be altered to explore the centers	The sensor node is associated to the concerned domain by taking maximum membership value and with the least estimated load
SGMIP [20]', DSGMIP [22], Chou and Nakajima [23]	Directionality based	Distributing network into directional sector zones	These algorithms are limited in getting optimal threshold value of θ	Single MA can be deployed to each sector zone		No need to identify any angle value, using fuzzy value, automatically node will e connected to concerned domain initial
AG-MIP [24, 25], SLMADA [26]	Angle based	Distributing network into directional sector zones but these sector zones are defined in between two beelines	These algorithms are limited in getting optimal threshold value of $\Delta\theta$	Outperforms when almost nodes are in same direction or in straight line	Difficult to identify optimal angle value	No need to identify any angle value, using fuzzy value, automatically node will e connected to concerned domain initial
BM-FPA [27]	Evolutionary technique	Partitions their network with GA using fuzzy based fitness selection operator and then flower pollination evolutionary technique has been used for migration of MA	Due to collaboration of number of evolutionary techniques this strategy is too complex	After using the fuzzy based selection operator, execution process become fast	Complexity increases, fuzzy based membership results are deliberated fed into PSO based clustering technique and executed till to determine global optimal results	With the fuzzy membership value disjoint and load balanced clustering has been done
RA-MDP [28]	k-mediods	After choosing CHs using angle gap based strategy, network has been distributed into k clusters and path determination has been done using Markov Decision	Again, this methodology is also limited in obtaining threshold value of $\Delta\theta$		Difficult to identify the k value	No need to identify or assume c value, proposed algorithm takes itself

[2], Spawn Multi Mobile Agent Itinerary Planning (SMIP) [3], Pourroostaei Ardakani [4].

- **Tree structured**: Minimum Spanning Tree MIP (MST-MIP) [5], Tree Based Itinerary Design (TBID) [6], Mobile Agent Itinerary Planning Using Named Data Networking (MINDS) [7], Near Optimal Itinerary Design (NOID) [8], Iterative Local Search (ILS) [9], Disjoint MIP [10], Clone Based Itinerary Design (CBID) [11], Near Optimal Itinerary Design (SNOID) [12].
- **Genetic algorithm based:** Clonal Selection Algorithm for Multi-agent Itinerary Planning (CSA-MIP) [13], Aloui et al. [14], Wu et al. [15], Qadori et al. [16],Genetic algorithm based Multi Mobile Agent Itinerary Planning (GA-MIP) [17].
- **Center locations based**: Central Location based MIP (CL-MIP) [18], Energy efficient MIP (EMIP) [19], Optimized MIP (OM-MIP) [20], Multi Mobile Agent itinerary planning- based Energy and Fault aware data aggregation in Wireless Sensor Networks (MAEF) [21].
- **Directional based**: Source Grouping based MIP (SGMIP) [20], Directional Source Grouping based MIP (DSGMIP) [22], Chou and Nakajima [23].
- **Angle based:** Angle Gap based MIP (AG-MIP) [24] [25], Scalable and Load Balanced Mobile Agents based Data Aggregation (SLMADA) [25].
- **Evolutionary technique based:** Brownian Motion-Based Flower Pollination Algorithm (BMFPA) [26, 27].
- **k-mediods based**: Route planning of mobile agents using Markov Decision Process (RA-MDP) [28].

Inferences drawn from the observation made from the table are:

1. Most strategies involve dividing networks by starting from the center and executing outward.
2. Once a central processing element (PE) is chosen, network partitioning occurs through consideration of geographic proximity distances and abundance density, resulting in disjoint clusters.
3. The optimal number of MAs can be determined through static analysis.

With incomplete, imperfect, and uncertain information, finding optimal solutions using heuristic approaches, iterative methods, or any optimization algorithm becomes challenging. Soft computing techniques have gained popularity to address these problems and provide optimal solutions. These techniques require less computation as well. Based on these findings, the paper proposes and implements an algorithm that uses fuzzy c-means clustering to partition the network. Python has been used to implement algorithm for experimental evaluations.

3 Proposition: an adaptive FCM clustering algorithm for sensor networks with dynamic k-values

The primary limitation of the *k*-means clustering algorithm is the need to pre-determine the number of clusters. The *x*-means and existing FCM clustering algorithms are variations of the *k*-means approach. In *x*-means clustering, the assumed number of centroids (*x*) is set to a minimum value and each cluster is decomposed to achieve optimal clustering. Existing FCM algorithms assume a fixed value for *k*, then iteratively recalculate new centroids and assign data items to *k* clusters using weighted values to obtain optimal clusters.

In contrast, an adaptive FCM Clustering Algorithm for Sensor Networks with dynamic *k*-values (AFCM) is proposed which does not require a pre-determined *k*-value. Instead, after selecting a centralized processing node (PE), the number of Sensor Nodes (SNs) within its vicinity becomes the value of *k*. These *k* nodes are referred to as the domain initials (DI).

In the proposed Adaptive FCM Clustering Algorithm for Sensor Networks with dynamic k-values (AFCM), the need for a pre-determined k-value is eliminated. Instead, the value of k, representing the number of Sensor Nodes (SNs), is determined based on the number of SNs within the vicinity of a centralized processing node (PE).

The central processing element is currently selected as the node positioned at the network's approximate center without specific predefined criteria. The goal is to utilize this central node to facilitate efficient clustering of the wireless sensor network (WSN), enabling the initiation of multi-mobile agent itinerary planning for optimal route coverage.

The initial k nodes, termed domain initials (DI), are selected based on their proximity to the PE. Each SN within a vicinity range of 5 units from the PE is included in the DI set to establish an efficient cluster. The selection of 5 units is arbitrary for experimental ease but can be adjusted for real-world applications depending on specific WSN requirements. Fine-tuning this distance threshold according to the application ensures optimal performance in practical deployment scenarios.

The remaining SNs are assigned to the elements (DI_i) of the set DI. To achieve this, the membership value ($\mu_{i,j}$) of each remaining SN is calculated with respect to each DI_i that is directly within its vicinity. The membership value is determined with the given Eq. (1). The sum of membership values of each remaining sensor node with respect to each DI_i (i.e., $\sum \mu_{i,j}$) is then calculated in advance. Subsequently, each SN is assigned to the DI_i with the maximum membership value. The sum of membership values ($\sum \mu_{i,j}$) is updated after each SN is assigned, and this

process continues until all sensor nodes in the network are assigned to their respective DI_i. If the membership value of an SN with respect to two or more domain initials is the same, then the SN is assigned to the DI_i with the lowest value of $\sum \mu_{i,j}$. After assigning all SNs to their respective k DI_s, the updated $\sum \mu_{i,j}$ values are compared to the threshold value (minimum value of $\sum \mu_{i,j}$ for which a single MA can be deployed). Any DI_i with $\sum \mu_{i,j}$ less than the threshold value is dropped out. To reduce the number of DIs or DI_i, the domain initials and assigned nodes are assigned to existing domain initials. This reduces k domains to c domains and results in a distribution of the sensor nodes in non-overlapping and load-balanced domains.

$$\mu i,j = \frac{di,j^{\frac{-2}{m-1}}}{\sum_{l=1}^{|DI|} di,j^{\frac{-2}{m-1}}} \tag{1}$$

- |DI| is the cardinality of set containing source nodes under PE's vicinity.
- The exponent 'm' regulates the degree of fuzziness or crispness within the clustering process. This parameter, 'm,' is adaptable and influences the boundaries between clusters: a lower 'm' value creates clearer cluster boundaries, whereas a higher 'm' value results in more blurred boundaries between clusters.

The AFCM algorithm differs from existing FCM algorithms in several ways:

- One notable difference is that AFCM is capable of determining and optimizing the number of clusters on its own, while FCM requires the user to specify the number of clusters using methods such as the elbow, Dunn index, Davies Bouldin (DB) index, silhouette index, etc.
- Both algorithms assign a degree of membership to each estimated centroid and associate data items with the centroid with the highest membership value. However, AFCM differs when there is a dilemma, that is, when the membership value corresponds to more than one centroid is the same.
- To address this issue, the proposed algorithm estimates the sum of membership values of each data item with respect to all relevant centroids in advance. With this estimation, each data item is associated with the appropriate centroid that has the minimum sum of membership values. This ensures that the data item is associated with the centroid that is likely to have fewer nodes associated with it in the future.
- Furthermore, the AFCM algorithm executes in a hierarchical manner until all nodes are associated, while FCM iteratively shifts the centers of its clusters from the current position to the optimal position to minimize the objective function. The objective function defines the spatial separation from the data points to the concerned centers.

3.1 Algorithm overview and description

This algorithm outlines a process for establishing connections among sensor nodes (SNs) in a network. It begins by defining key elements: PE as the Processing Element, DI as the set of Domain Initials, SN as Sensor Nodes, and Dist(x, y) as a function returning the Euclidean distance between xth and yth sensor nodes.

- **Initialization:** It starts by setting a vicinity range of 5 (arbitrarily chosen for ease of experimentation and size of networks chosen for experimentation) for each SN. It creates a DI set containing SNs within this vicinity of a designated PE. For each SN not equal to PE and within the vicinity range, it appends them to DI, designates PE as their parent, and marks them as connected.
- **Remaining Sensor Nodes (RSN):** RSN comprises SNs outside the DI. It aims to find the closest mapping of each RSN element with respect to elements in DI. It calculates the distance between each DIi and every RSN node, ensuring it's within the vicinity. Then, it identifies the DIi that has the lowest cumulative mapping with RSN. If there's a tie, it selects the DIi with the least SUM(DIi). This process continues until all SNs are connected.
- **Threshold-based Decision:** If the cumulative SUM(DIi) falls below a specified threshold, indicating weak connectivity, it drops that DIi and treats it along with its connected nodes as part of the RSN. Then, it restarts the process to connect these nodes.
- **Stopping Condition:** The process stops when all SNs are marked as connected.

In essence, this algorithm is designed to establish connections between sensor nodes in a network, iteratively evaluating proximity and connectivity until all nodes are appropriately linked within a defined vicinity.

3.2 *P*seudo code for the proposed adaptive fuzzy c-means clustering (AFCM) algorithm is as follows

Algorithm: Proposed Adaptive Fuzzy c-means clustering Algorithm (AFCM)

Let:

- *PE: Processing Element*
- *DI: Set of Domain initials*
- *DI_i: Element of set DI*
- *PE: Processing Element*
- *SN: Sensor Node*
- *Dist (x,y): returns the Euclidian distance between x^{th} and y^{th} sensor nodes*
- *The Vicinity range of each SN is set to 5*

1. *Initialize DI as an empty set.*

2. *for (each SN)*

If ((SN ≠PE) and Dist (SN, PE) ≤5) then:

- Add *SN to DI*
- Set *SN.parent =PE*
- Set *SN.connected* = true

3. *Set RSN as the set of all remaining sensor nodes : ∀SN – DI*

4. *Find the closest mapping of each element of RSN with respect to DIi:*

- *For each remaining j in RSN:*
  - *Calculate { μi,j ∀ i ∈DI, ∀j ∈RSN : Dist (i,j) ≤ 5*
  - *For each element in the set DI:*
    - *Calculate* $\boldsymbol{SUM(DIi) = \sum_{j \in RSN} \mu i,j}$

▪ If there exists a node j in RSN where the value of $\mu_{i,j}$ is the same for two DI_i:

- *Append j to the RSN for which the $SUM(DI_i)$ is less.*

▪ *Else*

- *Append the closest mapping of RSN to DI_i.*

- *Update the value of SUM(DI_i)*

5. *Repeat step 4 until SN.connected = true*

6. *If ($\boldsymbol{SUM(DIi) <}$ Threshold value) Then*

- *Drop DIi and treat DIi and connected nodes as members of set RSN*
- *Follow step-4 to connect DIi and its further connected nodes*

7. *Stop*

4 Experimental evaluations

4.1 Validation indices

A set of indices is used to evaluate, validate, and interpret the performance of clustering algorithms. These indices include metrics such as the Dunn index and silhouette index. The primary purpose of these validation indices is to confirm the effectiveness of clustering algorithms. In addition, they play a crucial role in determining the number of clusters in a network. The indices are calculated based on the ratio of cohesion to separation, and their values serve as the criteria for assessing the quality of clustering algorithms. Table 2 provides a brief overview of the metrics used.

4.1.1 Cohesion (compactness)

Cohesion metric measures the distance within a cluster. A low cohesion value indicates well-clustered data, while a high intra-cluster value indicates poor clustering quality.

4.1.2 Separation (spatial separation)

Separation refers to the measurement of inter-cluster distances. This metric reveals the degree to which a cluster is isolated or distinct from other clusters within the network.

4.1.3 Dunn index

The Dunn Index is a metric that evaluates two crucial aspects of clustering: cohesion/compactness and separation. Specifically, it gauges the relationship between the minimum separation distance and the maximum compactness value. A higher index value indicates greater segregation between clusters. Importantly, the index value is always non-negative.

4.1.4 Silhouette index

The Silhouette Index is a metric that measures the degree of belongingness of a data item to its cluster as compared to other clusters. This index takes values between -1 and 1, where a higher value indicates a better match of the data item with its cluster. In addition, a clustering configuration is considered appropriate if most objects have a high Silhouette Index value.

4.2 Data sets

In this empirical study, Table 3 illustrates the various deployments of WSN. These datasets were utilized to validate and evaluate the proposed algorithm's performance. Specifically,

Table 2 Different evaluation Indices to validate the proposed algorithm

Evaluation Index Method Name	Measuring Formula	Explanation
Compactness (Δ)	$\Delta i = \{\frac{1}{\lvert Ci\rvert(\lvert Ci\rvert-1)}\sum_{i\in Ci,i\neq j} d(i,j)\}$; $\lvert Ci\rvert$ represents the cardinality of the ith cluster, $d(i,j)$ is the Euclidean distance between two objects in a cluster	It quantifies the intra-cluster adjacency of the objects
Separation (δ)	$\delta i = min[(i \neq j)\{\frac{1}{\lvert Cj\rvert}\sum_{i\in Cj} d(i,j)\}]$; $\lvert Cj\rvert$ represents the cardinality of jth cluster, $d(i,j)$ is the Euclidean distance between two objects from two different clusters	It quantifies the inter-cluster segregation of the clusters
Dunn Index (DI)	$DI = \frac{\{\delta i(Ci,Cj)\}}{\{\Delta k\}}$; $1 \le i \le j \le m, 1 \le k \le m$; Ci and Cj represent ith and jth cluster in the network, stands for the cohesion of kth cluster, m is the total number of clusters in the network	Division of minimum intra-cluster cohesion value and maximum inter-cluster separation spatial value
Silhouette Index (SI)	$SI = \frac{\delta i-\Delta i}{max\{\delta i,\Delta i\}}$; $1 \le i \le m$; δi, Δi are the separation and compactness of the ith cluster in the network of m clusters	Division of difference of average inter-cluster separation and average intra-cluster cohesion value and a maximum of inter-cluster separation and intra-cluster cohesion value

Table 3 Different data sets to validate the proposed algorithm

Data Set	No. of Nodes
Dataset 1	15
Dataset 2	20
Dataset 3	30
Dataset 4	40

datasets 1, 2, 3 and 4 were designed to represent distinct domains with 15, 20, 30, and 40 nodes, respectively. Each node is characterized by its two-dimensional coordinates (x, y), and a corresponding Euclidean value has been computed for each coordinate.

4.3 Empirical findings and performance evaluations

To assess the effectiveness of the AFCM algorithm, only the Dunn and Silhouette indices are calculated. These indices were chosen because they inherently encompass both cohesion and separation making them ideal measures of the algorithm's effectiveness.

These indices were also computed for the Birch, Fuzzy c-means, k-means, Mean shift, Hierarchical and OPTICS algorithms for comparison.

In fuzzy c-means clustering algorithms, sometimes the chosen value for 'c' does not produce a significant impact, so it needs to be optimized. This can be achieved by selecting different numbers of 'c' values based on the resulting validation values to optimize the clustering. The optimal 'c' value can be determined by identifying the value that produces the highest index values.

Unlike the k-means clustering algorithm, which is inadequate for determining the 'k' value and relies on heuristics such as the elbow technique, the proposed AFCM algorithm does not require any additional methods to select the 'c' value. Instead, the algorithm itself selects an initial 'c' value and optimizes it. Tables 4 and 5 provide the evidences of the algorithm's proficiency in determining the optimal 'c' value.

Regarding Tables 4 and 5 above, the indices values of the AFCM algorithm indicate the effectiveness of the algorithm in optimizing the 'c' value. Additionally, the modest indices values of the AFCM algorithm indicate that the resulting domains are well separated, and each node is tightly packed within its respective domain.

5 Results and analysis

This paper aims to validate and evaluate the performance of the AFCM (Adaptive Fuzzy c-means) clustering algorithm in WSN. The algorithm is compared with existing benchmarked approaches, showing moderate results. However, since the proposed algorithm was specifically designed for the itinerary planning criteria of MAs in WSN, the results are justified. The algorithm effectively distributes the network into multiple domains, with an optimized number of MAs for each domain. Tables 4 and 5 provide evidence of this optimization. The efficiency of the clustering algorithm is analyzed by representing the graphical clusters of a network with 40 nodes using various algorithms, including Birch, Fuzzy c-means, k-means, Mean shift, OPTICS, and the proposed algorithm. The

Table 4 Effectiveness of Dunn Validation Index on Different Data Sets

Data Deployment	*K*-means	Fuzzy *C*-means	Proposed (AFCM)	BIRCH	OPTICS	Hierarchical	Mean Shift
Dataset 1	0.0323	0.0355	0.0383	0.0243	0.0216	0.0136	0.0196
Dataset 2	0.0389	0.0495	0.0489	0.0285	0.0224	0.0224	0.0214
Dataset 3	0.0655	0.0655	0.0655	0.0327	0.0288	0.0288	0.0288
Dataset 4	0.0921	0.1015	0.0891	0.0269	0.0252	0.0252	0.0252

Table 5 Effectiveness of Silhoutte Validation Index on Different Data Sets

Data Deployment	*K*-Means	Fuzzy *C*-Means	Proposed (AFCM)	BIRCH	OPTICS	Hierarchical	Mean Shift
Dataset 1	0.4211	0.4322	0.4332	0.4324	0.3411	0.3211	0.3208
Dataset 2	0.4122	0.4211	0.4220	0.4221	0.3211	0.3122	0.3198
Dataset 3	0.3951	0.3951	0.3951	0.3951	0.2795	0.2695	0.2635
Dataset 4	0.3586	0.3712	0.3732	0.345	0.2519	0.2409	0.2211

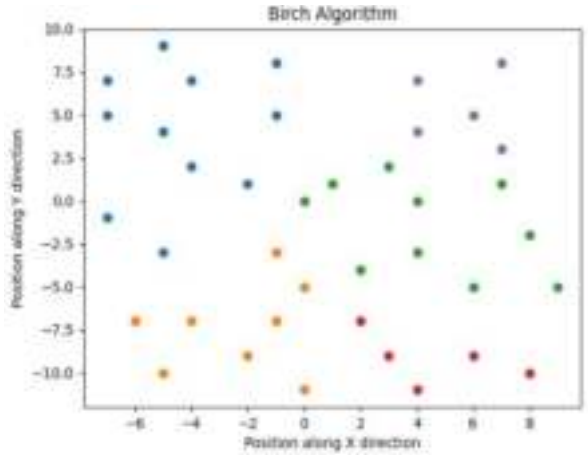

(a) 5 Clusters

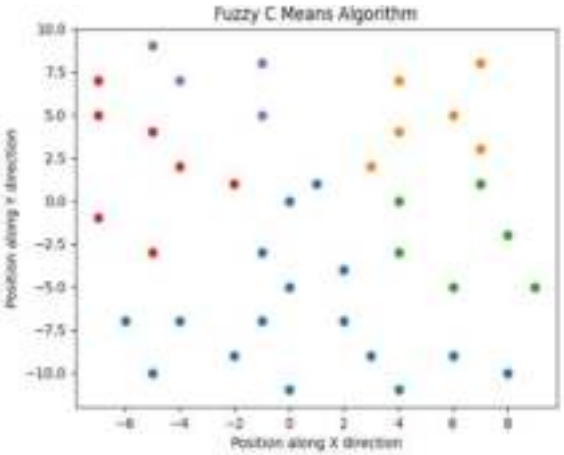

(b) 5 Clusters

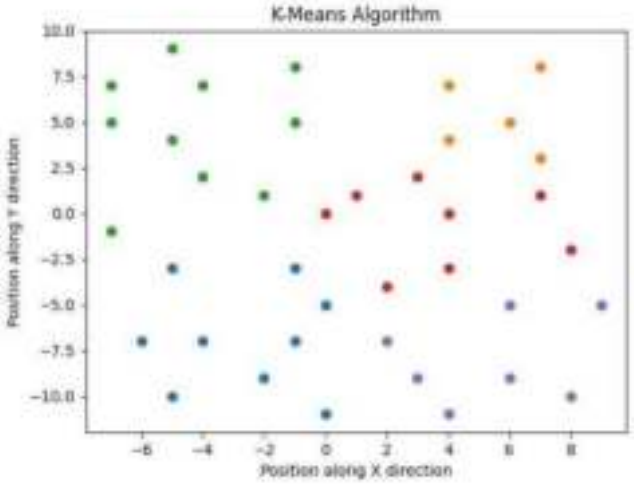

(c) 5 Clusters

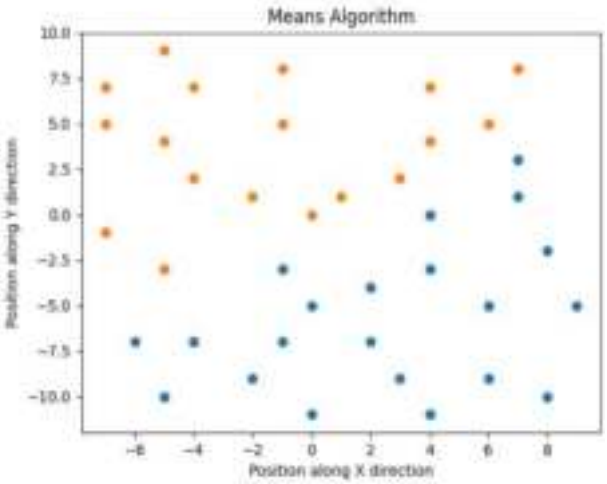

(d) 2 Clusters

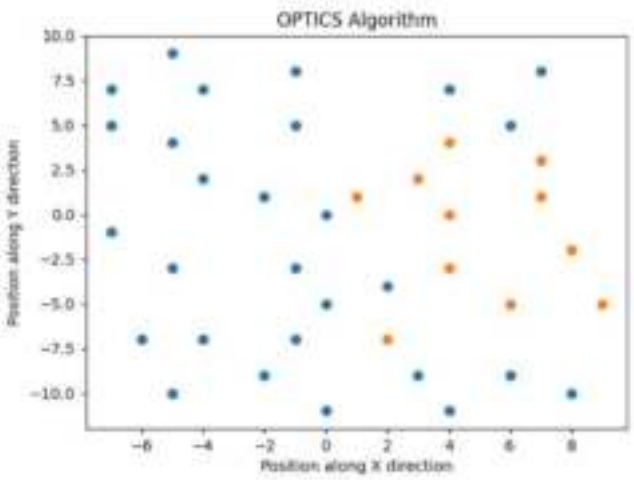

(e) 2 Clusters

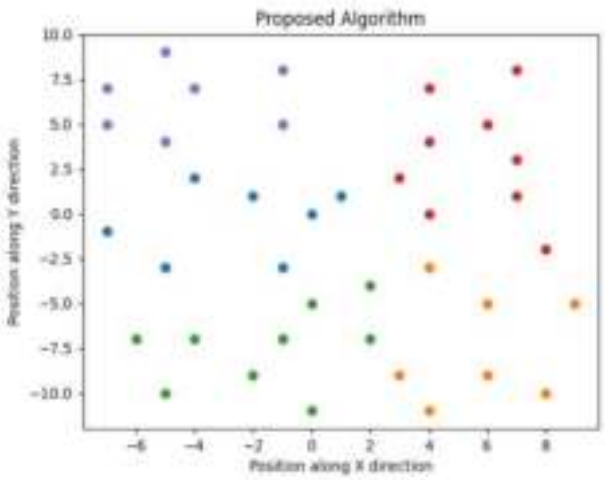

(f) 5 Clusters

Fig. 1 Clusters formed for 40 nodes network **a** Birch Algorithm **b** Fuzzy *C*-means **c** *K*-means Algorithm **d** Mean shift **e** OPTICS Algorithm **f** Proposed algorithm

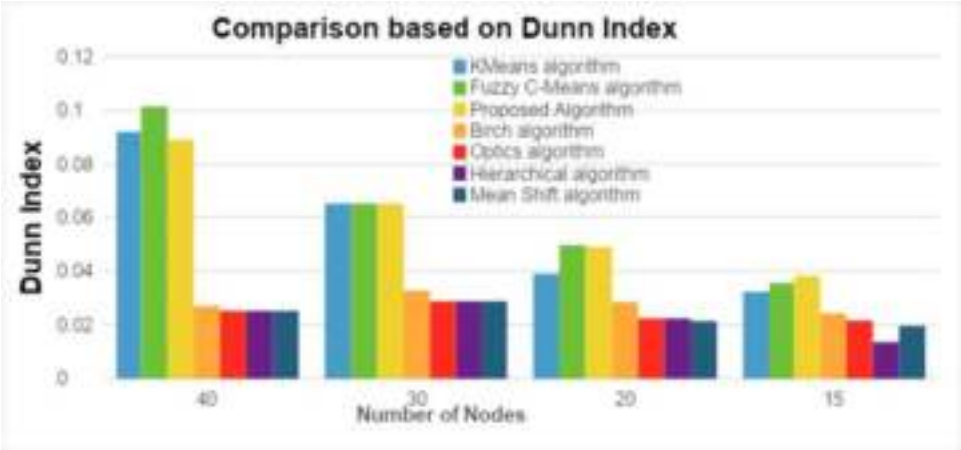

Fig. 2 Comparison of Dunn Index

clusters formed by these algorithms are depicted in Fig. 1(a) to (f) respectively.

The comparison of various algorithms has been summarized in the Figs. 2 and 3 below, with results evaluated based on Dunn index and Silhouette index.

The results in Fig. 2 indicate that AFCM performs moderately well when evaluated with Dunn index. On the other hand, the clustering results of AFCM outperform other algorithms when evaluated with Silhouette index in Fig. 3.

The analysis of AFCM in the context of Dunn and Silhouette indices indicates that the algorithm performs well in the application. AFCM clustering algorithm has been developed to distribute the network into multiple domains, with each domain having an appropriate number of MAs deployed. By selecting a threshold value, the appropriate number of MAs for each domain can be determined, ensuring that all dispatched MAs are load balanced. As a result, task delays will be reduced, leading to improved performance.

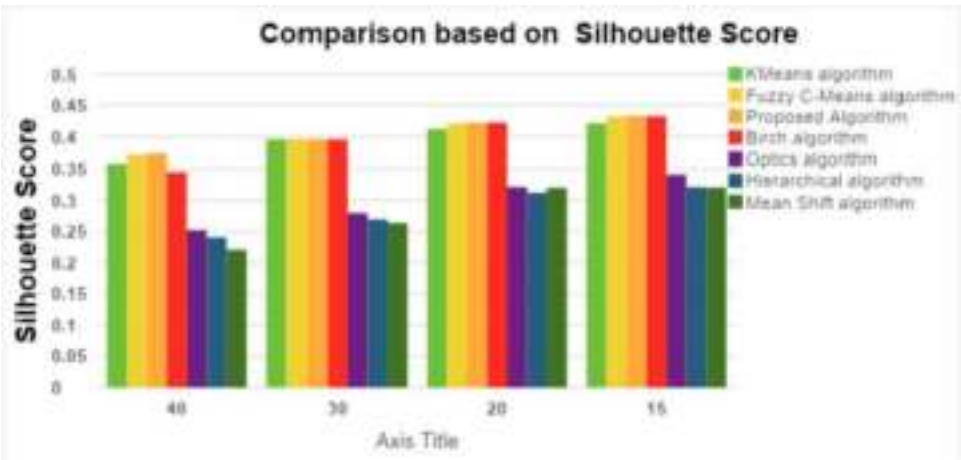

Fig. 3 Comparison of Silhouette Score

6 Conclusion

This paper explores the challenge of clustering in multi-mobile agent routing for Wireless Sensor Networks and emphasizes the significance of deploying an appropriate number of mobile agents per domain. To address this challenge, a novel strategy called AFCM (Adaptive Fuzzy c-means) has been introduced which aims to divide the network into a number of disjoint domains.

The proposed AFCM algorithm has been compared and validated with clustering evaluation indices for network deployment. The performance of Birch, Fuzzy c-means, k-means, Means, and OPTICS algorithms against the AFCM clustering algorithm using Dunn and Silhouette indices has also been evaluated.

The results demonstrate that AFCM achieves modest index values, indicating its adaptability and ability to cluster sensor nodes tightly while separating domains. The AFCM algorithm determines the number of mobile agents for each domain by selecting an appropriate threshold value. However, evaluating the performance of this algorithm can be complex and challenging, and approximate computations can be used to strike a balance between complexity and accuracy.

Author contributions Each author has made substantial contributions to the conception or design of the work; or the acquisition, analysis, or interpretation of data.

Funding All the co-authors have seen and agree with the contents of the manuscript and there is no financial interest to report.

Data availability All data generated or analyzed during this study are included in this published article.

Declarations

Ethics approval This work does not contain any studies with human participants or animals performed by any of the authors.

Consent for publication Not applicable.

Competing interests The authors declare no competing interests.

References

1. Bendjima M, Feham M, Lehsaini M (2021) Directional itinerary planning for multiple mobile agents. Wirel Sens Netw. https://doi.org/10.1155/2021/5584581
2. Chen M, Gonzalez S, Leung VCM (2007) Applications and design issues for mobile agents in wireless sensor networks. IEEE Wirel Commun 14(6):20–26. https://doi.org/10.1109/MWC.2007.4407223
3. El Fissaoui M, Beni-hssane A, Saadi M (2018) Multi-mobile agent itinerary planning-based energy and fault aware data aggregation in wireless sensor networks. EURASIP J Wirel Commun Network 92. https://doi.org/10.1186/s13638-018-1099-0
4. Pourroostaei Ardakani S (2021) MINDS: mobile agent itinerary planning using named data networking in wireless sensor networks. J Sens Actuat Netw 10(2):28. https://doi.org/10.3390/jsan10020028
5. Lohani D, Varma S (2013) Itinerary planning using grey relational analysis for mobile agent based wireless sensor networks. Sixth International Conference Contemporary Computing (IC3), Noida, India, pp 29–34. https://doi.org/10.1109/IC3.2013.6612215
6. Daramola OA, Fakoya JT, Danjuma HI, Egwuche OS (2021) Towards clustering technique for a fault tolerance mobile agent-based system in wireless sensor networks. Int J Comput Sci Inf Secur 19(1):48–58. https://doi.org/10.5281/zenodo.4533402
7. Prapulla SB, Chandra J, Mudakavi MB, Shobha G, Thanuja TC (2016) Multi mobile agent itinerary planning using farthest node first nearest node next (FNFNNN) technique. 2016 International Conference on Computation System and Information Technology for Sustainable Solutions (CSITSS). IEEE, pp 105–111. https://doi.org/10.1109/CSITSS.2016.7779404
8. Chen M, Leung V, Mao S, Kwon T, Li M (2009) Energy-efficient itinerary planning for mobile agents in wireless sensor networks. IEEE International Conference on Communications, Dresden, Germany, pp 1–5. https://doi.org/10.1109/ICC.2009.5198997
9. Gavalas D, Venetis IE, Konstantopoulos C, Pantziou G (2016) Energy-efficient multiple itinerary planning for mobile agents-based data aggregation in WSNs. Telecommun Syst 63(4):531–545. https://doi.org/10.1007/s11235-016-0140-z
10. Hong W, Liu Z, Chen Y, Guo W (2016) Energy-efficient mobile agent communications for maximizing lifetime of wireless sensor networks. Wireless communications, networking and applications. Springer, New Delhi, pp 305–317. https://doi.org/10.1007/978-81-322-2580-5_29
11. Makki S, Wunnava SV (2007) Application of mobile agents in managing the traffic in the network and improving the reliability and quality of service. Int J Comput Sci 33(1):135
12. Nidhi, Upadhyaya S (2022) Fuzzy C-means clustering of network for multi mobile agent itinerary planning. Smart trends in computing and communications, vol 396. Springer, Warsaw, Poland, pp 589–598
13. Aloui I, Kazar O, Kahloul L, Servigne S (2015) A new itinerary planning approach among multiple mobile agents in wireless sensor networks (WSN) to reduce energy consumption. Int J Commun Netw Inf Secur 7(2):116–122. https://doi.org/10.17762/ijcnis.v7i2.1276
14. Aloui I, Kazar O, Kahloul L, Aissaoui A, Servigne S (2016) A new "data size" based algorithm for itinerary planning among mobile agents in wireless sensor networks, vol 36. Proceedings of the International Conference on Big Data and Advanced Wireless Technologies, pp 1–9. https://doi.org/10.1145/3010089.3010121
15. Wu C, Yan B, Yu R, Yu B, Zhou X, Yu Y, Chen N (2021) k-means clustering algorithm and its simulation based on distributed computing platform. Complexity. https://doi.org/10.1155/2021/9446653
16. Qadori HQ, Zulkarnain ZA, Hanapi ZM, Subramaniam S (2017) A spawn mobile agent itinerary planning approach for energy-efficient data gathering in wireless sensor networks. Sensors 17(6):1280–1296. https://doi.org/10.3390/s17061280
17. Chen M, Cai W, Gonzalez S, Leung VC (2010) Balanced itinerary planning for multiple mobile agents in wireless sensor networks. In: Zheng J, Simplot-Ryl D, Leung VCM (eds) Ad hoc networks. ADHOCNETS 2010. Lecture Notes of the Institute for Computer Sciences, Social Informatics and Telecommunications Engineering, vol 49. Springer, Berlin, Heidelberg. https://doi.org/10.1007/978-3-642-17994-5_28
18. Konstantopoulos C, Mpitziopoulos A, Gavalas D, Pantziou G (2009) Effective determination of mobile agent itineraries for data aggregation on sensor networks. IEEE Trans Knowl Data Eng 22(12):1679–1693. https://doi.org/10.1109/TKDE.2009.2032009

19. Mpitziopoulos A, Gavalas D, Konstantopoulos C, Pantziou G (2007) Deriving efficient mobile agent routes in wireless sensor networks with NOID algorithm. IEEE 18th International Symposium on Personal, Indoor and Mobile Radio Communications, pp 1–5. https://doi.org/10.1109/PIMRC.2007.4394337
20. Liu B, Cao J, Yin J, Yu W, Liu B, Fu X (2016) Disjoint multi mobile agent itinerary planning for big data analytics. J Wirel Commun Netw 1:1–12. https://doi.org/10.1186/s13638-016-0607-3
21. Mpitziopoulos A, Gavalas D, Konstantopoulos C, Pantziou G (2010) CBID: a scalable method for distributed data aggregation in WSNs. Int J Distrib Sens Netw 6(1):206517. https://doi.org/10.1155/2010/206517
22. Gavalas D, Pantziou G, Konstantopoulos C, Mamalis B (2006) New techniques for incremental data fusion in distributed sensor networks. Proceedings of the 11th Panhellenic Conference on Informatics, pp 599–608
23. Chou YC, Nakajima M (2018) A clonal selection algorithm for energy-efficient mobile agent itinerary planning in wireless sensor networks. Mob Netw Appl 23(5):1233–1246. https://doi.org/10.1007/s11036-017-0814-0
24. Kuila P, Gupta SK, Jana PK (2013) A novel evolutionary approach for load balanced clustering problem for wireless sensor networks. Swarm Evol Comput 12:48–56. https://doi.org/10.1016/j.swevo.2013.04.002
25. Mahmoudi M, Avokh A, Barekatain B (2022) SDN-DVFS: an enhanced QoS-aware load-balancing method in software defined networks. Cluster Comput 25:1237–1262. https://doi.org/10.1007/s10586-021-03522-x
26. Wu Q, Rao NS, Barhen J, Iyenger SS, Vaishnavi VK, Qi H, Chakrabarty K (2004) On computing mobile agent routes for data fusion in distributed sensor networks. IEEE Trans Knowl Data Eng 16(6):740–753. https://doi.org/10.1109/TKDE.2004.12
27. Sadrishojaei M, Navimipour NJ, Reshadi M et al (2022) A new clustering-based routing method in the mobile internet of things using a krill herd algorithm. Cluster Comput 25:351–361. https://doi.org/10.1007/s10586-021-03394-1
28. Rajagopalan R, Mohan CK, Varshney P, Mehrotra K (2005) Multi-objective mobile agent routing in wireless sensor networks, vol 2. 2005 IEEE Congress on Evolutionary Computation, pp 1730–1737. https://doi.org/10.1109/CEC.2005.1554897

Nidhi Kashyap received the M.Sc. in Computer Science and M.C.A. from Kurukshetra University, Kurukshetra, Haryana, India and M.Phil. degree in Computer Science from Chaudhary Devi Lal University, Sirsa. She was an assistant professor in the Department of Computer Applications, National Institute of Technology, Kurukshetra (2011-2016). Presently she is doing Ph.D. in Computer Science from Kurukshetra University, Kurukshetra. Her research interests include computer Networks and Soft Computing Techniques.

Dr. Shuchita Upadhyaya Bhasin is a distinguished Professor and former Chairperson of the Department of Computer Science & Applications at Kurukshetra University, Kurukshetra. With over 35 years of experience in teaching and research, her expertise spans a wide range of areas including Computer Networks & Data Communication, Internet Technologies, Network Security, Wireless Sensor Networks, Data Mining, Machine Learning, and Blockchain technology. She has been recognized for her exemplary contributions to academia, receiving awards for Academic Achievements. Dr. Shuchita Upadhyaya Bhasin has authored numerous research publications and lessons for distance education programs of Kurukshetra University, guided several Ph.D. and M.Tech students, and delivered lectures at various international conferences, seminars, workshops etc. She is a member of prestigious academic bodies and actively contributes to the development of academic programs and research initiatives.

Dr. Monika Poriye is currently working as Assistant Professor in Department of Computer Science and Applications, Kurukshetra University, Kurukshetra. She has done her Ph.D in Computer Science and Applications from Department of Computer Science and Applications, Kurukshetra University, Kurukshetra. She has more than 13 years' experience in teaching and research. Her main research work focuses on Security in wireless Sensor Netwroks, Cloud Computing, Cyber Security and Cryptography.

Dr. Sachin Lalar is working as Assistant Professor in Kurukshetra University in Department of Computer Science and Applications. He had received his Ph.D. in Computer Science and Engineering. He has more than 14 years' experience in teaching and research. His research interests are Computer Networks, Data Structure and Programming. He has visited many universities for presenting the research papers. Several research papers of his work published in the leading National and International Journals.

Dr. Shalini Aggarwal is currently working as an Assistant Professor in the Department of Computer Science, S.U.S. Govt. College, Matak Majri, Indri (Karnal). She has published a number of research papers in the various national and international journals. She has presented her research in various conferences. She has done her Ph.D in Computer Science and Applications from Department of Computer Science and Applications Kurukshetra University, Kurukshetra in the field of Computer Networks. Her research areas include Computer Networking, Machine Learning, Soft Computing, etc. She is having more than 16 years of teaching experience and more than 10 years of research experience.

International Journal of Computing and Digital Systems
ISSN (2210-142X)
Int. J. Com. Dig. Sys. 16, No.1 (Jul-24)

http://dx.doi.org/10.12785/ijcds/160119

Improving Sentiment Analysis using Negation Scope Detection and Negation Handling

Kartika Makkar[1], Pardeep Kumar[2], Monika Poriye[3] and Shalini Aggarwal[4]

[1,2,3]*Department of Computer Science and Applications Kurukshetra University, Kurukshetra, Haryana, India*
[4]*Department of Computer Science S.U.S. Govt. College, Matak Majri (Indri), Karnal, India*

Received 3 Feb. 2024, Revised 9 Apr. 2024, Accepted 16 Apr. 2024, Published 1 Jul. 2024

Abstract: Negation is one of the challenges in sentiment analysis. Negation has an immense influence on how accurately text data can be classified. To find accurate sentiments of users this research identifies that the impact of negations in a sentence needs to be properly handled. Traditional approaches are unable to properly determine the scope of negations. In the proposed approach Machine learning (ML) is used to find the scope of negations. Moreover, the removal of negative stopwords during pre-processing leads to the flipped polarity of sentences. To resolve these challenges this research proposes a method for negation scope detection and handling in sentiment analysis. First, negation cue (negative words) and non_cue words are determined, these negation cue and non_cue words in addition to lexical and syntactic features determine the negation scope (part of sentence affected by cue) using the Machine Learning (ML) approach i.e. Conditional Random Fields (CRF). Subsequently, in negation handling the sentiment intensity of each token in a sentence is established, and affected tokens are processed to determine the final polarity. It is revealed that sentiment analysis with negation handling and calculated polarity gives 3.61%, 2.64%, 2.7%, and 1.42% increase in accuracy for Logistic regression, Support Vector Machine, Decision Tree (DT), and Naive Bayes (NB) consecutively for Amazon food products dataset. Consecutively, 9.4%, 3%, and 2% improvement for Logistic Regression (LR), Support Vector Machine (SVM), and Naive Bayes for electronic dataset.

Keywords: : Conditional Random Field, Decision Tree, Logistic Regression, Machine Learning, Naive Bayes, Support Vector Machine.

1. Introduction

The proposed work demonstrates negation scope detection with various syntactic and lexical features trained using CRF then this scope is used for negation handling. Further, sentiment classification of reviews is done using a customized stopwords list and calculated polarity of reviews after negation handling by considering the impact of negations on each word in a sentence. Finally, sentiment analysis is performed on these sentences. In the proposed work a customized stopwords list is being used that only removes limited words from sentences. But, this list will not remove negations like can't, wouldn't, etc. that affect the polarity of sentences. This method deals with explicit negations where negative words are present in the data and the results depict that the accuracy of sentiment analysis is enhanced with the use of negation handling.

Sentiment analysis is a key sub-domain of natural language processing, which is an integral part of ML technology. This technology space is catalyzed by how well human language is understood, making it necessary for global firms to stay competitive. Businesses analyze the emotions and attitudes of customers towards a product by performing sentiment analysis of reviews and feedback provided by customers over numerous e-commerce and social media platforms. In such analysis, some challenges make it arduous to gauge the real emotions of consumers, and negation is identified as one such key challenge. Negations refer to negative words in a sentence that can affect the orientation of sentiments. It is one of the linguistic phenomena that leads to flipping the polarity of reviews or feedback and results in wrong predictions of sentiments. For instance, *"I hate this product less than I used to"*, here, *"less than I used to"* act as a sentiment shifter. Some other examples are *"fairly good, but not of my style"*, *"I don't dislike this movie"*, where *"not"* and *"don't"* are the negations and if removed will lead to sentiment orientation change [1]. Literature review revealed that during the classification of sentiments, usually the stopwords (no, I, we, you, they, the, not, is, am, are, cannot, etc.) are removed in the preprocessing phase given by [2], [3], [4], [5], [6], [7], [8], and [9] because it helps to bring down the dimensions of text for classification. Some of the negative stopwords are responsible for accurate sentiment predictions, however, if eliminated may lead to polarity flipping. For instance, *"He is not a bad boy"*, here *"not"* is one of the stopwords and its removal may flip the

E-mail address: sonikartika19@kuk.ac.in, pmittal@kuk.ac.in, monikaporiye@gmail.com

polarity of the sentence. Negations may be implicit and explicit given by [10] and this research deals with explicit negations. Explicit negations are those negations in which negation cue is present (no, not, nothing, don't etc.) in the sentence. The adverse impact of negations on the sentiment orientation of text has been spotted by [1], [11]. Many approaches such as rule-based [11], [12], regular expression based [13], lexicon-based [14], semantic, syntactic, and linguistic features-based given by [15]. Rule-based and lexicon approaches have limited scope and are unable to handle complex linguistic structures due to domain dependency. It also requires human intervention for creation and maintenance. However, ML approaches are better and minimize the manual work given by [16], [16] for negation scope detection. UCM-I [17] and UCM-II [13] are two rule-based approaches used for negation cue and scope detection. These two approaches properly finding negation cues and scopes but UCM-II [12] was not able to properly manage the sentences having two or more scopes corresponding to cues in a sentence. Moreover, UCM-I [17] also works well but it fails to determine the proper scope of negations when subject and object of some events are negated. In the Proposed approach these shortcomings are handled using ML approach to find the scope of negations. According to the literature, it is revealed that there are very few approaches that perform negation handling and sentiment analysis [16], [18] after negation scope detection and handling. Numerous approaches perform only negation cue and scope detection. In this research, not only negation cues and scope are detected but we also handle the impact of negation and find the correct polarity of the sentence then sentiment analysis is done using Amazon datasets. In the proposed approach, negation scope detection is performed using CRF and sentiment analysis using supervised ML [19] classifiers such as SVM, LR, DT, and NB. As per our literature knowledge, few ML approaches [1], [15], [16], [18], [20] and [21] utilize negation scope detection, and handling in sentiment analysis. Among these approaches, only [21], [1], and [21] are compared with the proposed approach for sentiment analysis after negation handling. In the proposed approach LR exhibits 85%, 86%, and SVM exhibits 85%, 83% accuracy for product and electronics datasets. This accuracy is improved as compared to [21], [1], and [20] but the performance of NB declined to 71%, 70% as compared to [1]. For scope detection, the proposed approach gives a 98% f-score which is better than [22], [23], [17] and [12].

This article is divided into six sections where sections 1 and 2 lead with an introduction and related work. Sections 3 to 6 explain the proposed methodology, results, and the final comparison to existing approaches, and conclusion.

2. Related Work

The rule-based approach is a static and manual technique to resolve the negation challenge. It involves the manual creation of regular expressions to handle negations but due to the dynamic nature of negation, these static rules are unable to determine all the contextual relations among all the words. NegEX is one such negation handling approach used in the medical domain and due to its static nature, it may cause wrong predictions of patient data given by [24]. One of the limitations of this work is the wrong interpretation of word's sentiment if same word appears more than once in a sentence. For instance, *"the patient was placed under neutropenic precaution, and two days later the patient was no longer neutropenic"*. In this sentence first *"neutropenic"* was interpreted by the model as positive and second as negative. To minimize this error rate, a DEEPEN algorithm was proposed that can consider dependency relations among all the words. It uses the Stanford dependency parser (SDP) and helps to reduce incorrect predictions with an accuracy of 91% and 97% given by [13]. One of the major limitations of this work is some of the dependency relations generated by SDP are not accurate for clinical data because the SDP was created using English web Treebank. This tree bank contains only the sentences of newsgroups, weblogs etc. Lexicon-based approach makes use of pre-annotated lexicons which consist of words and their sentiment intensity. SentiWordNet (SWN) is one such lexicon that provides various English words and their polarity given by [18], and an antonym dictionary given by [25] for assigning antonyms. A lexicon-based sentiment analyzer with negation handling for the Urdu language also improves the efficiency of sentiment analysis due to the use of a vast lexicon for the Urdu language, effective negation handling, intensifiers, and context-dependent words for the Urdu language given by [14]. However, this approach has some limitations such as it assigns neutral sentiment to a sentence in the absence of any positive or negative word, for instance *"Is there any solution to this problem?"*. Although, the polarity of this sentence is positive. Lexical approaches were unable to determine the dependency of words, so the semantic disambiguation technique given by [18] was proposed to find the sentiments of sentences. Here, correct negation words were determined by including grammatical relations among words. Rule-based and lexical approaches require manual work for creation and maintenance. For automation and better results ML approaches are used by [16]. Once these models are trained with the required data, they can make predictions according to learned patterns. In [16] it was revealed that due to the presence of multiword cues the classifier performs wrong classifications. In [26] Explicit negations were handled using ML approaches and it was revealed that the performance was improved with negation handling. While performing negation handling it is essential to maintain the semantics of words in a sentence. So, a feature-based negation handling model was introduced that can extract semantic and syntactic features such as lexicon features, POS, n-gram, and morphological features. The inclusion of these features with negation handling enhanced the accuracy of SVM, NB, and DT for sentiment analysis of tweets given by [15]. In [20] a mathematical modelling approach was introduced for negation handling in sentiment analysis, but this approach has several limitations such as it interprets wrong polarity of sentences when

there are multiple positive and negative parts in a sentence. However, proposed approach handle this by finding the proper scope of negative words in a sentence using CRF. In proposed approach negation scope detection, handling is done and finally the sentences generated after negation handling are used for sentiment analysis.

3. Proposed Methodology for Negation Scope Detection and Handling in Sentiment Analysis

This section presents the research methodology used for negation cue, scope detection, negation handling, and sentiment analysis of user review as shown in Figure 1. Here, processed Conan Doyle dataset is trained using various lexical and syntactic features for BIO (begin, inside, outside) labels prediction. After performance evaluation, this trained CRF is used for scope prediction in Amazon dataset. Finally sentiment analysis is done before and after negation handling.

A. Data collection

In this research, Conan Doyle's (Sherlock) story dataset annotated with negation cue and scope is used to train and test CRF for negation scope prediction using BIO (beginning, inside, outside) labels. This dataset is collected from GitHub, and another two datasets used in this research are related to consumer reviews (electronics and food products) collected from amazon.com and kaggle.com. These datasets consists of various attributes such as UserId, profile name, helpfulness numerator, helpfulness denominator, score, time, summary and text. Among all these attribute score and text attributes are used in the proposed method. These datasets consist of various anomalies removed by applying data cleaning.

B. Data cleaning and transformation

In data cleaning, all the numbers, special characters, HTML tags, and hyperlinks are removed from the dataset. Data cleaning ensures there should not be any unwanted characters present in the data, increasing the dimensions of the data given by [27]. Further, each sentence is split into different rows to work with each word in that sentence. Subsequently, these datasets are used for negation scope prediction, negation handling, and sentiment analysis of reviews with and without negation handling.

C. Negation Cue and scope detection

Negation cue prediction is considered a classification problem and 0, 1 (cue, non_cue) is assigned to all the tokens in the dataset. 1 is assigned to tokens annotated with B_cue and 0 is assigned to other tokens. Also, an additional lexicon of cues is provided for better prediction of cues. Negation cues may impact the polarity of words in a sentence, and negation scope helps to determine those affected words. To determine the correct scope of cues various syntactic and lexical features of cues, tokens, and neighboring tokens are required. These features help to predict the scope in the form of BIO labels in a sentence. In this work ML approach is used to find the scope of negation which perform well as compared to static approaches.

1) Features for Scope Detection

It is an important phase for a machine [2] learning model to be more specific and efficient about predictions. The feature of raw data helps the model to learn and predict the patterns of data. In this research, various token-level features have been extracted and transformed into vector form for the predictions of the negation scope. Various token level features of targeted word, preceding and subsequent word of the targeted word such as parts of speech (POS) tag, lemma of cue and token are extracted.

$$(lemma_{i+1}, POS_{i+1}, lemma_{i-1}, POS_{i-1}, lemma_i, POS_i)$$

Along with the features of cue and token, the neighboring features of cue and token are also used for negation scope prediction. All these features are vectorized and provided to the classifier for scope prediction in data. In addition to these features, a lexicon of explicit cues is also provided. All features used for scope prediction are mentioned in Table 1. The final list of lexical and syntactic features used to detect the scope is determined by performing various experiments. In these experiments, we used different lexical and syntactic features, and it was revealed that both lexical and syntactic features are important for scope prediction. This list of features improves the prediction of BIO labels rather than using other combinations of lexical and syntactic features. Natural Language ToolKit (NLTK) provides WordNetLemmatizer() to find the root word and the POS tagger provides noun, verb, adjective, adverb, etc. tags to the words in a sentence. These tags help to determine the syntactic structure and text information of a sentence. To find the relationship among all the neighboring words the features of neighboring words such as chain of POS, lemma, cue and focused word, etc. are also provided to CRF for BIO labels prediction. Figure 2 shows the dependency graph for the sentence *"not good i would never buy it again"*. This figure represents the dependencies using edges and nodes which shows the semantic relationship among these edges and nodes. To find the path between *"not"* and *"buy"*, it is required to traverse the path between these two nodes. The critical path between *"not"* and *"buy"* is neg ↑ccomp, number of traversed nodes is 2. Similarly, the path between the node *"again"* and *"good"* is ↓advmod ↑ccomp.
Table 1 shows various lexical feature such as POS tag and lemma of cue and focused word. Along with the features of cue and focused words chain of features is also provided for neighboring words. Similarly, syntactic features such as dependency information for cue and neighboring words are also provided in the form of features as shown in Figure 2.

2) Training and Testing of CRF for Scope Prediction using BIO Labels

The whole dataset is split into train (80%), and test (20%) data for training and testing of CRF. In ML, the CRF is mainly used for sequence labeling tasks by considering the label of dependent tokens. CRF is a class of probabilistic graphical models that learn various features and patterns of input text during training. Based on the learned patterns it

TABLE I. FEATURES USED FOR NEGATION SCOPE PREDICTION

Feature	Description
Token	Focused word
BOS	Beginning of sentence
EOS	End of sentence
Cue	Negative word
Lemma_cue	The root form of the cue
POS_cue	Parts of speech of the cue
Chain_lemma	Lemma of neighboring words
Chain_POS	Parts of speech of neighboring words
Dependency information	Traversed syntactic dependency direction and relation of the edge
Critical path	Shortest dependency path from cue to the focused token
Nodes	Count of nodes to be traversed in the critical path

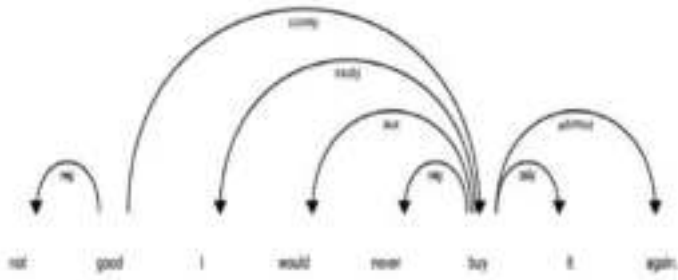

Figure 1. Dependency graph of a sentence.

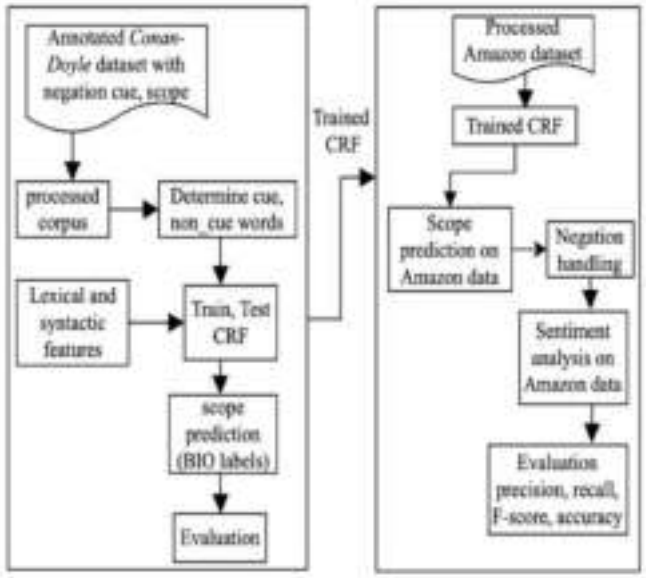

Figure 2. Proposed methodology for negation detection and handling in sentiment analysis.

predicts the labels of each token [28] shown in Equation 1. The conditional probability of labels Y for a given input sequence W can be represented as

$$P(Y|W) = \frac{1}{Z(W)} \prod_{i=1}^{m} exp\left(\sum_{j=1}^{n} \lambda_j . f_j(y_i, y_{i-1}, w, i)\right) \quad (1)$$

Where:

$P(Y|W)$ denotes the conditional probability of label sequence Y given input sequence or token W.
$Z(W)$ denotes the partition function which, for a given input sequence, normalizes the probability to sum up to 1 over all possible label sequences.
λ_j are the weights/parameters associated with each feature.
$f_j(y_i, y_{i-1}, w, i)$ represents a feature function that finds the relationship between negation cues and label sequence at position i.
y_i, y_{i-1} represent the BIO labels that can be B (begin), I (inside), or O (outside) or negation_cue for token w at position i.

This function checks the presence of negation at position i and the model learns the weights λ_j of features during training and based on the learned relationships model predicts the labels of tokens in the prediction step. CRF works with two types of features i.e. document specific features and word embedding features. In Equation 1 CRF is trained with both features. In Figure 1 CRF is trained and tested on Conan Doyle dataset for BIO labels prediction. Then the trained CRF model is stored in a Python pickle file, this trained model is used to make predictions of BIO labels on Amazon dataset as shown in Figure 1 and the predicted BIO labels are shown in Table II. Consequently, negation handling, polarity prediction of reviews, and sentiment analysis is done on Amazon datasets using predicted polarity (1, 0, -1). Table II shows the sentence number, token number corresponding token and predicted BIO of each token in a sentence.

D. Negation Handling

Scope of negation cues are predicted in the form of BIO labels then determine the sentiment strength of each token in a sentence using SWN. Next, flip the polarity of each word inside the BIO scope i.e. affected by the negation cue, and make the value of cue=0. The polarity of each sentence is calculated by the sum of all the polarities of tokens in a sentence. Here, a threshold of 0.7 is used if the calculated polarity is less than 0.7 then it is given a polarity score of -1 for greater than it is 1 and equal to 0.7 it is considered as 0. This final predicted polarity is considered for the final sentiment analysis of reviews.

TABLE II. Displays the predicted BIO Labels on the Amazon Dataset

Sent_no	Token_no	Token	BIO_Label
74	2	is	I_scope
74	3	okay	I_scope
74	4	i	I_scope
74	5	would	I_scope
74	6	not	B_cue
74	7	go	B_scope
75	1	no	B_cue
75	2	tea	B_scope
75	3	flavor	I_scope
75	4	at	I_scope
75	5	all	I_scope

TABLE III. Displays the Accuracy and F-Score of CRF for Negation Scope Prediction

CRF	Accuracy	F-Score
Train Data	99.7%	99.7%
Test Data	98.4%	98.3%

TABLE IV. Results of sentiment analysis for Product dataset before Negation Handling

Amazon (Food Products Dataset)				
Before negation handling				
ML Model	F-Score	Recall	Precision	Accuracy
LR	81.9 %	82.9 %	81.1 %	83.0 %
SVM	81.5 %	82.4 %	80.7 %	83.2 %
DT	73.2 %	73.3 %	73.4 %	73.0 %
NB	68.7 %	67.7 %	69.8 %	70.0 %

TABLE V. Results of sentiment analysis for Product dataset after Negation Handling

Amazon (Food Products Dataset)				
After negation handling				
ML Model	F-Score	Recall	Precision	Accuracy
LR	86.2%	86.3%	86.1%	86.0%
SVM	85.5%	85.6%	85.4%	85.4%
DT	75.4%	75.4%	75.5%	75.4%
NB	69.2%	68.7%	69.9%	71%

TABLE VI. Results of sentiment analysis for Electronics dataset before Negation Handling

Amazon (Electronic Dataset)				
Before negation handling				
ML Model	F-Score	Recall	Precision	Accuracy
LR	82.4%	82%	83%	84.4%
SVM	74.5%	74.5%	74.6%	81%
DT	67.3%	67.3%	67.3%	67.4%
NB	68.5%	68.6%	68.5%	68.6%

TABLE VII. Results of sentiment analysis for Electronics dataset after Negation Handling

Amazon (Electronic Dataset)				
After negation handling				
ML Model	F-Score	Recall	Precision	Accuracy
LR	85.1%	85.5%	85.2%	85.2%
SVM	75.49%	75%	76%	83.4%
DT	67.4%	67.5%	67.4%	67.4%
NB	69.2%	68.7%	69.8%	70%

E. Sentiment Analysis

Sentiment analysis of Amazon datasets is performed using the predicted polarity. This calculated polarity is used in the next phase of sentiment analysis. The classification of sentences is executed using supervised ML algorithms due to their enhanced performance in classification given by [19]. SVM, LR, DT, and NB classifiers are used before and after the negation handling of reviews. Before negation handling, the sentiment analysis is done using original polarity, and post negation handling the sentiment analysis is performed using the predicted polarity by the proposed system. The results indicate an improvement in the classification performance after negation handling and all the used classifiers are given below.

1) Logistic Regression (LR)

For multiclass classification LR uses Equation 2 as shown below to predict the output.

TABLE VIII. DISPLAY THE COMPARISON OF VARIOUS APPROACHES FOR NEGATION SCOPE PREDICTION USING CONANDOYLE DATASET (SHERLOCK)

Paper	Approach	F-score
[12]	Rule based	76.03%
[13]	Rule based	62.65%
[18]	ML (Deep parsing system)	88.2%
[23]	ML(SVM)	76.23%
Proposed approach	ML(CRF)	98.3%

TABLE IX. COMPARISON OF VARIOUS APPROACHES FOR SENTIMENT ANALYSIS AFTER NEGATION HANDLING.

Paper	Dataset	Approach	Accuracy	Precision	Recall	F-score
[1] Xia et al.	Electronics	LR	83.4%	–	–	–
		SVM	83%	–	–	–
		NB	82.5%	–	–	–
[29]Li et al.	Electronics	SVM(stacking)	83%	–	–	–
[20] Punetha et al.	Products	NEGVOT	83%	84%	81%	80%
Proposed approach	Product	LR	86%	86.1%	86.3%	86.1%
		SVM	85.4%	85.4%	85.6%	85.5%
		NB	71.1%	69.9%	68.7%	69.2%
Proposed approach	Electronics	LR	85.2%	85.2%	85%	85.1%
		SVM	83.4%	76%	75%	76%
		NB	70%	69.8%	68.7%	69.2%

$$P(Y=1|X) = \frac{1}{1+e^{-(\beta_0+\beta_1 x_1+\beta_2 x_2+\ldots+\beta_n x_n)}} \quad (2)$$

Where :
$P(Y = 1 \mid X)$ *represents the probability of the class label 1 for given input feature* X.
e *represents the base of natural logarithm.*
$\beta_0, \beta_1, \beta_2, \ldots, \beta_n$ *represents the coefficients (weights) corresponding to each feature* $x_1, x_2, \ldots, x_n$.
x_0, *set to 1, corresponding to the intercept term.*

2) Support Vector Machine (SVM)

SVM is a supervised ML model that is used to resolve regression and classification challenges. It is used to resolve linear and non-linear problems by generating hyperplanes to separate different data points into different categories. SVM performs classification using Equation 3 given below.

$$f(x) = \text{sign}\left(\sum_{j=1}^{n} \alpha_j y_j \langle x, x_j \rangle + b\right) \quad (3)$$

where :
$f(x)$ *represents a decision function that determines the class labels for input* x. x_0 *is set to 1, corresponding to the intercept term.*
α_j *represents the Lagrange multiplier that is determined during training.*
y_j *denotes class labels.*
x_j *denotes class labels.*
$\langle x, x_j \rangle$ *represents the dot product between the support vector* x_j *and the input vector* x.
b *represents the bias.*

3) Decision Tree (DT)

It is a supervised ML model that can be used for both regression and classification problems. It is in tree form and consists of three parts i.e. branch, internal node and leaf node. Branch represents decision, internal node represents feature and leaf represents label. This algorithm selects the best features based on entropy and gini impurity etc. and continue until some criteria are met. Then it makes predictions by traversing the tree from root to leaf node [27].

4) Naive Bayes (NB)

It is a probabilistic classification model that can be used for both binary and multi-class classification problems by considering the probability of each element [27]. It is an easy-to-implement and fast algorithm that converges faster than LR and requires less training data. NB predicts the output according to Equation 4 given below.
NB selects the class that maximizes posterior probability $P(C \mid X)$ for classification.

$$P(C|X) \propto P(C). \prod_{i=1}^{n} p\left(x_i|C\right) \quad (4)$$

Where :
$P(C \mid X)$ *represents the posterior probability of class* C *for feature* X.
$P(C)$ *represents the probability of element belong to class* C.
n *represents the number of features* x_i is the i^{th}feature in the instance.

4. Experimental Setup and Results

In this research, all the implementation has been executed on Jupyter Notebook using Python 3.7 along with 16 GB RAM and i7 processor. In this research, three datasets are used as discussed in section 3.1. Among all these datasets Conan Doyle's (Sherlock) story dataset is used to train and test CRF with lexical and syntactic features described in section 3. Then this trained CRF is

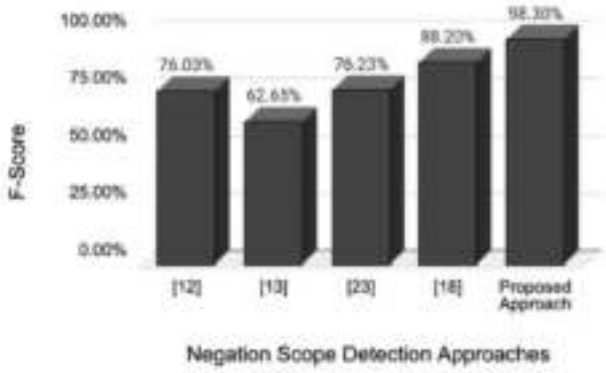

Figure 3. Comparison of various approaches and the proposed method for negation scope detection.

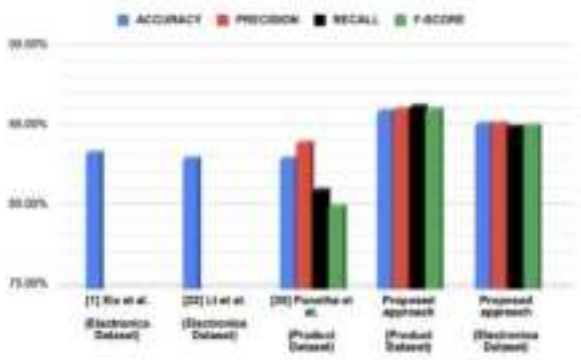

Figure 4. Performance comparison of various sentiment analysis approaches across electronic and product datasets.

used to predict the scope of negation on Amazon datasets. Further, negation handling is performed on Amazon datasets and sentiment analysis is done after and before negation handling using LR, SVM, DT, and NB with K=5 (K stands for K-fold cross-validation) as shown in Table IV, V, VI and VII and the detailed description of implementation is given in the various parts of section 3.

Table III shows the training and test results of the CRF for negation scope prediction. According to the results, the performance of CRF is pretty good for negation scope prediction in comparison to approaches given in Table VIII. From Tables IV and V, it is identified that LR and SVM, DT, and NB give better performance for all metrics after negation handling. Table IV and V shows that there is 3.61%, 2.64% 2.7% and 1.42% increase in accuracy for LR, SVM, DT and NB for food product dataset. Consecutively, 9.4%, 3%, and 2% improvement for LR, SVM, and NB for electronic dataset.

5. Discussion and Comparison

Table VIII shows the performance of the proposed approach is better as compared to other approaches for scope prediction. Table IX shows the comparison of the proposed approach with [1], [20] and [21] for sentiment analysis after negation handling. In all these approaches different datasets are used but comparison is performed only with products and electronics datasets because these are common datasets among proposed and compared approaches.

Table IX demonstrates that the accuracy of sentiment analysis after negation handling gives better performance as compared to other approaches. LR gives 86%, 85%for both datasets which is better than [1], [20], and [29]. SVM also gives an improved accuracy of 85% and 83.4%, but NB performs poorly compared to [1] for sentiment classification after negation handling. In case of f-score, the proposed approach performs poorly with 71% for product dataset but NEGVOT gives 80% score. Also, figure 4 shows that NEGVOT performs well in precision, recall and F-score for NB. NEVGOT also gives improved precision and recall score of 84% and 81% as compared to SVM on the electronics dataset. Figure 3 shows the performance comparison of the proposed approach and various approaches using F-score for negation scope prediction. From Figure 3 it is revealed that the proposed approach gives a 98.3% score which is 11.3% enhancement compared to [22].

From the literature, we found most of the approaches limit their work up to negation cue and scope detection and there are limited approaches that perform negation handling and sentiment analysis after finding negation cues and their scope. However, the proposed work also has a few limitations for instance, if the model is unable to find the negation properly then it can cause a wrong prediction of the scope and polarity of the sentence which can cause the wrong classification of sentences. To resolve these challenges we will try to enhance the performance of the proposed work using deep learning techniques in our future work.

6. Conclusion and Future Directions

Negation is responsible for affecting the orientation of sentiments. To resolve this challenge and to improve sentiment accuracy a negation scope detection, and handling approach is proposed. Various experiments were carried out on different datasets using the proposed approach and the results revealed that the majority of ML classifiers enhance the accuracy of sentiment analysis with negation handling. Hence, it can be inferred that the proposed approach when used with sentiment analysis proves to be more efficient. However, in this research, only explicit negations are handled. In future work, explicit negations may be analyzed using deep learning techniques. Moreover, in the future, the proposed method may also be applied to mixed language datasets.

References

[1] R. Xia, F. Xu, J. Yu, Y. Qi, and E. Cambria, "Polarity shift detection, elimination and ensemble: A three-stage model for document-level sentiment analysis," *Information Processing & Management*, vol. 52, no. 1, pp. 36–45, Jan. 2016, number: 1. [Online]. Available: https://linkinghub.elsevier.com/retrieve/pii/S0306457315000485

[2] A. Asiaee T., M. Tepper, A. Banerjee, and G. Sapiro, "If you are happy and you know it... tweet," in *Proceedings of the 21st ACM international conference on Information and knowledge management*. Maui Hawaii USA: ACM, Oct. 2012, pp. 1602–1606.

[3] A. Bakliwal, P. Arora, S. Madhappan, N. Kapre, M. Singh, and V. Varma, "Mining sentiments from tweets," 2012, pp. 11–18.

[4] B. Gokulakrishnan, P. Priyanthan, T. Ragavan, N. Prasath, and A. Perera, "Opinion mining and sentiment analysis on a twitter data stream." IEEE, 2012, pp. 182–188.

[5] E. Kouloumpis, T. Wilson, and J. Moore, "Twitter sentiment analysis: The good the bad and the omg!" vol. 5, 2011, pp. 538–541, issue: 1.

[6] A. Pak and P. Paroubek, "Twitter as a corpus for sentiment analysis and opinion mining." vol. 10, 2010, pp. 1320–1326, issue: 2010.

[7] M. Speriosu, N. Sudan, S. Upadhyay, and J. Baldridge, "Twitter polarity classification with label propagation over lexical links and the follower graph," 2011, pp. 53–63.

[8] H. Raza, M. Faizan, A. Hamza, M. Ahmed, and N. Akhtar, "Scientific text sentiment analysis using machine learning techniques," *International Journal of Advanced Computer Science and Applications*, vol. 10, no. 12, 2019, number: 12 Publisher: Science and Information (SAI) Organization Limited.

[9] C. J. Fox, "Lexical Analysis and Stoplists." 1992.

[10] K. Makkar, P. Kumar, and M. Poriye, "Improvisation in Opinion Mining Using Negation Detection and Negation Handling Techniques: A Survey," in *Soft Computing: Theories and Applications*, R. Kumar, A. K. Verma, T. K. Sharma, O. P. Verma, and S. Sharma, Eds. Singapore: Springer Nature Singapore, 2023, vol. 627, pp. 799–808, series Title: Lecture Notes in Networks and Systems. [Online]. Available: https://link.springer.com/10.1007/978-981-19-9858-4_68

[11] M. Wiegand, A. Balahur, B. Roth, D. Klakow, and A. Montoyo, "A survey on the role of negation in sentiment analysis," 2010, pp. 60–68.

[12] M. Ballesteros, A. Díaz, V. Francisco, P. Gervás, J. C. de Albornoz, and L. Plaza, "UCM-2: a rule-based approach to infer the scope of negation via dependency parsing," 2012, pp. 288–293.

[13] W. W. Chapman, W. Bridewell, P. Hanbury, G. F. Cooper, and B. G. Buchanan, "A simple algorithm for identifying negated findings and diseases in discharge summaries," *Journal of biomedical informatics*, vol. 34, no. 5, pp. 301–310, 2001, number: 5 Publisher: Elsevier.

[14] N. Mukhtar and M. A. Khan, "Effective lexicon-based approach for Urdu sentiment analysis," *Artificial Intelligence Review*, vol. 53, no. 4, pp. 2521–2548, 2020, number: 4 Publisher: Springer.

[15] I. Gupta and N. Joshi, "Feature-based twitter sentiment analysis with improved negation handling," *IEEE Transactions on Computational Social Systems*, vol. 8, no. 4, pp. 917–927, 2021, number: 4 Publisher: IEEE.

[16] N. P. Cruz, M. Taboada, and R. Mitkov, "A machine-learning approach to negation and speculation detection for sentiment analysis," *Journal of the Association for Information Science and Technology*, vol. 67, no. 9, pp. 2118–2136, 2016, number: 9 Publisher: Wiley Online Library.

[17] J. C. de Albornoz, L. Plaza, A. Díaz, and M. Ballesteros, "Ucm-i: A rule-based syntactic approach for resolving the scope of negation," 2012, pp. 282–287.

[18] A. Hogenboom, P. Van Iterson, B. Heerschop, F. Frasincar, and U. Kaymak, "Determining negation scope and strength in sentiment analysis." IEEE, 2011, pp. 2589–2594.

[19] K. Makkar, P. Kumar, M. Poriye, and S. Aggarwal, "A Comparative Study of Supervised and Unsupervised Machine Learning Algorithms on Consumer Reviews," in *2022 IEEE World Conference on Applied Intelligence and Computing (AIC)*. Sonbhadra, India: IEEE, Jun. 2022, pp. 598–603.

[20] N. Punetha and G. Jain, "Optimizing sentiment analysis: a cognitive approach with negation handling via mathematical modelling," *Cognitive Computation*, vol. 16, no. 2, pp. 624–640, 2024.

[21] S. Li, S. Y. Lee, Y. Chen, C.-R. Huang, and G. Zhou, "Sentiment classification and polarity shifting," 2010, pp. 635–643.

[22] W. Packard, E. M. Bender, J. Read, S. Oepen, and R. Dridan, "Simple negation scope resolution through deep parsing: A semantic solution to a semantic problem," 2014, pp. 69–78.

[23] *UABCoRAL: a preliminary study for resolving the scope of negation*, 2012.

[24] S. Mehrabi, A. Krishnan, S. Sohn, A. M. Roch, H. Schmidt, J. Kesterson, C. Beesley, P. Dexter, C. M. Schmidt, and H. Liu, "DEEPEN: A negation detection system for clinical text incorporating dependency relation into NegEx," *Journal of biomedical informatics*, vol. 54, pp. 213–219, 2015, publisher: Elsevier.

[25] S. Zirpe and B. Joglekar, "Negation handling using stacking ensemble method." IEEE, 2017, pp. 1–5.

[26] P. Mukherjee, Y. Badr, S. Doppalapudi, S. M. Srinivasan, R. S. Sangwan, and R. Sharma, "Effect of negation in sentences on sentiment analysis and polarity detection," *Procedia Computer Science*, vol. 185, pp. 370–379, 2021, publisher: Elsevier.

[27] K. Makkar, P. Kumar, M. Poriye, and S. Aggarwal, "Improvisation in opinion mining using data preprocessing techniques based on consumer's review," *International Journal of Advanced Technology and Engineering Exploration*, vol. 10, no. 99, Feb. 2023, number: 99. [Online]. Available: https://www.accentsjournals.org/paperInfo.php?journalPaperId=1520

[28] K. Patel and C. Caragea, "Exploring word embeddings in crf-based keyphrase extraction from research papers," in *Proceedings of the 10th International Conference on Knowledge Capture*, 2019, pp. 37–44.

[29] S. Li, S. Y. Lee, Y. Chen, C.-R. Huang, and G. Zhou, "Sentiment classification and polarity shifting," in *Proceedings of the 23rd international conference on computational linguistics (Coling 2010)*, 2010, pp. 635–643.

Kartika Makkar has received her Master's degree in Computer Science & Applications from the Department of Computer Science & Applications. Now, she is pursuing Ph.D. in Computer Science & Applications from the Department of Computer Science & Applications, Kurukshetra University, Kurukshetra (Haryana) and her current research work is in Machine Learning and NLP. Email: sonikartika19@gmail.com

Dr. Pardeep Kumar received his PhD in Computer Science & Applications from Kurukshetra University, Kurukshetra. Presently he is working as Associate Professor in Kurukshetra University, Kurukshetra. His research interest lies in Optimization, Cloud Computing, Network Routing, and Soft Computing. He has published more than 75 research papers in referred journals and international conferences. Email: pmittal@kuk.ac.in

Dr. Monika Poriye is currently working as an Assistant Professor in the Department of Computer Science & Applications, at Kurukshetra University. She has completed her doctorate in Computer Science & Applications from Kurukshetra University, Kurukshetra. Her areas of interest are Information Security, Web Development, Cloud Computing, Machine Learning, etc. Email: monikaporiye@gmail.com

Dr. Shalini Aggarwal is currently working as an Assistant Professor in the Department of Computer Science, S.U.S. Govt. College, Matak Majri, Indri (Karnal). She has done her Ph.D. in Computer Science & Applications from the Department of Computer Science and Applications at Kurukshetra University, Kurukshetra in the field of Computer Networks.Her research areas include Computer Networking, Machine Learning, Soft Computing, etc. She is having more than 16 years of teaching experience and more than 10 years of research experience. Email: aggshamit@gmail.com

INTERNATIONAL JOURNAL OF RESEARCH CULTURE SOCIETY

A monthly Peer-Reviewed, Refereed, Indexed International Research Journal

UGC Approved Journal No. : 64291

Certificate of Publication

is awarded to

For the research paper / article entitled

The Linguistic and Sociopolitical Dimensions of Control in George Orwell's Nineteen Eighty-Four

Published in IJRCS Volume - 8, Issue - 4, April - 2024.

DOIs:10.2017/IJRCS/202404017

IMPACT FACTOR : 7.148

PAPER ID : IJRCS202404017

The Managing Editor
Research Culture Society and Publication
WWW.IJRCS.ORG
Email: editorijrcs@gmail.com
Email: editor@ijrcs.org

Journal of the Oriental Institute

CERTIFICATE OF PUBLICATION

This is to certify that the article entitled

ADVANCING MULTI-CRITERIA DECISION MAKING IN INTUITIONISTIC FUZZY ENVIRONMENTS: A LINGUISTIC ASSESSMENT APPROACH

Authored By

Mr. Raj Kumar
Assistant Professor of Mathematics, S.U.S. Government College, Matak-Majri, Karnal

Published in

Journal of the **Oriental Institute** ; ISSN: 0030-5324

Vol. 73, Issue. 01, No. 1, January - March: 2024 **I.F.-7.3**

UGC Care Approved, Group I,
Peer Reviewed and Referred Journal

Editor
B. J. Sandesara

THE MAHARAJA SAYAJIRAO UNIVERSITY OF BARODA
सत्यं शिवं सुन्दरम्